



Fisica

CORSO DI DOTTORATO DI RICERCA IN

XXXVII

CICLO DEL CORSO DI DOTTORATO

*Probing the geometry and the evolution of the Universe with
Cosmic Voids*

Giulia Degni

Nome e cognome del dottorando

firma

Prof. Giorgio Matt

Supervisor e Coordinatore del corso di Dottorato

firma

Prof. Enzo Branchini

Co-supervisor

firma

Prof. Helene Courtois

Co-supervisor

firma

Dr. Elena Sarpa

Co-supervisor

firma



Ph.D. in Physics
37th Cycle

Ph.D. Thesis

Titolo

Ph.D. candidate: Giulia Degni

Supervisor: Giorgio Matt

Co-supervisor: Enzo Branchini

Helene Courtois

Elena Sarpa

To Raffaella and Attilio

Acknowledgements

I truly thank my supervisors. Their wise guidance has been essential to the success of this work. I am grateful to Enzo for his immense generosity and for encouraging my academic growth over the years. To Helene, I extend my thanks for her wisdom, enthusiasm, and boundless support. I thank Giorgio for his constant availability and for accompanying me throughout these three years. Finally, I offer my gratitude to Elena for the interest she devoted to this project.

Together with my supervisors, I am grateful to all my collaborators, who generously shared their deep expertise with me and who conveyed their enthusiasm, a precious gift in this work. Special thanks to Alice, Marie (*Merci Marie*), Giovanni, Simone (a dear brother to whom I can only say *mmmM mm mmm*), Sofia, Carlos, Nico, and my greatest cheerleader, Mar, whose motto “*Visteme despacio que tengo prisa*” I’ve taken to heart. You are all amazing, incredible, and full of energy; it is an honor to work with you.

This PhD journey has felt like a voyage, one that brought me to new places, led me to explore fascinating topics, and, most importantly, allowed me to meet people who enriched every step of this adventure. In these pages, I seize the opportunity to leave a mark of deep gratitude, a lasting record of the appreciation I hold for each encounter and each lesson learned.

My journey began at Roma Tre, where I met my colleagues. We walked the same path, always encouraging one another. I thank you all from the bottom of my heart; I will miss our days in Aula 81. I am grateful to everyone, especially those with whom I share a special bond: my wonderful friends Vittoria and Elisabetta, Matteo, Daniele, Raul, Ivano, Gabriele, Ottavio Tuno, Simone, Roberto, Paolo, Andrea, Sacha, Silvia, Romy, Rita, and many more. There are so many of you—please forgive me if I haven’t mentioned every name.

This journey then led me to other stops in Genova, where I met wonderful people I am eager to thank: Antonio, Ilaria, Punya, and everyone else. I am especially grateful to Alfonso, a constant support, whom I consider a friend.

Over these three years, I ventured even further, to Lyon and New York, where I had the privilege of joining the cosmology groups and meeting incredible people at IP2I and CCA who made me feel at home. Special thanks to Mar, Kate, Giulio, Lucrezia, Elisa, and Ginevra.

And I can’t forget the fantastic people I met at EAS 2022: the RadioCity group, Pierluigi, Ariel, and Alessandro.

Finally, my last stop was Bologna. I thank the PhD students and postdocs for welcoming me into their group, where enthusiasm shines both in life and in science. My heartfelt thanks to Professor Marulli, who, with a touch of irony, understood and softened my moments of despair, making the journey all the more enjoyable, *saluti*.

And then there is someone who has been there for every step of this journey; we crossed paths, chose each other, and he became my endless source of happiness and strength. Dear Massimo, I thank you with all my heart.

Outside this complex academic world, I have been blessed with the immense support of my friends. I am truly fortunate to have you, and while here you may only seem like a point on a list, to me, you are so much more. Thank you to my closest friends for always standing by me, for sharing your wisdom, and for bringing me the priceless gift of joy. Thank you to my best friend Claudia, to my lifelong friend Irene, to my precious friends Martina and Benedetta, and to my adventure companion Rigerta.

In addition, there are whole constellations of friends to whom I am deeply grateful for believing in me and for making every moment joyful. Starting with the Amiketti: Alessandro, Ginevra, Sabrina, Adi, Federica, Alessandro, Andrea, Marrero, Claudia, Chiara, Marco, Giulia, Stefan, Eleonora, Fabrizia, Lorenzo, Giordano, Ilaria, Gianmarco, Martina, Veronica, Pietro, Pippo, Roberta, Vincenzo, and Simone. And to those who have stood by my side for years, whom I met along various paths, thank you for motivating me and believing in me. Thank you, Roberta, Ion, Alessio, Martina, Giorgia, Fabrizio, Silia, Lucrezia, Gabriele, Fra, Alessio, ClaudioTo, Cristina, and to my companions on many adventures, Sidorela, Manjola, Stela (and Righe): Ju dua shoqe.

Lastly, I wish to express my affection and deepest thanks to my family. I thank my parents, Raffaella and Attilio, for giving me life and for allowing me to chase my dreams, both big and small. You are my rocks, my mountains. I admire you and love you deeply. I will always be grateful to you for giving me the greatest gift that could ever exist: the other half of me, my sister Valeria.

I am grateful to the rest of my family, who always believe in me and follow me on my journey: my aunts and uncles, Pierpaolo, Chiara, Paola, Leonardo, Antonella, Vincenzo, Federico, Dragana, my cousins, Emilia, Federica, Lorenzo, Isabella, Francesco, and Giacomo; and Francesca, who is family. My heartfelt thanks go to zia Antonella, zio Vincenzo, and Paola Romanzi for their kindness throughout the work leading to this thesis.

And finally, my thoughts turn to my grandparents, who are no longer with us but who guide me like shooting stars. Thank you, Nonna Luisa, for teaching me resilience and the profound value of kindness; this Thesis is dedicated to you, too.

Abstract

In recent decades, the large-scale distribution of galaxies has emerged as one of the most informative sources for addressing open questions in cosmology, particularly regarding the Universe's dark components: dark matter and dark energy. The study of the statistical properties of this distribution, known as Galaxy Clustering, can also encompass the distribution of underdense regions that dominate the Universe by volume: cosmic voids.

This doctoral Thesis investigates the void-galaxy cross-correlation function, which describes the density profile of galaxies within these voids, representing void shape. In an isotropic universe, cosmic voids should, on average, appear spherical, reflecting the Universe's large-scale isotropy. However, observed distortions—specifically Redshift Space Distortions (RSD) and Alcock-Paczyński (AP) effects—disrupt this symmetry. The first, RSD, is a dynamical distortion driven by the growth rate of structures, while the second, AP, is a geometrical distortion arising from deviations of the assumed fiducial cosmological model from the true one.

This Thesis applies models of these distortions to infer cosmological parameters and includes a forecast analysis to estimate the constraints achievable with forthcoming data from the Nancy Grace Roman Space Telescope. Furthermore, a novel method is introduced to disentangle these two distortional effects, enhancing parameter constraints by employing reconstruction techniques based on the Zel'dovich approximation. This approach effectively mitigates RSD, which are degenerate with AP distortions, thereby significantly improving statistical significance and accuracy by increasing the number of voids matched by the modelling.

Keywords: cosmology: large-scale structure of Universe – theory – cosmic voids -
methods: statistical

Contents

List of Figures	xi
List of Tables	xix
Introduction	3
1 Background cosmology	7
1.1 Describing the expanding universe	7
1.1.1 Einstein's Equations	7
1.1.2 Cosmological principle	8
1.1.3 The Friedmann-Lemaître-Robertson-Walker metric	9
1.1.4 Friedmann's equations	9
1.1.5 Cosmological Redshift	11
1.1.6 Cosmic species of the Universe and background evolution	12
1.1.7 Hubble's Law	14
1.1.8 Distances in cosmology	15
1.2 The standard cosmological model	17
1.2.1 Dark matter	18
1.2.2 Dark energy	19
1.2.3 Testing the standard cosmological model	21
1.2.4 Challenges to the Λ CDM model	25
2 Structure evolution	27
2.1 Linear perturbation theory	28
2.1.1 Peculiar velocities	32
2.2 Beyond linear theory	33
2.2.1 Spherical collapse model	34
2.2.2 Zel'dovich approximation	38

3	Statistical properties of the observed Universe	41
3.1	Two-point statistics for galaxy clustering	42
3.1.1	The matter power spectrum	42
3.1.2	The two-point correlation function	43
3.2	Galaxy-matter connection	45
3.3	Sources in anisotropy and their impact on the clustering analyses	46
3.3.1	Redshift space distortions	47
3.3.2	Alcock-Paczyński distortions	50
3.4	Reconstruction techniques	53
3.4.1	Zel’dovich reconstruction	54
4	Cosmic voids in cosmology	57
4.1	Distortions in voids	59
4.2	Void size function	62
4.3	Void-galaxy cross-correlation function	69
4.3.1	Modelling the void-galaxy cross-correlation function	71
5	Tools for void analyses	81
5.1	Void finder	81
5.2	Void-galaxy cross-correlation function estimator	85
5.3	Numerical simulation catalogs	87
5.3.1	Quijote simulations	88
5.3.2	Roman HLSS mocks	92
6	On the optimization of the extraction of AP signal from voids	95
6.1	Strategy	96
6.2	Likelihood analysis	97
6.3	Results	100
6.3.1	Results in redshift space	100
6.3.2	Results in reconstructed space	102
6.3.3	Results in real space	104
6.3.4	Sensitivity to the void size	106
6.4	Robustness tests	109
6.4.1	Sensitivity to the choice of parameters that regulate the reconstruction	109
6.4.2	Sensitivity to the covariance matrices	115
6.4.3	Consistency test against multiple mocks	120

7	Cosmology with voids from the Nancy Grace Roman Space Telescope	123
7.1	The void-galaxy cross-correlation function	124
7.1.1	Likelihood analysis	124
7.1.2	Results	126
7.2	The void size function	135
7.2.1	Catalog preparation	135
7.2.2	Void size function model	137
7.2.3	Methodology	138
7.2.4	Analysis and results	141
7.3	VOIDS' PROBE COMBINATION	146
8	Conclusions	151
	Conclusions	151
A	Halo bias estimate	157
	List of publications	161
	List of contributions	163
	References	165

List of Figures

1.1	The content of the universe in various forms of energy in the Λ CDM model, as measured by CMB observations and large-scale structure surveys. Source: Max-Planck-Institute for Astrophysics Garching and Pixabay.	18
1.2	Upper panel: In red, the estimated angular power spectrum of the temperature fluctuations of the CMB of the Planck 2018 data release. In blue, best fit theoretical prediction from a Λ CDM model. Lower panel: Residuals in regards to the model prediction. Errors displayed are the 1σ interval which include the cosmic variance. Credits: (Planck Collaboration et al., 2020)	23
1.3	the 68% and 95% marginalized posterior constraints from DESI BAO combined with CMB and each of the PantheonPlus, Union3 and DESY5 SN Ia datasets. The significance of the tension with Λ CDM ($w_0 = -1$, $w_a = 0$) estimated from the $\Delta\chi^2$ MAP values is 2.5σ , 3.5σ , and 3.9σ for these three cases respectively. Credits: (DESI Collaboration et al., 2024).	24
2.1	The Large Scale Structure of the Universe traced by galaxies in the early data from the Sloan Digital Sky Survey in which can be seen the different cosmic structures from which the Universe is formed: voids, filaments, and clusters. Credits: (Blanton et al., 2003)	33
3.1	Simplified illustration of the effect of distortions for a galaxy in redshift space. The real position of a galaxy, (the closer to the observer) is shifted due to the combination of the contribution from the peculiar velocity along the line of sight (LOS), denoted as \mathbf{v}_r (i.e., RSD), and the incorrect distance estimate δd resulting from the use of an inaccurate fiducial cosmological model, AP effect.	47

- 3.2 *Left-hand and central panels.* Schematic representation of the effect of redshift- space distortions on large and linear scales for overdensity (left) and underdensity (center). As galaxies move away from underdense regions, and are directed towards overdense regions, these regions appear elongated and flattened along the line of sight when seen in redshift space, respectively. *Right-hand panel.* Representation of the RSD effect in a smaller and virialised region like a cluster. Here, the galaxies are spread out in redshift space due to the large velocity dispersion, yielding large radial patterns in the wedge diagrams, the so-called fingers-of-God effect. 49
- 4.1 Separation vector between the comoving void center location \mathbf{X} and the galaxy location \mathbf{x} in real space (\mathbf{r} , left) and in redshift space (\mathbf{s} , right). The peculiar LOS velocity \mathbf{v}_{\parallel} of every galaxy that defines the void can be decomposed into the peculiar velocity of the void center \mathbf{V}_{\parallel} and the galaxy's relative velocity \mathbf{u}_{\parallel} with respect to this center. Velocity displacement is in units of $(1 + z_h)/H(z_h)$ and μ is the cosine of the angle between the separation vector and the LOS. This yields the relation for the mapping of the separation vector between real and redshift space $\mathbf{s} = \mathbf{r} + \mathbf{u}_{\parallel}$. Credits: Hamaus et al. (2020). 60
- 4.2 Four scenarios of the excursion set formalism. Each row illustrates one of the four basic modes of hierarchical clustering: the cloud-in-cloud process, cloud-in-void process, void-in-void process and void-in-cloud process (from top to bottom). Each mode is illustrated using three frames. Leftmost panels show 'random walks': the local density perturbation $\delta_0(\mathbf{x})$ as a function of (mass) resolution scale S_m at an early time in an N-body simulation of cosmic structure formation. In each graph, the dashed horizontal lines indicate the collapse barrier δ_c and the void barrier δ_v . The two frames on the right show how the associated particle distribution evolves. Whereas halos within voids may be observable (second row depicts a halo within a larger void), voids within collapsed halos are not (last row depicts a small void which will be squeezed to small size as the surrounding halo collapses). It is this fact which makes the calculation of void sizes qualitatively different from that usually used to estimate the mass function of collapsed halos. Credits: Sheth and van de Weygaert (2004) 65

4.3	Illustration of the system of coordinates used for the VGCF. In blue the separation vector \mathbf{r} between the void center v and the galaxy g . In orange the component parallel r_{\parallel} and perpendicular r_{\perp} respect to the LOS (represented with the dashed line).	70
4.4	Representation of the method to reconstruct the sphere in real space starting from the distorted sphere in redshift space: the distorted void is projected along the LOS (velocities do not affect the parallel direction, hence the projection). From the projection, we reconstruct the sphere in real space. The red arrow represents r_v , the radius of the void in real space; the yellow arrow r_p , the radius of the projection. Credits: Pisani et al. (2014).	75
5.1	Illustrations of the principle of the watershed transform. Starting from the local minima the surrounding basins of the surface start to flood as the water level continues to rise. Where two basins meet up near a ridge of the density surface, a “dam” is erected (left frame). Ultimately, the entire surface is flooded, leaving a network of dams defines a segmented volume and delineates the corresponding cosmic web (right frame). Credits: Platen et al. (2007).	83
5.2	Illustration of the creation of voids: (a) slice of galaxy field where galaxies are represented by dots. (b) 2D Voronoi tessellation of galaxies in this slice, which each particle’s Voronoi cell shaded according to its area. The galaxies outside the slice are shown because contribute to the tessellation. (c) Zones of galaxies. The core (density minima) of each zone are shown with crosses, the different colors demarcate different zones. (d) The watershed growth of 1 void, the deepest void in the sample. Colors from dark to light indicate the stage at which the zone is added to the void. The darkest color is the original zone, the next-darkest is the first zone or set of zones added, etc. The only zone that is never included is that with the highest-density link to another zone, in the lower-right corner. Credits: Neyrinck (2008)	84
5.3	An example of a watershed void in VIDE. The Voronoi cells that define the void are in purple with galaxies in red. We show a void with effective radius $20 h^{-1}\text{Mpc}$ within a $50 h^{-1}\text{Mpc}$ spherical region. Galaxy point sizes are proportional to their distance from the point of view. Galaxies interior to the void are shaded dark red. Credits: Sutter et al. (2015)	84

5.4	The abundance of voids that <code>VIDE</code> found in real (left), redshift (middle), and reconstructed (right) space as a function of their effective radius R (i.e., void size function). Poisson statistic is assumed for the error bars. In dashed vertical lines: the value of the mean particle separation for the halo sample. Here it is possible to see that the void distribution for the case of real (left panel) and reconstructed space (right panel) is very similar.	91
5.5	Histograms showing the number density of <code>VIDE</code> voids as a function of the void effective radius, here called R_{eff} . Each color corresponds to a different redshift bin, as listed in the legend.	93
6.1	Schematic illustration of the strategy followed in the analysis presented in this Chapter.	96
6.2	Monopole (left), quadrupole (center), and hexadecapole (right) of the VGCF ξ (solid orange line and dots) and best-fit model (dashed black line) for halos and voids in redshift space. Error bars are computed with the diagonal of the jackknife covariance matrix. The central panel shows the evidence of a moment of quadrupole in redshift space, highlighting the presence of RSD.	101
6.3	Posterior probability distribution of the model parameters that enter in Equations (4.43) and (4.42), obtained via the MCMC from the data measured in redshift space, shown in Figure 6.2. Dark and light-shaded areas represent the 68% and 95% confidence regions, and dashed lines indicate fiducial values of the RSD and AP parameters β and ε . The top of each column states the mean and standard deviation of the 1-dimensional marginal distributions.	102
6.4	Monopole (left), quadrupole (center), and hexadecapole (right) of the VGCF ξ (solid blue line and dots) and best-fit model (dashed red curve) for tracers and voids in reconstructed space. Error bars are computed with the diagonal of the covariance matrix. Dotted black curve in the central panel indicates the zero quadrupole for reference, $\xi_2^{\text{th}} = 0$. The central panel shows a quadrupole consistent with 0, proving the absence of distortions.	103
6.5	Posterior probability distribution of the model parameters that enter in Equations (4.43) and (4.42), obtained via MCMC from the data measured in reconstructed space, shown in Figure 6.4. Dark and light-shaded areas represent 68% and 95% confidence regions, and dashed lines indicate fiducial values of the RSD and AP parameters. The top of each column states the mean and standard deviation of the 1-dimensional marginal distributions.	104

- 6.6 Monopole (left), quadrupole (center), and hexadecapole (right) of the VGCF ξ (solid green line and dots) and best-fit model (dashed purple line) for tracers and voids in real space. Error bars are computed with the diagonal of the covariance matrix. Dotted black line in the central panel indicates the zero quadrupole for reference, $\xi_2^{\text{th}} = 0$. As in reconstructed space, Figure 6.4, the central panel shows a quadrupole consistent with 0, proving the absence of distortions. 105
- 6.7 Posterior probability distribution of the model parameters that enter in Equations (4.43) and (4.42), obtained via MCMC from the data measured in real space, shown in Figure 6.6. Dark and light-shaded areas represent 68% and 95% confidence regions, and dashed lines indicate fiducial values of the RSD and AP parameters. The top of each column states the mean and standard deviation of the 1-dimensional marginal distributions. 106
- 6.8 *Top panel:* comparison of the values of the AP parameter ε with its error σ_ε (error bars), obtained with the fitting procedure described in Section 6.2, for the analysis with tracers and voids in redshift-space (purple dots, left panel) and the analysis with tracers and voids in reconstructed space (orange triangles, right panel). Each dot represents the ε value as a function of the minimum radius R_{min} for the voids in that specific subsample, expressed in mean tracer separation (mps) units, used for computing VGCF. *Bottom panel:* comparison of the residuals of ε with respect to its expected value 1 in units of its estimated error σ_ε , as a function of R_{min} ; left panel is redshift space analysis and right panel is reconstructed space analysis. The gray horizontal band corresponds the zone of the plot where the residuals are in between -1 and 1. 108
- 6.9 Quadrupole of the VGCF computed with reconstructed data, for different choices of the fixed smoothing scale R_s used in the reconstruction procedure. Error bars are computed as the diagonal of the covariance matrix. The choice $R_s = 5.0 h^{-1}\text{Mpc}$ results in an isotropic correlation function, corresponding in a measured quadrupole matching with the dashed black line, which is the expected zero quadrupole $\xi_2^{\text{th}} = 0$. Residual anisotropies are seen for other values of R_s . The quadrupole moment, and consequently the effect of R_s , is accentuated near the edge of the void due to the presence of nonlinearities caused by a higher density contrast. 111

- 6.10 Estimated values of the parameters ε (left panel) and β (right panel) for different analyses performed in reconstructed space, each using data reconstructed with a different smoothing scale R_s . The purple dots represent the estimated parameter values for each analysis at a specific R_s , while the black dashed line indicates the expected values, $\varepsilon = 1$ and $\beta = 0$ 113
- 6.11 *Top panel:* Quadrupole ξ_2 of the stacked void-galaxy cross-correlation function computed with voids and halos in reconstructed space, where reconstruction is computed with different values of f , separating the values of $f < f^{\text{true}}$ (left) and $f > f^{\text{true}}$ (right). *Bottom panel:* Residuals between the quadrupoles of the top panel and the reference quadrupole computed with the fiducial cosmology of the simulation $\xi_2^{f=\text{true}}$, separating the values of $f < f^{\text{true}}$ (left) and $f > f^{\text{true}}$ (right). The color bar indicates the different values of f . Error bars are computed with the diagonals of the covariance matrices. 114
- 6.12 Estimated values of the parameters ε (left panel) and β (right panel) for different analyses performed in reconstructed space, each using data reconstructed with a different values of the input parameter f . The purple dots represent the estimated parameter values for each analysis at a specific f , while the black dashed line indicates the expected values, $\varepsilon = 1$ and $\beta = 0$. The orange vertical dotted lines indicate the true value of f 115
- 6.13 Normalized covariance $\text{Corr}[\xi]_{ij}$ obtained from the jackknife resampling. 116
- 6.14 Normalized covariance matrix $\text{Corr}[\xi]_{ij}$ obtained from the 100 mocks. 117
- 6.15 Comparison of the elements along the diagonal, C_{ii} of the two covariance matrices, jackknife resampling (orange) and mock covariance (purple). Each panel of the figure represents the diagonal of the i -th multipole as illustrated with the text. 118
- 6.16 Posterior probability distribution of the model parameters computed with the likelihood analysis presented in Section 6.2, from the data of the single mock (mock 0) shown in Fig. 6.4, obtained using two different covariance matrices. Orange: jackknife resampling covariance matrix, and purple: mock covariance matrix corrected with Hartlap and Percival factors. Dark and light-shaded areas represent 68% and 95% confidence regions, and dashed lines indicate fiducial values of the RSD and AP parameters β and ε 119

- 6.17 Comparison of the error on ε estimated from the likelihood analysis for 100 mocks in redshift space (x-axis) and reconstructed space (y-axis). Each point represents the error value from one mock. The figure shows that the errors in reconstructed space are consistently smaller than those in redshift space, highlighting the improvement in precision achieved through the reconstruction process. 121
- 7.1 Void-galaxy cross-correlation function in redshift space. Left: $\xi^s(s_\perp, s_\parallel)$ in 2D (color scale with black contours) and best-fit model from Equations (4.41) and (4.42) (in white contours). Right: monopole (blue dots), quadrupole (orange triangles) and hexadecapole (green wedges) of $\xi^s(s_\perp, s_\parallel)$ with their best-fit model (solid, dashed, dotted lines). The mean void redshift, \bar{Z} , and effective radius, \bar{R}_{eff} , of each redshift bin are indicated. 127
- 7.2 Projected void-galaxy cross-correlation function $\xi_p^s(s_\perp)$ in redshift space (green wedges, interpolated with dashed line) and its real-space counterpart $\xi(r)$ in 3D after deprojection (orange triangles interpolated with dotted line). The redshift-space monopole $\xi_0^s(s)$ (blue dots) and its best-fit model based on Equations (4.41) and (4.42) are shown for comparison (solid line). Adjacent bins in redshift increase from top to bottom, with mean void redshift, \bar{Z} , and effective radius, \bar{R}_{eff} , as indicated in each panel. 129
- 7.3 VGCF: posterior probability distribution of the model parameters that enter in Equations (4.41) and (4.42), obtained via MCMC from the data shown on the left of Figure 7.1. Dark and light-shaded areas represent the 68% and 95% CL, with a cross marking the best fit, dashed lines indicate fiducial values of the RSD and AP parameters. The top of each column states the mean and standard deviation of the 1D marginal distributions. Adjacent bins in void redshift with mean value \bar{Z} increase from top to bottom, as indicated. 131
- 7.4 VGCF: expected constraints on Ω_m , w_0 , and w_a for the three different cosmologies tested here. In blue we show the Λ CDM model, while orange and green correspond to w CDM and w_0w_a CDM respectively. Dashed lines indicate the true values. Numbers in color correspond to the estimated values for the parameters, for the different cosmological models. 135
- 7.5 2D marginalized posterior distributions for the moving barrier parameters, Equation (7.11), for each redshift bin, as labelled in the legend. The shaded area shows the 68%CL, while the outer contours corresponds to 95%CL. The crosses show the maximum of the posterior distributions. 138

7.6	From left to right: VSF from the Roman reference HLSS-like mock (Zhai et al., 2021), in each of the three redshift bins considered. Upper panels: black dots with error bars show the measured VSF from the post-processed void catalog as described in Section 7.2.1 with $\delta_{v,g} = -0.7$, the error bars are Poissonian; blue solid lines show the best-fit moving barrier calibrated as described in Section 7.2.3; blue shaded areas show 68% CL. Lower panel: blue solid lines show the relative values of the best VSF theoretical model with respect to measurements in σ units; blue shaded areas show the 68% CL; gray hatched areas show the $\pm 1\sigma$ interval.	139
7.7	VSF: posterior distributions of the cosmological parameters explored in the optimistic scenario, for the three cosmological models explored: Λ CDM (blue), w CDM (orange), w_0w_a CDM (green). The filled internal region shows the 68% CL, the outer line shows the 95% CL. Black dashed lines show the true values, crosses correspond to the maximum of the posterior distribution, the numbers in the panels along the diagonal list the parameter values corresponding to the maximum of the likelihood.	144
7.8	VSF: posterior distributions of the cosmological parameters explored in the pessimistic scenario, for the three explored cosmological models. The plot is organized as Figure 7.7.	145
7.9	Combination of the VGCF and VSF: posterior distributions of the cosmological parameters explored in the Λ CDM (left) and the w CDM model (right), obtained from the VSF (blue), VGCF (orange), and combining the two statistics (dark grey). The filled internal region shows the 68% CL, the outer line shows the 95% CL. Black dashed lines indicate the true values, crosses correspond to the maximum of the posterior distributions.	147
7.10	Combination of the VGCF and VSF: posterior distributions of the cosmological parameters explored in the w_0w_a CDM model, obtained from the VSF (blue), VGCF (orange), and combining the two statistics (dark grey). The plot is organized as Fig 7.9.	148
A.1	In blue: measurements of the halo 2PCF $\xi_{hh}(r)$ of the mocks described in Section 5.3.1, with the associated error bars from the covariance matrix of the mocks $\text{Cov}[\xi_{hh}]/N$. In orange: the best fit model estimated with the procedure implemented in <code>BAOFitter</code>	159

List of Tables

5.1	Table summarizing the catalogs used for the results in this analysis. Column 2 contains the values of the number of halos, N_H , in the catalogs, while column 3 contains the values of the number of voids, N_V , found with <code>VIDE</code> in the respective halo catalog	90
6.1	Table summarizing the values of the parameters ε and β , associated to their estimated errors, for the analyses in redshift, reconstructed, and real space. .	106
6.2	Table of the χ^2 values of the measured quadrupole ξ_2 fitted with the theoretically expected zero quadrupole ξ_2^{th} against different smoothing scales R_s	112
7.1	VGCF: forecasted constraints on RSD and AP parameters ε , β , $f\sigma_8$, and $D_A H/c$ (mean values with 68% CL). Results are given in three redshift bins with mean \bar{z} , and large-scale galaxy bias b	132
7.2	VGCF: forecasted constraints on cosmological parameters, Ω_m , w_0 , and, w_a , estimated assuming three different cosmological models: Λ CDM, w CDM, and $w_0 w_a$ CDM.	134
7.3	Maximum posterior distribution values and 1D 68% CL interval for the moving barrier parameters, see Equation (7.11). The first column lists the redshift bins range, the other columns list the corresponding α , β , and γ parameters, respectively.	138
7.4	VSF: maximum posterior distribution values and 1D 68% CL interval for the cosmological parameters explored, for each considered cosmological model (we show both the optimistic and pessimistic scenarios).	146
7.5	Combination of the VGCF and VSF: maximum posterior distribution values and 1D 68% CL interval of the cosmological parameters explored for each considered cosmological model (we show both the optimistic and pessimistic scenarios).	147

Introduction

In recent decades, cosmology has entered a groundbreaking era known as precision cosmology. Over the past 25 years, a series of extensive experiments probing the Cosmic Microwave Background (CMB) and the large-scale structure (LSS) of the Universe, have led to the establishment of the standard cosmological model, Λ CDM. This model provides an exceptional fit to a wide array of cosmological observables, characterizing the Universe as a flat, expanding space-time governed by General Relativity. According to Λ CDM, the evolution of the Universe is driven by its primary constituents: ordinary baryonic matter, comprising only about 5% of the total mass-energy; cold dark matter (CDM), constituting nearly 27%; and the cosmological constant, Λ , which dominates at 68%.

Remarkably, this standard model of cosmology depicts a Universe composed of 95% constituents that remain fundamentally unknown. This presents a profound mystery in modern cosmology: understanding the so-called "dark sector" of the Universe. The major challenge lies in the cosmological constant, Λ , introduced to explain the observed late-time acceleration of the Universe (Perlmutter et al., 1999; Riess et al., 1998). Although this model aligns well with current data, the nature and, notably, the magnitude of Λ lack a satisfying theoretical explanation. The discovery of this accelerated expansion represents one of the most groundbreaking revelations in cosmology. Today, the scientific community's greatest endeavor is to uncover the physical origins of this accelerated expansion, develop methods to measure and characterize it, and design experiments to investigate its effects.

The Λ CDM model attributes the accelerating expansion of the Universe to the presence of a cosmological constant, Λ . However, alternative models have been proposed to explain the dark energy component, some of which interpret it as a dynamic variable that slowly evolves over cosmic time or as an exotic form of energy responsible for the observed late-time acceleration. Additional approaches suggest that this acceleration might instead result from modifications to General Relativity, offering a new pathway to achieve accelerating solutions.

In the upcoming decades, a huge amount of highly precise data from numerous observational campaigns is expected to deepen our understanding of the Universe, potentially

uncovering the nature of dark components and new physics. Notably, these efforts will include measurements of CMB temperature and polarization, observations from gravitational wave detectors, and large-scale galaxy surveys. Prominent among these are four galaxy surveys, the ongoing DESI (DESI Collaboration et al., 2022) and Euclid (Euclid Collaboration et al., 2024) satellite mission, the upcoming survey of the Vera Rubin Observatory (Ivezić et al., 2019) and the planned Nancy Grace Roman Space Telescope (Dore et al., 2019).

Given the precision now achievable in cosmological analyses, the standard probes for cosmological constraints are nearing their limit in constraining power. Consequently, further insights into the physics governing our Universe may lie in identifying new, independent cosmological probes. Combining multiple probes not only reduces uncertainty on cosmological parameters but also allows diverse approaches that may open new observational and theoretical pathways. Among these emerging probes, our attention turns to the darkest regions of the Universe, those vast, nearly empty areas where luminous matter is scarce and primarily concentrated along the edges: cosmic voids.

Cosmic voids are vast, under-dense regions that occupy a large portion of the Universe (Gregory and Thompson, 1978; Szapudi et al., 2015; Tikhonov and Karachentsev, 2006), defining the bulk of the large-scale structure and shaping the cosmic web, i.e., the pattern of the Universe in which matter is organized, and dominating the Universe in terms of volume (Platen et al., 2007). These regions, nearly empty of baryonic matter, contribute in shaping a web-like structure across the cosmos, interlacing with sheets, filaments, and clusters of galaxies (De Lapparent et al., 1986; Sheth and van de Weygaert, 2004; van de Weygaert and Schaap, 2009; Zeldovich et al., 1982). Voids serve as unique laboratories in cosmology due to their low-density interiors, which allow for simplified modeling of their evolution compared to more complex cosmic structures. This simplicity makes voids especially sensitive to the Universe's initial conditions and provides a window into its fundamental properties, including dark matter, dark energy, and modified gravity (Achitouv, 2016; Biswas et al., 2010; Cai et al., 2015; Clampitt et al., 2013; Falck et al., 2018; Lee and Park, 2009; Li and Efstathiou, 2012; Paillas et al., 2019; Perico et al., 2019; Pisani et al., 2015a; Pollina et al., 2016; Sahlén and Silk, 2018; Sahlén et al., 2016; Spolyar et al., 2013; Verza et al., 2019; Zivick et al., 2015), as well as massive neutrinos neutrino properties (Banerjee and Dalal, 2016; Kreisch et al., 2019, 2022; Massara et al., 2015; Sahlén, 2019; Schuster et al., 2019), primordial non-Gaussianity (Chan et al., 2019), and physics beyond the standard model (Baldi and Villaescusa-Navarro, 2016; Peebles, 2001; Reed et al., 2015; Yang et al., 2015).

The analysis of cosmic voids involves exploring various statistical tools, with the most significant being the void-galaxy cross-correlation function (VGCF) and the void size function

(VSF). The VGCF examines the density profile of matter both within voids and in their surroundings, while the VSF investigates the abundance of voids across different scales.

In this Thesis, we focus primarily on the VGCF, a subject that has been at the center of my research over recent years. We both showcase its potential in contributing to the resolution of the dark energy problem, and propose a methodology addressing several unresolved aspects of VGCF modeling. In addition, I will also investigate the possibility to combine VGCF and VSF to further improve the precision and the constraining power of the void analyses.

Before embarking on this exploration, it is essential to equip ourselves with the necessary theoretical background and computational tools to fully engage with the cosmological framework under investigation. For this reason the Thesis is structured as follows,

- In Chapter 1, we briefly introduce the fundamental theoretical concepts of the standard cosmological model. We discuss the key elements of the Friedmann-Lemaître-Robertson-Walker (FLRW) metric, which characterizes the geometry of the Universe, progressing through the derivation of the Friedmann Equations, and finally presenting the main features of the currently adopted standard model of cosmology, the Λ CDM model.
- In Chapter 2 we briefly outline an in-depth treatment of the theory governing the growth of perturbations in cosmology. We begin discussing the linear theory of cosmological perturbation, based on gravitational instability, and then move beyond linear approximation by presenting two approaches that describe the nonlinear growth of cosmic structures: the spherical collapse theory and the Zel'dovich approximation.
- In Chapter 3, we explore the statistical properties of the observed Universe by introducing concepts such as galaxy clustering, while clarifying the link between cosmological perturbation theory and the statistical tools that serve to characterize the properties of the cosmic structures that we observe. We examine the influence of observational effects on the distribution of matter tracers, focusing on distortions that affect observations and, consequently, clustering analyses. Additionally, we present methodologies for mitigating these systematics, specifically through the so-called reconstruction techniques.
- In Chapter 4, we delve deeper into the nature of cosmic voids, discussing the primary statistical tools used in their analysis—namely, the Void Size Function (VSF) and the Void-Galaxy Cross-Correlation Function (VGCF)—along with their modeling. The focus is primarily on the VGCF. We first present a simpler linear approach to model VGCF, followed by an exploration of more sophisticated methods to include nonlinear effects, to overcome the challenges introduced by nonlinearities. In particular,

we introduce our novel methodology, which leverages reconstruction techniques to improve the accuracy of VGCF analyses.

- In Chapter 5, we outline the numerical tools essential for conducting the VGCF analyses in different types of datasets. Specifically, we discuss the algorithm used to identify voids within the distribution of matter tracers, along with the data catalogs employed in the analyses presented in subsequent chapters. This section covers the void-finding algorithms and their parameters, as well as the VGCF estimator adopted in this Thesis and the simulated datasets we have used in the analyses.
- In Chapter 6, we present the main results of this Thesis, centered on testing a novel methodology based on reconstruction techniques. This approach is designed to address the challenges posed by distortions that impact the observed VGCF. By mitigating these distortions, the methodology brings an improvement significantly enhancing the statistical power for future cosmic void analyses, providing more robust and precise cosmological constraints.
- In Chapter 7, we outline a forecast study aimed at estimating cosmological parameters by leveraging void statistics. In this collaborative effort, I contributed through the analysis of the VGCF. This work provides predictions on future constraints for cosmological parameters, with a particular focus on those probing the nature of dark energy, using forthcoming data from the Roman Telescope.
- Finally, in Chapter 8, we present the conclusions of this Thesis, summarizing the main results and discussing their implications for void cosmology. This work layout the path for future applications, where the methodologies developed here will be applied to the new data that will be obtained by the new galaxy surveys.

1

Background cosmology

In this chapter, I will present a comprehensive overview of the so-called background cosmology that constitutes the backbone of the Standard Cosmological Model. Its building blocks are the Friedmann-Robertson-Walker-Lemaître (FRWL) metric, which describes a homogeneous and isotropic universe, the Hubble law, offering insights into the expansion of the universe, and the Friedmann equations, which govern the dynamics of cosmic expansion. I will also present the concept of redshift and the various types of distances used in cosmology as they constitute the main observational tool to probe the structure of the homogeneous isotropic Universe. Finally, I will introduce the Lambda Cold Dark Matter (Λ CDM) model, the standard cosmological model, along with a discussion of alternative theories that challenge or extend the standard paradigm allowing the possibility of a dark energy component described by a different equation of state.

1.1 Describing the expanding universe

1.1.1 Einstein's Equations

At the core of our current understanding of the observable Universe is gravitational interaction, an attractive force between massive objects that extends across infinite distances, influencing even the most remote regions of the cosmos. In Einstein's view of the Universe, gravitational force is the manifestation of distortions in the four-dimensional structure of space-time, and vice versa, space-time is curved by the gravitational interaction of massive bodies. This intimate connection is described by the Einstein field equations:

$$G_{\mu\nu} = R_{\mu\nu} - \frac{1}{2}g_{\mu\nu}R = 8\pi GT_{\mu\nu} + \Lambda g_{\mu\nu}, \quad (1.1)$$

where the right side features Newton's gravitational constant G and the energy contents of the Universe are described by the energy-momentum tensor $T_{\mu\nu}$, and the left side describes the distortions in the space time metric via the Ricci tensor $R_{\mu\nu}$, the Ricci scalar $R \equiv R^\mu{}_\mu$, and the metric components $g_{\mu\nu}$. The cosmological constant, Λ , can be either added as a geometry-related term (right-hand side) or included in $T_{\mu\nu}$ as an effective fluid that contributes to the energy budget. Equation (1.1) illustrates the connection between the geometry and the energy contents. A second consequence of Equation (1.1) is that it implies a dynamically evolving Universe. The constant Λ was at first added by Einstein to the equation as a way to counteract the gravitational pull and obtain a static, rather than evolving, Universe. The Λ constant was then to be regarded as a fundamental constant. If positive, it acts as a repulsive force, opposite to that of gravity. If negative, it becomes an additional contribution to the gravitational interaction. If null, the evolution of the Universe is solely governed by the energetic content carried by the $T_{\mu\nu}$ tensor. The cosmological constant was largely abandoned after the discovery of the Hubble expansion and recently resurrected to explain the accelerated expansion of the Universe. Its current interpretation, however, is that of an additional effective fluid, characterized by a negative isotropic pressure, that contributes to the stress-energy tensor.

This general formulation itself provides a theoretical framework to model the laws governing the Universe. To solve Einstein's equations, it is necessary to define a metric $g_{\mu\nu}$. This definition derives from general assumptions and justified by the observed properties of our Universe.

1.1.2 Cosmological principle

The cosmological principle (CP) states that, on sufficiently large scales, the Universe is homogeneous and isotropic. Homogeneity implies that the Universe appears to have the same properties regardless of the location, while isotropy means it looks the same in all directions. Together, these properties suggest a universe with no preferred positions or orientations. Although the nearby Universe exhibits local (in an astronomical sense) inhomogeneities, such as galaxies, clusters, and vast almost empty regions known as voids, the cosmological principle holds true when observed on scales of hundreds of megaparsecs ($1 \text{ Mpc} = 10^6 \text{ pc} \simeq 3.09 \cdot 10^{13} \text{ km}$). These vast scales smooth out local fluctuations in density, allowing the principle to govern the Universe's on scales larger than the cosmic structures.

1.1.3 The Friedmann-Lemaître-Robertson-Walker metric

Solving the Einstein equations, (1.1), requires specifying the metrics $g_{\mu\nu}$, which defines the line element:

$$ds^2 = g_{\mu\nu} dx^\mu dx^\nu. \quad (1.2)$$

The Friedmann-Lemaître-Robertson-Walker metric (FLRW) is a particular definition of the metric $g_{\mu\nu}$ that satisfies the cosmological principle and provides the mathematical description of a universe that adheres to those assumptions. The associated line element governing the evolution of the cosmic background is defined as,:

$$ds^2 = -c^2 dt^2 + a^2(t) \left[\frac{dr^2}{1 - \kappa r^2} + r^2 d\Omega \right], \quad (1.3)$$

where $a(t)$ is the scale factor (or the expansion parameter), having the dimensions of a length, $d\Omega = d\theta^2 + \sin^2(\theta)d\phi^2$, c is the speed of light, θ and ϕ are the two angles in spherical coordinates, and κ is the curvature parameter. It is possible to rescale the coordinates in such a way that the curvature κ of a homogeneous isotropic space-time can assume one of three possible values -positive, zero, or negative. This parameter determines the overall geometry of the Universe:

- $\kappa = 1$ positively curved Universe, closed geometry, analogous to the surface of a sphere in two dimensions
- $\kappa = 0$ flat, Euclidean geometry, extending infinitely in all directions
- $\kappa = -1$ negatively curved Universe, hyperbolic geometry, resembling the shape of a saddle in two dimensions, and is both open and infinite.

As such, the curvature that defines the geometry of the Universe can be either Spherical, Flat, or Hyperbolic and therefore depict either a finite (closed) universe or an infinite (open) universe.

1.1.4 Friedmann's equations

The scale factor $a(t)$ plays a crucial role in describing the evolution of the Universe, and it is worth noting that the values of $g_{00} = 1$ and $g_{0i} = 0$ allow for a global definition of a time coordinate. Einstein's equations (1.1), rewritten adopting the FLRW metric as presented below, play a key role in determining the scale factor dynamics

$$G_{\mu\nu} = \frac{8\pi G}{c^4} T_{\mu\nu}, \quad (1.4)$$

with $T_{\mu\nu}$ being the stress-energy tensor for a cosmological perfect fluid, considered appropriate to describe the properties of the species of types of matter and energies that populate the Universe, with

$$T_{\mu\nu} = (\rho + p)u_\mu u_\nu - pg_{\mu\nu}, \quad (1.5)$$

where p and ρ are representing the pressure and energy density of the fluid. Choosing a cosmic rest frame, i.e. the frame where the average velocity of energy forms in the Universe is zero, $u_\mu = (1, 0, 0, 0)$ and $T_{\mu\nu}$ takes the following form

$$T_{\mu\nu} = \begin{pmatrix} \rho & 0 & 0 & 0 \\ 0 & p & 0 & 0 \\ 0 & 0 & p & 0 \\ 0 & 0 & 0 & p \end{pmatrix} \quad (1.6)$$

We define now the Hubble function, describing the expansion rate of the Universe at time t as

$$H \equiv \frac{\dot{a}}{a}, \quad (1.7)$$

and considering the 00 component of $T_{\mu\nu}$, we can write the first Friedmann's equation as follows:

$$H^2 \equiv \left(\frac{\dot{a}}{a}\right)^2 = \frac{8\pi Gc^2}{3}\rho - \kappa\frac{c^2}{a^2}. \quad (1.8)$$

Focusing on the spatial component of Einstein's equation in an FLRW metric, it is possible to derive the following expression

$$\frac{\ddot{a}}{a} + 2\left(\frac{\dot{a}}{a}\right)^2 + 2\kappa\frac{c^2}{a^2} = -c^2\frac{4\pi G}{c^3}(\rho - p). \quad (1.9)$$

By plugging Equation (1.8) into the latter we obtain the expression for the second Friedmann's equation:

$$\frac{\ddot{a}}{a} = -c^2\frac{4\pi G}{3}(\rho + 3p). \quad (1.10)$$

In the case of absence of cosmological constant Λ , it is possible to see how the curvature term affects the scale factor evolution, in fact:

- if $\kappa = 0$, then $\left(\frac{\dot{a}}{a}\right)^2 = \frac{8\pi Gc^2}{3}\rho \geq 0$ and $\dot{a} = 0$ asymptotically corresponding to a static universe,
- if $\kappa = -1$, then $\left(\frac{\dot{a}}{a}\right)^2 = \frac{8\pi Gc^2}{3}\rho + \frac{c^2}{a^2} \geq 0$ and $\dot{a} \neq 0$,
- if $\kappa = 1$, then $\left(\frac{\dot{a}}{a}\right)^2 = \frac{8\pi Gc^2}{3}\rho - \frac{c^2}{a^2} \geq 0$ and this represents the turning point case.

The last essential equation describing the evolution of the Universe is derived from the first law of thermodynamics

$$dU = \delta Q - PdV, \quad (1.11)$$

with $\delta Q = TdS$. By definition, the Universe is an adiabatic system, hence $\delta Q = 0$. Using $U = \rho V$ and FLRW metric presented in Equation (1.3) it is possible to derive the continuity equation:

$$\dot{\rho} = -3H(\rho + p). \quad (1.12)$$

1.1.5 Cosmological Redshift

In the study of the evolution of the FLRW Universe, one of the most significant phenomena is the cosmological redshift. This effect arises naturally from the expansion of space and provides crucial insights into the evolution of the Universe. Unlike the classical Doppler effect, cosmological redshift results from the stretching of wavelengths of photons as they traverse the expanding space-time, making it a fundamental observational tool in cosmology. To illustrate this point, let us consider the geodesic equation for a photon, massless particle, specifically, the photon in the FLRW metric:

$$\frac{d^2 x^\alpha}{d\eta^2} + \Gamma_{\mu\nu}^\alpha \frac{dx^\mu}{d\eta} \frac{dx^\nu}{d\eta} = 0, \quad (1.13)$$

where η is the conformal time, defined via:

$$\eta = \int \frac{dt}{a(t)}. \quad (1.14)$$

The 00 component of a geodesic equation can be rewritten in the form

$$\frac{dE}{d\eta} + \frac{\dot{a}}{a} E = 0, \quad (1.15)$$

with $E = hc/\lambda$. This equation gives us the energy-scale factor relation

$$E \simeq \frac{1}{a}. \quad (1.16)$$

Therefore, reminding $E = \frac{hc}{\lambda}$, the redshift relation due to geometry at large scale can be expressed as

$$\frac{\lambda_0}{\lambda(t)} = \frac{a_0}{a(t)} = 1 + z, \quad (1.17)$$

where z is the redshift, defined as

$$z = \frac{\lambda_{\text{obs}} - \lambda_{\text{em}}}{\lambda_{\text{em}}}, \quad (1.18)$$

and it can in principle be less than zero (blueshift), when the source is approaching the observer, or greater than zero (redshift), when the source is receding. By measuring the photon redshift, it is possible to acknowledge the scale factor evolution from t_0 to t .

1.1.6 Cosmic species of the Universe and background evolution

The density term present in Equation (1.8), is the result of the sum of different components of the Universe:

- Non relativistic matter, comprising two contributions: standard massive particles, and non-relativistic (late-time) neutrinos and dark matter particles, whose nature remains unknown.
- Relativistic particles like photons and relativistic (early-time) neutrinos.
- Dark energy, eventually in the form of a cosmological constant Λ , which can effectively be treated as a non-classical fluid with a well-defined energy density.
- Curvature, encoded in the term dependent on κ , which describes the curvature of space-time in cases where the Universe is not flat. It is important to note that curvature itself can be formally equated to a contribution to the Universe's energy budget. In this sense, the effects of spatial curvature influence the overall dynamics of the Universe, just as different forms of energy density (such as matter, radiation, or dark energy) do.

All fluids relevant to cosmology are assumed to be perfect, which implies that they possess an equation of state (EoS) that relates their density and pressure:

$$p = w\rho, \quad (1.19)$$

which connects the density and pressure of different types of matter and energy. Combining this general equation of state with the continuity equation (2.1) reveals the scaling of density with respect to the scale factor:

$$\rho(t) = \rho_0 a^{-3(w+1)}, \quad (1.20)$$

where $\rho_0 = \rho(t_0)$ is the density at present time. Isolating each species to an associated density, pressure, and therefore EoS, allow to identify the evolution of their energy in terms of the

expansion. Radiation and relativistic particles have $w_r = 1/3$, while non-relativistic matter is treated as dust with zero pressure, i.e. $w_m = 0$, and the cosmological constant has $w_\Lambda = -1$. In this spirit, one can formally consider the curvature as an effective fluid with equation of state:

$$\rho_{\kappa,0} = \frac{-3\kappa}{a^2 8\pi G}, \quad (1.21)$$

which yields a parametric EoS with $w = -1/3$. Hence, the energy densities of the different components evolve as:

- $\rho_r \propto a^{-4}$ for radiation
- $\rho_m \propto a^{-3}$ for matter
- $\rho_\kappa \propto a^{-2}$ for curvature
- $\rho_\Lambda = \text{constant}$ for cosmological constant.

Therefore, the Friedmann equation (1.8) can be expressed in terms of the different content of the Universe:

$$H^2 = \frac{8\pi G}{3} (\rho_{r,0} a^{-4} + \rho_{m,0} a^{-3} + \rho_{\kappa,0} a^{-2} + \rho_{\Lambda,0}). \quad (1.22)$$

It is useful to parametrize the latter equation as a function of adimensional quantities which are invariant with respect to change in the coordinate system. To this end, we define the density parameters, specifically Ω_r , Ω_m , Ω_κ , Ω_Λ , for radiation, matter, curvature and cosmological constant Λ , respectively. These are defined as following:

$$\Omega_n = \frac{\rho_n}{\rho_c}, \quad (1.23)$$

with ρ_c being the critical density parameter

$$\rho_c = \frac{3H^2}{8\pi G} = 1.8788 \times 10^{-26} h^2 \text{ kg m}^{-3}, \quad (1.24)$$

which by definition represents the density requested to obtain a universe with flat geometry ($\kappa = 0$).

Using the definition of Ω , the second Friedmann equation can be rewritten as:

$$1 - \Omega(t) = -\frac{\kappa c^2}{a^2(t) H^2(t)}, \quad (1.25)$$

where the right-hand side can not change the sign during the expansion of the Universe, so neither can the left side, having as a consequence that a universe governed by the Friedmann equations can not change its geometry during its evolution.

Now it is useful to rewrite Equation (1.22) and express the Hubble parameter in terms of the dimensionless densities Ω and H_0 :

$$H^2 = H_0^2 \left(\Omega_{\text{m},0} a^{-3} + \Omega_{\text{r},0} a^{-4} + \Omega_{\kappa,0} a^{-2} + \Omega_{\Lambda,0} \right) \quad (1.26)$$

where H_0 is the present-day value of the expansion rate parameter H , and we refer to it as the Hubble constant. This constant is usually parametrized in terms of a dimensionless quantity h in the following way:

$$H_0 = 100 h \text{ km s}^{-1} \text{ Mpc}^{-1}. \quad (1.27)$$

Expressing the scale factor in terms of redshift, using Equation (1.17), we obtain the following expression of the expansion rate:

$$H(z) = H_0 \sqrt{\Omega_{\text{m},0}(1+z)^3 + \Omega_{\text{r},0}(1+z)^4 + \Omega_{\kappa,0}(1+z)^2 + \Omega_{\Lambda,0}}. \quad (1.28)$$

the behavior of our Universe can thus be described by an ensemble of cosmological parameters $H_0, \Omega_{\text{m},0}, \Omega_{\text{r},0}, \Omega_{\kappa},$ and Ω_{Λ} which we will call through the name of *cosmology*.

Moreover, at small redshift, z , we can neglect the contribution of radiation to the energy budget, i.e. $\Omega_{\text{r}} = 0$. This allows us to further simplify Equation (1.28) to:

$$H(z) = H_0 \sqrt{\Omega_{\text{m}}(1+z)^3 + 1 - \Omega_{\text{m}}}. \quad (1.29)$$

1.1.7 Hubble's Law

In 1929, Edwin Hubble made a groundbreaking observation that distant galaxies exhibit a recessional motion, which he quantified through what is now known as *Hubble's Law*. This discovery was revolutionary because, until that time, the prevailing belief was that the Universe was static and unchanging. Hubble's work provided the first observational evidence for an expanding Universe, reshaping our understanding of cosmology. Hubble's law provides a direct relationship between the distance of a galaxy from the observer, d , and its recessional velocity away from us, v , expressed as:

$$v = H_0 d \quad (1.30)$$

Hubble's discovery was a pivotal moment in cosmology, providing the first observational evidence for the expansion of the Universe and laying the foundation for modern cosmological models, including the FLRW metric. This recessional motion is fundamentally linked to the phenomenon of the cosmological redshift.

1.1.8 Distances in cosmology

Let's start by defining the *comoving distance* as the distance traveled by a photon emitted at time t_i , which moves along a null geodesic, i.e., $ds = 0$, and is observed at time t , as:

$$d_P(t) = \int_{t_i}^t c \frac{dt'}{a(t')}. \quad (1.31)$$

By expressing the latter as a function of redshift, we obtain the relation between the comoving distance and redshift as a function of the expansion rate history $H(z)$, i.e., ultimately in the matter-energy content and curvature of the Universe:

$$d_P(z) = c \int_0^z \frac{dz'}{H(z')}. \quad (1.32)$$

where $a_0 \equiv a(t_0) = 1$, and assuming that the distance is calculated by an observer located at $z(t_0) = 0$. The upper limit of integration corresponds to the redshift at the time of emission. Considering a source located at the proper comoving distance because of the expansion of the universe, it is possible to define the proper distance in physical units:

$$D_c = (1+z)d_P(z) = \frac{d_P(t)}{a(t)}. \quad (1.33)$$

In the comoving distance defined in Equation (1.31) the dependence of the curvature is implicit through $a(t)$. The explicit dependence is seen in the transverse comoving distance D_M , defined as the distance between two events measured at the same time coordinate ($dt = 0$):

$$D_M = \begin{cases} D_H \sqrt{|\Omega_\kappa|} \sin \left[\sqrt{|\Omega_\kappa|} d_P / D_H \right] & \Omega_\kappa < 0 \\ d_P & \Omega_\kappa = 0 \\ D_H \sqrt{|\Omega_\kappa|} \sinh c \left[\sqrt{|\Omega_\kappa|} d_P / D_H \right] & \Omega_\kappa > 0 \end{cases} \quad (1.34)$$

where $D_H = c/H_0$, defined as the Hubble distance. In the case of a flat Universe, we recover the Euclidean distance.

The existence of a well-defined relation between d_P and the redshift z , Equation (1.31) justifies the use of the observed redshift as a proxy to object distances and has triggered the completion of large observational campaigns, the spectroscopic galaxy redshift surveys, to map the 3D distribution of mass in the Universe.

Ideally, one may want to exploit this relation to determine the cosmological parameters that enter the relation, i.e., H_0 and the Ω parameters. To do so, one needs to measure redshifts and proper distances separately. The latter, however, cannot be directly estimated from

the data since it would imply instantaneous measurements from two different observers. Nevertheless, one can operatively define other kinds of distances corresponding to observable quantities (luminosity distance, angular diameter), all related to the proper distance d_P .

Luminosity distance The distance measured by Hubble, and used to derive Equation (1.30), is the luminosity distance d_L , whose definition is based on the preservation of the Euclidean inverse-square law for the diminution of light with distance from a source. Being L the luminosity emitted by a source at a point P , with coordinate r at time t , and F the flux received from the observer at time t_0 placed at P_0 , we define

$$d_L = \left(\frac{L}{4\pi F} \right)^{1/2}. \quad (1.35)$$

The area of a spherical surface centered on P and passing through P_0 at time t_0 is $4\pi a_0^2 r^2$. The photons arriving at P_0 are redshifted by the Hubble expansion by a factor a/a_0 . Also, photons emitted by the source at a small time interval δt arrive at P_0 in an interval $\delta t_0 = (a_0/a)\delta t$ since there is a time-dilation effect. We find that

$$F = \frac{L}{4\pi a_0^2 r^2} \left(\frac{a}{a_0} \right)^2, \quad (1.36)$$

from which

$$d_L = a_0^2 \frac{r}{a} = (1+z)D_M. \quad (1.37)$$

Angular diameter distance The primary information we obtain about a distant astronomical object comes from the light it emits and the photon flux that reaches us. This light allows us to observe the object and infer its general shape, provided that the object is extended and the angular resolution of the instrument is high enough. One of the key observational quantities in astronomy is the object's angular diameter, $\Delta\theta$. The concept of the angular diameter distance is constructed to preserve a geometric property of Euclidean space: the way an object's angular size varies with its distance from the observer. Defining $D_P(t)$ as the proper diameter of a source located at a coordinate distance r at time t , i.e., $D_P = ar\Delta\theta$, we can write the angular diameter distance as:

$$D_A = \frac{D_P}{\Delta\theta} = ar, \quad (1.38)$$

which is also equal to

$$D_A = (1+z)^{-2} d_L = \frac{D_M}{1+z}. \quad (1.39)$$

For a flat universe, $D_M = d_P$, which corresponds to the comoving distance.

1.2 The standard cosmological model

As we have seen, the expansion history of the Universe $H(z)$ is determined by a set of parameters, each contributing to a comprehensive description of a specific cosmological model. Observational data from various sources increasingly converge toward a single favored model known as the Λ CDM model. In this model, Λ represents the cosmological constant, corresponding to dark energy, while CDM stands for Cold Dark Matter, a mysterious form of invisible matter that, despite being undetectable directly, by its gravitational interactions, has significant mass and plays a crucial role in shaping the large-scale structure of the observable Universe. Recent constraints on cosmological parameters, particularly those that describe the mass-energy budget determining, together with H_0 , the expansion history of the Universe, have been provided by the 2018 results from the Planck Collaboration (Planck Collaboration et al., 2020), investigating the temperature and polarization anisotropies in the CMB, offering the most precise measurements to date:

$$\begin{aligned}\Omega_m &= 0.3111 \pm 0.0056, \\ \Omega_\Lambda &= 0.6889 \pm 0.0056, \\ \Omega_\kappa &= 0.001 \pm 0.002.\end{aligned}\tag{1.40}$$

As a result, the Universe is considered to be flat, with its curvature consistent with $\kappa = 0$, and primarily dominated by what is known as the dark sector, as illustrated in Figure 1.1. This dark sector encompasses the unseen components of the Universe, specifically dark matter and the cosmological constant Λ . The presence of the cosmological constant accounts for the ongoing late-time acceleration of the Universe's expansion.

The existence of a dark sector, which dominates the energy budget, poses a significant challenge for cosmology: while we can measure the density parameters, Ω_Λ and Ω_m , they provide little insight into the true nature of the fundamental processes underlying dark matter and dark energy.

The Λ CDM model is widely accepted as the standard model of cosmology. However, despite its refinements and notable successes, several theoretical aspects remain poorly understood. For instance, we haven't detected the dark matter yet and we ignore its nature. Furthermore, the very existence of *dark energy* (*DE*) is even more enigmatic. As discussed in Section 1.1.1, dark energy was introduced to explain the accelerated expansion of the Universe, yet it cannot be attributed to any known form of energy.

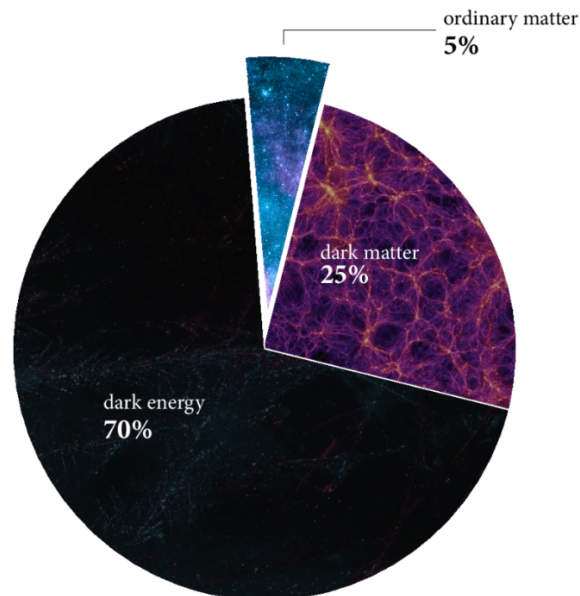


Figure 1.1 The content of the universe in various forms of energy in the Λ CDM model, as measured by CMB observations and large-scale structure surveys. Source: Max-Planck-Institute for Astrophysics Garching and Pixabay.

Dark matter (DM) was first introduced by Zwicky (Zwicky, 1937) to explain gravitational effects that could not be accounted for, without invoking an excess of non-visible mass. DM can be interpreted as particles or compact objects that significantly interact only with matter (including self-interactions) through gravity whereas the cross-section for non-gravitational interaction must be very small. The existence of DM is now widely confirmed through several lines of evidence. Some of the most reliable probes to quantify its effects include gravitational lensing by galaxy clusters, galaxy rotational curves, redshift-space distortions in the large-scale mass distribution, and fluctuations in the density spectrum due to baryon acoustic oscillations (BAO); see Bertone and Hooper (2018) for an extensive review on DM.

1.2.1 Dark matter

DM is typically classified into two main types:

- Hot dark matter (HDM), consists of low-mass relativistic particles, with massive neutrinos being the leading candidates.
- Cold dark matter (CDM), composed of massive, non-relativistic particles, for which weakly interacting massive particles (WIMPs) are the most prominent candidates.

Dark matter represents the major contribution of matter in the Ω_m energy density term, amounting to $\sim 80\%$. The remaining 20% is attributed to ordinary matter, also called *baryonic* matter.

Over the past few decades, numerous particle candidates for DM have been proposed and tested. Although none of the proposed candidates has been detected yet, the study of the large-scale structure allows us to infer some of its properties, the most important of which is the fact that these are non-relativistic, i.e., "cold", massive particles.

1.2.2 Dark energy

While the contribution of dark matter to the Universe has been a long-standing assumption, the discovery of a dark energy component is relatively recent. At the beginning of the 1990s, the prevailing view of a matter-dominated Universe was no longer favored by observations, such as the age estimates of the oldest globular clusters Ostriker and Steinhardt (1995) and the excess of angular auto-correlation of galaxies on very large scales, observed in early photometric surveys. In this context, the study of Type Ia supernovae (SNIa)—a type of thermonuclear supernova explosions—that were found to be dimmer than expected, suggested what appeared to be a late-time cosmic acceleration in the expansion of the Universe. SNIa events occur in a binary system consisting of a white dwarf and a giant star. Through gravitational interactions, the white dwarf accretes gas from the giant star until its mass exceeds $1.4M_\odot$, the Chandrasekhar limit. At this point, a thermonuclear explosion occurs, resulting in a Type Ia supernova. These objects have very similar light curves with a peak of almost universal luminosity, making them the most precise standard candle, for measuring astronomical distances, at our disposal. One significant consequence of Type Ia Supernova (SNIa) observations was that their flux appeared dimmer than expected, implying they were farther away than predicted based on their observed redshift. This deviation in the distance-redshift relationship could only be explained by introducing a non-negligible Ω_Λ term, indicating the presence of dark energy and suggesting a late-time accelerated expansion of the Universe. To investigate this, both the Supernovae Search Team (Filippenko and Riess, 1998) and the Supernova Cosmology Project (Perlmutter et al., 1999) measured the apparent luminosity of SNIa across different redshifts to reconstruct the luminosity-redshift relation, which is sensitive to cosmological parameters. Their analyses revealed a significant contribution from a non-zero cosmological constant Λ , indicating a late-time acceleration in the Universe's expansion (Perlmutter et al., 1999; Riess et al., 1998). More recent results on both SNIa and other probes (see next section) have established the Λ constant as a contribution to the overall expansion of the Universe.

Explaining the cosmological constant Λ as the source of the Universe's acceleration leads to the well-known cosmological constant problem. When Λ is interpreted as the vacuum energy density, its measured contribution in cosmology is 120 orders of magnitude smaller than the naive theoretical predictions. This significant discrepancy leaves the physical process associated with the non-zero Λ unexplained, commonly referred to as the dark-energy problem. Attempts to model this dark energy can be categorized into two main approaches. The first involves dynamical dark energy models and similar theories, which attempt to retain the idea of a non-classical contribution to the stress-energy tensor, that drives the late-time cosmic acceleration. The second approach involves modifications of the law of gravity on large scales, which lead to alterations of the $G_{\mu\nu}$ tensor. Here I will focus on the first possibility and, in the next section, I will give a broad overview of the first category of theories.

Dynamical dark energy A popular model of dynamical dark energy involves the use of a time-evolving scalar field ϕ and its potential $V(\phi)$ to describe dark energy as a time-dependent field that acts in opposition to the gravitational field. In its simplest form, these models assume a spatially homogeneous field that evolves according to the framework of GR and the FLRW metric, as described by the following equation.

$$\ddot{\phi} + 3H\dot{\phi} + \frac{dV(\phi)}{d\phi} = 0$$

Such models typically yield an observable that can be expressed in terms of a time-evolving equation of state:

$$w_\phi = \frac{\frac{1}{2}\dot{\phi}^2 - V(\phi)}{\frac{1}{2}\dot{\phi}^2 + V(\phi)}. \quad (1.41)$$

To account for the evolution of the dark energy equation of state during cosmic expansion, the Chevallier-Polarski-Linder (CPL) parametrization is often employed (Chevallier and Polarski, 2001; Linder, 2003). This parametrization is given by:

$$w(a) = w_0 + (1 - a)w_a \Rightarrow w(z) = w_0 + \frac{z}{1+z}w_a, \quad (1.42)$$

which is the Taylor expansion of any possible equation of state truncated at the linear order. Here, w_0 represents the value of the equation of state today, and w_a describes its variation over time. As such, it is possible to place bounds on the value of the equation of state today, denoted w_0 , within the range $-1 < w_0 < -1/3$, where the upper boundary is derived directly from Equation (1.20), representing the maximum value that ensures a late-time

acceleration of the expansion. Such models of dynamical dark energy are often referred to as *quintessence* models. The resulting new definition of the dark energy equation of state leads to the following expression for the dark energy density:

$$\rho_{\text{DE}} = \rho_{\text{DE},0} a^{-3(1+w_0+w_a)} e^{-3w_a(1-a)}. \quad (1.43)$$

This class of models, by allowing various parameterizations of ϕ and $V(\phi)$, and the resulting equation of state, remains consistent with general relativity theories.

There exist various models of dark energy, and the w_0w_a parametrization, Equation (1.42), effectively describes their impact on the evolution of the Universe. From a theoretical standpoint, these models represent the first and most straightforward generalization of the Λ CDM model, where $w_a = 0$ and $w_0 = -1$. For this reason, they are often considered as reference models in cosmological analyses. Additionally, interest in these models has recently increased following the analysis of DESI data (DESI Collaboration et al., 2024), which I will discuss in a subsequent paragraph, as they indicate some level of departure from the standard Λ CDM model, deviating from $w = -1$ and $w_a = 0$. Two examples of these generalizations of the Λ CMD are the so-called w CDM model, which assumes w to be a constant, potentially different from -1 , allowing for scenarios involving dynamic dark energy; and its extension, the w_0w_a CDM model, where w is no longer constant but evolves over time. In this case, the parametrization of Equation (1.42) is used, where w_0 is the current value of the equation of state and w_a describes its time evolution. These models provide greater flexibility in exploring the nature of dark energy compared to the Λ CDM model.

1.2.3 Testing the standard cosmological model

Cosmic microwave background The expanding Universe implies that, in its early stages, it underwent a period characterized by extremely high density and temperature, where matter and radiation were tightly coupled in a plasma. During this phase, the Universe was highly homogeneous and isotropic, with very small deviations from the mean density in all its components. Although small in amplitude, fluctuations in the coupled baryon and density underwent oscillations due to the competing pull of self-gravity and radiation pressure. The resulting propagating sound waves are the so-called Baryonic Acoustic Oscillations (BAO) (Hu and Sugiyama, 1996).

As the Universe expanded and cooled, the mean density of all its components decreased, allowing photons to decouple from matter, marking the era of decoupling. This event left an imprint of the initial density fluctuations in the form of free-streaming radiation, while the free electrons re-combined to protons forming neutral hydrogen atoms (marking the

recombination era). The existence of this relic radiation, known as the cosmic microwave background (CMB), was first theorized by Gamow, Alpher, and Bethe (Alpher et al., 1948; Gamow, 1948), but it was only confirmed years later by Dicke et al. (1965), who predicted that such radiation would be redshifted to microwave wavelengths. In the same year, Penzias and Wilson (1965) serendipitously detected the CMB as a white noise signal in the microwave regime.

The discovery of the CMB provided a crucial observational tool to study the early Universe. Due to atmospheric interference, space missions were launched to measure the black-body spectrum of this radiation with higher precision. The COBE satellite (Mather et al., 1994) measured a near-perfect black-body spectrum at a temperature of 2.73 K , but detected small temperature anisotropies on the order of $\delta T/T \sim 10^{-5}$ (Smoot et al., 1992). These temperature fluctuations corresponded to the primordial density perturbations, and their statistical analysis offered insights into the early Universe as well as constraints on modern cosmological parameters (Hu and White, 1997). One of the first, indirect, hints for a non-zero Λ component came from the BOOMERANG experiment (de Bernardis et al., 1999), which used high-altitude balloons to map density fluctuations. The resulting power spectrum strongly supported an $\Omega_{\kappa} = 0$ Universe (de Bernardis et al., 2000). Following BOOMERANG, the WMAP satellite (Bennett et al., 2013; Hinshaw et al., 2013; Komatsu et al., 2011) provided further evidence favoring the Λ CDM model, and the subsequent Planck mission released its final cosmological data in 2018 (Planck Collaboration et al., 2020).

The analysis of temperature fluctuations in the CMB, through the angular power spectrum, has provided precise constraints on cosmological parameters. As shown in Figure 1.2, the oscillations in the power spectrum are directly linked to the initial baryon acoustic oscillations in the primordial plasma. The location of the first peak is sensitive to the total energy density Ω_m , while the shape of the spectrum depends on the baryon density Ω_b .

The existence of the CMB confirmed several important aspects of cosmology. It validated the presence of primordial density fluctuations, which are believed to be the seeds of the large-scale structure of matter observed today. Additionally, it confirmed the cosmological principle on large scales and provided strong evidence that the geometry of the Universe is flat.

Baryonic acoustic oscillations in the distribution of galaxies The expansion of the Universe, combined with gravitational interactions, caused the initial density fluctuations to evolve into the large-scale structure of matter we observe today. These fluctuations in the tracers of the mass distributions, such as the galaxies, exhibit features in their 3-dimensional power spectrum that are similar to those seen in the CMB radiation. As the Universe cooled,

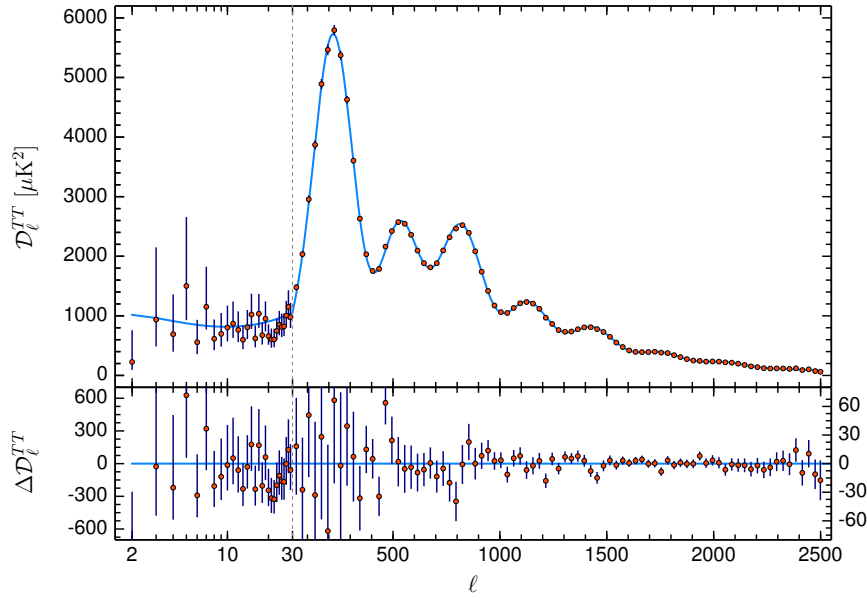


Figure 1.2 Upper panel: In red, the estimated angular power spectrum of the temperature fluctuations of the CMB of the Planck 2018 data release. In blue, best fit theoretical prediction from a Λ CDM model. Lower panel: Residuals in regards to the model prediction. Errors displayed are the 1σ interval which include the cosmic variance. Credits: (Planck Collaboration et al., 2020)

the primordial plasma, through which these perturbations propagated, began to decouple from radiation, leading to the end of baryon-photon interactions. Unlike the CMB photons, which are subject to various foreground contamination, the BAO feature is imprinted in the spatial distribution of the matter, preserving its information. Its characteristic signature is an excess of mass correlation at separations of $\simeq 100h^{-1}$ Mpc which roughly corresponds to the scale of the cosmological horizon at the epoch of decoupling. This characteristic scale can be used as a standard ruler. Comparing its apparent angular size to its observed redshift allows us to constrain the distance-to-redshift relation, (1.32), and, therefore the expansion history $H(z)$ of the Universe.

The comoving distance, which depends on cosmological parameters, can be constrained by comparing this standard BAO scale to predictions. Additionally, the study of the galaxy density field, a late-time probe, offers valuable insight into the expansion rate of the Universe and helps identify any potential discrepancies between early- and late-time measurements. The investigation of the BAO feature is a relatively recent development in cosmology. It was first noticed as an unusual pattern in the large-scale matter distribution by Broadhurst et al. (1990), with a theoretical explanation provided later by Eisenstein and Hu (1999). The first major detection of BAO came from the sample of Luminous Red Galaxies (LRG), i.e. galaxies particularly luminous and nearby that are observed when the sky is not fully dark,

from the SDSS-I program (Eisenstein et al., 2005). Since then, BAO has become a powerful and robust probe of cosmology, contributing to highly accurate measurements at different epochs, enabling the extraction of cosmological parameters consistent with a flat Λ CDM cosmology (Alam et al., 2017, 2021).

The most recent galaxy clustering analysis involving the BAO feature has been recently performed using the first data release of the DESI survey (DESI Collaboration et al., 2024), where BAO analyses were conducted using data from bright galaxies, LRGs, ELGs (emission line galaxies, i.e., galaxies with strong emission lines in their spectra, which allow precise redshift measurements), quasars (extremely luminous active galactic nuclei powered by supermassive black holes, whose light can be observed across vast cosmological distances), and $\text{Ly}\alpha$ forest tracers (a series of absorption lines in the spectra of distant quasars, caused by intervening clouds of neutral hydrogen, which help map the large-scale structure of the Universe) in the redshift range $0.1 < z < 4.2$. To fit the cosmological model, a dynamical dark energy model was used, incorporating the parameters w_0 and w_a according to equation (1.42). The results of this analysis, combined with those from other probes and summarized in Figure 1.3, show some level of departure from the Λ CDM model combinations of DESI with CMB, in particular CMB anisotropies from Planck and CMB lensing data from Planck and Atacama Cosmology Telescope (ACT), or with SN Ia, PantheonPlus, Union3, and DESY 5 samples, individually prefer $w_0 > -1$ and $w_a < 0$. For more details see (DESI Collaboration et al., 2024).

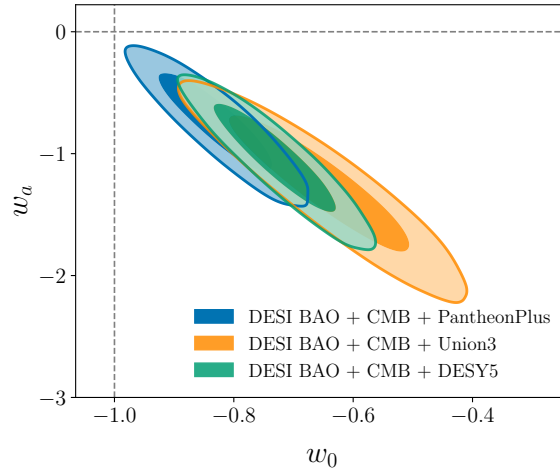


Figure 1.3 the 68% and 95% marginalized posterior constraints from DESI BAO combined with CMB and each of the PantheonPlus, Union3 and DESY5 SN Ia datasets. The significance of the tension with Λ CDM ($w_0 = -1$, $w_a = 0$) estimated from the $\Delta\chi^2$ MAP values is 2.5σ , 3.5σ , and 3.9σ for these three cases respectively. Credits: (DESI Collaboration et al., 2024).

Although the significance of the departure from a Λ CDM model is still modest, this result highlights the importance of investigating alternative to the standard cosmological model and illustrates the fundamental role that the study of the large scale structure will have in this effort.

1.2.4 Challenges to the Λ CDM model

While cosmological constraints have reached unprecedented precision over the past decade, several unresolved issues remain within the Λ CDM framework:

- *Flatness problem:* The notion of a flat Universe, dominated by Ω_m and Ω_Λ , implies that during its early evolution, these parameters needed to be extremely finely tuned to result in the Universe we observe today. Any deviation from this fine balance would have led to a drastically different cosmological scenario. This issue is addressed by the theory of cosmic inflation, which suggests that a rapid expansion of the Universe in its early moments naturally drives it towards flatness. However, despite its success in resolving the flatness problem, the exact nature of inflation remains unknown and is still a topic of active research. The flatness problem highlights that we are part of a unique, non-reproducible experiment, which poses challenges for thorough empirical testing (Dicke, 1972).
- *The nature of late-time cosmic acceleration:* Although often described by the presence of a non-zero cosmological constant, no compelling explanation for this acceleration has been settled on. Precise measurements of the dark energy equation of state have become crucial, as they may allow us to distinguish between different dark energy models or modified gravity scenarios (Motta et al., 2021).
- *The mass of neutrinos:* Massive neutrinos can have a significant impact on the large-scale clustering of galaxies. Therefore, accurately measuring their mass is essential to understanding their contribution to the overall energy content of the Universe. A key question is whether neutrinos can be considered as a component of dark matter (Abdalla et al., 2022).
- *Tension between local and large-scale H_0 estimates:* The wealth of observational data has produced a variety of estimates for the present-day expansion rate, H_0 . However, there is a persistent tension between measurements derived from local Universe observations, such as supernovae and Cepheids, that report a value $H_0 = 73.04 \pm 1.04$ km/s/Mpc (Riess et al., 2022), and those based on large-scale structure and the CMB, with a value $H_0 = 67.36 \pm 0.54$ km/s/Mpc (Planck Collaboration et al., 2020).

Despite being favored by multiple observations, the Λ CDM model remains incomplete, as no definitive explanation has been provided for the aforementioned challenges. To properly distinguish between the different available scenarios, large datasets and a diverse range of cosmological probes are needed. In this context, the next generation of large-scale surveys, such as Euclid (Euclid Collaboration et al., 2024), DESI (DESI Collaboration et al., 2022), and the Nancy Grace Roman Space Telescope (Dore et al., 2019; Spergel et al., 2015; Wang et al., 2022), aim to deliver vast amounts of data, including supernovae, galaxy, and quasar positions, measured through both photometry and spectroscopy.

2

Structure evolution

On megaparsec (Mpc) scales, the matter distribution of the Universe appears to be highly inhomogeneous, reflecting the characteristics of a strongly nonlinear evolution of an initially highly uniform density field. Indeed, the temperature fluctuations in the CMB maps, as described in Section 1.2.3 are on the order of $\delta T/T \simeq 10^{-5}$, where T represents the mean blackbody temperature of the CMB and the corresponding fluctuations in the matter density field are expected to be of the same order. This implies that the mechanism that amplified these original fluctuations to form the cosmic structures that we observe today must have been very efficient.

As early as 1902, Sir James Jeans developed a theory that would later provide an analytical description of this gravitational amplification process. As will be discussed in this chapter Jeans' theory predicts that small inhomogeneities in a self gravitating fluid are amplified over time, ultimately leading to the formation of the collapsed structures we observe today. An analytic solutions to the equations that describe the process, however, exists only in the limit of small density fluctuations where linear perturbation theory can be applied. Or for highly symmetric systems like spherical fluctuations. Linear solutions breaks down for gravitationally bound objects, in which fluctuations in the dark matter component that dominates the gravity field have entered the nonlinear regime and the dissipative baryonic component becomes gravitationally important in correspondence of the density peaks. An analytical description of matter evolution in the nonlinear regime can only be achieved for a few, highly idealized models, such as the spherical collapse model and the Zel'dovich approximation. In this chapter, I will describe the evolution of structure according to linear theory, along with velocity perturbations and their effects on the observed redshift, i.e., redshift-space distortions. Additionally, I will cover the spherical collapse model and the Zel'dovich approximation. The latter, in particular, forms the foundation of the Zel'dovich

reconstruction technique, which I employed in this Thesis and will describe in detail in Section 3.4.

2.1 Linear perturbation theory

The existence of initial density perturbations implies variations in the mass distribution, leading to corresponding perturbations in the gravitational potential. Over-dense regions exert a stronger gravitational pull compared to under-dense ones, and this uneven distribution of the gravitational potential is referred to as gravitational instabilities. In this framework, the formation of large-scale structures (LSS) is driven by the evolution of gravitational instabilities within an expanding background Universe. For a self-gravitating, non-relativistic fluid such as collisional matter, its dynamics can be described by the following set of equations:

$$\frac{\partial \rho}{\partial t} + \nabla \cdot (\rho \mathbf{v}) = 0, \quad \text{Continuity equation} \quad (2.1)$$

$$\frac{\partial \mathbf{v}}{\partial t} + (\mathbf{v} \cdot \nabla) \mathbf{v} = -\frac{1}{\rho} \nabla P - \nabla \Phi, \quad \text{Euler equation} \quad (2.2)$$

$$\nabla^2 \Phi = 4\pi G \rho, \quad \text{Poisson equation} \quad (2.3)$$

where ρ denotes the density of the fluid, \mathbf{v} its velocity, P the pressure and Φ the gravitational potential. The continuity equation for non-relativistic fluid, (2.1), governs the transport of density in time. The Euler equation, (2.2), depicts the variation of the fluid velocity through the interaction of opposite forces at play, in this case, pressure and gravity. Finally, the Poisson equation, (2.3) relates the gravitational potential to its surrounding density field. The understanding of the growth of structures, is based on initial perturbations in the medium. The quantities of interest are described as the sum of their background values and small perturbations, assuming that the perturbations are adiabatic:

$$\rho = \rho_0 + \tilde{\rho} \quad (2.4)$$

$$P = P_0 + \tilde{P} \quad (2.5)$$

$$\mathbf{v} = \mathbf{v}_0 + \tilde{\mathbf{v}} \quad (2.6)$$

$$\Phi = \Phi_0 + \tilde{\Phi}. \quad (2.7)$$

The equations of motion of the fluid, (2.1), (2.2), (2.3), can be rewritten as:

$$\frac{\partial \tilde{\rho}}{\partial t} + \nabla \cdot (\rho_0 \tilde{\mathbf{v}}) + \tilde{\rho} (\nabla \cdot \mathbf{v}_0) + \mathbf{v}_0 \cdot \nabla \tilde{\rho} = 0 \quad (2.8)$$

$$\frac{\partial \tilde{\mathbf{v}}}{\partial t} + (\mathbf{v}_0 \cdot \nabla) \tilde{\mathbf{v}} + (\tilde{\mathbf{v}} \cdot \nabla) \mathbf{v}_0 = -\frac{1}{\rho_0} \nabla \tilde{P} - \nabla \tilde{\Phi} \quad (2.9)$$

$$\nabla^2 \tilde{\Phi} = 4\pi G \tilde{\rho}, \quad (2.10)$$

where we have neglected the products of perturbations since these are second-order terms and we are considering linear perturbations only. This system of equations represents the Eulerian description of the fluid, which describes the evolution of quantities at a specific coordinate. However, to express the displacement of perturbations under both gravitational interactions and the expansion of the background, we switch to a Lagrangian description:

$$\frac{\partial \tilde{\rho}}{\partial t} = \frac{d\tilde{\rho}}{dt} - (\mathbf{v}_0 \cdot \nabla) \tilde{\rho} \quad (2.11)$$

$$\frac{\partial \tilde{\mathbf{v}}}{\partial t} = \frac{d\tilde{\mathbf{v}}}{dt} - (\mathbf{v}_0 \cdot \nabla) \tilde{\mathbf{v}} \quad (2.12)$$

and substitute them in the continuity and Euler equations, (2.8) and (2.9), obtaining the following:

$$\frac{d\tilde{\rho}}{dt} + \nabla \cdot (\rho_0 \tilde{\mathbf{v}}) + \mathbf{v}_0 \cdot \nabla \tilde{\rho} = 0 \quad (2.13)$$

$$\frac{d\tilde{\mathbf{v}}}{dt} + (\tilde{\mathbf{v}} \cdot \nabla) \mathbf{v}_0 = -\frac{1}{\rho_0} \nabla \tilde{P} - \nabla \tilde{\Phi}. \quad (2.14)$$

Let's consider the density fluctuation δ , evaluated in the proper coordinate \mathbf{x} at time t , defined as the value of the density field in regard to a background density ρ_0 :

$$\delta(\mathbf{x}, t) = \frac{\rho(\mathbf{x}, t) - \rho_0}{\rho_0}. \quad (2.15)$$

The continuity equation can then be rewritten in terms of δ :

$$\frac{d\delta}{dt} + (\nabla \cdot \tilde{\mathbf{v}}) = 0. \quad (2.16)$$

Finally, to properly account for the expanding background influence on the spatial reference frame suggested by ∇ , we use the comoving distance:

$$\mathbf{r} = \frac{\mathbf{x}}{a(t)} \quad (2.17)$$

obtaining the following expression for the derivative:

$$\nabla_r = \frac{1}{a} \nabla. \quad (2.18)$$

The velocity can be rewritten as:

$$\mathbf{v} = \frac{d\mathbf{x}}{dt} = \mathbf{r} \frac{da}{dt} + \frac{d\mathbf{r}}{dt} a, \quad (2.19)$$

where the first term corresponds to the expansion of the Universe and the second is linked to the perturbations. The perturbed velocity vector rewrites as follow:

$$\tilde{\mathbf{v}} = a\mathbf{u}, \quad (2.20)$$

with $\mathbf{u} = d\mathbf{r}/dt$ being the comoving peculiar velocity. By applying these new definitions, the linearized continuity equation can be written as:

$$\frac{d\delta}{dt} + (\nabla_r \cdot \mathbf{u}) = 0, \quad (2.21)$$

and the Euler equation:

$$\frac{d\mathbf{u}}{dt} + 2H\mathbf{u} = -\frac{\nabla \tilde{P}}{a^2 \rho_0} - \frac{\nabla \tilde{\Phi}}{a^2}. \quad (2.22)$$

Applying the divergence operator and using Equation (2.22) we obtain:

$$\frac{d^2\delta}{dt^2} + 2H \frac{d\delta}{dt} = \frac{\nabla^2 \tilde{P}}{a^2 \rho_0} + \frac{\nabla^2 \tilde{\Phi}}{a^2}. \quad (2.23)$$

Furthermore, the latter equation can be rewritten by using Equation (2.3), and considering the density fluctuation to be adiabatic, i.e., relating pressure and by considering the sound speed definition for adiabatic perturbations $c_s = \tilde{P}/\tilde{\rho} = \sqrt{\partial p/\partial \rho}$, obtaining:

$$\frac{d^2\delta}{dt^2} + 2H \frac{d\delta}{dt} = \delta \left(4\pi G \rho_0 - \frac{k^2 c_s^2}{a^2} \right). \quad (2.24)$$

Expanding the overdensity field delta in Fourier modes $\delta_{\mathbf{k}}$, Equation (2.24) can be expressed as a *dispersion relation*:

$$\ddot{\delta}_{\mathbf{k}} + 2H \dot{\delta}_{\mathbf{k}} + (k^2 c_s^2 - 4\pi G \rho_0) \delta_{\mathbf{k}} = 0, \quad (2.25)$$

where $k = |\mathbf{k}|$ is the absolute value of the wavenumber, $\delta_{\mathbf{k}} = \delta_k(t)$ is the amplitude of the Fourier transform of $\delta(\mathbf{x}, t)$. In the equation above, the term $2H \dot{\delta}_k$ is related to the Hubble friction and the term $k^2 c_s^2 \delta_k$ describes the characteristic velocity field of the fluid. These two terms tend to dissipate the fluctuations, hampering their growth. The solutions of Equation (2.25), which is a second order differential equation for δ_k , can be separated depending on

the value of the wavelength $\lambda = 2\pi/k$, in relation to the characteristics scale called *Jeans length*, defined as:

$$\lambda_J = \frac{2\pi}{k_j} = \frac{2\pi c_s}{a\sqrt{4\pi G\rho_0}}, \quad (2.26)$$

which is expressed in physical units. Let's consider two limiting cases: When $\lambda \ll \lambda_J$, the perturbation propagates as sound wave with constant amplitude and with a phase velocity $c_{\text{ph}} = \omega/k$, where $\omega(k) = \sqrt{k^2 c_s^2 - 4\pi G\rho_0}$, with this velocity becoming equal to c_s in the limit $\lambda \ll \lambda_J$. Thus, in this case, the perturbation oscillates due to the interaction between pressure and density in the medium. On the other hand, when $\lambda \gg \lambda_J$, the dispersion relation has growing and decaying mode solutions, which in configuration space are expressed as:

$$\delta(\mathbf{x}, t) = A(\mathbf{x})\delta_+(t) + B\delta_-(t), \quad (2.27)$$

where A and B are two functions of the comoving coordinates, while δ_+ and δ_- are the time-dependent growing and decaying mode, respectively. For a matter-dominated EdS universe, where $a(t) \propto t^{2/3}$, we obtain the following trends:

$$\delta_+ \propto t^{2/3} \propto a(t) \quad (2.28)$$

$$\delta_- \propto t^{-1} \propto a(t)^{-3/2}. \quad (2.29)$$

The decaying mode does not give rise to gravitational instability, i.e., collapsed structures, thus, we are interested only in the growing solution. For a generic universe, the growing solution has an integral form given by:

$$\delta_+(z) = H(z) \int_z^\infty \frac{dz'(1+z')}{H^3(z')}, \quad (2.30)$$

which has no analytical solution. However, it is possible to provide a parametric solution, in the case of a Λ Universe, to approximate its trend:

$$f \equiv \frac{d \log \delta_+}{d \log a} \simeq \Omega_m^\gamma + \frac{\Omega_\Lambda}{70} \left(1 + \frac{1}{2} \Omega_m \right), \quad (2.31)$$

where the factor f is referred to as the linear growth rate of structures. The exponent γ is predicted by GR to have an approximate value of 0.545 (Coles & Lucchin, 2002). This relation indicates that, while the matter-energy density Ω_m plays a dominant role in the growth of cosmic fluctuations, the cosmological constant Λ has a relatively minor influence. Observational estimates of the linear growth rate are valuable for probing potential deviations from GR on cosmological scales. The exponent γ is of premier importance as it explicitly

depends on the expansion history of the Universe. For example, if its accelerated expansion were driven by a dark energy rather than a cosmological constant then (Linder, 2003):

$$\gamma = \frac{3(w_{\text{DE}} - 1)}{6w_{\text{DE}} - 5}. \quad (2.32)$$

2.1.1 Peculiar velocities

In linear perturbation theory, divergence of the peculiar velocity field is linked to the density field through the continuity equation (2.16)(Peebles, 1980). By using the conformal time η , introduced by Equation (1.14), that we rewrite here for simplicity as

$$dt = a(\eta)d\eta, \quad (2.33)$$

it is possible to write the continuity equation as:

$$\frac{d\delta(\mathbf{x}, \eta)}{d\eta} = -\nabla \cdot \mathbf{v}(\mathbf{x}, \eta), \quad (2.34)$$

that in Fourier space reads

$$\frac{d\delta(\mathbf{k}, \eta)}{d\eta} = -i\mathbf{k} \cdot \mathbf{v}(\mathbf{k}, \eta). \quad (2.35)$$

In a matter-dominated era the density perturbations evolve as δ_+ , therefore, the left-hand side of Equation (2.35) becomes:

$$\begin{aligned} \frac{d\delta}{d\eta} &= a \frac{d\delta}{dt} = a\delta \frac{\dot{\delta}_+}{\delta_+} = \delta \frac{d\delta_+}{da} \frac{da}{dt} \frac{a}{\delta_+} = \\ &= \left(\frac{a}{\delta_+} \frac{d\delta_+}{da} \right) \frac{da}{dt} \delta = afH\delta, \end{aligned} \quad (2.36)$$

where we used the definition of the growth rate of structures (2.31). Therefore, the continuity equation can be rewritten as:

$$-i\mathbf{k} \cdot \mathbf{v}(\mathbf{k}, \eta) = afH\delta(\mathbf{k}, \eta), \quad (2.37)$$

leading to

$$\mathbf{v} = \frac{i\mathbf{k}}{k^2} afH\delta(\mathbf{k}, \eta), \quad (2.38)$$

that in configuration space has the following form:

$$\nabla \cdot \mathbf{v} = afH\delta(\mathbf{x}, \eta). \quad (2.39)$$

2.2 Beyond linear theory

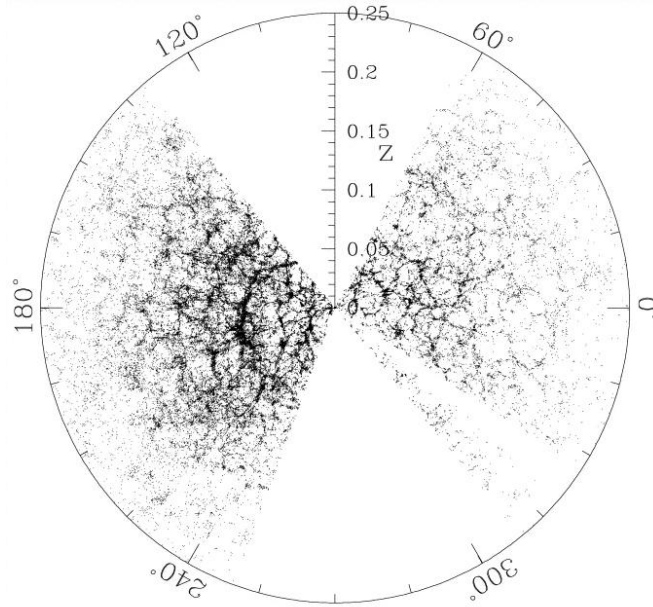


Figure 2.1 The Large Scale Structure of the Universe traced by galaxies in the early data from the Sloan Digital Sky Survey in which can be seen the different cosmic structures from which the Universe is formed: voids, filaments, and clusters. Credits: (Blanton et al., 2003)

The cosmic structures we observe in the present-day Universe, organized in a coherent network of nodes and filaments punctuated by clusters and galaxies (see Figure 2.1), are the end product of the gravitational instability process that we have described in the previous sections.

To describe the evolution of these objects, which are characterized by large overdensities ($\delta \gg 1$), linear perturbation theory is not sufficient. Once the linear regime breaks down, which typically occurs for δ comparable to unity, the Fourier modes δ_k couple with each other, and the distribution of the mass overdensity does not follow anymore a Gaussian statistics. Additionally, it is important to consider that the evolution of the baryonic component differs from that of DM. Baryons are a collisional and dissipative fluid whose physical status and chemical composition are affected by stellar feedback processes like Active Galactic Nuclei (AGN) physics and SN explosions, making it very difficult to elaborate a model to describe their cosmological evolution. Although one typically relies on numerical methods like N-body to simulate the evolution of matter perturbations in the non-linear regime, it is important to elaborate simplified analytical models to capture the nonlinear evolution of cosmic structures under simplifying hypotheses (about geometry or dynamics). If properly

applied these models can be very useful to describe the properties of specific types of cosmic structures, such as voids, and their cosmic evolution. In this section, we discuss two of these methods that are relevant for this Thesis: the spherical collapse model and the Zel'dovich approximation.

2.2.1 Spherical collapse model

The simplest dynamical model that approximately describes the formation of self-gravitating structures is the evolution of a spherical fluctuation in a homogeneous background, commonly referred to as the *top-hat model*. This toy model provides valuable insight into the gravitational evolution of a density perturbation, from the linear regime to the strongly nonlinear regime. To analytically study the fully nonlinear gravitational evolution, spherical symmetry is assumed, which simplifies the differential equations by reducing the degrees of freedom. Furthermore, this model serves as a bridge between the linear statistical properties of the matter density field and the formation of large-scale structures (LSS).

The evolution of a spherically symmetric perturbation can be analytically described well into the nonlinear regime, all the way to the gravitational collapse of the formation of the structure. This so-called *spherical collapse model* was originally introduced by Gunn and Gott III (1972), applied to describe the formation and evolution of dark matter halos (Cooray and Sheth, 2002) and of cosmic voids (Sheth and van de Weygaert, 2004).

Considering an initially spherical perturbation, which may be either positive or negative, it can be modeled as a closed or open universe, respectively, evolving within an EdS background. We focus on an initial time $t_i > t_{\text{eq}}$, where t_{eq} represents the matter-radiation equivalence time. Therefore, we examine the evolution of a spherical perturbation with a top-hat density profile during the matter-dominated cosmic epoch, at sufficiently high redshifts to assume an EdS model for the background. Assuming the validity of the CP each perturbation can be treated as an independent Friedmann universe as long as it evolves adiabatically. The only interaction that needs to be considered in this model is gravitational. We model the spherical top-hat perturbation as a series of concentric shells. As noted by Sheth and van de Weygaert (2004), the evolution of the perturbation depends solely on the total energy within the shell and its peculiar velocity, but not on the radial distribution of the density field inside the shell.

Let's consider spherically symmetric perturbation as a set of concentric shells with respective radii R_i . The mass M contained within the perturbation radius R determines the acceleration experienced by each shell, and in the Newtonian regime ($\dot{R} \ll c$ and $R \ll c/H$) it is expressed as:

$$\frac{d^2 R}{dt^2} = -\frac{GM}{R^2} = -\frac{4\pi G}{3}\rho(1 + \Delta)R. \quad (2.40)$$

At the initial time:

$$M = \frac{4\pi}{3} \rho_0 R_i^3 (1 + \Delta_i), \quad (2.41)$$

$$\Delta_i = \frac{3}{R_i^3} \int_0^{R_i} \delta_i(r) r^2 dr, \quad (2.42)$$

with Δ_i being the average value of δ_i within r_i . In the following, we will study the evolution of a top-hat perturbation in a EdS universe, i.e., flat matter dominated universe. The average density contrast, detached from the background, can be parametrized as follows (Sheth and van de Weygaert, 2004), distinguishing between the case of initial overdensities $\Delta_i > 0$ and initial underdensities $\Delta_i < 0$:

$$1 + \Delta(\tau) = \begin{cases} \frac{9}{2} \frac{(\tau - \sin \tau)^2}{(1 - \cos \tau)^3} & \Delta_i > 0 \\ \frac{9}{2} \frac{(\sinh \tau - \tau)^2}{(\cosh \tau - 1)^3} & \Delta_i < 0 \end{cases} \quad (2.43)$$

where τ is the adimensional conformal time:

$$d\tau = \frac{R_i}{R} \sqrt{\left| \frac{5}{3} \Delta_i \right|} H(t_i) dt. \quad (2.44)$$

In a matter-dominated Universe, the linear growth of perturbations is proportional to the scale factor $\Delta^L(a) = \Delta_i a/a(t_i)$. Therefore, by substituting this into Equation (2.43) we find the following relation

$$\Delta^L(\tau) = \begin{cases} \frac{3}{20} [6(\sinh \tau - \tau)^{2/3}] & \Delta_i < 0 \\ \frac{3}{20} [6(\tau - \sin \tau)^{2/3}] & \Delta_i > 0 \end{cases} \quad (2.45)$$

In this way, by comparing the evolution of the linear and nonlinear density contrast at the same conformal time τ , it becomes possible to recover the linear density contrast value corresponding to a given nonlinear one, and vice versa. This allows us to map the formation of halos (overdensities) and voids (underdensities) in the nonlinear regime back to their counterparts in linear theory.

Overdense perturbations Let us rewrite the nonlinear dynamics of overdensities, $\Delta_i > 0$, to express it in a form that emphasizes the crucial events occurring in spherical halo formation. For an overdensity Equation (2.43) has the form:

$$\Delta(\tau) = \frac{9}{2} \frac{(\tau - \sin \tau)^2}{(1 - \cos \tau)^3} - 1 \quad (2.46)$$

It is possible to distinguish three phases in the evolution of a spherical overdensity:

- Expanding phase: the overdensity starts expanding following the background dynamics, but it stops growing when it reaches the maximum radius R_{\max} at the so-called turnaround time t_{\max} reached at $\tau = \pi$.
- Collapsing phase: the overdensity evolves independently of the background and starts collapsing toward a singularity of vanishing size $R \rightarrow 0$. The spherical collapse model remains predictive during this phase, as long as the shells do not cross each other. The collapse is reached at $\tau = 2\pi$.
- Virialization: at $\tau = 2\pi$ the collapse is predicted. In practice, however, even a small deviation from sphericity is sufficient to break the symmetry, leading the perturbation to undergo a non-collisional collapse followed by virialization (Lynden-Bell, 1967). The size and density contrast of the virialized object can be calculated using the virial theorem, $2T = W$ leading to $E = T + W = W/2$, where T is the kinetic energy and W is the potential energy. From this, it follows that the virial radius is approximately $R_{\text{vir}} \simeq R_{\max}/2$. Assuming that the virialization occurs at $t_{\text{vir}} = t(\tau = 2\pi)$, this implies that $t_{\text{vir}} = 2t_{\max}$. It follows that the density at virialization is

$$\Delta(t_{\text{vir}}) \simeq 178. \quad (2.47)$$

As an object begins to virialize, the fluid elements are no longer confined to a single stream regime; instead, multiple streams cross each other, leading to the so-called *shell crossing* condition. The equations above have significant implications for the spherical halo formation model. The result from Equation (2.47) explains why the virialized region of a cluster is typically modeled as a sphere with an average density approximately 200 times the critical density of the universe. This is also the reason why a density contrast of $\Delta \sim 200$ is commonly used in spherical halo finders to identify virialized regions. Another important point, is that it is possible to match the non-linear evolution and virialization in linear theory. In particular, using Equation (2.45) we find the linear density contrast corresponding to full collapse evaluated at $\tau = 2\pi$, indicated with δ_c to recover the notation commonly used in literature:

$$\delta_c \simeq 1.69 \quad (2.48)$$

The quantities in Equation (2.47) are highly sensitive to the cosmological model assumed for the background universe, particularly with respect to its curvature. Conversely, the dependence of their linearly extrapolated counterparts is significantly weaker (Jenkins et al., 2001; Kitayama and Suto, 1996). The quantity δ_c is the critical threshold for spherical

collapse, and it is almost cosmology independent. This threshold plays a central role in models that use the statistics of the initial density fluctuation field to describe the clustering of virialized objects. The power of this simple model is that the linear theory can state when spherical collapse will eventually occur. The spherical collapse model provides a critical framework for understanding the nonlinear evolution of overdensities, forming the basis for the study of virialized structures such as galaxies and clusters, and now extends to the analysis of the main characters of this Thesis, i.e., voids.

Underdense perturbations Let's see the evolution of underdense regions $\Delta_i < 0$, which significantly differs from those of its overdense counterparts. The evolution of an underdensity never reaches turnaround and continues to expand forever, unless $\Delta_i > 0$ on some larger scale, as in the void-in-cloud scenario (Sheth and van de Weygaert, 2004). These underdensities, typically referred to as *voids*, exhibit a net radial acceleration directed outward from the sphere's center. This acceleration is directly proportional to the mean density contrast $\Delta(r, t)$ of the void. Notably, the inner shells, being more underdense, experience a greater outward acceleration compared to the outer shells. In the case of underdensities, Equation (2.43) becomes

$$\Delta(\tau) = \frac{9 (\sinh \tau - \tau)^2}{2 (\cosh \tau - 1)^3} - 1. \quad (2.49)$$

Nevertheless, Sheth and van de Weygaert (2004) showed that under particular conditions of the initial density profile, shell crossing can also occur also for spherical underdensities. In particular, they find that the density contrast corresponding to shell crossing is

$$\Delta_{sc} \simeq -0.7953 \quad (2.50)$$

to which corresponds a linear density contrast of $\Delta_{sc}^L \simeq -2.717$.

In the literature (Jennings et al., 2013; Sheth and van de Weygaert, 2004), shell crossing has often been considered the defining event for void formation, similar to halo formation. However, this parallelism is unnecessary, as shell crossing in voids is dependent on the initial density profile and is unlikely to occur for realistic profiles (Verza, 2022). While halos form through collapse and virialization, which can be mapped to linear theory using the collapse threshold δ_c , voids are extended regions that evolve by reaching a fixed density contrast. The linear threshold for void formation δ_v does not correspond to any specific event, but since shell crossing typically does not occur for observable voids, a map between linear and nonlinear theory always exists. Thus, void formation can be understood through linear theory without requiring shell crossing, and this constitute a key point for the modeling that will be presented in Section 4.2.

In conclusion, the evolution of spherical voids is characterized by expansion, in contrast to the collapse observed in overdense regions. As this expansion progresses, the boundaries of the voids become denser, while the central regions experience a further reduction in density contrast. Icke (1984) demonstrated that voids tend to evolve into spherical shapes, unlike collapsing structures, which typically develop into filamentary or sheet-like forms. Additionally, the expansion of a void can be viewed as a time-reversed version of overdensity collapse, leading to the suppression of any initial asphericity in the underdense regions.

2.2.2 Zel'dovich approximation

Another analytical solution to the cosmological density perturbation evolution can be obtained by making a simplifying hypothesis on the kinematic of the system rather than on its geometry. This approximation was first proposed by Zel'dovich (Zel'dovich, 1970) and later recognized as a 1st order perturbative solution to the growth of density fluctuations in a lagrangian framework. Despite its simplicity the so-called Zel'dovich approximation (ZA) is able to describe the evolution of the cosmological overdensity well into the nonlinear regime and to predict the occurrence of the different types of cosmic structures (clusters, voids, filaments); see Shandarin and Zeldovich (1989) for an extensive review of the ZA and its applications. Here we briefly outline the theory behind the ZA focusing on its use in the context of the back in time cosmological reconstruction.

The cosmological perturbation theory presented above, is formulated within the Eulerian framework, which examines the evolution of perturbations in terms of the density field $\rho(\mathbf{x})$ and the velocity field $\mathbf{v}(\mathbf{x})$ at a specific spatial position \mathbf{x} within the fluid element. An alternative approach can be formulated within the Lagrangian framework, the so-called Lagrangian Perturbation Theory (LPT), where the evolution of individual fluid elements is tracked through both space and time. Each element within the fluid is defined via its Lagrangian coordinate \mathbf{q} , and the dynamics of the cosmological fluid is fully characterized by the displacement field $\Psi(\mathbf{q}, t)$, such that at a generic time t , the Eulerian position of the fluid element labeled by its initial position \mathbf{q} . The relation between these quantities is expressed by the Zel'dovich approximation:

$$\mathbf{x}(\mathbf{q}, t) = \mathbf{q} + \Psi(\mathbf{q}, t). \quad (2.51)$$

The ZA constitutes a linear approximation with respect to the particle displacements rather than the density. It is also clear that Equation (2.51) involves the assumption that the position and time dependence of the displacement between initial and final positions can be separated. Notice that particles in the ZA execute a kind of inertial motion on straight line trajectories.

An important consequence of the ZA comes from the fact that it is conventional to describe the ZA as a first-order Lagrangian perturbation theory, and the aim of LPT is to obtain a perturbative solution for the displacement field Ψ .

The displacement can be linked to the matter overdensity via the following relation:

$$\delta(\mathbf{x}, t) \equiv \frac{\rho(\mathbf{x}, t) - \bar{\rho}}{\bar{\rho}} = \int d^3\mathbf{q} \delta_D^{(3)}(\mathbf{x}(t) - \mathbf{q} - \Psi(\mathbf{q}, t)) - 1 \quad (2.52)$$

where $\delta_D^{(3)}$ is the three-dimensional Dirac function. The latter equation in Fourier space becomes

$$\delta(\mathbf{k}, t) = \int d^3\mathbf{q} e^{-i\mathbf{k}\cdot\mathbf{q}} \left(e^{-i\mathbf{k}\cdot\Psi(\mathbf{q}, t)} - 1 \right) \quad (2.53)$$

Let's expand Ψ as in (Padmanabhan et al., 2009) $\Psi = \Psi^{(1)} + \Psi^{(2)} + \dots$, obtaining the following relation for Equation (2.53):

$$\begin{aligned} \delta(\mathbf{k}, t) &= \int d^3\mathbf{q} e^{-i\mathbf{k}\cdot\mathbf{q}} \left(e^{-i\mathbf{k}\cdot(\Psi^{(1)} + \Psi^{(2)} + \dots)} - 1 \right) = \\ &= \int d^3\mathbf{q} e^{-i\mathbf{k}\cdot\mathbf{q}} \left(-i\mathbf{k}\cdot\Psi^{(1)} \right) + \int d^3\mathbf{q} e^{-i\mathbf{k}\cdot\mathbf{q}} \left[-i\mathbf{k}\cdot\Psi^{(2)} - \frac{(\mathbf{k}\cdot\Psi^{(1)})^2}{2} + \dots \right] \end{aligned} \quad (2.54)$$

Truncating the perturbative expansion to order n in the displacement field Ψ yields the recursive equations for the overdensity field δ in term of the displacement field. Considering only the first order in the expansion, we obtain the following relation :

$$\delta_L(\mathbf{k}) = \int d^3\mathbf{q} e^{-i\mathbf{k}\cdot\mathbf{q}} \left(-i\mathbf{k}\cdot\Psi^{(1)} \right). \quad (2.55)$$

Considering that the right hand side of the latter equation corresponds to the Fourier transform of the divergence of the displacement field, it can be rewritten in the following form:

$$\nabla \cdot \Psi^{(1)}(\mathbf{q}, t) = -\delta_L(\mathbf{x}, t). \quad (2.56)$$

which in Fourier space becomes:

$$\Psi^{(1)}(\mathbf{k}) = \frac{i\mathbf{k}}{k^2} \delta_L(\mathbf{k}), \quad (2.57)$$

The solution to these differential equations, specifically the ability to derive the displacement field from the knowledge of the matter density field, forms the core of the Zel'dovich

reconstruction technique, which will be presented in detail in Section 3.4 and extensively employed in our analysis of cosmic voids.

3

Statistical properties of the observed Universe

In the previous chapter, we examined the evolution of dark matter structures in both the linear and nonlinear regimes. However, in observational cosmology, we do not have direct access to the distribution of matter itself but rather to its luminous counterpart, namely galaxies, whose distance must be estimated. This process inevitably introduces errors of random and systematic type. The latter being usually referred to as *distortions*. In this chapter, I focus on the connection between the theory of structure evolution and the observable galaxy field, by studying the statistical properties of the density fluctuation field, $\delta(\mathbf{x}, t)$, as traced by galaxies. This connection can be done by implying a specific observational probe: *Galaxy clustering*, which refers to the clustering patterns exhibited by galaxies in their spatial distribution. In order for galaxy clustering to be a probe for precision cosmology very large datasets containing millions of objects distributed over very large volumes are required. These datasets are acquired through extensive observational programs known as galaxy surveys, which map the three-dimensional positions of galaxies. Their analysis requires efficient statistical tools to compress information and sophisticated techniques to account for the systematic uncertainties derived from the observational techniques adopted to map the distribution of the galaxies. In the following sections, I will introduce the statistical tools used in the study of Galaxy Clustering (Sections 3.1.1 and 3.1.2), together with the connection between the observed galaxy fields and the underlying matter distribution 3.2, which is the important for bridging the theory of structure formation with the observations. In Section 3.3, I will discuss the challenges posed by observational effects and the associated distortions. Finally, I will describe a key technique used to mitigate the effect of one of the sources of distortions (Section 3.4).

3.1 Two-point statistics for galaxy clustering

An efficient way to compress the information contained in a cosmological matter density field is through its two-point statistics. This is because the initial cosmological density fluctuation field, as confirmed by observations of the CMB, is highly Gaussian. The statistical properties of a Gaussian field are fully determined by its two-point statistics. These statistics can be expressed either in Fourier space, through the *power spectrum*, or in configuration space, via the *two-point correlation function*. Both will be described in detail in the following two sections.

3.1.1 The matter power spectrum

The evolution equation, (2.25), obtained in the linear approximation is solved independently for each Fourier mode $\delta_{\mathbf{k}}$ in which the mass density field can be expanded giving:

$$\delta(\mathbf{x}) = \frac{1}{(2\pi)^3} \int d^3\mathbf{k} e^{-i\mathbf{k}\cdot\mathbf{x}} \delta(\mathbf{k}). \quad (3.1)$$

In other words, linear evolution does not mix different Fourier modes and, for this reason, all relevant information is contained in the Power spectrum, $P(k)$, defined as the expectation value of the product

$$\langle \delta(\mathbf{k}) \delta^*(\mathbf{k}') \rangle = (2\pi)^3 P(k) \delta_D^{(3)}(\mathbf{k} - \mathbf{k}'), \quad (3.2)$$

i.e. the first non trivial moment of the $\delta(\mathbf{k})$ field, where $\delta_D^{(3)}$ is the 3-dimensional Dirac delta function, and $\delta^*(\mathbf{k}) = \delta(-\mathbf{k})$ due to the reality condition of δ , with the superscript "*" indicating the complex conjugate. The CP guarantees the statistical isotropy, therefore $P(k)$ should depend only on $k = |\mathbf{k}|$.

According to inflationary theory, primordial density perturbations arise from stochastic quantum fluctuations in a scalar field (i.e., the inflaton) (see Guth and Pi (1982)). The 1-point probability of their amplitude is well approximated by a Gaussian distribution whose width is fully characterized by the $P(k)$. The shape of this primordial $P(k)$ is expected to exhibit a power law behavior, expressed as

$$P(k) = Ak^n, \quad (3.3)$$

where A is the amplitude of the primordial power spectrum, and the spectral index n is typically assumed to be close to unity (Zeldovich, 1972). The amplitude A grows linearly when fluctuations are small, and it can be directly inferred from observations of temperature fluctuations in the CMB (Planck Collaboration et al., 2020).

However, when the evolution of structures becomes nonlinear, the relationship with the primordial amplitude becomes more complex to determine. For this reason, the amplitude of the power spectrum at later times (closer to the present epoch) is specified after filtering the density field on large enough scales to eliminate nonlinear effects. Conventionally, this is done by filtering the observed overdensity field with a spherical top-hat function of radius $8 h^{-1}$ Mpc which defines the commonly used parameter σ_8 :

$$\sigma_8^2 = \frac{1}{2\pi^2} \int P(k) k^2 W^2(R = 8 h^{-1} \text{Mpc}) dk, \quad (3.4)$$

where W represents the window function employed for the filtering process.

After discussing about the amplitude, it is important to note that $P(k)$ is also characterized by its shape, which reflects the relative importance of fluctuations on different scales. At the present epoch, the shape of the power spectrum is no longer the primordial power-law form, as various processes throughout cosmic history have affected the dynamics of structure formation differently across different scales. Finally, as will be discussed in Section 3.3, systematic effects associated with the quantities observed to determine the power spectrum experimentally can break the assumption of statistical isotropy, causing $P(k)$ to depend not only on the magnitude of k but also on its direction.

3.1.2 The two-point correlation function

Alternatively, when clustering analyses are carried out in configuration, rather than Fourier space, the tool for accessing 2-point statistics is the 2-point correlation function (2PCF). In analogy with the $P(k)$, it is defined as the expectation value of two overdensities measured at any two spatial locations \mathbf{x}_1 and \mathbf{x}_2 :

$$\xi(\mathbf{x}_1, \mathbf{x}_2) = \langle \delta(\mathbf{x}_1) \delta(\mathbf{x}_2) \rangle, \quad (3.5)$$

or, by implying the CP, leveraging on the statistical homogeneity, the previous relation becomes:

$$\xi(\mathbf{r}) = \langle \delta(\mathbf{x}) \delta(\mathbf{r}) \rangle, \quad (3.6)$$

where $\mathbf{r} = \mathbf{x}_2 - \mathbf{x}_1$ is the separation vector. Because of statistical isotropy, this statistics is only sensitive to the modulus of the separation vector $r = |\mathbf{r}|$:

$$\xi(\mathbf{r}) = \xi(r). \quad (3.7)$$

By combining (3.1) and (3.5) one can show that the 2PCF and the $P(k)$ form a Fourier pair

$$\xi(r) = \frac{1}{(2\pi)^3} \int d^3\mathbf{k} P(k) e^{i\mathbf{k}\cdot\mathbf{x}}. \quad (3.8)$$

Assuming that the mass density field $\rho(\mathbf{x})$ is traced by a discrete set of point-like masses $\rho(\mathbf{x}) = \sum_i m_i \delta_D(\mathbf{x} - \mathbf{x}_i)$, where the sum is taken over all the mass points labelled by i and found at position \mathbf{x}_i . If we identify galaxies as mass tracers then the 2PCF can be interpreted as the excess probability of an object at a distance r from another, randomly selected in the sample. To see this let us assume that all galaxies have the same mass, i.e., $m_i = m$, then the mean density is $\langle \rho \rangle = n_V m$, where n_V is the mean number density of tracers in the sampled volume V . The probability of finding a point in a small volume dV centered at the position \mathbf{x} is $dP = m^{-1} \rho(\mathbf{x}) dV$. The joint probability finding a point in dV_1 and dV_2 separated by a distance \mathbf{r} is then:

$$\begin{aligned} d^2P &= \frac{\langle \rho(\mathbf{x}) \rho(\mathbf{x} + \mathbf{r}) \rangle}{m^2} dV_1 dV_2 = \\ &= n_V^2 \frac{\langle \rho(\mathbf{x}) \rho(\mathbf{x} + \mathbf{r}) \rangle}{\langle \rho \rangle^2} dV_1 dV_2 = \\ &= n_V^2 [1 + \xi(r)] dV_1 dV_2, \end{aligned} \quad (3.9)$$

where isotropy is assumed in the last equation. The probability $1 + \xi(r)$ can also be interpreted as the mean mass density profile surrounding a generic galaxy in the Universe. If there were no clustering, the galaxies would be Poisson distributed and the 2PCF would result null $\xi(r) = 0$. Alternatively, overdense regions will be characterized by $\xi(r) > 0$, while underdense regions by $\xi(r) < 0$. As a result, integrating $n_V \xi(r)$ over a spherical shell provides the excess of objects in the shell with respect to the Poisson case, i.e., allows to trace the over or under density profile of mass tracers around a generic object in the sample. If one considers two sets of tracers, i.e., galaxies and voids in our case, the 2PCF will naturally become the *cross-correlation function* of void-galaxy pairs, described in details in Section 4.3, and will then provide the mass density profile of the generic void as traced by galaxies.

It is worth mentioning that all these definitions are given considering the true positions of objects, the so-called *real space*, assuming that distances of all galaxies and, consequently, their relative separations, were correctly measured. Distortions effects deriving from systematic errors in assigning distances will be discussed in Section 3.3.

3.2 Galaxy-matter connection

Since we cannot directly observe dark matter, but only luminous mass tracers of the underlying matter distribution, a fundamental challenge in cosmology is to quantify the mapping between a set of discrete mass tracers such as galaxies and the continuous density field of the matter, a large fraction of which is, according to the Λ CDM mode, dark.

One simple observations reveals the complexity of the problems: different types of mass tracers, e.g., galaxies vs. clusters or early vs. late type galaxies, do not have the same clustering properties. This means that that the galaxy-to-mass mapping is non trivial. We call this mapping the *galaxy bias* (Desjacques et al., 2018). To get more quantitative, we need to establish a relation between the overdensity in the number counts of the mass tracers, expressed via

$$\delta_{\text{tr}} \equiv \frac{N_{\text{tr}}(V) - \bar{N}_{\text{tr}}(V)}{\bar{N}_{\text{tr}}(V)}, \quad (3.10)$$

where N_{tr} and \bar{N}_{tr} are the number of tracers and the mean number of tracers, respectively, and the overdensity of the underlying matter δ_{M} as a function of space and time.

Ideally, the biasing relation could be obtained from first principles if we had a self consistent theory for the formation and evolution of the galaxies. Unfortunately, such a theory does not exists yet. However, the most advanced galaxy formation models show that the biasing relation is a very complicated one, being scale-dependent, nonlinear, non-local and, possibly, non deterministic. However, these models also suggests that on scales significantly larger than those interested by galaxy formation processes, that is to above a few tens of Mpc, the biasing relation is expected to be a simple linear one (Kaiser, 1984):

$$\delta_{\text{m}} = b\delta_{\text{tr}}, \quad (3.11)$$

with the so-called linear biasing parameter b capturing the essentials of the galaxy populations included in the sample used to under the clustering properties of the matter. In other words, the linear bias parameter is expected to depend on the galaxy type (or the galaxy mix) and to evolve with the time, but to be spatially constant (Sheth and Tormen, 1999). Because of this, the 2PCF of the tracers is expected to be simply proportional to that of the matter on sufficiently large scales

$$\xi_{\text{tr}} = b^2\xi_{\text{m}}. \quad (3.12)$$

In this Thesis we will be interested in tracing the void density profile using halos and galaxies by measuring their spatial cross-correlation function. And, more specifically, to include small voids that are typically discarded in this type of analysis. Therefore, it may seem questionable to adopt the linear bias hypothesis when considering structures whose size is of the order of a few tens of Mpc. It should be kept in mind, however, that galaxies in voids have separations that are, on average, significantly larger than that in the rest of the Universe. As a result, galaxy formation processes are less likely to affect their clustering properties and the linear biasing assumption more likely to remain valid.

3.3 Sources in anisotropy and their impact on the clustering analyses

So far, the discussion on clustering statistics has assumed that all tracers are located at their *real-space* positions. However, actual positions can only be determined for specific types of objects, known as distance indicators, for which distances can be measured directly—though typically with significant uncertainties. For this reason, catalogs of distance indicators contain a limited number of objects that trace the underlying mass distribution sparsely and non-uniformly, making them quite ineffective for clustering analyses.

For this reason, spectroscopic redshift surveys are generally preferred. These are large observational campaigns where both the angular position (expressed as Right Ascension, RA, and Declination, DEC, when using Equatorial coordinates) and the redshift of each detected object are measured with good precision. To map the three-dimensional distribution of these objects, redshifts must be converted into distances, and the clustering analysis is then conducted in what is known as *redshift space*. This transformation is not straightforward for two main reasons: first, the challenge of measuring galaxies' peculiar velocities often leads to the assumption that the total measured redshift is solely due to the Hubble expansion; second, the conversion depends on an assumed cosmological model, which may differ from the true one. These effects, referred to as Redshift Space Distortions (RSDs) and the Alcock-Paczyński (AP) effect, respectively, must be carefully addressed when analyzing data in redshift space, as will be discussed in the following sections.

The two types of distortions are illustrated in a simplified way in Figure 3.1, where the real position of a galaxy is shifted due to the combination of having ignored the peculiar velocity along the line of sight (LOS), denoted as v_r (i.e., RSD), and the incorrect distance estimate resulting from the use of an inaccurate fiducial cosmological model. Both effects displace objects along one preferential direction, the radial one, and therefore the resulting

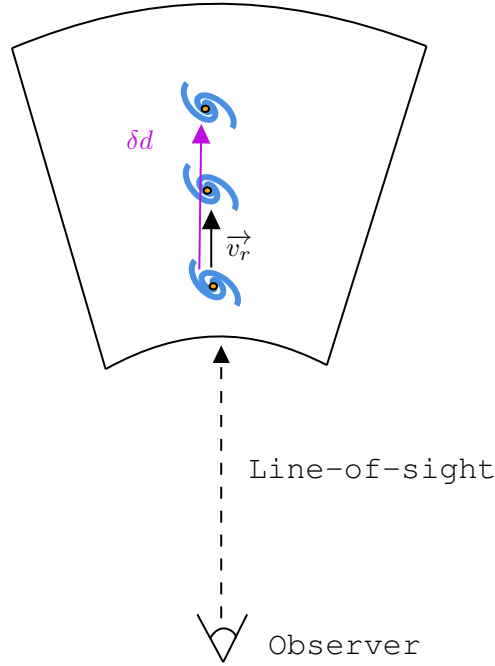


Figure 3.1 Simplified illustration of the effect of distortions for a galaxy in redshift space. The real position of a galaxy, (the closer to the observer) is shifted due to the combination of the contribution from the peculiar velocity along the line of sight (LOS), denoted as \mathbf{v}_r (i.e., RSD), and the incorrect distance estimate δd resulting from the use of an inaccurate fiducial cosmological model, AP effect.

3-dimensional distribution of the objects violate statistical isotropy. Also, the two effects are partly degenerate and induce similar distortions in the clustering statistics, as described in details in the following sections.

3.3.1 Redshift space distortions

The observed redshift z_{obs} results from the combination of two contributions: the cosmological redshift, z_h of a galaxy, and a Doppler effect due to the LOS component of its peculiar velocity, $z_d = v_{\parallel}/c$. The observed redshift can be expressed as:

$$1 + z_{\text{obs}} = (1 + z_h)(1 + z_d). \quad (3.13)$$

The true position of the galaxy is computed by estimating its distance corresponding to the cosmological redshift z_h via the distance-redshift relation, Equation (1.31),

$$d(z_h) = \int_0^{z_h} \frac{cdz'}{H(z')}. \quad (3.14)$$

However, in redshift surveys, distances of galaxies are estimated from the observed redshift that includes both contributions. Since peculiar velocities are related to the underlying density field and highly correlated, ignoring their contribution in (3.14) results in systematic errors in the estimated distance of the galaxies and, consequently, in systematic distortions in their 3-dimensional map.

Figure 3.2 shows a schematic representation of the effect of RSD. In the upper panel, three different types of circularly symmetric structures as seen in real space along with their respective peculiar velocity field (yellow arrow). The case on the right represents the case of a moderate overdensity. Since in the linear regime the negative divergence of the velocity field is proportional to the mass overdensity, all arrows are directed towards the center of the structure, representing matter accretion. In the center it is shown the case of an underdense region. The divergence of the peculiar velocity field is now positive and the matter is outflowing. On the right is shown the case of a large overdensity, for which linear theory does not apply anymore and the peculiar velocity field is spatially incoherent, as in a virialized galaxy cluster. The middle row, labeled as "Redshift space", shows the same structures as seen by an observer that has used the observed redshift (rather than the cosmological redshift) as a distance proxy. The corresponding distortion along the radial direction is described in the figure caption.

These distortions need either to be corrected for or modeled before comparing observations to theory prediction. In this thesis we shall follow the first route and use reconstruction techniques to correct for RSD before performing a clustering analysis. However, for a better understanding of the impact of the RSD and the whatever residual RSD-related effect could still be present after an imperfect reconstruction it is useful to explicitly model the effect of the RSD on the 2-point clustering statistics. Let us then write explicitly the relation between the estimated position of the object \mathbf{x}_{obs} , the true one \mathbf{x} and its peculiar velocity vector \mathbf{v} :

$$\mathbf{x}_{\text{obs}} = \mathbf{x} + \frac{1+z}{H(z)} \mathbf{v} \cdot \hat{\mathbf{n}}, \quad (3.15)$$

where $\hat{\mathbf{n}} = \mathbf{x}_{\text{obs}}/|\mathbf{x}_{\text{obs}}|$ is the LOS direction. The latter equation is expressed in the limit $z_{\text{d}} \ll z_{\text{h}}$.

The galaxy overdensity measured in redshift space can be expressed as the sum of the galaxy overdensity in real space plus a term depending on the first derivative of the peculiar velocity field:

$$\delta_{\text{g,RSD}}(\mathbf{x}_{\text{obs}}) = b\delta_{\text{m}}(\mathbf{x}(\mathbf{x}_{\text{obs}})) - \frac{\partial}{\partial x} \left[\frac{\mathbf{v} \cdot \hat{\mathbf{n}}}{a(z)H(z)} \right]. \quad (3.16)$$

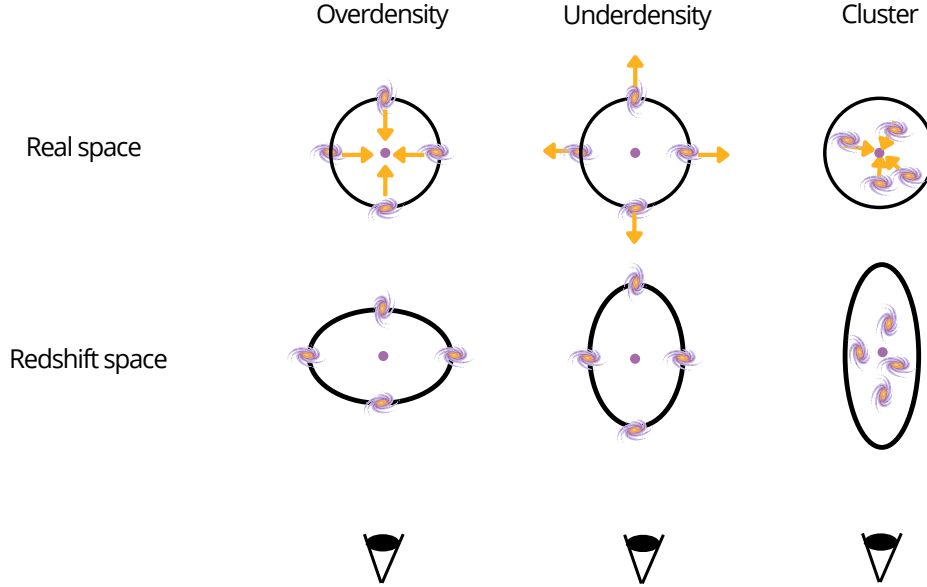


Figure 3.2 *Left-hand and central panels.* Schematic representation of the effect of redshift-space distortions on large and linear scales for overdensity (left) and underdensity (center). As galaxies move away from underdense regions, and are directed towards overdense regions, these regions appear elongated and flattened along the line of sight when seen in redshift space, respectively. *Right-hand panel.* Representation of the RSD effect in a smaller and virialised region like a cluster. Here, the galaxies are spread out in redshift space due to the large velocity dispersion, yielding large radial patterns in the wedge diagrams, the so-called fingers-of-God effect.

This expression holds under the following assumptions: linear galaxy bias, mass conservation (also valid for tracers), peculiar velocities are small compared to the expansion velocity, and overdensities are sufficiently small to apply linear theory (Hamilton, 1998).

Applying the distant observer approximation (flat sky), allows us to approximate the direction vector of each galaxy in the sample with the direction pointing in the center of the volume containing the sample. It is convenient to place this direction along the z -axis. Therefore, replacing $\hat{\mathbf{n}}$ with $\hat{\mathbf{z}}$ in the previous equation, and performing the Fourier transform we obtain:

$$\delta_{\text{g,RSD}}(\mathbf{k}) = b\delta_{\text{m}} + f \int \frac{d^3\mathbf{k}'}{(2\pi)^3} \delta_{\text{m}}(\mathbf{k}') (\mathbf{k}' \cdot \hat{\mathbf{z}})^2 \int d^3\mathbf{x} e^{i(\mathbf{k}' - \mathbf{k}) \cdot \mathbf{x}}. \quad (3.17)$$

The integral over \mathbf{x} yields $(2\pi)^3 \delta_{\text{D}}^{(3)}(\mathbf{k}' - \mathbf{k})$. Therefore, defining $\mu_k = \hat{\mathbf{k}} \cdot \hat{\mathbf{z}}$ as the cosine of the angle between the LOS and the wavevector we obtain the *Kaiser formula* (Kaiser, 1987) that relates the observed density field in redshift space with the underlying matter density field in real space at linear order:

$$\delta_{\text{g,RSD}}(\mathbf{k}) = [b + f\mu_k^2] \delta_{\text{m}}(\mathbf{k}). \quad (3.18)$$

It is possible to notice that, since the factor $f\mu_k^2$ is positive definite, the overdensity measured in redshift space is enhanced with respect to the real space counterpart. While, for underdensity is the opposite, being more deployed of matter in redshift space with respect of real space, with the constraint that $\delta < -1$. It is often useful to work with the adimensional distortion parameter:

$$\beta = \frac{f}{b} \quad (3.19)$$

By putting β in Equation (3.18) we obtain:

$$\delta_{g,\text{RSD}}(\mathbf{k}) = b[1 + \beta\mu_k^2]\delta_m(\mathbf{k}). \quad (3.20)$$

The corresponding 2-point clustering statistics evaluated in redshift space can be expressed as follows

$$\begin{aligned} P_{g,\text{RSD}}(\mathbf{k}) &= P(k) [b + f\mu_k^2]^2 && \text{Power spectrum} \\ \xi_{g,\text{RSD}}(\mathbf{r}) &= \xi(r) [b + f\mu^2]^2 && \text{2-point correlation function} \end{aligned} \quad (3.21)$$

3.3.2 Alcock-Paczyński distortions

In cosmology, distances are estimated from the measured redshift using Equation (1.31). This relationship depends on the expansion history parameter $H(z)$, which itself depends on cosmological parameters such as H_0 , Ω_m , and Ω_Λ , as described in Section 1.1.6. To compute the distance to galaxies, which is crucial for performing clustering analyses, one must assume a *fiducial cosmology*, i.e., specific values for the parameters that define $H'(z)$, where the primed superscript stands for fiducial quantities.

If the fiducial cosmology differs from the true cosmology of the Universe, represented by H , the parameter H' would be incorrect, and thus the derived distances, denoted by d' , would also be inaccurate and different from the true ones d . However, this discrepancy presents an opportunity to test the cosmological model and determine how much the fiducial cosmology deviates from the true one. Although we do not have direct measurements of distances for comparison, we can rely on the methodology introduced by Alcock and Paczynski (1979). This method is known as the Alcock-Paczyński (AP) test, and the distortions arising from an incorrect cosmological model are referred to as AP distortions. The AP test uses objects that, on average, are spherically symmetric in real space, according to the CP, and are known as *standard spheres*. For these objects, the extent along the line of sight, d_{\parallel} , is expected to be equal to the extent perpendicular to the line of sight, d_{\perp} . In the presence of AP distortions, this equality no longer holds.

The transverse position assigned to a pair of galaxies are

$$(x'_{\perp,1}, x'_{\perp,2}) = D'_A \times (\theta_1, \theta_2), \quad (3.22)$$

where D_A is the angular-diameter distance defined in Equation (1.38) and (θ_1, θ_2) is the angular separation from the center of the pair. The true transverse position can be evaluated via

$$(x_{\perp,1}, x_{\perp,2}) = D_A \times (\theta_1, \theta_2). \quad (3.23)$$

Taking the ratio of Equation (3.22) and (3.23), and indicating with x_{\perp} the perpendicular component of the pair separation, we obtain:

$$x'_{\perp} = \frac{D'_A(z)}{D_A(z)} x_{\perp}, \quad (3.24)$$

where the redshift z is that of the pair center which, for the galaxy pairs that are typically used for clustering analyses, is similar to that of the galaxy members. Similarly, clustering analyses over large volumes are typically subdivided into independent redshift shells, with each shell having a mean redshift $z = \bar{z}$. One can thus define the radial component of the pair separation as follows:

$$x'_{\parallel} = d'(z) - d'(\bar{z}) = \int_{\bar{z}}^z \frac{d\hat{z}}{H'(\hat{z})} = \frac{z - \bar{z}}{H'(\bar{z})} + O(z - \bar{z}), \quad (3.25)$$

where it was used $d(d)/dz = 1/H$, and it was assumed that the width of the redshift shell encompassing the pair is small compared to its distance from the observer, $\delta d \ll d$. The same relation of Equation (3.25) holds for the true cosmology:

$$x_{\parallel} = d(z) - d(\bar{z}) = \int_{\bar{z}}^z \frac{d\hat{z}}{H(\hat{z})} = \frac{z - \bar{z}}{H(\bar{z})} + O(z - \bar{z}). \quad (3.26)$$

Combining the two equations it is possible to obtain a relation that quantifies the radial stretch in terms of the Hubble functions in the fiducial and true cosmology:

$$x_{\parallel} = \frac{H'(\bar{z})}{H(\bar{z})} x'_{\parallel}. \quad (3.27)$$

Furthermore, we can quantify the magnitude of the AP effect along and across the LOS to the pair with the two *anisotropic dilation parameters* defined as:

$$q_{\parallel} = \frac{H'(\bar{z})}{H(\bar{z})} \quad q_{\perp} = \frac{D_A(\bar{z})}{D'_A(\bar{z})}. \quad (3.28)$$

It is also convenient to introduce the parameter ϵ defined as the ratio of the two parameters defined above:

$$\epsilon \equiv \frac{q_{\perp}}{q_{\parallel}} = \frac{D_A(\bar{z})H(\bar{z})}{D'_A(\bar{z})H'(\bar{z})}. \quad (3.29)$$

The AP distortion affects the clustering statistics. It is possible to include the AP distortion term into the expression for the observed density field $\delta_{\mathbf{g},\text{obs}}$ by including the distortion term δd in the derivation of Equations (3.15) and (3.16), where δd is the difference between the distances in the true and in the fiducial cosmology

$$d'(z) = d(z) + \delta d. \quad (3.30)$$

By plugging this term in Equation (3.15), we get the mapping between real and redshift space including both geometric (AP) and dynamic (RSD) distortions (Dodelson and Schmidt, 2020):

$$\mathbf{x}_{\text{obs}} = \mathbf{x} + \left(\delta d(z) + \frac{\mathbf{v}_{\parallel}(\mathbf{x})}{aH(z)} \right) \hat{\mathbf{n}}. \quad (3.31)$$

With the same assumptions of Equation (3.16) we obtain the following relation that links the galaxy density field in redshift space (including both AP and RSD) with the matter density field in real space:

$$1 + \delta_{\mathbf{g},\text{obs}}(\mathbf{x}_{\text{obs}}) = \left(1 - \frac{2\delta d}{x} + \frac{H}{H' - H} \right) \left\{ 1 + b\delta_{\text{m}}[\mathbf{x}(\mathbf{x}_{\text{obs}})] - \frac{\partial}{\partial x} \left[\frac{\mathbf{v} \cdot \hat{\mathbf{n}}}{a(z)H(z)} \right] \right\}. \quad (3.32)$$

The corresponding 2-point clustering statistics evaluated in redshift space including both AP and RSD can be expressed using Equations (3.21) and evaluating the coordinates from true to fiducial ones vector transforming from the as follows

$$\begin{aligned} P_{\mathbf{g},\text{obs}}(\mathbf{k}_{\text{obs}}, \bar{z}) &= P(k) [b + f\mu_k^2]^2 \Bigg|_{\mathbf{k}=(k_{\text{obs}}^1/q_{\perp}, k_{\text{obs}}^2/q_{\perp}, k_{\text{obs}}^3/q_{\parallel})} && \text{Power spectrum} \\ \xi_{\mathbf{g},\text{obs}}(\mathbf{r}_{\text{obs}}, \bar{z}) &= \xi(r) [b + f\mu^2]^2 \Bigg|_{\mathbf{r}=(r_{\parallel}q_{\parallel}, r_{\perp}q_{\perp})} && \text{2-point correlation function} \end{aligned} \quad (3.33)$$

The AP test has been successfully applied or proposed for various cosmic structures expected to exhibit statistical isotropy. Examples include measurements of the auto-correlation function of brightness temperature in 21-cm maps of the epoch of reionization (Nusser, 2005), the BAO peak in the anisotropic galaxy 2PCF (Percival et al., 2010), the full-shape analyses of the same statistics (Marulli et al., 2012), and the density profile of cosmic voids (Lavaux and Wandelt, 2012; Ryden, 1995), a key aspect of this Thesis.

3.4 Reconstruction techniques

In the previous section, we introduced the distortions encountered when measuring galaxy distances. From Equation (3.32), it is clear that these distortions, though caused by different sources—one geometric (AP) and the other dynamical (RSD)—are degenerate. Consequently, it is not possible to analyze the two distortions independently to extract cosmological information. It is therefore necessary to develop models that first takes into account for RSD, and consequently performs the AP test. However, modeling RSD requires understanding the peculiar velocity field of galaxies, which is a complex task. Fortunately, there are powerful techniques that, instead of modeling the RSD analytically, allow for a numerical treatment. These methods reconstruct the tracer field in the absence of RSD and are referred to as *velocity reconstruction techniques* (here referred to as reconstruction techniques) .

By employing reconstruction, it is possible to reconstruct the real-space positions of galaxies, which allows to correct for the distortions introduced by peculiar velocities along the LOS. Reconstruction techniques like these are widely applied in cosmological surveys, allowing researchers to improve the accuracy of cosmological parameter estimation by making the density field more interpretable. They help isolate the effects of cosmic expansion from those caused by local dynamics (i.e., peculiar velocities), leading to a more precise measurement of the underlying matter distribution. Reconstructions are not only used for removing RSD, but also for "undoing" the displacement of galaxies caused by the growth of structures, effectively tracing this displacement back in time. This process is crucial for mitigating the non-linear effects that arise during the late stages of structure evolution, when gravitational collapse becomes dominant. Nonlinearities in the density field make it more difficult to analyze large-scale structure, as they blur the features that are valuable for cosmological analysis, such as the BAO peak. By applying the reconstruction technique, we attempt to recover a more linear version of the density field, enhancing the signal-to-noise ratio for features like the BAO peak, (see e.g. Eisenstein et al., 2005; Padmanabhan et al., 2012; Ross et al., 2017). There are several types of reconstruction algorithms, each based on different principles. Among them, we can mention reconstructions based on the cosmological least action principle, such as FAM and eFAM (Nusser and Branchini, 2000; Sarpa et al., 2021), or Deep Learning-based reconstructions (Veena et al., 2022).

In this Thesis, I used a reconstruction method based on the Zel'dovich approximation, previously introduced in Section 2.2.2, with the purpose of removing RSD without moving tracers back in time. Recently, the method of Zel'dovich reconstruction for eliminating RSD has also been applied to cosmic voids, with a focus on estimating the linear growth rate, f (Nadathur et al., 2019; Radinović et al., 2023).

3.4.1 Zel'dovich reconstruction

The core of the Zel'dovich reconstruction is based on Equation (2.56) and its Fourier space analog (2.57), that we rewrite here for sake of clarity:

$$\begin{aligned}\nabla \cdot \Psi^{(1)}(\mathbf{q}, t) &= -\delta_L(\mathbf{x}, t) && \text{Configuration space} \\ \Psi^{(1)}(\mathbf{k}) &= \frac{i\mathbf{k}}{k^2} \delta_L(\mathbf{k}) && \text{Fourier space}\end{aligned}\tag{3.34}$$

The solution of this differential equations allows one to estimate a displacement field $\Psi^{(1)}$ from a linearly evolved mass overdensity field. The initial step in addressing Equation (3.34) involves filtering out nonlinear modes to obtain a linear overdensity field, indicated by the subscript L in Equation (3.34). This is achieved by smoothing the galaxy number density field using an appropriate filter. The linear biasing hypothesis can then be applied to this smoothed filter, implying that the linear mass overdensity field is simply proportional to the smoothed galaxy density one. In Fourier space this operation corresponds to (Padmanabhan et al., 2009)

$$\mathcal{S}(k)\delta_{\text{obs}} \propto \mathcal{S}(k)\delta_L,\tag{3.35}$$

where $\mathcal{S}(k)$ represents the smoothing kernel that acts like a low-pass spatial filter, damping high k modes (lower scales in x), which are more affected by nonlinearities. The choice of the smoothing is crucial, as it depends on the characteristics of the sample. A filter that is too large would overdamp density fluctuations, systematically underestimating the displacement field's amplitude. In contrast, a filter that is too narrow would not adequately reduce nonlinear effects, introducing biases into the reconstruction. Thus, the appropriateness of the smoothing kernel must be evaluated through numerical simulations on a case-by-case basis. By combining Equations (3.35) and (3.34) one obtains:

$$\Psi_{\text{ZA}}(\mathbf{k}) = i \frac{\mathbf{k}}{k^2} \mathcal{S}(k) \delta_{\text{obs}} = \mathcal{S}(k) \Psi^{(1)}(\mathbf{k}),\tag{3.36}$$

which links the smoothed version of the observed density field with the displacement field. As described in Section 3.3.1, matter density perturbations are observed at the redshift space positions for which the radial coordinates was inferred from the measured redshift. The ZA reconstruction can account for this distortion as long as perturbation theory applies. In this case, the linearized continuity equation that links the peculiar velocity to the linear mass density contrast, Equation (2.35) also repeated below, can be expressed in terms of the displacement field

$$\mathbf{v}(\mathbf{k}) = aHf \frac{i\mathbf{k}}{k^2} \delta_L(\mathbf{k}) = aHf \Psi_{\text{ZA}}(\mathbf{k}).\tag{3.37}$$

The latter equation is exploited for writing the expression for the displacement field in redshift space (Nusser, 1994), which reads as:

$$\Psi^s = \Psi_{ZA} + \Psi_{\text{RSD}} = \Psi_{ZA} + f(\Psi_{ZA} \cdot \hat{\mathbf{z}})\hat{\mathbf{z}}, \quad (3.38)$$

where $\Psi_{\text{RSD}} = \mathbf{v}/aHf$ is the apparent displacement in the radial direction which we identify with that of the $\hat{\mathbf{z}}$ axis having assumed the distant observer approximation. The analogous expression reads

$$\Psi^s(\mathbf{k}) = (1 + f\mu_k^2)\Psi_{ZA}(\mathbf{k}), \quad (3.39)$$

where the second term in parenthesis is the Kaiser linear factor that accounts for RSD (3.18), and μ_k is the cosine angle between the displacement vector and the LOS. Therefore, assuming a linear bias approximation b , the equation to solve for ZA, Equation (3.34), becomes:

$$\nabla \cdot \Psi_{ZA}(\mathbf{k}) + \beta \nabla \cdot [(\Psi_{ZA}(\mathbf{k}) \cdot \hat{\mathbf{z}})\hat{\mathbf{z}}] = -\frac{\delta_{\text{sm}}}{b}, \quad (3.40)$$

where δ_{sm} is the galaxy density field convolved with the smoothing filter $\delta_{\text{sm}} = \delta_g \mathcal{S}(k)$. The solution of this differential equation is the displacement vector field which, combined with Equation (3.39), allows one to estimate the apparent displacement and applying it to move the objects from their redshift to their real space positions. We notice that to solve (3.40) one needs to assume a value for both the bias parameter b and the distortion parameter β (or, alternatively, for the growth rate f). Hence, the so-called *reconstructed space* is obtained shifting galaxy positions by $-\Psi_{\text{RSD}}$ to approximately remove RSD from the galaxy observed field.

Implementation

In this Thesis to perform the Zel'dovich reconstruction we use the publicly available `LinearVelocity` package (Sarpa et al. in prep)¹. The code takes in input the galaxies positions in redshift space and returns their positions in real space. The reconstruction code employs the `MultiGridReconstruction` method, proposed by White (2021) and integrated in the Python package `PYRECON`².

In addition to galaxy positions one needs to specify a fiducial value for R_s the radius of the smoothing filter $\mathcal{S}(k)$ set to be Gaussian, the number of the cells N_{cell} in the cubic grid on which the various fields are interpolated and the selection function of the catalog. This quantity, defined as the probability to observe a galaxy at any point in space, is provided in

¹https://gitlab.com/esarpa1/linear_velocity available upon request at esarpa@sissa.it

²<https://github.com/cosmodesi/pyrecon/tree/main>

the form of a catalog of unclustered objects whose number density fluctuations match those induced by selection effects in the real catalog.

The reconstruction is performed in multiple steps. In the first step, the mass of the galaxies is interpolated from their position to the points of a cubic grid that encompasses the volume of the survey. The same procedure is repeated to estimate the number density of the objects in the random catalog ρ_r . The galaxy number overdensity is then estimated at the gridpoints as

$$\delta_{\text{obs}} = \frac{\rho_{\text{obs}}}{\rho_r} - 1, \quad (3.41)$$

and the mass overdensity is simply obtained by dividing this value by that of the linear galaxy bias provided by the user.

Because the mean number density of "random" objects is smaller than the grid-size, this should reduce the occurrence of empty cells. Despite of this, and to avoid possible divergence, we explicitly set the mass overdensity equal to zero if $\rho_r = 0$ at the gridpoint.

In the second step, a Gaussian smoothing filter is applied to the overdensity field. Since this operation corresponds to a simple multiplication in Fourier space, we first Fourier transform the overdensity field. The Gaussian smoothing filter in Fourier space has the form

$$\mathcal{S}(k) = e^{-k^2 R_s^2 / 2} \quad (3.42)$$

where R_s is the smoothing scale. Finally, we inverse Fourier transform the smoothed field back to configuration space. By performing these steps we obtain: $\delta_{\text{sm}} = \delta_{\text{obs}} \mathcal{S}(k)$.

In the third, and central step, we evaluate the displacement field Ψ_{RSD} by solving Equation (3.40), where the estimated overdensity field δ_{sm} is used to derive the Zel'dovich displacement field, Ψ_{ZA} , which describes the straight orbits back to the initial positions. This system of equations is solved using a multigrid technique with a full V-cycle and damped Jacobi iterations. This displacement field is then used to derive Ψ_{RSD} via Equation (3.38) evaluated at the observed positions of the galaxies.

In the fourth and final step, the displacement field Ψ_{RSD} is used to shift galaxies from their redshift-space positions to their real-space positions, completing the reconstruction process.

4

Cosmic voids in cosmology

In previous chapters, cosmic voids have already been mentioned several times. Now, we delve deeper into this topic and focus specifically on these key structures, which are the main subject of this Thesis. Voids are large underdense regions in the galaxy distribution. Since their discovery (De Lapparent et al., 1986; Gregory and Thompson, 1978; Kirshner et al., 1981), voids have been recognized as powerful cosmological laboratories (Pisani et al., 2019; van de Weygaert et al., 2016). Their sizes range from tens to hundreds of Mpc, and they occupy most of the cosmic volume (Ceccarelli et al., 2013), making them the largest observable structures in the Universe. Their unique combination of geometrical and dynamical properties can be exploited to extract key information on the geometry of the Universe and its energy budget.

Traditionally, large-scale studies of the galaxy distribution rely on 2-point statistics and have exploited the BAO feature to trace the expansion history of the Universe (DESI Collaboration et al., 2024). However, since the mass overdensity field becomes non-Gaussian at late times, additional information is contained in higher-order statistics. In the early Universe, where initial conditions were nearly Gaussian, the cosmic volume is split between high- and low-density regions, each containing a portion of the cosmological information. Standard galaxy clustering analyses, even those considering higher-order statistics such as the three-point correlation function, are primarily sensitive to collapsed regions corresponding to positive density fluctuations. In dense regions, virialization erases much of the memory of the initial conditions. Conversely, in low-density regions departures from primordial Gaussianity are mild and much of the initial information is preserved (Pisani et al., 2019). Thus, voids provide access to both higher-order information (Fry, 1985; Hamilton, 1985; White, 1979) and the initial conditions, therefore, are ideal laboratories for gaining insights into the Universe. Void science, however, requires both large volumes to build a statistical sample of these structures, and detailed 3-dimensional maps to unambiguously detect them.

From this point of view, the voids samples extracted from the currently available galaxy surveys have not yet reached their full potential (Pisani et al., 2019). This situation is about to change as ongoing and upcoming surveys like Euclid (Euclid Collaboration et al., 2024) and Roman (Spergel et al., 2015) are expected to meet these requirements, making future analyses promising for addressing open cosmological questions, such as the nature of dark energy.

As described in Section 2.2.1, for an expanding Universe, voids are structures that do not collapse but instead expand indefinitely. However, because of statistical isotropy, they do not have a preferred direction of expansion. Individual voids are not expected to be spherically symmetric, as the surrounding large scale structures generate tidal fields that guide the expansion along preferential direction. However, the CP guarantees that these directions are random when averaged over a large sample of objects and therefore stacking a large number of voids is expected to produce a meta structure which is, to a high degree of approximation, spherically symmetric. This spherical symmetry is key for cosmological tests because it is broken when voids are observed, due to the RSD and AP distortions described in Section 3.3, and illustrated for the void framework in Section 4.1. These distortions, however, offer an opportunity to extract cosmological parameters, as they are linked to the underlying cosmology. Departures from sphericity can either be modeled or corrected for, providing an effective way to infer key cosmological parameters.

Despite the growing usage of cosmic void statistics in the recent literature, a universal definition of cosmic voids has yet to be established. This lack of consensus presents one of the main challenges in their cosmological application. For example, there is no common set of values, or even a range of values, to classify voids based on their internal density, size, and shape. Various algorithms, the so-called void finders, exist to identify voids in the distribution of matter tracers, but they differ significantly from one another. In fact, the statistical properties of voids depend heavily on the method used to identify them. Different classes of void finders exist, and one of these will be described in detail in Section 5.1. Despite their differences, all void finders aim to find the minima of the mass overdensity field to identify the void centers and to define a void radius as a proxy to its physical size.

Cosmological inference using voids relies on a number of statistical estimators. These include the void abundance, studied through the *void size function*, the density profile of tracers in the void region (and in the surroundings), analyzed using the *void-galaxy cross-correlation function*, and the clustering of voids themselves, examined via the *void-void auto-correlation function*. Emerging studies will also cross-correlating voids with other probes, such as the CMB. In the following sections, I will focus on the two most commonly

used statistics, which are also the ones applied in this thesis: the *void size function* (Section 4.2) and the *void-galaxy cross-correlation function* (Section 4.3).

4.1 Distortions in voids

As mentioned previously, cosmic voids extracted from the observed distribution of galaxies exhibit two types of shape distortions: the geometrical one, which we dubbed AP, and the dynamical ones, which we labeled RSD. Both effects have been described in Section 3.3. Here we focus on their impact on voids and their statistics.

We have already discussed the impact of redshift space distortions (RSD) and Alcock-Paczyński (AP) effects on clustering of galaxies in Section 3.3. Here, we will use those concepts and apply them to our case, where the separation vector is considered to be the one connecting a galaxy to the void center.

Redshift space distortions In Section 3.3.1, Equation (3.15) provides the relation between the estimated position of the object \mathbf{x}_{obs} , the true one \mathbf{x} and its peculiar velocity vector \mathbf{v} , that we rewrite here for reference:

$$\mathbf{x}_{\text{obs}} = \mathbf{x} + \frac{1+z}{H(z)} \mathbf{v} \cdot \hat{\mathbf{n}} . \quad (4.1)$$

In the framework of voids, we have two sets of observables, which we will denote as follows: uppercase letters will indicate quantities related to voids, while lowercase letters will refer to quantities related to galaxies. Specifically, we denote the position of the void center inferred from the redshift Z as \mathbf{X} , and the position of the galaxy at redshift z as \mathbf{x} . The observer is located at the origin of the coordinate system. The redshift of the void center, Z , is not a direct observable but is instead obtained from the redshifts of the surrounding galaxies that define the void (see Section 5.1). We assume the direction to the void center as our LOS, expressed as $\hat{\mathbf{n}} = \mathbf{X}/|\mathbf{X}|$, and under the distant observer approximation, we can assume that \mathbf{x} and \mathbf{X} are parallel. In real space, in the absence of Doppler shifts, $z_d = 0$ in Equation (3.13), $\mathbf{x}(z) = \mathbf{x}(z_h)$. The separation vector between the void center and the galaxy is $\mathbf{r} = \mathbf{x} - \mathbf{X}$. The relative velocity between the void center of velocity \mathbf{V} and the galaxy \mathbf{v} is defined as $\mathbf{u} \equiv \mathbf{v} - \mathbf{V}$. In redshift space $z_d \neq 0$ the mapping between the separation vectors in real to redshift space can be obtained by combining Equations (3.15) and (3.13):

$$\mathbf{r} = \mathbf{x}(z) - \mathbf{X}(Z) \simeq \mathbf{x}(z_h) - \mathbf{X} + \frac{1+z_h}{H(z_h)} (\mathbf{v}_{\parallel} - \mathbf{V}_{\parallel}) = \mathbf{r} + \frac{1+z_h}{H(z_h)} \mathbf{u}_{\parallel} \equiv \mathbf{s} , \quad (4.2)$$

where the subscript \parallel indicates quantities parallel to the LOS. In the latter equation we assumed $z_{\text{obs}} \sim z_{\text{h}} \sim Z_{\text{h}}$. This is a valid approximation since for any far away object, including void, $z_{\text{obs}} \sim z_{\text{h}}$, and for a void of size $r \sim \mathcal{O}(10^1) h^{-1}\text{Mpc}$ and a typical peculiar velocity $u_{\parallel} \sim \mathcal{O}(10^2) \text{ km/s/Mpc}$ the ratio $z_{\text{h}}/Z_{\text{h}}$ is $\sim \mathcal{O}(10^{-3})$. Moreover since CP ensures no preferential direction for the void expansion the averaging operation implied in the void stacking guarantees that $\langle \mathbf{V} \rangle = \langle \mathbf{V}_{\parallel} \rangle$, i.e. the stacked void follows the Hubble expansion (Hamaus et al., 2020). The separation vector \mathbf{s} , which links void centers to galaxies in redshift space, is determined not by the individual motions of either the galaxies or the void centers, but rather by their relative velocity, \mathbf{u}_{\parallel} , along the line of sight. This consideration is valid only for galaxies that reside within the same void, and does not account for the relative velocities of galaxies belonging to distinct voids at greater separations (for more on large-scale void-galaxy cross-correlations, see Chan et al. (2014); Hamaus et al. (2014a,b); Liang et al. (2016), and for details on the motions and pairwise velocity statistics of voids, refer to Ceccarelli et al. (2016); Lambas et al. (2015); Sutter et al. (2014); Wojtak et al. (2016)).

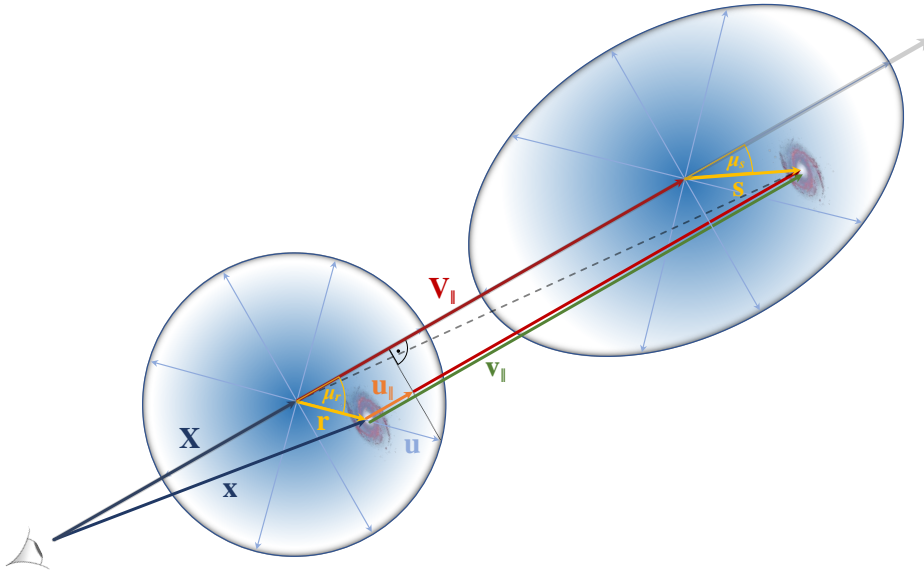


Figure 4.1 Separation vector between the comoving void center location \mathbf{X} and the galaxy location \mathbf{x} in real space (\mathbf{r} , left) and in redshift space (\mathbf{s} , right). The peculiar LOS velocity \mathbf{v}_{\parallel} of every galaxy that defines the void can be decomposed into the peculiar velocity of the void center \mathbf{V}_{\parallel} and the galaxy's relative velocity \mathbf{u}_{\parallel} with respect to this center. Velocity displacement is in units of $(1 + z_{\text{h}})/H(z_{\text{h}})$ and μ is the cosine of the angle between the separation vector and the LOS. This yields the relation for the mapping of the separation vector between real and redshift space $\mathbf{s} = \mathbf{r} + \mathbf{u}_{\parallel}$. Credits: Hamaus et al. (2020).

An example of this behavior is depicted in Figure 4.1: voids undergo both translation and deformation when transitioning from real space to redshift space, but for galaxies that

belong to the same void, the translational component does not influence the separation vector s . As long as voids are considered as coherent, extended structures, their centers move consistently with the galaxies that define them, as they transition from real to redshift space. This distinguishes voids from galaxies, which are typically treated as point-like objects in studies of large-scale structure.

Alcock-Paczyński distortions We already dealt with AP distortions in Section 3.3.2. Being $r = \sqrt{r_{\parallel}^2 + r_{\perp}^2}$ the separation vector between the void center and the galaxy, we rewrite Equation (3.28) as:

$$r'_{\parallel} = \frac{H(z)}{H'(z)} r_{\parallel} = q_{\parallel}^{-1} r_{\parallel} \quad r'_{\perp} = \frac{D'_A(z)}{D_A(z)} r_{\perp} = q_{\perp}^{-1} r_{\perp}, \quad (4.3)$$

where the primed quantities refer to the distances evaluated within the fiducial cosmology framework. Let's introduce the quantity μ , defined as the cosine of the angle between r and the LOS direction:

$$\mu = \frac{r_{\parallel}}{r}. \quad (4.4)$$

According to the Equations (4.3), one can obtain the transformation of the true coordinates r and μ , from true to fiducial r' and μ' via

$$r = \sqrt{q_{\parallel}^2 r_{\parallel}^2 + q_{\perp}^2 r_{\perp}^2} = r' \mu' q_{\parallel} \sqrt{1 + \varepsilon^2 (\mu'^{-2} - 1)} \quad (4.5)$$

$$\mu = \frac{\text{sgn}(\mu')}{\sqrt{1 + \varepsilon^2 (\mu'^{-2} - 1)}} \quad (4.6)$$

where ε is defined as

$$\varepsilon = \frac{q_{\perp}}{q_{\parallel}} = \frac{D_A(z) H(z)}{D'_A(z) H'(z)}. \quad (4.7)$$

If the fiducial cosmology matches the true one, then $\varepsilon = 1$, and consequently, $r'_{\parallel} = r_{\parallel}$ and $r'_{\perp} = r_{\perp}$. In Equation (4.5), the absolute distance r depends on both q_{\parallel} and q_{\perp} , thus, these parameters remain degenerate (unless the scale r can be calibrated using a known reference such as the BAO scale). However void-centric distances are generally expressed in terms of the effective void radius R calculated as the cubic root of the void volume in redshift space. The observed volume scales with $r_{\perp}^2 r'_{\parallel}$, implying the following relation to relate the true to fiducial void radius (Correa et al., 2021; Hamaus et al., 2020):

$$R = q_{\parallel}^{1/3} q_{\perp}^{2/3} R' \quad (4.8)$$

Then, the separation r rescaled by R is only dependent from ε as:

$$\frac{r}{R} = \frac{r'}{R'} \mu' \varepsilon^{-2/3} \sqrt{1 + \varepsilon^2 (\mu' - 2 - 1)}. \quad (4.9)$$

As mentioned earlier, distortions in voids are crucial for extracting constraints on cosmological parameters. The AP test was first proposed for voids by Ryden (1995) and then performed by Lavaux and Wandelt (2012). It provides access to the combination of parameters $D_A(z)H(z)$. The product $D_A(z)H(z)$ offers information on cosmological parameters such as the matter density Ω_m , the cosmological constant Ω_Λ , curvature Ω_k , the dark energy equation of state $w(z)$, and the Hubble parameter H_0 . This combination is essential for constraining the expansion history and geometry of the Universe. In this Thesis, the AP test plays a fundamental role to extract cosmological information. It will be used to determine the constraining power in two different scenarios: one involves an analysis in redshift space combining both RSD and AP, see Chapter 7, and the second one leverages on the AP optimization to propose a new method for disentangling the two distortions (i.e., RSD and AP), see Chapter 6.

4.2 Void size function

The *void size function* (VSF) is defined as the comoving number density of cosmic voids as a function of their size. The theoretical foundation of this function is the *excursion set formalism* (ESF) (Jennings et al., 2013; Sheth and van de Weygaert, 2004). This theory is widely used in cosmology to describe the formation of dark matter halos and voids within the hierarchical structure growth model.

The excursion-set formalism The ESF is an analytical framework to study the LSS of the Universe. This approach allows to predict the number density of structures by relating the linear perturbation theory to its nonlinear counterpart at late time. The ESF is based on the spherical collapse theory, see Section 2.2.1, which assumes that all structures forming in the Universe exhibit spherical symmetry. This assumption allows for a direct relationship between the density contrast of the forming structure and the density contrast that the same region would have had if the evolution were linear and the field had remained Gaussian, thus being fully characterized by the power spectrum $P(k)$. Initially, the ESF was introduced to track the formation and evolution of positive density perturbations that collapse into halos. Subsequently, this framework has been extended to model the evolution of cosmic voids, making it versatile for studying both overdense and underdense regions in the Universe.

For the case of halos, we discussed in Section 2.2.1 that a collapse occur when the linear density fluctuation reaches a critical value or barrier δ_c^L , whose value is computed in linear theory $\delta_c^L \simeq 1.69$. In this formalism, the evolution of the density contrast $\delta(R)$ is treated as a stochastic process as a function of the smoothing scale R , which corresponds to the physical size of the structure that is formed. As we examine smaller scales, the random walks of the density field are followed, and the probability of reaching the collapse barrier is interpreted as the number of halos forming at the corresponding mass scale. The method smooths or averages the density field over various scales, from large regions to smaller ones. On large scales, the overdensity may be too low to collapse, but on smaller scales, the overdensity can exceed the threshold δ_c^L , leading to the formation of a halo. The mass of the halo depends on the scale at which the random walk crosses the collapse barrier.

For modeling the collapse of perturbations, the spherical evolution model combined with the excursion set formalism provides a robust description of the statistics of dark matter halos. The ESF can be used to determine the fraction of trajectories that cross this barrier for the first time, solving the so-called *one-barrier problem*, and also addressing the *cloud-in-cloud problem*, which ensures that only objects not embedded in larger structures are counted as halos.

The ESF has been extended to the underdense regions, becoming a two-barrier problem because the density perturbation can either exceed the upper threshold δ_c^L leading to halo formation, or fall below the lower threshold δ_v^L , resulting in the formation of a void. These two barriers represent the conditions for collapse into halos or expansion into voids. Hence, we must define a threshold related to void formation. One possibility is to use the value associated with the shell-crossing phenomenon, but, as discussed in Section 2.2.1, this value is not well-suited for indicating void formation, and shell crossing in voids may never actually occur. Thus, a more general negative density contrast value, δ_v^L , is preferred to keep the treatment more flexible (see e.g., Contarini et al. (2019); Ronconi et al. (2019); Verza et al. (2024)).

Considering the formation of voids, there are three possible processes that contribute to the number of voids that are formed, in a negative or positive way. The first one is the *void-in-void* process, related to void merging, that has to be taken into account to avoid double counting voids. The second one is to account for the possibility for a void to be embedded in a larger overdense region, the *void-in-cloud* process. Finally, the opposite situation can occur, the *cloud-in-void*, where a large underdensity embeds a small overdense region. However, this process is irrelevant for the formation of high-density collapsed structures, as dark matter halos, which are unlikely to be torn apart by the expansion of the surrounding void.

The asymmetry between the void-in-cloud and cloud-in-void processes leads to a symmetry breaking between the emerging halo and void populations: although they evolve from the same initial conditions, overdensities and underdensities are expected to evolve toward distributions with different characteristics. In Figure 4.2 we present a summary of the four processes of halo and void formation as described by the excursion set formalism. This approach provides the theoretical foundation for modeling the void size function.

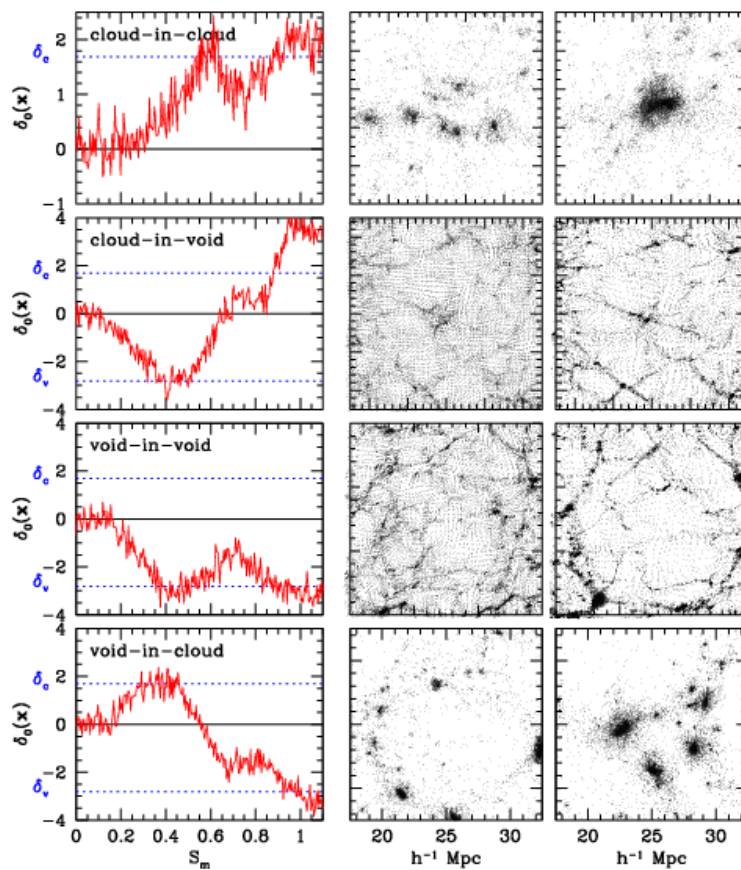


Figure 4.2 Four scenarios of the excursion set formalism. Each row illustrates one of the four basic modes of hierarchical clustering: the cloud-in-cloud process, cloud-in-void process, void-in-void process and void-in-cloud process (from top to bottom). Each mode is illustrated using three frames. Leftmost panels show ‘random walks’: the local density perturbation $\delta_0(\mathbf{x})$ as a function of (mass) resolution scale S_m at an early time in an N-body simulation of cosmic structure formation. In each graph, the dashed horizontal lines indicate the collapse barrier δ_c and the void barrier δ_v . The two frames on the right show how the associated particle distribution evolves. Whereas halos within voids may be observable (second row depicts a halo within a larger void), voids within collapsed halos are not (last row depicts a small void which will be squeezed to small size as the surrounding halo collapses). It is this fact which makes the calculation of void sizes qualitatively different from that usually used to estimate the mass function of collapsed halos. Credits: Sheth and van de Weygaert (2004)

Modeling the void size function The modeling of the VSF relies on the ESF illustrated above. The distribution of fluctuations that become voids, the so-called multiplicity function, is obtained as the conditional first crossing distribution of the matter density contrast filtered at decreasing Lagrangian radius, i.e., the radius of the fluctuation in Lagrangian space r_L , in a double barrier problem. The multiplicity function of (Sheth and van de Weygaert, 2004) is derived for spherical fluctuations in Lagrangian space while the observed voids live in the Eulerian space. We recall that the Lagrangian space is the initial density field linearly evolved up to the epoch of interest. In this context, “initial” means at redshift high enough to be fully described by linear theory, and “linearly evolved” means that the global amplitude of the density contrast field is rescaled with the linear growth factor. The Eulerian space is the fully non-linear evolution of the density field at the epoch of interest. The map from Lagrangian to Eulerian space is performed by considering how voids (or halos) evolve. Nevertheless, the spherical approximation allows us to easily go back and forth from Lagrangian to Eulerian space in all the computations. Practically, a fluctuation become a void at radius r_L if the filtered density contrast first crosses the void formation threshold δ_v^L at r_L , without having crossed the threshold for collapse δ_c^L at any larger scale.

The multiplicity function, as given by Sheth and van de Weygaert (2004) is:

$$\mathcal{F}_{\ln\sigma}(\sigma) = 2 \sum_{j=1}^{\infty} \exp\left(-\frac{(j\pi x)^2}{2}\right) j\pi x^2 \sin(j\pi\mathcal{D}), \quad (4.10)$$

with

$$\mathcal{D} = \frac{|\delta_v^L|}{\delta_c^L + |\delta_v^L|}, \quad x = \frac{\mathcal{D}}{|\delta_v^L|} \sigma, \quad (4.11)$$

and σ being the square root of the variance of linear matter perturbations on the Lagrangian scale r_L . All these quantities are computed in linear regime, on which the ESF relies. The void size function in Lagrangian space can be expressed as (Jennings et al., 2013; Sheth and van de Weygaert, 2004):

$$\frac{dn_L}{d\ln r_L} = \frac{\mathcal{F}_{\ln\sigma}(\sigma)}{V(r_L)} \frac{d\ln\sigma^{-1}}{d\ln r_L}, \quad (4.12)$$

where $V(r_L) = 4\pi r_L^3/3$ is the volume of the spherical fluctuation of radius r_L . However, the VSF in Eulerian space differs from its Lagrangian counterpart. This is due to the necessity of incorporating the expansion of voids when transitioning from linear to nonlinear theory. The evolution of perturbations in the nonlinear regime allows for the conversion from linear to nonlinear shell radius, as given by:

$$\frac{r}{r_L} = \left(\frac{\bar{\rho}}{\rho_v}\right)^{1/3}, \quad (4.13)$$

where $\bar{\rho}$ is the mean density of the Universe and ρ_v is the density within the void. Furthermore, to ensure that the fraction of volume occupied by voids does not exceed unity during the transition from linear to nonlinear regimes, Contarini et al. (2022) imposed a constraint that equates the void volume fraction in both regimes (Jennings et al., 2013):

$$V(r)dn = V(r_L)dn_L|_{r_L=r_L(r)} \quad (4.14)$$

With this requirement the model ensures void volume conservation and from Equation (4.12), it is possible to derive the final definition of the theoretical void size function (Contarini et al., 2022):

$$\frac{dn_L}{d \ln r_L} = \frac{\mathcal{F}_{\ln \sigma}(\sigma)}{V(r_L)} \frac{d \ln \sigma^{-1}}{d \ln r_L} \Big|_{r_L=r_L(r)} \quad (4.15)$$

together with Equation (4.13). The model for the VSF described above has been further improved by Verza et al. (2024). Their new approach combines the excursion-set framework (Bond et al., 1991; Peacock and Heavens, 1990) with the Lagrangian density peaks theory (Bardeen et al., 1986), through an effective, scale-dependent void formation barrier. The framework leverages both excursion-set theory, which models the formation of cosmic structures based on random walks of the density field, and the peak theory, which focuses on the properties of maxima in the density field to predict the location of structure formation. This hybrid model provides a more accurate description of the distribution of dark matter halos and voids in Lagrangian space and enables a proper mapping of these statistics to Eulerian space. The improvements introduced in the VSF modeling are threefold:

- in the standard excursion-set approach, the Lagrangian position at which the structure formed is random, while in this model it corresponds to a minimum in the density contrast field filtered at scale R
- the model includes both void-in-void exclusion and cloud-in-cloud exclusion, unlike the original framework
- the model properly accounts for the smoothing of the density contrast field, including correlations across different smoothing lengths and the exact relation between the smoothing length and the Lagrangian void size, resolving normalization issues of the Sheth and van de Weygaert (2004) multiplicity function in Eulerian space, as highlighted by Jennings et al. (2013).

The key quantity in modeling the size distribution of halos and voids is the formation threshold. The multiplicity function adopted by Verza et al. (2024) is:

$$\mathcal{F}(S) = \frac{e^{-B_S^2/2S}}{\sqrt{2\pi S}} \left\{ \sqrt{\frac{\Gamma_{\delta\delta}}{2\pi S}} \exp \left[-\frac{S}{2\Gamma_{\delta\delta}} \left(\frac{B_S}{2S} - B'_S \right)^2 \right] + \frac{1}{2} \left(\frac{B_S}{2S} - B'_S \right) \left\{ \operatorname{erf} \left[\sqrt{\frac{S}{2\Gamma_{\delta\delta}}} \left(\frac{B_S}{2S} - B'_S \right) \right] + 1 \right\} \right\} \quad (4.16)$$

where

$$S = \sigma^2(R) = \langle \delta_S^2 \rangle = \int \frac{dk k^2}{2\pi^2} P(k) |W(kR)|^2. \quad (4.17)$$

with δ_S the linear density contrast field filtered at the scale $S = S(R)$, $P(k)$ the linear power spectrum, $W(kR)$ the top-hat filter function in Fourier space, $\Gamma_{\delta\delta} = SD_S - 1/4$, and $D_S = \langle (d\delta_S/dS)^2 \rangle$. The moving barrier $B_S = B(S, \delta_v^L)$, is a function of the physical void formation barrier δ_v^L , while $B'_S = dB(S)/dS$.

Like any other cosmic structures, voids identified in redshift space are prone to both type of distortions, AP and RSD. Their impact on the VSF can be absorbed by rescaling the voids size by a factor proportional to the distortion parameter β for RSD (Correa et al., 2021), and by a combination of the AP dilation parameters from Equation (4.3). As noted by Contarini et al. (2022), when modeling RSD in the VSF, the most effective approach is to calibrate the void formation threshold δ_v^L , or formation barrier, directly in redshift space. This method not only accounts for RSD but also helps to mitigate other potential systematics that may affect the analysis. By calibrating the barrier in redshift-space, the model becomes more robust to a wider range of observational effects, improving the accuracy of void-based cosmological measurements. For modeling AP, the size of the voids rescales according to Equation (4.8):

$$R = q_{\parallel}^{1/3} q_{\perp}^{2/3} R'. \quad (4.18)$$

However, in Section 7.2 it is demonstrated that the threshold value is not affected by geometrical distortions.

With the VSF is possible to put constraints on various cosmological parameters. For instance, in Contarini et al. (2019), the VSF was employed to measure parameters such as σ_8 (the amplitude of matter fluctuations) and Ω_m (the total matter density parameter). Similarly, Verza et al. (2022) demonstrated how the VSF is sensitive to the influence of dark energy and the presence of massive neutrinos, showing that voids are valuable probes of these fundamental components of the Universe. In addition, Contarini et al. (2024) showed that the VSF can be use to measure the Hubble constant H_0 , contributing in the resolution

of the so-called Hubble tension, which refers to the discrepancy between the value of H_0 inferred from the early Universe, using the CMB, and the value measured in the local Universe using supernovae. These examples underscore the VSF's relevance in advancing our understanding of cosmological models and the nature of the Universe. Furthermore, the ongoing development of more sophisticated models of the VSF continues to improve its precision and utility of this probe in testing the cosmological model.

4.3 Void-galaxy cross-correlation function

Let us now focus on the other main cosmological probe based on cosmic voids: the void-galaxy 2-point cross-correlation function (VGCF), $\xi_{vg}(r)$. Its definition builds upon that of the auto-correlation function defined in Section 3.1.2 except that now the number density of two types of objects are correlated: the galaxy number density δ_g and the void number density δ_v , the latter estimated at the void center position.

Following Equation (3.6), the VGCF is defined as the expectation value of these two quantities at any two locations separated by a vector \mathbf{r}

$$\xi_{vg}(\mathbf{r}) = \langle \delta_v(\mathbf{x}) \delta_g(\mathbf{x} + \mathbf{r}) \rangle \quad (4.19)$$

In the Poisson model, in which the galaxies and voids are described as discrete tracers of the density field, the VGCF is implicitly defined by the probability of a void galaxy pair:

$$dP_v dP_g = \bar{n}_v \bar{n}_g [1 + \xi_{vg}(\mathbf{r})] dV_v dV_g \quad (4.20)$$

For simplicity, from now on we will drop the subscript vg and indicate the VGCF as $\xi(\mathbf{r})$, whereas the galaxy two-point correlation function will be referred to as $\xi_{gg}(\mathbf{r})$.

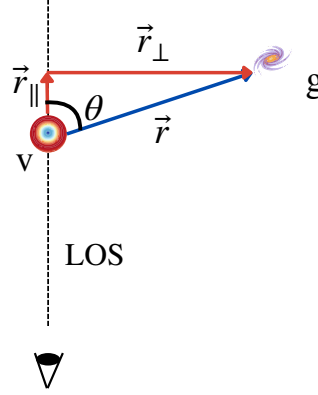


Figure 4.3 Illustration of the system of coordinates used for the VGCF. In blue the separation vector \mathbf{r} between the void center v and the galaxy g . In orange the component parallel r_{\parallel} and perpendicular r_{\perp} respect to the LOS (represented with the dashed line).

As for the auto-correlation case, the CP guarantees that, in absence of distortions, the VGCF is isotropic and depends on the modulus of the galaxy-void separation vector only, $\xi(r)$. However, in redshift space, this isotropy is violated by distortions (see Section 4.1). In this case, $\xi(r)$ will depend not only on r , but also on $\mu = \cos\theta$, i.e., the cosine of the angle between the separation vector \mathbf{r} and the LOS, that, assuming distant observer approximation, is taken to be the vector pointing to the center of the void. Figure 4.3 illustrates the separation vector, the cosine and its parallel and perpendicular components, r_{\parallel} and r_{\perp} , to the LOS. The relation between the two sets of coordinates is:

$$r = \sqrt{r_{\parallel}^2 + r_{\perp}^2} \quad \mu = \frac{r_{\parallel}}{r} \quad (4.21)$$

In presence of distortions it is convenient to expand the VGCF $\xi(r, \mu)$ in Legendre polynomials \mathcal{P}_{ℓ} of order ℓ , and define the corresponding multipoles:

$$\xi_{\ell}(r) = \frac{2\ell + 1}{2} \int_{-1}^1 \xi(r, \mu) P_{\ell}(\mu) d\mu. \quad (4.22)$$

that can be conveniently estimated. The monopole component ξ_0 is obtained by averaging over all μ angular separations and correspond to the usual $\xi(r)$ in absence of distortions. RSD and AP distortions only generate non-zero even multipoles of order up to 4. Therefore we shall only consider the monopole ($\ell = 0$), the quadrupole ($\ell = 2$) and the hexadecapole ($\ell = 4$) moments in this Thesis.

The VGCF has been the subject of numerous studies in the literature, with the primary goal of estimating cosmological parameters such as $f\sigma_8$, Ω_m , w_0 , and w_a , as well as their evolution with redshift z . These estimates are typically obtained by performing a complete analysis that involves comparing the measured multipoles of the VGCF with theoretical predictions, that will be introduced in the following section. This comparison allows for the extraction of constraints on the aforementioned parameters, providing valuable insights into the dynamics of the Universe and the nature of dark energy, see e.g., Aubert et al. (2022); Correa et al. (2022); Hamaus et al. (2022, 2020); Nadathur et al. (2020b); Radinović et al. (2023). Not all the analyses have been performed fully in redshift space. Nadathur et al. (2019) explored a different route by performing a cosmological reconstruction similar to that described in Section 3.4.1 and cross-correlating the void positions in the reconstructed space with those for the galaxies in redshift space. A recent overview of the RSD effect on VGCF-based analysis has been presented by Correa et al. (2022) along with a discussion on the limitation and possible improvements of this technique.

4.3.1 Modelling the void-galaxy cross-correlation function

The difference between the modeling of the VGCF and that of the galaxy 2PCF lies in the fact that, within the void framework, we consider the relative peculiar velocities with respect to a single central point, the void center. The bulk motion of voids does not affect the VGCF on scales where the bulk velocity field can be considered coherent (Cai et al., 2016).

Distortions in the VGCF are modeled in two ways:

- The AP effect is accounted for by applying a coordinate transformation from the true to the fiducial coordinates, employing Equations (4.9) and (4.6).
- The RSD modeling is more challenging. RSD have been modeled using linear perturbation theory and distant observer approximation, i.e. using the Kaiser model (3.18), as for example in Cai et al. (2016). However, the accuracy of this model is limited in describing mildly nonlinear structures like voids. For this reason, phenomenological extension of the linear model have been proposed by (Hamaus et al., 2020; Nadathur and Percival, 2018).

In this section, I will focus on modeling the VGCF in redshift space, ignoring AP. I will start by presenting the linear model then move to more sophisticated approaches.

Linear model Since RSD causes displacement along the LOS only, one can eliminate their impact by projecting the correlation function onto the plane of the sky. In this way, the

projected correlation function ξ_p is in principle free of dynamic distortions

$$1 + \xi_p(r_\perp) = \frac{\int [1 + \xi(r)] dr_\parallel}{\int dr_\parallel} = \frac{\int [1 + \xi^s(\mathbf{s})] ds_\parallel}{\int ds_\parallel} = 1 + \xi_p^s(s_\perp) \quad (4.23)$$

where $\xi^s(\mathbf{s})$ is the redshift space VGCF. The equation above yield the following relation between the VGCFs in real and redshift space:

$$1 + \xi^s(\mathbf{s}) = [1 + \xi(r)] \frac{dr_\parallel}{ds_\parallel}. \quad (4.24)$$

Equation (4.2) yields the relation between r and s , in particular:

$$s_\parallel = r_\parallel + \frac{1 + z_h}{H(z_h)} u_\parallel \quad (4.25)$$

and hence

$$\frac{dr_\parallel}{ds_\parallel} = \left(1 + \frac{1 + z_h}{H(z_h)} u_\parallel \right)^{-1}. \quad (4.26)$$

The relation between peculiar velocities and the mass overdensity can be obtained assuming linear theory from Equation (2.35) which, assuming spherical symmetry, becomes

$$\mathbf{u}(\mathbf{r}) = -\frac{f(z_h)}{3} \frac{H(z_h)}{1 + z_h} \Delta(r) \mathbf{r}, \quad (4.27)$$

where f is the linear growth rate of structures and $\Delta(r)$ is the average matter-density contrast inside a spherical region of comoving radius r

$$\Delta(r) = \frac{3}{r^3} \int_0^r \delta(r') r'^2 dr'. \quad (4.28)$$

By plugging Equation (4.27) into Equation (4.26), and using the identify $\frac{d\Delta(r)}{dr} = \frac{3}{r} [\delta(r) - \Delta(r)]$, we obtain the following relation:

$$\frac{dr_\parallel}{ds_\parallel} = \left(1 - \frac{f(z_h)}{3} \Delta(r) - f(z_h) \mu^2 [\delta(r) - \Delta(r)] \right)^{-1} \quad (4.29)$$

Hence, Equation (4.24) becomes:

$$1 + \xi^s(\mathbf{s}) = \frac{1 + \xi(r)}{1 - \frac{f}{3}\Delta(r) - f\mu^2[\delta(r) - \Delta(r)]}, \quad (4.30)$$

and Equation (4.2) describing the mapping between real and redshift space can be rewritten as:

$$r_{\parallel} = \frac{s_{\parallel}}{1 - \frac{f}{3}\Delta(r)} \quad (4.31)$$

that combined with $r = \sqrt{r_{\parallel}^2 + r_{\perp}^2}$ and $r_{\perp} = s_{\perp}$, gives the possibility to estimate the separation \mathbf{r} for a given measured separation \mathbf{s} .

However, Equation (4.31) already requires the knowledge of r in the argument of $\Delta(r)$, so it can be only evaluated by iterations. Hamaus et al. (2020) propose the method to evaluate this quantity: we start with using $\Delta(s)$ as initial guess for $\Delta(r)$, and iteratively calculate r_{\parallel} and $\Delta(r)$ until convergence is reached. They find that 5 iterations are fully sufficient for that purpose.

Furthermore, in Equation (4.30), the quantities $\delta(r)$ and $\Delta(r)$ appear, which are not directly accessible through observations because they refer to the unobservable galaxy counterpart, i.e., dark matter. Finding an analytical model for $\delta(r)$ is notoriously challenging, primarily because there is no universally accepted definition of a void. As a result, it is difficult to establish a model that can accurately describe their properties across different studies. The sensitivity to the identification method introduces variability in the derived void profiles, making it problematic to generalize results without a precise and consistent definition of voids. This remains an open problem in the field of void cosmology.

To overcome this issue, we can measure $\delta(r)$ via its relation to $\xi(r)$. Specifically, it can be shown that, for matter in real space, the equality $\delta(r) = \xi_{\text{vm}}(r)$ holds, where $\xi_{\text{vm}}(r)$ is the void-matter cross-correlation function. In particular the quantities ξ_{vm} and $\delta(r)$ are related via the following relation

$$\xi_{\text{vm}}(r) = \frac{1}{3r^2} \frac{d}{dr} [r^3 \Delta(r)], \quad (4.32)$$

and $\Delta(r)$ is the average of $\delta(r)$ in spherical shells, see Equation (4.28).

It is important to recall that $\delta(r)$ in the void framework refers to the matter density contrast function, averaged over all voids in the sample (i.e., we work with stacked voids) and assuming spherical symmetry. Consequently, it corresponds to counting the void-matter pairs found within a void at a given separation r , in the same way as for $\xi_{\text{vm}}(r)$, see Equation (11) in Pollina et al. (2017). Subsequently, we can link the quantity ξ_{vm} , and hence $\delta(r)$, to

the VGCF in real space $\xi(r)$. It was observed both by simulation-based studies (Contarini et al., 2019; Pollina et al., 2017; Ronconi et al., 2019) and observational analyses (Fang et al., 2019; Pollina et al., 2019) that the relationship between $\delta(r)$ and $\xi(r)$ is predominantly linear, expressed as:

$$\xi(r) = b\xi_{\text{vm}}(r) = b\delta(r) , \quad (4.33)$$

where b is the large-scale linear galaxy bias presented in Section 3.2. However, this linearity does not necessarily hold near the center of the void or in its immediate surroundings. In such regions, the linear bias approximation could still be valid, but the linear relation may be verified with a different slope. Nevertheless, as the size of voids increases, the two bias factors begin to align, ultimately converging in the limit of large effective void radii, R (Contarini et al., 2019; Pollina et al., 2019; Pollina et al., 2017). By adopting the relation from Equation 4.33 for $\delta(r)$, we can readily substitute it for $\xi(r)$, with the replacements $f \rightarrow f/b$ and $\Delta(r) \rightarrow \bar{\xi}(r)$, with

$$\bar{\xi}(r) = \frac{3}{r^3} \int_0^r \xi(r') r'^2 dr' . \quad (4.34)$$

The challenge of modeling $\xi(r)$ remains, and the issue of not having an analytical model persists, for the same reasons that hinder the modeling of $\delta(r)$. An analytically unified and universally accepted model does not yet exist, and various models have been proposed in the literature (see, for example, Hamaus et al. (2014)). Two primary approaches have been followed in the literature for modeling the void-galaxy correlation function. In this Thesis, I have employed both approaches to explore their effectiveness and applicability in the context of my analyses. The first approach, employed in Chapter 6 and also used by Nadathur et al. (2020b) and Radinović et al. (2023), is a purely empirical model based on the measurement of $\xi(r)$ from cosmological simulations. With access to several such simulations, that will be described in Section 5.3.1, I measured this quantity and use it as a model for $\xi(r)$. However, this technique has some limitations: (1) several independent realizations are required to minimize cosmic variance and obtain a universal ξ model, (2) the empirical VGCF depends on the cosmological model assumed to run the simulation and one needs to assess the sensitivity of the VGCF model on the assumed cosmology.

The second method used in this Thesis, employed in Chapter 7 and also in several works, e.g., Hamaus et al. (2022, 2020), is based on a phenomenological approach in which the observed projected VGCF is used to infer the 3D VGCF. This technique, presented by Pisani et al. (2014), is particularly effective for recovering the spherical profile of stacked voids in real space. Its main drawback is the deprojection step required to model ξ from the projected

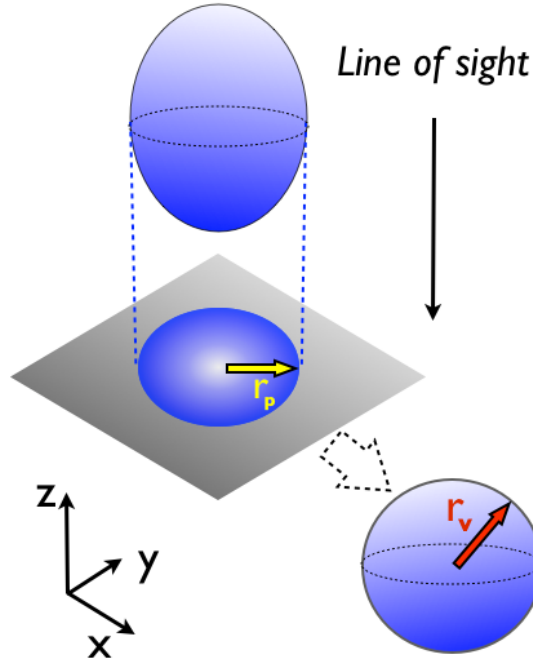


Figure 4.4 Representation of the method to reconstruct the sphere in real space starting from the distorted sphere in redshift space: the distorted void is projected along the LOS (velocities do not affect the parallel direction, hence the projection). From the projection, we reconstruct the sphere in real space. The red arrow represents r_v , the radius of the void in real space; the yellow arrow r_p , the radius of the projection. Credits: Pisani et al. (2014).

VGCF, which is prone to Poisson errors and, for this reason, becomes very noisy when small voids traced by a few galaxies are included in the sample.

The deprojection technique, schematically illustrated in Figure 4.4, is based on the idea of using the expected spherical symmetry of stacked voids to reconstruct the shape of the spherical density profile, without making any assumptions about the underlying cosmological model. The core concept involves measuring the cross-correlation function in redshift space, projected along the direction perpendicular to the LOS, $\xi_p^s(s_\perp)$, as RSD affect only the LOS direction. Once the projected cross-correlation, $\xi_p^s(s_\perp)$, is measured, the spherical shape of $\xi(r)$ can be recovered through the deprojection process, by solving the integral:

$$\xi(r) = -\frac{1}{\pi} \int_r^\infty \frac{d\xi_p^s(s_\perp)}{ds_\perp} \frac{ds_\perp}{\sqrt{s_\perp^2 - r^2}}, \quad (4.35)$$

using the inverse Abel transform (N. H. Abel, 1842).

Let's go back to the redshift space modelling. With the substitutions $\delta(r) \rightarrow \xi(r)$, $\Delta(r) \rightarrow \bar{\xi}(r)$, and $f \rightarrow f/b$, Equation (4.30) becomes:

$$1 + \xi^s(\mathbf{s}) = \frac{1 + \xi(r)}{1 - \frac{\beta}{3}\bar{\xi}(r) - \beta\mu^2[\xi(r) - \bar{\xi}(r)]}, \quad (4.36)$$

while Equation (4.31) is rewritten as:

$$r_{\parallel} = \frac{s_{\parallel}}{1 - \frac{\beta}{3}\bar{\xi}(r)}. \quad (4.37)$$

Finally, one can expand Equation (4.36) to linear order in δ , or equivalently in ξ for consistency with the perturbative level of the mass conservation equation (4.27), obtaining (Cai et al., 2016; Hamaus et al., 2017):

$$\xi^s(\mathbf{s}) \simeq \xi(r) + \frac{f}{3}\bar{\xi}(r) + \beta\mu^2[\xi(r) - \bar{\xi}(r)]. \quad (4.38)$$

Up to this point, we have derived the expression for modeling the VGCF in the presence of dynamic distortions. Geometric distortions are incorporated into the model by applying a coordinate transformation from true to fiducial coordinates, as outlined in Equations (4.9) and (4.6). We now rewrite the model, including both RSD and AP effects, using the following notation:

$$\xi^s(\mathbf{s}) \simeq \xi(r) + \frac{\beta}{3}\bar{\xi}(r) + \beta\mu^2[\xi(r) - \bar{\xi}(r)] \Bigg|_{r=r'(\varepsilon), \mu=\mu'(\varepsilon)} \quad (4.39)$$

where $r = r'(\varepsilon)$, $\mu = \mu'(\varepsilon)$ refer to Equations (4.9) and (4.6). The mapping from \mathbf{s} to \mathbf{r} also depends on this transformation in the following way

$$r_{\perp} = q_{\perp}s_{\perp} \quad r_{\parallel} = q_{\parallel}s_{\parallel} \left[1 - \frac{\beta}{3}\bar{\xi}(r) \right]^{-1}. \quad (4.40)$$

In this Thesis, as in most of the VGCF studies in the literature (Hamaus et al., 2022, 2017, 2020), we express the void-galaxy separation vector in units of the void's radius, R , both in real and in redshift space. In what follow, we shall use the same symbols r (s) to indicate the adimensional separations r/R and s/R_s , respectively.

Beyond linear modeling In the previous section, we derived a linear model for VGCF that features RSD and AP distortions. The core of the model is the linearized continuity equation (4.27) that, as shown by numerical simulations, describes the dynamics around most cosmic

voids with good accuracy (Schuster et al., 2023). This may seem surprising, since peculiar velocities inside and around voids can be nonlinear. However, we are interested in describing the dynamics around an average structure obtained by rescaling and stacking many voids, an operation that effectively smooths out nonlinear effects, and guarantees the validity of Equation (4.27).

Equation (4.27) may break down for either small or in the very underdense core of voids. These structures are characterized by a more complex dynamics, especially near their center, where deviations from a purely divergent flow become significant and do not average out. In some cases these voids can even collapse in a directionally dependent manner, driven by the external gravitational forces of surrounding mass (van de Weygaert and van Kampen, 1993). Such anisotropic collapse highlights the limitations of linear theory in describing the dynamics of voids at these smaller scales, requiring more sophisticated nonlinear models for accurate predictions. Hence, in the application, the VGCF model for the RSD has shown limited accuracy (Nadathur and Percival, 2018).

Limitations in the VGCF model are not the only factors that hinder void analyses. The void identification and characterization process, which will be described in Section 5.1, is also prone to uncertainties that significantly contribute to the error budget. The void identification algorithms used in most analyses are based on topological rather than dynamical criteria. Voids are identified solely by the spatial distribution of a discrete set of mass density tracers, such as galaxies. These type of void finders suffers from two main limitations. The first issue is the selection of spurious voids—Poisson fluctuations mistaken for genuine voids—which reduces the purity of the void catalog and lowers the amplitude of the VGCF’s quadrupole moment (Cousinou et al., 2019). Another source of issues is that these finders identify different sets of voids depending on whether the search is performed in redshift space or real space. As a result, voids identified in redshift space—along with their centers and radii—do not necessarily correspond to those identified in real space. One hint for this possible effect can be found in Correa et al. (2022). Furthermore, an additional potential source of disturbance in the model is the assumption of linear galaxy bias, which may not hold in the inner regions of cosmic voids, or may have a value different from the one valid on large-scales. This issue, in relation to the VGCF analysis, is thoroughly discussed by Hamaus et al. (2020); Nadathur and Percival (2018).

To overcome and absorb these uncertainties, Hamaus et al. (2020) proposed a generalization of the model, which was further extended in Hamaus et al. (2022). They propose a phenomenological approach and modify the linear VGCF model incorporating some empirical based modifications, in order to mitigate the nonlinearities. Thus, Equation (4.39) and consequently (4.40), revisited by Hamaus et al. (2022) assumes the following expression,

used for the analysis in Chapter 7:

$$\xi^s(s, \mu) = \mathcal{M} \left\{ \xi(r) + \beta \bar{\xi}(r) + 2\mathcal{Q}\beta\mu^2 [\xi(r) - \bar{\xi}(r)] \right\} \Big|_{r=r'(\varepsilon), \mu=\mu'(\varepsilon)}, \quad (4.41)$$

and the mapping becomes

$$r_{\perp} = q_{\perp} s_{\perp} \quad r_{\parallel} = q_{\parallel} s_{\parallel} \left[1 - \mathcal{M} \frac{\beta}{3} \bar{\xi}(r) \right]^{-1}. \quad (4.42)$$

This model features two additional nuisance parameters, \mathcal{M} and \mathcal{Q} , and modifying the expression for the Jacobian of the transformation, $dr_{\parallel}/ds_{\parallel}$.

The model coefficients were further refined for the work presented in Chapter 6. This modification process was carried out after testing the model on simulations. The resulting expression is:

$$\xi^s(s, \mu) = \mathcal{M} \left\{ \xi(r) + \frac{2}{3} \beta \bar{\xi}(r) + \mathcal{Q}\beta\mu^2 [\xi(r) - \bar{\xi}(r)] \right\} \Big|_{r=r'(\varepsilon), \mu=\mu'(\varepsilon)}. \quad (4.43)$$

The nuisance parameters \mathcal{M} and \mathcal{Q} are introduced to account for deviations from linear theory, both in the dynamics and the bias parameter, as well as to address the potential presence of spurious voids in the sample, which may reduce the amplitude of both the monopole and quadrupole moments of the VGCF (Cousinou et al., 2019). The monopole-like parameter \mathcal{M} regulates the overall amplitude of the VGCF and is intended to account for all factors that may influence the magnitude of void-galaxy clustering. The parameter \mathcal{Q} multiplies the μ^2 term, thereby regulating the quadrupole moment. It accounts for nonlinear effects contributing to the RSD and plays a crucial role when the analysis is performed with voids identified in redshift space rather than real space (Correa et al., 2021, 2022; Pisani et al., 2015b). The $2/3$ coefficient in front of the second term specifically amplifies the effect of RSD distortions on the overall clustering amplitude, in addition to the one induced by \mathcal{M} . The monopole term nuisance parameter, \mathcal{M} also account for possible uncertainties that will mainly affect the amplitude of the VGCF real space model, $\xi(r)$, even if derived with deprojection technique or from simulations.

However, even Hamaus et al. (2022) model, designed for the analysis of voids in redshift space, has its limitations. On one hand, this has led to the development of alternative models that attempt to incorporate at least the nonlinearities (e.g., Nadathur and Percival (2018), Paz et al. (2013)). On the other hand, an alternative approach involves moving away from analytical modeling in favor of numerical modeling of peculiar velocities. This

approach requires the use of the reconstruction algorithms, described in Section 3.4, to recover the positions of objects in the reconstructed space, where RSD effects are absent. This methodology has previously been applied with the goal of locating void centers in reconstructed space, and subsequently cross-correlating these centers with galaxies in redshift space to model the RSD still using analytical models (Nadathur et al., 2019; Radinović et al., 2023).

In my work, presented in Chapter 6, I propose a novel approach that directly analyzes voids in reconstructed space and, for the first time, performs a cross-correlation analysis between voids and galaxies entirely within the reconstructed framework, thereby eliminating the need to account for RSD during both void identification and VGCF modeling.

Specifically, we employ the following strategy: (1) we use the reconstruction method outlined in Section 3.4.1 to minimize nonlinearities in the data; (2) both the void identification and the statistical analysis, including the void-galaxy cross-correlation, are conducted in reconstructed space; and (3) we model the results using the VGCF model by Hamaus et al. (2022), allowing for the absorption of any residual uncertainties, regardless of their nature.

In the following chapters, beyond discussing the tools used for these analyses, we will focus on two main contributions:

- In Chapter 6, I present the main results of this Thesis, the first analysis of the VGCF between voids and galaxies in reconstructed space, demonstrating that an AP test on reconstructed voids yields more precise and accurate results compared to those in redshift space. This analysis was conducted on simulated data and will be applied to observational data for the first time in future studies.
- In Chapter 7, I participated in a forecast analysis of the parameters that will be constrained by measurements of void statistics employing data from a future survey, the Nancy Grace Roman Space Telescope. The chapter presents an analysis of both the VSF and VGCF. My contribution focused on the latter, using the "standard" methodology, where RSD are modeled analytically, rather than through the reconstruction approach, which could be applied in future work, after refining the method for application to data.

5

Tools for void analyses

In this chapter, I will present the various tools used for the void analyses. In Section 5.1, I will discuss the void identification algorithm, which is employed to identify void regions within the distribution of galaxies (or tracers more generally). This void finder was mentioned in Chapter 4, and here I will provide a detailed description of how the algorithm I adopted for the analyses works.

Following that, in Section 5.2, I will describe the code I developed to estimate the void-galaxy cross-correlation function and its multipoles.

Finally, I will illustrate the simulated datasets used in this Thesis and the techniques used to generate them.

5.1 Void finder

Since there is not yet a general consensus on the definition of voids, numerous void finders have been proposed and utilized over the past decades (see Colberg et al. (2008) for a cross-comparison of various techniques available at that time). Following the strategy outlined by Lavaux and Wandelt (2010), void-finding algorithms can be broadly classified into three main categories, based on the criteria they apply:

Density criterion: These algorithms define voids as regions empty of tracers in which their local number density is below a predefined threshold (Elyiv et al., 2013; Micheletti et al., 2014). In this case, tracers are divided into wall tracers and field tracers depending on the density of the region in which they are located (“strongly overdense” regions and “mildly underdense” regions, respectively).

Geometry criterion: This class includes void finders that identify voids as underdense regions within a well defined geometry like spherical cells (Paz et al., 2023) or polyhedra (Neyrinck, 2008; Platen et al., 2007; Sutter et al., 2015). In particular, the strategy adopted

by these algorithms is first to generate a continuous density field of tracers and to search for local minima to define/obtain the void distribution.

Dynamical criterion: These void finders are based on dynamical criteria in which tracers are not exploited to reconstruct the underlying mass distribution but are used as test particles of the cosmic velocity field. Therefore, in these algorithms, a void is defined as a region from which matter is evacuated (Elyiv et al., 2015; Forero-Romero et al., 2009; Lavaux and Wandelt, 2010).

To generate our void catalogs we will use the Void IDentification and Examination toolkit (VIDE)¹ (Sutter et al., 2015). The algorithm is optimized to run both on cubic snapshots (simulations) and light cones with arbitrary geometry (observations). VIDE belongs to the category of algorithms that rely on geometrical criteria, implementing an improved version of the ZOnes Bordering On Voidness (ZOBOV) algorithm (Neyrinck, 2008). ZOBOV is a widely-used and publicly available code designed to identify density depressions in a 3D set of points, without requiring free parameters or assumptions about the shape of voids. The void-finding process in VIDE involves three main stages:

1. **Voronoi Tessellation:** The algorithm first reads the positions of the tracers and assigns to each tracer a Voronoi cell, a region of space closer to that tracer than to any other. The volume of each Voronoi cell is inversely related to its density, assuming equal weights for all particles. This step generates a continuous and well-defined density field.
2. **Identification of Local Density Minima:** The algorithm then locates local density minima, defined as cells with a density lower than all adjacent cells (also known as natural neighbors). From these minima, the surrounding Voronoi cells are merged iteratively, with the condition that the density of the merged cells must be higher than that of the previously merged cell. The merging process halts when a cell with lower density is encountered, resulting in the formation of local density basins, referred to as zones.

¹https://bitbucket.org/cosmicvoids/vide_public/wiki/Home

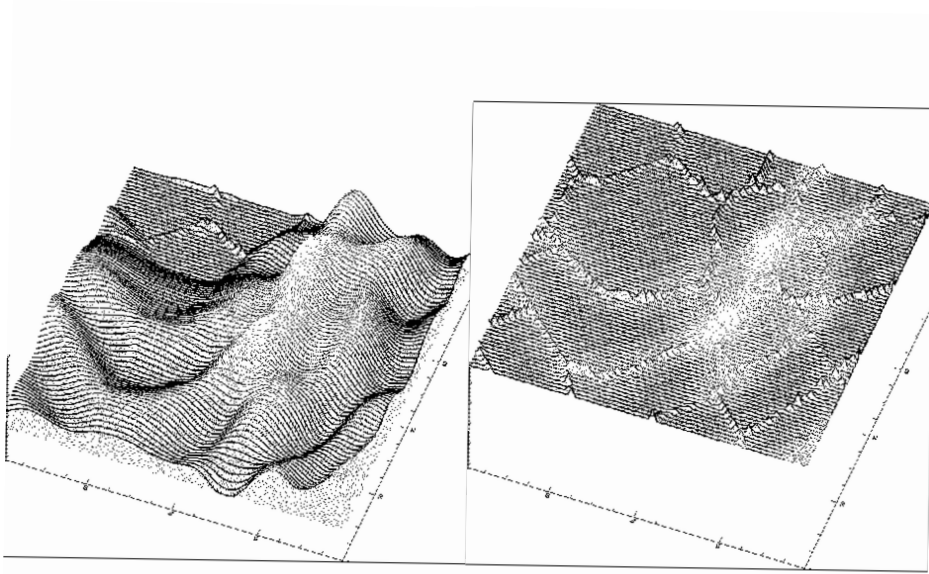


Figure 5.1 Illustrations of the principle of the watershed transform. Starting from the local minima the surrounding basins of the surface start to flood as the water level continues to rise. Where two basins meet up near a ridge of the density surface, a “dam” is erected (left frame). Ultimately, the entire surface is flooded, leaving a network of dams defines a segmented volume and delineates the corresponding cosmic web (right frame). Credits: Platen et al. (2007).

3. **Watershed Algorithm:** Finally, zones are merged into larger structures, or voids, using the watershed algorithm (Platen et al., 2007), illustrated in Figure 5.1. This method involves incrementally raising a density threshold from the local density minimum of each zone. Regions with densities below the threshold are progressively added to the void until a deeper zone is encountered, at which point the process stops. The final void consists of all the merged zones, with shallower zones recorded as sub-voids.

A visual representation of the whole process can be seen in Figure 5.2, and example of a void as a VIDE output is represented in Figure 5.3.

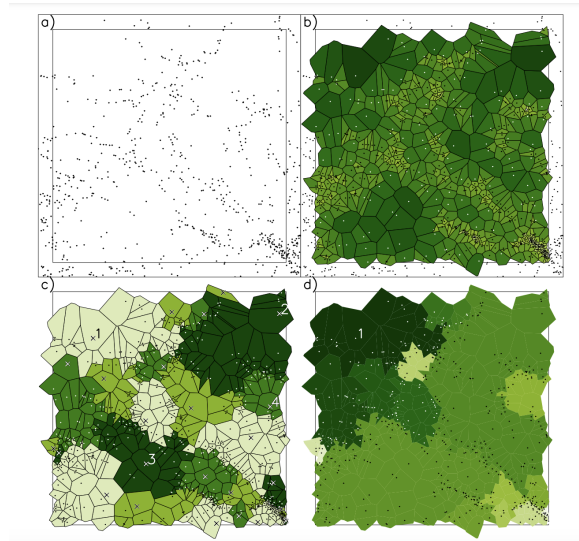


Figure 5.2 Illustration of the creation of voids: (a) slice of galaxy field where galaxies are represented by dots. (b) 2D Voronoi tessellation of galaxies in this slice, which each particle's Voronoi cell shaded according to its area. The galaxies outside the slice are shown because contribute to the tessellation. (c) Zones of galaxies. The core (density minima) of each zone are shown with crosses, the different colors demarcate different zones. (d) The watershed growth of 1 void, the deepest void in the sample. Colors from dark to light indicate the stage at which the zone is added to the void. The darkest color is the original zone, the next-darkest is the first zone or set of zones added, etc. The only zone that is never included is that with the highest-density link to another zone, in the lower-right corner. Credits: Neyrinck (2008)

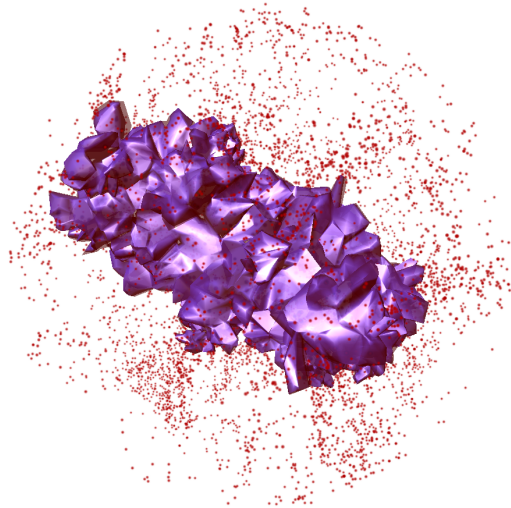


Figure 5.3 An example of a watershed void in `VIDE`. The Voronoi cells that define the void are in purple with galaxies in red. We show a void with effective radius $20 h^{-1}\text{Mpc}$ within a $50 h^{-1}\text{Mpc}$ spherical region. Galaxy point sizes are proportional to their distance from the point of view. Galaxies interior to the void are shaded dark red. Credits: Sutter et al. (2015)

The output after running `VIDE` is a catalog of voids characterized by the coordinates of their centers, \mathbf{X}_v and their effective radii R . Void centers are calculated as the volume-weighted barycenter of all tracer particles that have been associated with the void

$$\mathbf{X}_v = \frac{\sum_j \mathbf{X}_j V_j}{\sum_j V_j}, \quad (5.1)$$

where \mathbf{X}_j is the coordinate vector of tracer j and V_j is the associated Voronoi volume. The barycenter can be thought of as the geometric center of the void, as it is mostly constrained by its boundaries where the majority of tracers reside. This implies that it does not generally coincide with the minimum density inside the void, due to its non-spherical geometry. Conversely, the location of the minimum density is largely independent of the void boundaries, making it a poor indicator of the void geometry. Thus, the optimal center definition typically depends on the desired void observables. In this paper we are interested in measurements of the shape of stacked voids, so we want to maximize the sensitivity to their boundaries (Cautun et al., 2016). To retain knowledge of this defining property of watershed voids, we therefore choose the volume-weighted barycenter. Moreover, in contrast to center definitions that are based on merely a single or a few tracers, the barycenter is more robust against discreteness noise and peculiar motions of individual tracers (Hamaus et al., 2014a).

Since `VIDE` makes no assumptions about the shape of voids, and the geometry of the Voronoi cells is often complex and deviates significantly from spherical symmetry, it is convenient to define an effective radius, R , for each void. This effective radius is calculated as the radius of a sphere with the same total volume, V of the Voronoi cells $V = \sum V_i$

$$R = \left(\frac{3}{4\pi} \sum_j V_j \right)^{1/3}. \quad (5.2)$$

5.2 Void-galaxy cross-correlation function estimator

To estimate the two-point cross-correlation function of galaxy-void pairs, described in Section 4.3, we have adapted and implemented the Davis-Peebles (DP) auto-correlation function estimator (Davis and Peebles, 1983). Like all two-point estimators, the DP one is based on counting object pairs at a given separation and compare them with pair counts performed in a population of synthetic objects distributed over the same volume and sharing the same selection effects as the real ones but with no intrinsic spatial correlation properties. We call this reference population of synthetic objects the "random" sample.

The modified DP estimator, for the void-galaxy cross-correlation function is defined as:

$$\xi^{\text{DP}}(r, \mu) = \frac{n_{\text{R}}}{n_{\text{G}}} \frac{\mathcal{D}_{\text{v}}\mathcal{D}_{\text{g}}(r, \mu)}{\mathcal{D}_{\text{v}}\mathcal{R}_{\text{g}}(r, \mu)} - 1, \quad (5.3)$$

where $\mathcal{D}_{\text{v}}\mathcal{D}_{\text{g}}$ are the void-galaxy (or more generally void-tracer) pair counts at radial r and angular μ separation, and $\mathcal{D}_{\text{v}}\mathcal{R}_{\text{g}}$ are the void-random pair counts. The quantities n_{R} and n_{G} represent the total number counts of the random object and of halos respectively.

The numerical code that I have implemented estimates Equation (5.3) in the following steps:

- The code reads in a catalog of voids generated by `VIDE`, the corresponding galaxy catalogs from which voids were identified and the catalog of random objects.
- For each void, the separation from each galaxy in the catalogs is measured
- The same procedure is repeated for voids and random objects
- All separations are rescaled by the radius of the corresponding void
- The cosine of the angle, $\mu = \cos\theta$, between the separation vector and the LOS to the void is estimated
- $\mathcal{D}_{\text{v}}\mathcal{D}_{\text{g}}(r, \mu)$ and $\mathcal{D}_{\text{v}}\mathcal{R}_{\text{g}}(r, \mu)$ are obtained by summing up void-galaxy and void-random pair counts that belong to the same (r, μ) bin
- Equation (5.3) is used to estimate $\xi^{\text{DP}}(r, \mu)$.

Here r is a dimensionless quantity representing the physical separation between the center of the void and the halo divided by the void effective radius R . Once the VGCF is evaluated, multipoles can be computed via Equation (4.22). To estimate the VGCF, I implemented a `Python` code, designed to handle both cubic geometries (as in the case of simulations) and light-cone geometries, or more generally any geometry where the coordinates are given in right ascension (RA), declination (DEC), and redshift, being suitable for observational data.

Another method for calculating the cross-correlation is the Landy-Szalay (LS) estimator (Landy and Szalay, 1993), which, when adapted for voids (Hamaus et al., 2017), becomes:

$$\xi(r, \mu) = \frac{\langle \mathcal{D}_{\text{v}}\mathcal{D}_{\text{g}}(r, \mu) \rangle - \langle \mathcal{D}_{\text{v}}\mathcal{R}_{\text{g}}(r, \mu) \rangle - \langle \mathcal{R}_{\text{v}}\mathcal{D}_{\text{g}}(r, \mu) \rangle + \langle \mathcal{R}_{\text{v}}\mathcal{R}_{\text{g}}(r, \mu) \rangle}{\langle \mathcal{R}_{\text{v}}\mathcal{R}_{\text{g}}(r, \mu) \rangle}, \quad (5.4)$$

where \mathcal{R}_{v} represents a random void catalog, with random positions of void centers and radii, and the average means that these quantities are normalized by the total number of counts. In order to compute this estimator as a function of distance normalized to the mean

void radius \bar{R} , we simply divide every void-centric separation by its corresponding R_i . Since the random void positions \mathcal{R}_v have no effective radii associated to them, we can choose the mean effective radius \bar{R} of the data voids for each rescaling.

5.3 Numerical simulation catalogs

Numerical simulations are crucial in cosmology, allowing the study of the gravitational evolution of cosmic structures that cannot be solved analytically. *N-body simulations*, which focus on gravitational interactions, model the distribution of dark matter across large scales. Early simulations (Aarseth and Hoyle, 1963; Peebles, 1970; Press and Schechter, 1974) handled small systems, but modern advancements allow billions of particles to be simulated, providing more accurate predictions. The final output of an N-body simulation is a set of snapshots that capture the configuration of the particle system at different time steps, effectively tracing the evolution of the total matter density field.

It is important to note that objects in a snapshot, whether DM haloes or galaxies, all share the same cosmological age. However, to directly compare simulations with observations, we must account for the time evolution of astrophysical objects as seen from Earth. This is a direct consequence of the finite speed of light. Catalogues that incorporate this feature are called light-cones, and they are typically constructed by stacking sequential slices of snapshots corresponding to different cosmic epochs.

In this Thesis, we employed two different simulations for the analyses. In Chapter 6, we used haloes from the snapshots of the Quijote N-body simulations (Villaescusa-Navarro et al., 2020)². The purpose of using these simulations was to perform a reliable controlled test of a new method proposed for analyzing voids in reconstructed space. Having access to simulations allows us to control the effects of void reconstruction, or a new method in general, and mitigate potential systematics.

In Chapter 7, we used galaxies from N-body simulations, structured as light-cones, to simulate the data of the upcoming High Latitude Spectroscopic Survey (HLSS) (Wang et al., 2022), which will be conducted by the Nancy Grace Roman Telescope. The goal of using simulated data is to forecast the types of analyses that can be performed and to estimate cosmological parameters, along with their expected precision, based on future observations.

²<https://quijote-simulations.readthedocs.io/en/latest/>

5.3.1 Quijote simulations

The Quijote simulations is a suite of more than 82,000 full N-body simulations spanning more than 7,000 cosmological models in the $\Omega_m, \Omega_b, h, n_s, \sigma_8, M_\nu, w$ hyperplane, where n_s is the scalar spectral index that describes how the amplitude of primordial density fluctuations varies with scale (i.e., the n in Equation (3.3)) and M_ν is mass of neutrinos. The simulations are designed to: quantify the information content on cosmological observables and provide enough statistics to train machine learning algorithms. All simulations cover a cosmological volume of $1 (h^{-1} \text{Gpc})^3$, and have a cubic shape. Most of the simulations track the evolution of 512^3 CDM particles, which represents our fiducial resolution. However, we also have simulations with 256^3 (low-resolution) and 1024^3 (high-resolution) CDM particles. Snapshots are saved at redshifts $z = 0, 0.5, 1, 2, \text{ and } 3$.

In this Thesis, Chapter 6, we choose to work with a set of 100 independent high-resolution realizations, called mocks, of the same flat Λ CDM model, characterized by the following parameters: $h = 0.6711$, $\Omega_m = 0.3175$, $\Omega_b = 0.049$, $n_s = 0.9624$, and $\sigma_8 = 0.834$. Each of these simulations was run in a cubic box of comoving size $L_{\text{box}} = 1000 h^{-1} \text{Mpc}$.

We have considered a single snapshot at $z_{\text{snap}} = 0.5$, matching the typical redshift of the BOSS catalogs (Dawson et al., 2012) used in most recent void analyses. We work directly with the halo catalogs. In each snapshot, halos were identified in the dark matter particle distribution using the friends-of-friends (FoF) algorithm as implemented in `Pylians3`³. This approach considers only the parent halos, and not the subhalos, which correspond to trace the central galaxies while ignoring satellites. This approximation is adequate for describing the luminous red galaxy (LRG) samples extracted from the BOSS data, as these galaxies are expected to reside at the centers of massive halos. The simulation also provides the values for the peculiar velocities of galaxies, and this is necessary for creating catalogs with the position of halos in redshift space, which is crucial for the analysis.

To match the characteristics of the LOWZ and CMASS samples of the SDSS-III DR12 (Reid et al., 2016), with the aim of future applications to real data, we have applied a mass cut at $m_{\text{min}} = 10^{13} h^{-1} M_\odot$, to align with the typical number density of BOSS galaxies at $z = z_{\text{snap}}$, that is $n \simeq 4 \times 10^{-4} h^3 \text{Mpc}^{-3}$. The total number of halos in each mock catalogs is approximately 4×10^5 .

Since we use halos as mass tracers in our analysis, we need to estimate the large scale linear bias of the halos. This quantity is calculated following the procedure detailed in Appendix A. We obtain a value for the large-scale halo bias which is $b = 1.87 \pm 0.03$. The fiducial value of the linear growth is computed from the fiducial cosmology of the simulation

³<https://pylians3.readthedocs.io/en/master/>

at the redshift of the snapshot, giving $f(z_{\text{snap}}) = [\Omega_m(z_{\text{snap}})]^{0.55} = 0.763$. These values for f and b are then used to estimate the distortion parameter $\beta = f/b$ which is applied in the reconstruction procedure.

The redshift space halo catalogs

To construct halo catalogs in redshift space starting from the real space data, we adopt the distant observer approximation. This allows us to assign a common LOS for all halos in the box, which we identify with the Cartesian z -coordinate axis. The center of the box is placed at a comoving distance from the observer, $d(z_{\text{snap}})$ according to Equation (3.14). The distance to all objects in the cube is then estimated accordingly. Next, the observed redshift of each halo is computed using Equation (3.13), by combining the cosmological redshift with the Doppler redshift due to peculiar velocities, provided by the simulation, along the LOS, $z_d = v_{\parallel}/c$.

This transformation does not preserve the shape of the original cube, as some halos, once shifted along the LOS, cross the cube's boundaries. To restore the cubic shape, we trim the catalog by excluding these objects that were displaced outside the cube. The loss of objects due to this trimming is minimal, amounting to approximately 0.3 % of the total, thereby keeping the mean number density unchanged.

The resulting mock catalogs will be used for both the redshift space analysis and as input for the reconstruction algorithm.

The reconstructed halo catalogs

Halo catalogs in reconstructed space were obtained by applying the Zel'dovich reconstruction algorithm to the catalogs of halos in redshift space. To perform the reconstruction, described in Section 3.4.1, one needs to set the number of grid cells on which the tracer density field is interpolated and the radius of the Gaussian filter used to smooth the field.

We set $N_{\text{cell}} = 256$ and $R_s = 5 h^{-1}\text{Mpc}$. The choice of the smoothing scale will be justified in Section 6.4.1 in which we show that this value minimizes the residual RSD effect. As for the number of cells, we verified that its choice has no significant impact on the reconstruction as long as the size of the cell is smaller than the smoothing radius. This is a peculiarity of the multigrid method, see White (2021).

After performing the reconstruction, some halos may fall outside the boundaries of the cube. To avoid introducing inhomogeneities in the catalog, we remove all halos displaced outside the cube and trim the original volume to a slightly smaller cube, reducing the volume

by 0.08 % while maintaining the mean number density unchanged. This trimming is sufficient to eliminate any edge effects.

The random catalogs

To perform clustering analyses we need to generate a random catalog (only for the halos in this analysis). In this case we create a single random catalog that can be applied consistently across all three types of catalogs—real, redshift, and reconstructed space—since the number density and geometry remain the same in all three cases.

Since we are working with snapshots, with no selection function, the objects are uniformly distributed within the cube with a mean density 20 times larger than that of the halos to reduce shot noise in the estimation of the void-galaxy cross-correlation function. In typical clustering analyses, the galaxy autocorrelation function is estimated using random catalogs that are 50 times denser than the galaxy sample. However, we use random catalogs with 20 times the halo density, as in the VGCF analysis the shot noise is primarily driven by the number of voids rather than halos.

The void catalog

The void catalogs are generated by applying the void-finding algorithm `VIDE`, described in Section 5.1, to each of the three kinds of halo catalogs, real, redshift and reconstructed space, obtaining three corresponding void catalogs for the cross-correlation analyses. Table 5.1 lists the number of objects in the six halo and voids catalogs obtained from Mock 0, one of the 100 independent realizations, used in the analysis in Chapter 6.

mock 0	Halo catalog N_H	Void catalog N_V
Real space	400000	3402
Redshift space	398802	3057
Reconstructed space	398488	3386

Table 5.1 Table summarizing the catalogs used for the results in this analysis. Column 2 contains the values of the number of halos, N_H , in the catalogs, while column 3 contains the values of the number of voids, N_V , found with `VIDE` in the respective halo catalog

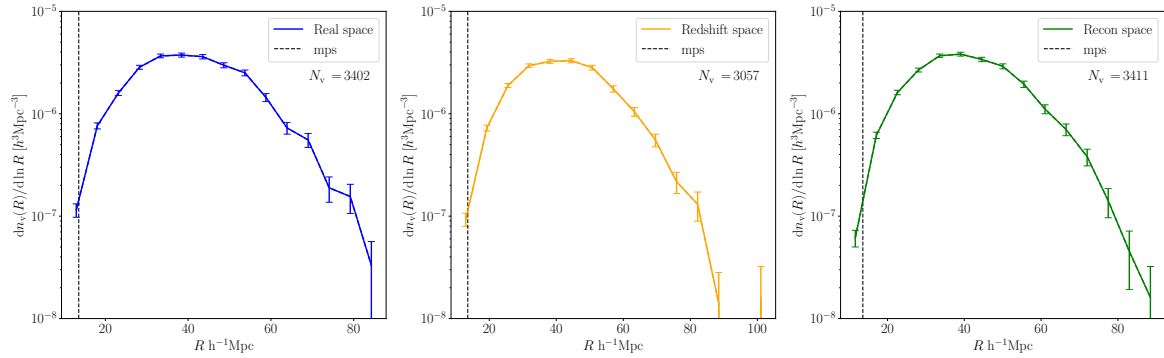


Figure 5.4 The abundance of voids that VIDE found in real (left), redshift (middle), and reconstructed (right) space as a function of their effective radius R (i.e., void size function). Poisson statistic is assumed for the error bars. In dashed vertical lines: the value of the mean particle separation for the halo sample. Here it is possible to see that the void distribution for the case of real (left panel) and reconstructed space (right panel) is very similar.

To extract the void catalogs, we used the void finder VIDE presented in Section 5.1. The output of the algorithm gives us a catalog with the centers, calculated as the volume-weighted barycenters, and the effective radii of the voids R . For simplicity we indicate here the values of the voids found with VIDE in the reference mock 0. From the real-space halo catalog, we identified $N_v = 3402$ voids. For the redshift-space and reconstructed-space catalogs, the number of identified voids is $N_v = 3057$, and $N_v = 3411$, respectively. The abundance of voids as a function of their size (i.e., the void size function) for the three different catalogs is represented in Figure 5.4. The distributions on the left, middle, and right panels refer to voids identified in real, redshift, and reconstructed space, respectively. A vertical dashed line is drawn in correspondence to the mean halo separation in the snapshot, below which no genuine void can be reliably identified.

We observe that the number of voids identified in redshift space is smaller than in the other cases. The causes of this mismatch are still under investigation. One possible explanation is that, in redshift space, the void finder may show a "preference" for identifying voids that are intrinsically elongated along the line of sight in real space, as suggested by Correa et al. (2022). In contrast, the number of voids in real and reconstructed space is quite similar, indicating that the reconstruction procedure is working effectively.

Spurious voids It is important to raise the point that shot noise from discrete mass tracers can lead void finders to identify spurious, typically shallow, voids. A common procedure to mitigate this contamination is to assume that smaller voids are more susceptible to such effects and remove them from the analysis. An arbitrary threshold radius is often set, equal to some multiple of the mean particle separation (Hamaus et al., 2022, 2020). However, in our

study, we choose not to apply this cut in order to avoid introducing unnecessary and poorly motivated constraints, thereby retaining all identified voids in the sample.

Our decision is motivated by the findings of (Cousinou et al., 2019), which show that applying a cut for voids with radii greater than N_s times the mean particle separation significantly reduces the sample size without effectively removing spurious voids, which span a wide range of sizes.

A key point of the work presented in Chapter 6 is to provide an analysis pipeline that is robust against the inclusion of small voids. By retaining these voids, we are able to increase the sample size relative to previous literature, thereby improving the precision of cosmological constraints. Since these ad hoc cuts do not effectively solve the contamination issue, we have opted to include small-sized voids in our analysis and assess the robustness a posteriori by comparing the outcomes when small voids are included or excluded, as discussed in Section 6.3.4. A dedicated study on the impact of spurious voids will be addressed in future works.

5.3.2 Roman HLSS mocks

In Chapter 7 we will present the result of an analysis that considers galaxies in the 2000 square degrees light-cone (Zhai et al., 2021), in the redshift range $1 < z < 2$. The light-cone simulates the $H\alpha$ galaxy redshift catalog expected from the Roman High Latitude Spectroscopic Survey (HLSS), and is constructed from the `unit` simulation (Chuang et al., 2019), characterized by a flat Λ CDM cosmology with parameters: $[h, \Omega_b, \Omega_m, \Omega_{\text{cdm}}, \sigma_8, n_s, A_s] = [0.6774, 0.0462, 0.3089, 0.2627, 0.8147, 0.9667, 2.06 \times 10^{-9}]$, where A_s represents the amplitude of the primordial scalar fluctuations in the Universe, as measured by Planck Collaboration et al. (2016). The light-cone has been populated with galaxies using the `GALACTICUS` (Benson, 2012) semi-analytical model (SAM). The emission line luminosities are evaluated with `CLOUDY` (Ferland et al., 2013; Merson et al., 2018) using the ionizing student spectrum of each galaxy as predicted by the SAM as input. In this case, the catalog is already provided in redshift space, and the analysis is performed directly in this space without any further manipulations. No real space catalog is available in this case.

Void catalog

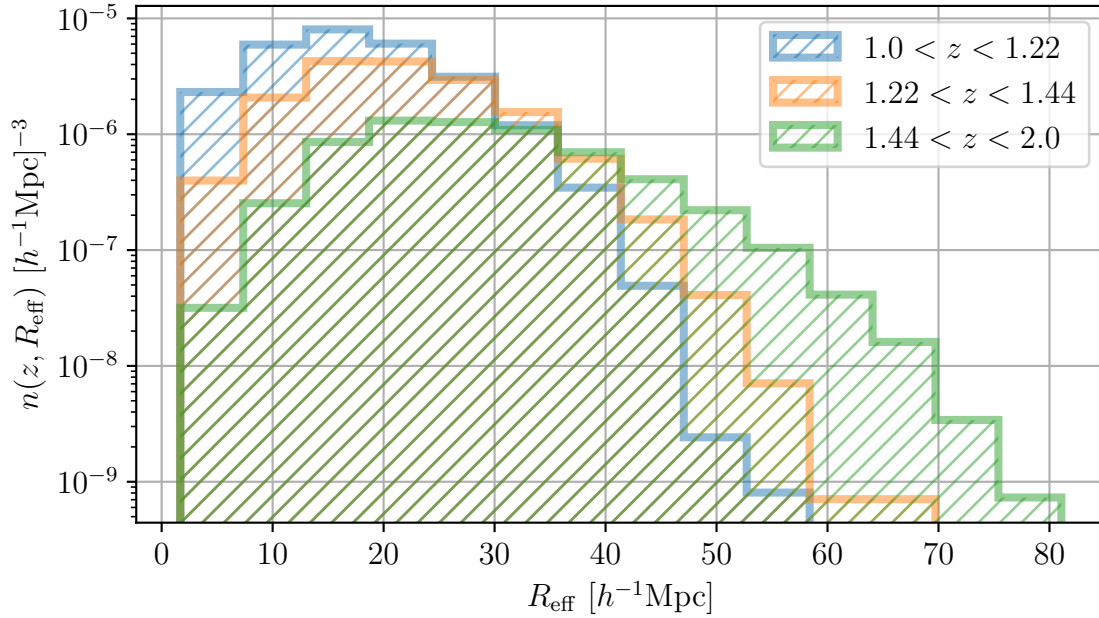


Figure 5.5 Histograms showing the number density of VIDE voids as a function of the void effective radius, here called R_{eff} . Each color corresponds to a different redshift bin, as listed in the legend.

The void catalogs were built using the void finder VIDE, described in Section 5.1. The final VIDE void catalog provides many void features, the most relevant for our work being i) the volume weighted barycenter, that is the void barycenter obtained weighting by the volumes of the contributing Voronoi cells; ii) the effective radius, R_{eff} , i.e. the radius of a sphere with the same volume as the void, $R_{\text{eff}} = [(3/4\pi) \sum_i V_i]^{1/3}$, where V_i is the volume of the i^{th} Voronoi cell belonging to the void.

We detect 82551 voids in the 2000 squared degrees galaxy light-cone. The redshift binning is chosen to have equi-populated bins for the VGCF analysis, that directly uses the VIDE catalog, pruning small voids (see Section 7.1 for details). Histograms in Figure 5.5 show the number density of VIDE voids as a function of the void effective radius, here called R_{eff} in each redshift bin considered in the analysis. The first redshift bin, $z \in [1, 1.22)$, contains 33574 voids (blue histogram), the second bin, $z \in [1.22, 1.44)$, 23114 voids (orange histogram), and the third bin, $z \in [1.44, 2]$, 25863 voids (green histogram). The higher the number density of galaxies is, the smaller the size of voids that void finders can detect over such a biased tracer distribution (Verza et al., 2023). This is visible in Figure 5.5 as the evolution of the effective radius distribution as a function of redshift.

For the clustering analysis, two random catalogs were prepared, one for the galaxies and the other one for voids. In particular, following Hamaus et al. (2022, 2020), we prepared random void catalogs by considering a number of random voids larger than the corresponding number of voids measured in the simulated light-cone. Moreover, the random catalogs share the same angular footprint as the corresponding void and galaxy catalogs from the light-cone. For the catalog of random voids we also applied to each void center an effective radius, randomly taken from the radius distribution of voids in the light-cone.

6

On the optimization of the extraction of AP signal from voids

In this chapter, I present the results of a VGCF analysis fully performed in reconstructed space and compare the results with those obtained by performing a more traditional analysis in redshift space.

As discussed previous Section 4.1, the data we observe are affected by both AP and RSD distortions. In order to perform an AP test, it is necessary to account for RSD, and this can be done in two ways: either by analytically modeling RSD (see Section 4.3.1) or by removing RSD using a reconstruction technique. The main drawback of the first approach is that VGCF models fail to accurately account for nonlinear dynamical effects. As a result, the structures more affected, the small size voids, are excluded from the analyses, significantly reducing the statistical signal of the VGCF measurements (Hamaus et al., 2020). The second approach has the potential to overcome this problem since nonlinear reconstructions algorithm correct for these effects, at least in the mildly nonlinear regime. Therefore, performing the analysis in the reconstructed space with all voids, including the small ones, should allows us to improve the precision with witch cosmological parameters are inferred from a void-galaxy clustering analysis.

The main goal of the VGCF analysis performed in this chapter is to estimate the ϵ parameter (introduced in Equation (4.7)) that quantifies the magnitude of the AP effect, and quantify the improvement in terms of both precision and accuracy with respect to a redshift space analysis. The strategy is outlined in Section 6.1, while in Section 6.2 I will describe the likelihood analysis. The results are presented in Section 6.3. Finally, Section 6.4 contains the robustness tests made to assess the reliability and stability of the results. The content of this chapter will form the basis for a scientific publication, which is ready for submission.

6.1 Strategy

Our proposed approach aims to enhance the statistical signal by including voids of all sizes, including the small ones, through a numerical modeling of peculiar velocities via a reconstruction algorithm (see Section 3.4.1). By applying this technique, one can ideally remove RSD, leaving only geometric distortions, if present, that can be exploited through AP test to trace the expansion history of the Universe.

This analysis addresses two key questions. First, does the reconstruction successfully eliminate RSD? Second, does this method enable a more precise and accurate AP test, particularly in estimating the AP parameter ε , with respect to analogous analysis performed in redshift space?

To answer these questions we perform the analyses, in both redshift space and reconstructed space, and compare the results, as depicted in Figure 6.1. The first row represents the analysis in redshift space using a VGCF model with combined RSD and AP effects similar to Hamaus et al. (2022). This involves extracting the void catalog using `VIDE` (Section 5.1) from the galaxy catalog in redshift space, and then calculating the VGCF in redshift space. By comparing the data with the theoretical model, we estimate the parameters β (RSD) and ε (AP).

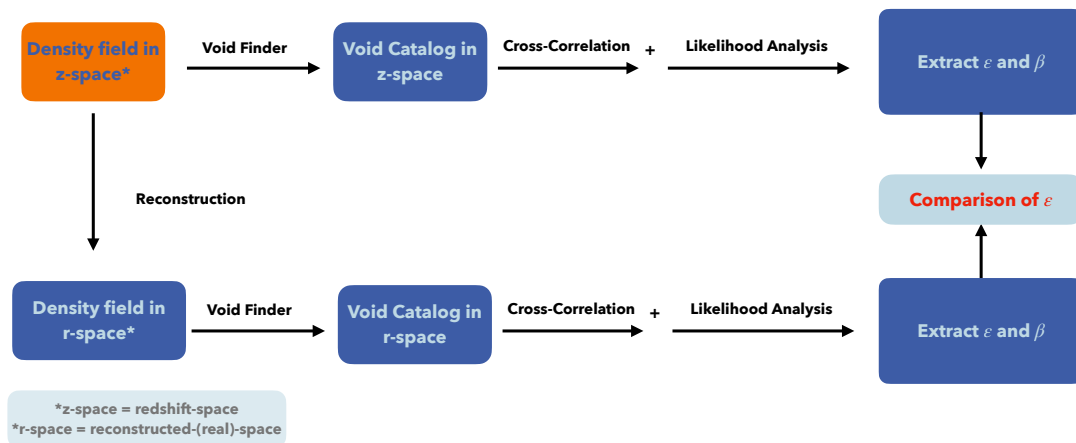


Figure 6.1 Schematic illustration of the strategy followed in the analysis presented in this Chapter.

In the second row, a reconstruction algorithm is applied to obtain the positions of halos in reconstructed space. These positions are used to extract a void catalog with `VIDE` in reconstructed space, which then serves as the input for the VGCF, also calculated in reconstructed space. The reconstruction is performed assuming a fiducial β parameter that we set equal to the one that nullifies the quadrupole moment of the VGCF in reconstructed space, indicating a successful subtraction of the RSD. Enforcing this provides us with an estimate of the β parameter. As this subtraction may not be perfect, we introduce it as a nuisance parameter in the VGCF model to absorb potential inaccuracies in the reconstruction, targeting instead the AP-distortions parameter ε . The goal is to determine whether the estimate of ε is more precise and accurate in the reconstructed space compared to the redshift space analysis.

It is important to highlight that this analysis is performed on simulated data (described in Section 5.3.1). Since we know the cosmology used to generate these simulations, when Equation (3.14) is used to estimate distances using redshifts we expect that the only distortions present are the dynamic ones. Thus, the analysis is conducted under controlled conditions, with the primary aim of assessing whether the reconstruction can eliminate the RSD and whether the precision of the ε estimate (which we expect to be equal to 1) performed in the reconstructed space is improved compared to the redshift-space analysis.

The results of the analysis are complemented with three tests aimed at assessing the goodness of the reconstruction. The first test, performed entirely in the reconstructed space, is targeted at assessing the ability of the reconstruction procedure and return a VGCF consistent with a value of $\beta = 0$. In the second one, whose goal is to assess the accuracy of the analysis, we compare the parameters β and ε , estimated in reconstructed space, with those estimated—using the same likelihood procedure—in real space. We expect that, if the reconstruction were perfect, the positions of the objects would match the real one and the results of the two analyses, in real and reconstructed spaces, should coincide.

Finally, we performed a third robustness test to assess the sensitivity of the output of the reconstruction to the variation of the input parameters of the algorithm. This allows us to draw conclusions about the influence of these input parameters on the analysis.

6.2 Likelihood analysis

Data vector

For the analysis presented in this Chapter, we make use of the data, halos and void catalogs, presented in Section 5.3.1. The analysis presented here is mainly conducted on a single mock,

referred to as mock 0, although the analysis is accompanied by a robustness test where the entire procedure was performed on all 100 mocks. Additionally, the 100 available mocks are used to calculate the empirical model for the real space VGCF $\xi(r)$, used in the likelihood analysis, and the mock covariance (that is used for a comparison test with the jackknife covariance matrix employed in the analysis above).

The data vector is composed by the three first even multipoles of the void-halo cross-correlation function (that we still call VGCF for simplicity), calculated via the DP estimator described in Section 5.2. The pair counts are evaluated in 25 equally-spaced bins in the range $[0, 3]$ (in void radius units r/R), while the angular separation μ is evaluated in 100 bins between $[0, 1]$. The first three even multipoles of the VGCF are evaluated using Equation (4.22). Particular focus is placed on the quadrupole, as it serves as a key diagnostic tool for understanding the impact of distortions.

The data vector, which we indicate as $\boldsymbol{\xi} = [\xi_0, \xi_2, \xi_4]$ is estimated with the same procedure for real, redshift and reconstructed space.

Covariance matrix

All the analyses performed in this Chapter compare the same type of data vector, $\boldsymbol{\xi}$, with different parameter vectors $\boldsymbol{\Theta}$. Additionally, all analyses use the same type of covariance matrix, which is estimated by jackknife resampling the void catalog obtained from mock 0. We lack of a high number of mock catalogs, but we have a large sample of voids at our disposal, which allows for an estimation of the covariance matrix by employing a jackknife resampling strategy (Hamaus et al., 2020), i.e., $\text{Cov}[\boldsymbol{\xi}]_{ij}$. This methodology relies on ergodicity, which allows us to average measurements across different spatial patches to estimate the covariance matrix. In this approach, we remove one void at a time from the sample when estimating $\xi_\ell(r)$, providing a total of N_V jackknife samples, where N_V is the total number of voids in the catalog. These samples can then be used in Equation (6.1) to calculate $\text{Cov}[\boldsymbol{\xi}]_{ij}$, with an additional normalization factor of $(N_V - 1)$ to account for the statistical weight of the jackknife sample size. The elements of the covariance matrix are computed as follows:

$$\text{Cov}[\boldsymbol{\xi}]_{ij} = \frac{N_V - 1}{N_V} \sum_{k=1}^{N_V} \left(\xi_i^{(k)} - \bar{\xi}_i \right) \left(\xi_j^{(k)} - \bar{\xi}_j \right) \quad (6.1)$$

where the sum runs over the N_V jackknife samples, with the indices i and j referring to the bins of the measured VGCF multipoles. We use the square root of the diagonal elements of the covariance matrix to calculate error bars on our measurements of $\xi_\ell(r)$.

We have opted for a jackknife approach, as this method is commonly used in several recent analyses of voids (Hamaus et al., 2022, 2020; Radinović et al., 2023). However, alternative approaches are also possible. In our case, with access to 100 independent mock catalogs of halos and voids, we can also construct a covariance matrix by combining the individual VGCF measurements as in Equation 6.1, where the mean value $\bar{\xi}$ is estimated by averaging over the measurements in the mocks. We verify and demonstrate in Section 6.4.2 that both approaches yield consistent results.

Likelihood

We performed two different likelihood analyses, involving two different data vectors and models depending whether the data are in redshift space (with RSD) or not (i.e., real and reconstructed space). In the first case, the data vector is created using the measured multipoles of the VGCF in redshift space and is compared with the model obtained from Equations (4.43) and (4.42), presented in Section 4.3.1. The model parameter vector is $\Theta = (\varepsilon, \beta, \mathcal{M}, \mathcal{Q})$.

In the second case we compare data and model in the real and in the reconstructed spaces. In this case the VGCF model is the one described by Equation (4.43), as in the previous case, and the free parameters in the model are $\Theta = (\varepsilon, \beta, \mathcal{M})$, while \mathcal{Q} is fixed at 1. This choice was motivated by the results of a series of tests that indicated that the \mathcal{Q} parameter was poorly constrained in real space analyses, i.e. where RSD are perfectly removed. The decision of fixing the value of \mathcal{Q} while keeping β as a free parameter implies that the latter becomes a proxy of the goodness of the RSD removal procedure when the analysis is performed in the reconstructed space.

The Gaussian likelihood function $\mathcal{L}(\xi|\Theta)$ of the data ξ given the model parameter vector Θ , which can be adapted in the two different scenarios, is:

$$\ln \mathcal{L}(\xi|\Theta) = -\frac{1}{2} \sum_{i,j} (\xi(r_i) - \xi(r_i|\Theta)) \text{Cov}[\xi]_{ij}^{-1} (\xi(r_j) - \xi(r_j|\Theta)). \quad (6.2)$$

For this analysis, we assume uniform priors with $\varepsilon = [0, 2]$, $\beta = [-1, 1]$, $\mathcal{M} = [-10, 10]$, and $\mathcal{Q} = [-10, 10]$. To sample the posterior probability distribution of all model parameters we make use of the affine-invariant Markov chain Monte Carlo (MCMC) ensemble sampler `emcee` (Foreman-Mackey et al., 2019). The quality of the maximum-likelihood model (best fit) is assessed via evaluation of the reduced χ^2 statistics:

$$\chi_{\text{red}}^2 = -\frac{2}{N_{\text{d.o.f.}}} \ln \mathcal{L}(\xi|\Theta), \quad (6.3)$$

where $N_{\text{d.o.f.}} = N_{\text{bin}} - N_{\text{par}}$ indicates the degrees of freedom, with N_{bin} being the number of bins of the data vector and N_{par} the number of free parameters. We use 25 bins for each multipole, leading to a total of 75 bins for the data vector containing monopole, quadrupole, and hexadecapole.

6.3 Results

Our analysis has two main goals. First, we aim to evaluate the effectiveness of the reconstruction algorithm by measuring the deviation of the best fit value of β from zero, i.e. from the value expected for a perfect RSD removal. A value of $\beta = 0$ would indicate that the RSD has been successfully eliminated, signifying a well-functioning reconstruction. All VGCF analyses, including those performed in real space, are affected by uncertainties. To minimize their impact on our tests we have also compared the β values obtained from reconstructed space with those obtained in real space, rather than with zero.

Second, we seek to determine whether the analysis of AP distortions yields a more accurate and precise estimation of the parameter ε in reconstructed space compared to redshift space. We first perform the analysis in redshift space, with the results detailed in Section 6.3.1. Subsequently, we analyze reconstructed space, as presented in Section 6.3.2, where we test the reconstruction and measure ε , followed by a comparative assessment of the parameter estimates obtained in the two analyses. Finally, in Section 6.3.4, we investigate the effect of excluding small-size voids, as in redshift space analyses (Hamaus et al., 2022, 2020), comparing the impact of these exclusions in the two scenarios: redshift and reconstructed space analyses. This exploration includes repeating the analysis in both redshift and reconstructed spaces, using sub-samples of voids obtained by applying a size cut to progressively remove small voids. This demonstrates the strength of our approach in retaining more voids without compromising the reliability of the results.

6.3.1 Results in redshift space

The data vector in redshift space, $\xi^s = (\xi_0^s, \xi_2^s, \xi_4^s)$, contains the multipoles of the VGCF estimated using halos and voids in redshift space. The three multipoles, measured in mock 0 are shown in Figure 6.2, represented by the orange solid line. It can be observed that the quadrupole (central panel), which we focus on to detect the presence of distortions, exhibits an excess of power, showing a positive signal both in the inner regions and near the void ridge, at $r/R \sim 1$. This suggests the presence of outflows, which, in redshift space, have caused these distortions, corresponding to an elongation of the void profile along the LOS.

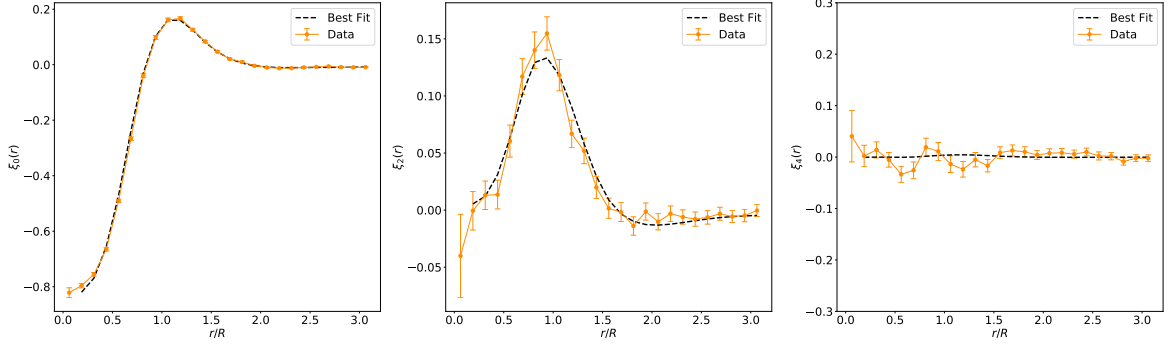


Figure 6.2 Monopole (left), quadrupole (center), and hexadecapole (right) of the VGCF ξ (solid orange line and dots) and best-fit model (dashed black line) for halos and voids in redshift space. Error bars are computed with the diagonal of the jackknife covariance matrix. The central panel shows the evidence of a moment of quadrupole in redshift space, highlighting the presence of RSD.

We performed a full MCMC analysis to fit the model described in redshift space, as described in Section 6.2. The resulting reduced χ^2 of this fit performed using data and model in redshift space is $\chi^2 = 1.57$. The best-fit model is outlined by the dashed black line in Figure 6.2, and seems to well represent the data. The posterior distributions for the model parameters $\Theta = (\varepsilon, \beta, \mathcal{M}, \mathcal{Q})$, are illustrated in Figure 6.3, where dark and light-shaded areas represent the 68% and 95% confidence regions, dashed lines indicate fiducial values of the RSD and AP parameters β and ε , and the top of each column states the mean and standard deviation of the 1-dimensional marginal distributions.

The parameters align with the expected values, represented by the dashed lines, at the 95% probability level. The fiducial value for ε is 1, since in this analysis we know the cosmological parameters (given by the simulation), resulting in the absence of the AP effect. The fiducial value for the parameter β can be calculated via $\beta = f/b$, see Section 5.3.1, yielding a value of $\beta = 0.408$. Additionally, there are no expected values for the nuisance parameters \mathcal{M} and \mathcal{Q} . The posterior distributions of these nuisance parameters do not hold cosmological significance.

Finally, for this analysis in redshift space, where we considered the contribution from all the voids in the sample, we find a value for ε is at 1.5σ from the true expected value, and the parameter ε is estimated with a relative precision of 1.7%.

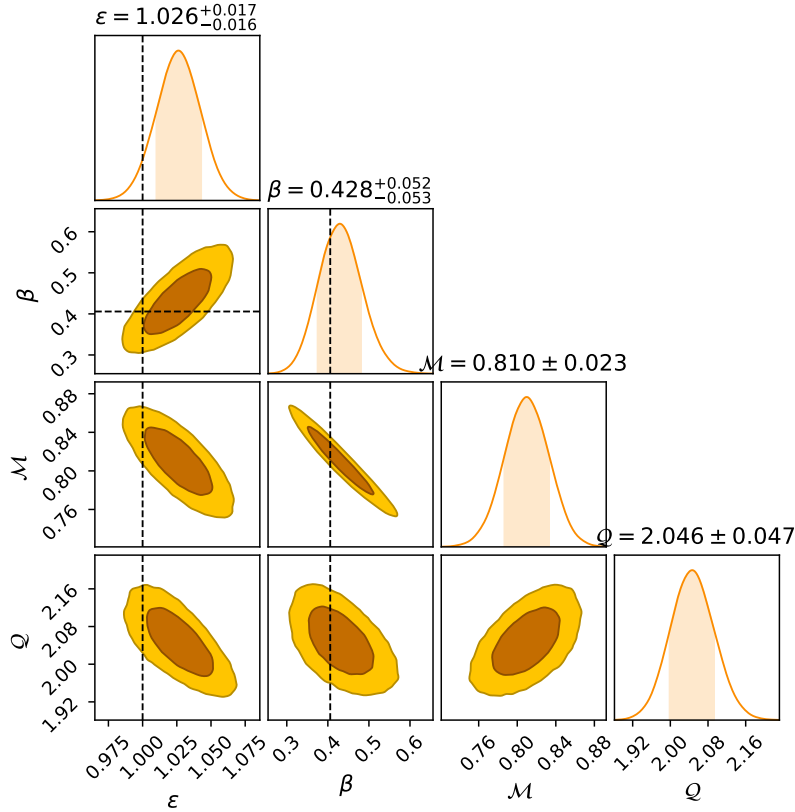


Figure 6.3 Posterior probability distribution of the model parameters that enter in Equations (4.43) and (4.42), obtained via the MCMC from the data measured in redshift space, shown in Figure 6.2. Dark and light-shaded areas represent the 68% and 95% confidence regions, and dashed lines indicate fiducial values of the RSD and AP parameters β and ε . The top of each column states the mean and standard deviation of the 1-dimensional marginal distributions.

The results of our analysis are qualitatively similar to those obtained by Hamaus et al. (2020) and Hamaus et al. (2022). Specifically, it is important to notice that there is a degeneracy between the distortion parameters, ε and β . This is a key point for this analysis, as it demonstrates that the two effects cannot be treated independently of each other. To successfully perform an AP test, it is necessary to account for RSD. In particular, if RSD are eliminated using the reconstruction technique we propose, our goal is to disentangle the two effects.

6.3.2 Results in reconstructed space

The data vector used in the reconstructed space analysis, $\xi = (\xi_0, \xi_2, \xi_4)$ is the same as in the redshift space, with the difference that measurements are performed in the reconstructed space. The measured multipoles are outlined by the blue solid line in Figure 6.4.

In this case, by again focusing on the quadrupole (central panel) as an indicator of distortions, we observe that its amplitude is consistent with zero at all separations, indicating the absence of distortions.

We performed a full MCMC analysis to fit the data with the model with the VGCF model in reconstructed space described in Section 6.2. As anticipated, the nuisance parameter \mathcal{Q} is set equal to 1. The resulting reduced χ^2 of this fit performed using data and model in reconstructed space is $\chi^2 = 1.20$. The best-fit model is outlined by the dashed black line in Figure 6.4, and seems to well represent the data. Additionally, Figure 6.4 shows the theoretical zero quadrupole (central panel, black dotted line) that we expect if the reconstruction has been successful. The measured data are in good agreement with the theoretical prediction, as represented by the black dashed line.

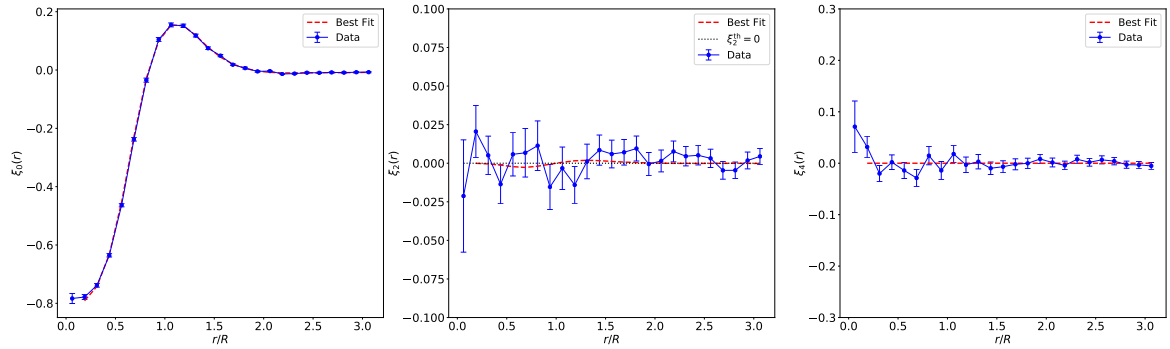


Figure 6.4 Monopole (left), quadrupole (center), and hexadecapole (right) of the VGCF ξ (solid blue line and dots) and best-fit model (dashed red curve) for tracers and voids in reconstructed space. Error bars are computed with the diagonal of the covariance matrix. Dotted black curve in the central panel indicates the zero quadrupole for reference, $\xi_2^{\text{th}} = 0$. The central panel shows a quadrupole consistent with 0, proving the absence of distortions.

The posterior distributions for the model parameters $\Theta = (\varepsilon, \beta, \mathcal{M})$, is illustrated in Figure 6.5, where dark and light-shaded areas represent the 68% and 95% confidence regions, dashed lines indicate fiducial values of the RSD and AP parameters β and ε . The best fit values of each parameter and their 1σ uncertainties are displayed on the top of each 1D marginalized posterior distributions. The best fitting values agree, to within the 68% contours, with the expected values, shown with a dashed line.

The parameter estimates align closely with the expected values at a 68% confidence level. Specifically, the expected value for ε is 1, and that for β is 0. The reconstruction procedure, has successfully removed the RSD resulting in β value in agreement with zero. Consequently, it has also removed the degeneracy between β and ε that was present in the redshift space analysis, as shown in Figure 6.5.

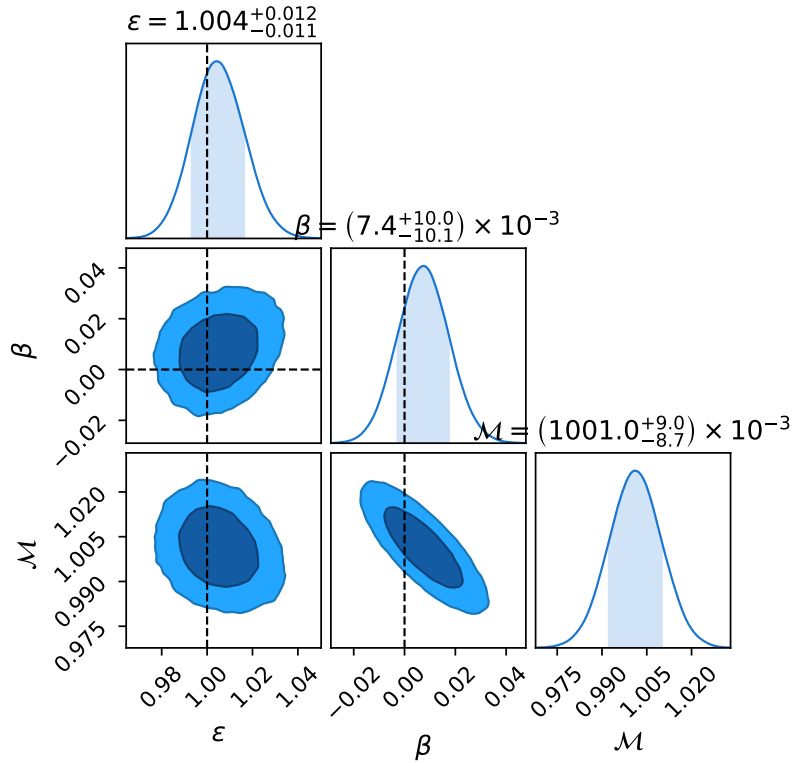


Figure 6.5 Posterior probability distribution of the model parameters that enter in Equations (4.43) and (4.42), obtained via MCMC from the data measured in reconstructed space, shown in Figure 6.4. Dark and light-shaded areas represent 68% and 95% confidence regions, and dashed lines indicate fiducial values of the RSD and AP parameters. The top of each column states the mean and standard deviation of the 1-dimensional marginal distributions.

Finally, we perform a comparison between the analysis in redshift space and reconstructed space, with a focus on the AP parameter. When considering all the voids in the sample, we find that in reconstructed space, the 1σ uncertainty in the estimate of ε decreases from 1.7% to 1.2%, a remarkable 30% precision improvement. Furthermore, the results are more accurate, as in reconstructed space, ε deviates from the true value by only 0.3σ , compared to 1.2σ in redshift space.

6.3.3 Results in real space

Finally, we present the results of the analysis performed in real space, using the exact same likelihood procedure and the VGCF model employed for the reconstructed space. The goal is to conduct a consistency test to check whether the results from these two analyses are in agreement. This is important because, in the case of simulated data where the cosmology is known, reconstructed space should be free from AP distortions, with only RSD present.

After applying the reconstruction, we expect that the VGCF measured in the reconstructed catalog to match that of the real catalog.

Data and best-fit model for the real space VGCF are illustrated in Figure 6.6, with the solid green and the dashed purple curves representing the data and the best-fit model respectively. The zero expected quadrupole for the real space (no distortion) case, is shown in black dotted line for reference. The resulting reduced χ^2 of this fit performed using data and model in real space is $\chi^2 = 0.99$.

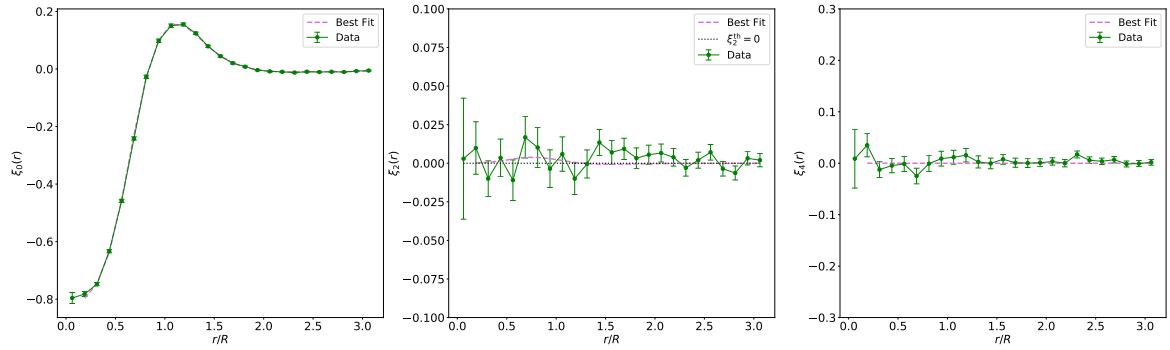


Figure 6.6 Monopole (left), quadrupole (center), and hexadecapole (right) of the VGCF ξ (solid green line and dots) and best-fit model (dashed purple line) for tracers and voids in real space. Error bars are computed with the diagonal of the covariance matrix. Dotted black line in the central panel indicates the zero quadrupole for reference, $\xi_2^{\text{th}} = 0$. As in reconstructed space, Figure 6.4, the central panel shows a quadrupole consistent with 0, proving the absence of distortions.

The posterior distributions for the model parameters $\Theta = (\varepsilon, \beta, \mathcal{M})$, is illustrated in Figure 6.7. For the real space analysis, we obtain the best-fit values for ε and β equal to $\varepsilon = 0.997 \pm 0.011$ and $\beta = 0.008 \pm 0.010$, resulting in a precision on ε of 1.1%, while in terms of accuracy, the real space best-fit value for ε lays at 0.3σ . These results are similar to the ones we obtain with the reconstructed space analysis presented above.

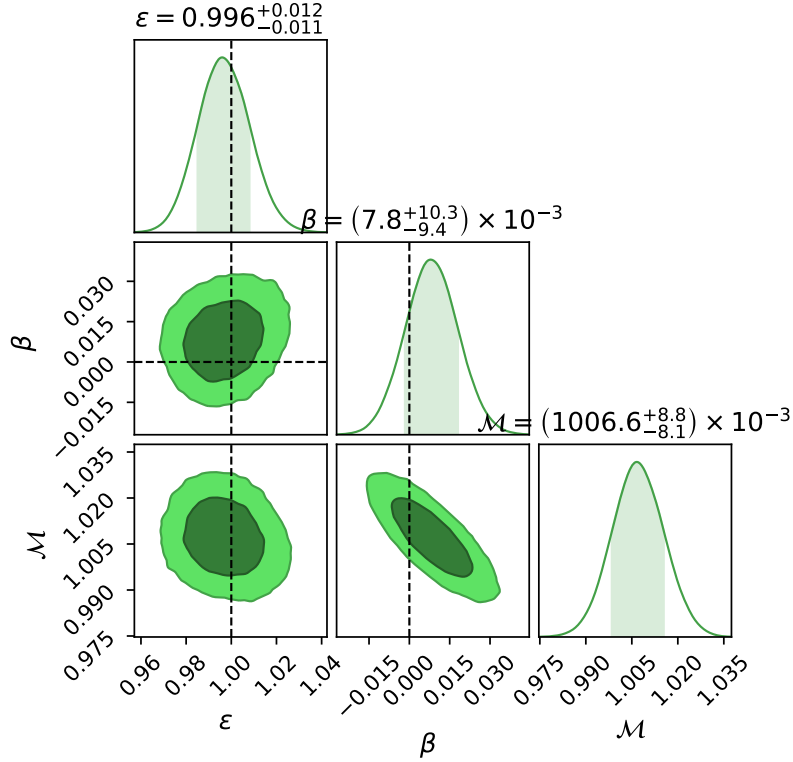


Figure 6.7 Posterior probability distribution of the model parameters that enter in Equations (4.43) and (4.42), obtained via MCMC from the data measured in real space, shown in Figure 6.6. Dark and light-shaded areas represent 68% and 95% confidence regions, and dashed lines indicate fiducial values of the RSD and AP parameters. The top of each column states the mean and standard deviation of the 1-dimensional marginal distributions.

A comparison between the values measured in the three cases (redshift, reconstructed, and real space) is illustrated in Table 6.1.

	$\varepsilon \pm \sigma_\varepsilon$	$\beta \pm \sigma_\beta$
Redshift space	1.026 ± 0.017	0.428 ± 0.053
Reconstructed space	1.004 ± 0.012	0.007 ± 0.010
Real space	0.997 ± 0.011	0.008 ± 0.010

Table 6.1 Table summarizing the values of the parameters ε and β , associated to their estimated errors, for the analyses in redshift, reconstructed, and real space.

6.3.4 Sensitivity to the void size

In the analyses conducted in the previous sections, all voids identified by the VIDE algorithm were included in the VGCF measurements. However, voids analyses typically exclude small voids from the sample; for example, Hamaus et al. (2020) and Hamaus et al. (2022) apply a

cut at 3 times the mean particle separation (mps) of the tracer sample. One reason for this exclusion is that the fraction of spurious voids may be larger in samples of small voids than in those of larger voids, although it never reaches zero, not even when the largest voids are considered (Cousinou et al., 2019). The presence of spurious voids typically reduces the amplitude of the VGCF, particularly that of the quadrupole moment that encodes information of the RSD and AP distortions. A detailed study of the impact of this contamination is deferred to future studies. Here, we address the issue in an indirect way by assessing the sensitivity of our results to the inclusion/exclusion of small scale voids in the sample. The goal is to demonstrate that including voids of progressively small radii, the accuracy in the estimate of ε decreases when the analysis is performed in redshift space, as a result of the increasing difficulty to account for the complex dynamics in these small structures with currently available VGCF models. In contrast, the opposite occurs in reconstructed space, where the constraint on ε remains robust, especially as smaller voids are included. This is because their inclusion increases the statistical signal, thereby improving the precision of the measurement.

Specifically we repeat the analyses performed in the previous section in both redshift and reconstructed space, after removing voids with radii smaller than $R_{\min} = N_s \times r_{\text{mps}}$, where $r_{\text{mps}} = 13 h^{-1}\text{Mpc}$ represents the mean particle separation of the tracers, and N_s is progressively increased from 0.5 to 3 in steps of 0.5.

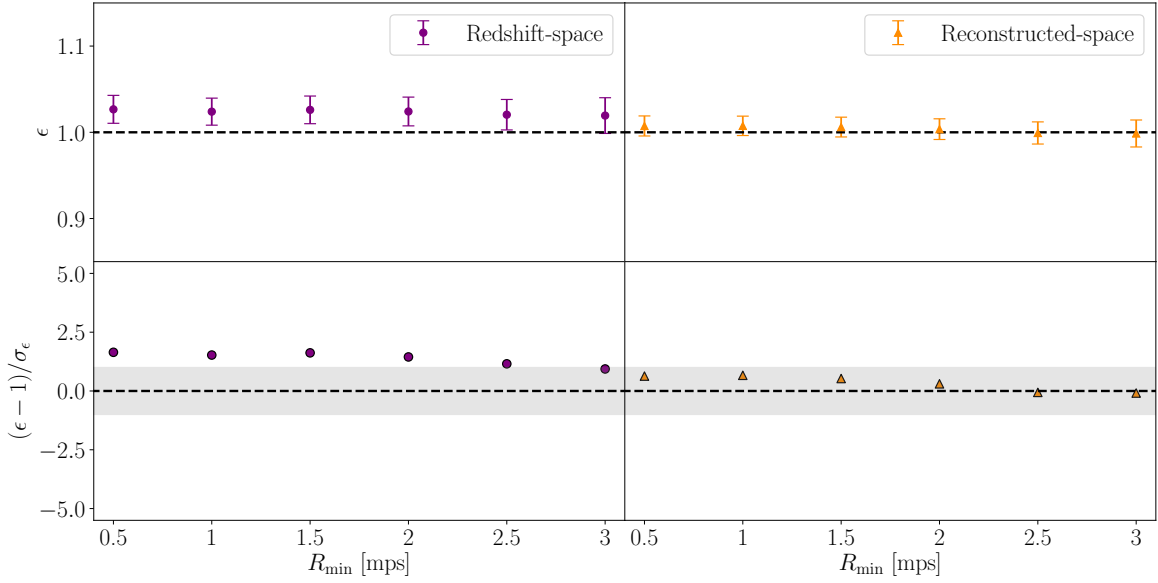


Figure 6.8 *Top panel:* comparison of the values of the AP parameter ϵ with its error σ_ϵ (error bars), obtained with the fitting procedure described in Section 6.2, for the analysis with tracers and voids in redshift-space (purple dots, left panel) and the analysis with tracers and voids in reconstructed space (orange triangles, right panel). Each dot represents the ϵ value as a function of the minimum radius R_{\min} for the voids in that specific subsample, expressed in mean tracer separation (mps) units, used for computing VGCF. *Bottom panel:* comparison of the residuals of ϵ with respect to its expected value 1 in units of its estimated error σ_ϵ , as a function of R_{\min} ; left panel is redshift space analysis and right panel is reconstructed space analysis. The gray horizontal band corresponds the zone of the plot where the residuals are in between -1 and 1.

The results of this test are shown in Figure 6.8 where we plot the values of the best fit ϵ values (upper panels) and its deviation from the expected unity value (bottom panels) in units of the 1σ uncertainty, also shown as error bars in the upper panels, as a function of R_{\min} . The left panels show the results of the analysis in redshift space and those on the right in reconstructed space. The results show that when the VGCF analysis is performed in redshift space the the ϵ parameter is systematically overestimated. As shown in the bottom panel the statistical significance of this overestimate is larger than 1σ when voids with a radius smaller than 2.5 times the mean tracer separation. This result justifies the choice of (Hamaus et al., 2022, 2020) to exclude voids with radii smaller than 3 times the mean tracer separation.

On the contrary, the estimate of the ϵ value obtained from the VGCF analysis in the reconstructed space does not show any significant offset from the expected value for all choices of the R_{\min} cut, including the most extreme case of $R_{\min} = 0.5$ mps.

The possibility to use a larger void sample that include the small ones, significantly reduces the statistical error on ε , i.e. the size of the error bars in the upper panel.

To conclude, by comparing our findings with the threshold commonly used in the literature, $R_{\min} = 3$ mps (Hamaus et al., 2020), we observe that for this sample, the value of ε is $\varepsilon = 1.019 \pm 0.021$, with a precision of 2.1%. In contrast, when analyzing the full sample of reconstructed voids, which does not require such a cut, we obtain $\varepsilon = 1.004 \pm 0.012$ with a precision of 1.2%. It is important to note that cutting at $R_{\min} = 3$ mps in redshift space results in a loss of approximately of $\simeq 60\%$ of voids, compared to using the entire void sample in reconstructed space. This demonstrates that using the reconstruction technique allows access to smaller scales for performing the AP test, enabling us to include all voids in the sample.

6.4 Robustness tests

In this section, we present a series of robustness tests aimed at evaluating the stability and reliability of the VGCF analysis and the estimated parameters ε and β . These tests are essential for verifying the consistency of the results and understanding how the output varies under different conditions.

First, we examine how changes in the input parameters of the reconstruction algorithm affect the VGCF output and the estimated parameters ε and β . Next, we compare the covariance matrix estimated using the jackknife resampling method with the covariance matrix obtained from the mock catalogs, providing further insight into the robustness and reliability of the analysis. Finally, we perform a consistency check by repeating the analyses presented in Sections 6.3.1 and 6.3.2, on 100 available mock catalogs to ensure that the main result, i.e., the reduction of the statistical error when the ε parameter is estimated in reconstructed space rather than in the redshift space, is not a statistical fluke, i.e., the sample variance does not significantly contribute to the total error budget.

These tests are crucial to assess the robustness of our findings and ensuring that the reconstruction method delivers consistent results across different datasets and conditions.

6.4.1 Sensitivity to the choice of parameters that regulate the reconstruction

The reconstruction algorithm described in Section 3.4.1 requires the definition of several input parameters. In this section, we aim to investigate the influence of these parameters,

specifically the radius of the smoothing filter applied to the input density field R_s and the fiducial value of the parameter f , on the results of the VGCF analysis.

To quantify the impact of R_s and f , we use both qualitative and quantitative approaches by analyzing the VGCF measured from halos and void samples obtained after performing different reconstructions using different choices of R_s and f . For each set of input parameters, the reconstructed catalog is regenerated, the void finder is rerun, and assuming the correct cosmology, so that no AP distortion is introduced and a best fit value $\varepsilon = 1$ is expected.

Each of these tests is performed in two steps. First we consider the quadrupole moment and search for deviations from the null signal expected in case of a successful reconstruction. To quantify deviations from a null hypothesis we run a χ^2 test in which the covariant errors are estimated with the jackknife resampling method, described in Section 6.2. Second, we perform a full statistical inference analysis, analogous to the one presented in Section 6.3, to estimate the best fitting values of ε and β .

Sensitivity to the smoothing scale

The reconstruction algorithm described in Section 3.4.1 requires smoothing the input density field with a Gaussian filter. The optimal choice of the smoothing radius R_s depends on the characteristics of the sample, mainly the mean number density of the tracers and their intrinsic clustering properties, and must be evaluated on a case-by-case basis.

The smoothing radius must be sufficiently large to ensure the validity of the Zel'dovich approximation; otherwise, small-scale nonlinear effects would not be effectively removed. However, excessively large smoothing scales would overcorrect for nonlinearities, effectively removing genuine power and systematically underpredicting the amplitude of peculiar velocities. We emphasize that the optimal smoothing scale depends not only on the sample but also on the specific type of cosmic structures considered.

To assess the sensitivity to the choice of R_s , we performed several reconstructions using increasing values in the range $[0, 15]h^{-1}\text{Mpc}$ encompassing a typical nonlinear scale at $\simeq 10 h^{-1}\text{Mpc}$. All reconstructions were performed using the same, correct cosmological model and f values. Voids are then identified in each of the reconstructed catalogs using VIDE, and the VGCF is evaluated with the DP estimator. Since a successful reconstruction is expected to place the halos back to their real-space positions, removing all RSD effects, we use the quadrupole moment ξ_2 as a tool to assess the quality of the reconstruction. A similar test was performed by Nadathur et al. (2019) to optimize the choice of R_s in their reconstruction.

The quantitative test involves evaluating the χ^2 difference between the measured quadrupole and the null signal, using the covariance matrix obtained via jackknife resampling. The values of the χ^2 are computed as follows:

$$\chi^2 = \sum_{i,j} [\xi_2^{\text{data}}(r_i) - \xi_2^{\text{th}}(r_i)] \text{Cov}_{ij}^{-1} [\xi_2^{\text{data}}(r_j) - \xi_2^{\text{th}}(r_j)] , \quad (6.4)$$

where ξ_2^{th} represents the theoretical VGCF quadrupole value expected in absence of distortions, i.e., $\xi_2^{\text{th}} = 0$.

Figure 6.9 illustrates the results of the test. The dots, shown in different colors, represent the VGCF evaluated from halos and void catalogs reconstructed with different smoothing radii, as indicated in the plot. Error bars are computed from the diagonal elements of the covariance matrix. Let us remember the interpretation of the quadrupole: a positive quadrupole indicates that the density profile of the stacked void is squeezed along the LOS, while a negative quadrupole is present when the density profile is elongated along the LOS. Clearly, only the choice $R_s = 5 h^{-1}\text{Mpc}$ results in a quadrupole consistent with zero. For all other choices, a residual quadrupole signal is detected.

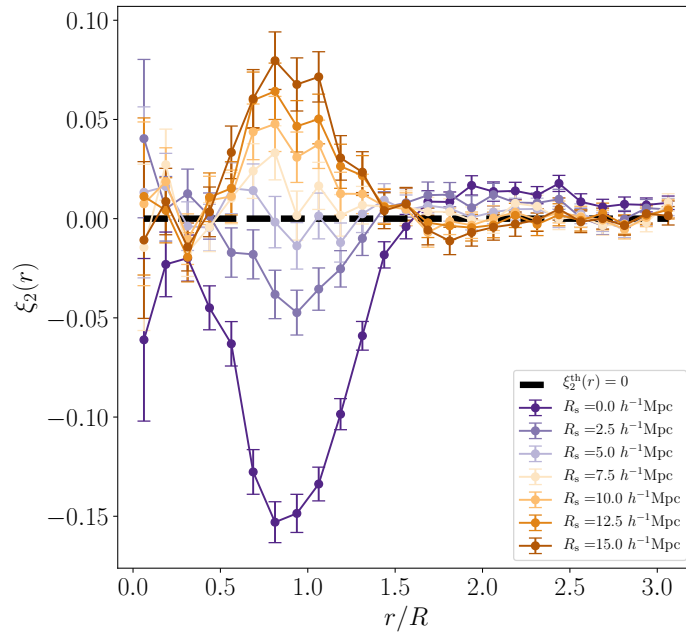


Figure 6.9 Quadrupole of the VGCF computed with reconstructed data, for different choices of the fixed smoothing scale R_s used in the reconstruction procedure. Error bars are computed as the diagonal of the covariance matrix. The choice $R_s = 5.0 h^{-1}\text{Mpc}$ results in an isotropic correlation function, corresponding in a measured quadrupole matching with the dashed black line, which is the expected zero quadrupole $\xi_2^{\text{th}} = 0$. Residual anisotropies are seen for other values of R_s . The quadrupole moment, and consequently the effect of R_s , is accentuated near the edge of the void due to the presence of nonlinearities caused by a higher density contrast.

More specifically, when the smoothing scale is larger than this optimal value, genuine large-scale power is ignored during reconstruction, making it ineffective at removing the coherent motions responsible for the characteristic positive bump near the ridge of the void. Conversely, a smoothing scale that is too small retains small-scale power, leading to the preservation of incoherent nonlinear motions responsible for the negative dip in the quadrupole function. Moreover, when R_s is too small, the density field entering in the reconstruction is the nonlinear one, and this includes some extra modes that can not accurately modeled by the reconstruction. This results in a significant overestimation of velocities, which excessively displaces the galaxies, leading to an inversion of the quadrupole moment—from positive (elongation along the LOS) to negative (compression along the LOS) (Sarpa et al., 2022).

The values of the reduced χ^2 obtained in all the explored cases, as listed in Table 6.2, quantitatively confirm the visual impression of Figure 6.9, indicating that $R_s = 5 h^{-1}\text{Mpc}$ is indeed the best choice for our void-halo correlation study.

$R_s [h^{-1} \text{Mpc}]$	2.5	5.0	7.5	10.0	12.5	15.0
χ^2	2.76	0.90	1.37	2.33	4.13	5.94

Table 6.2 Table of the χ^2 values of the measured quadrupole ξ_2 fitted with the theoretically expected zero quadrupole ξ_2^{th} against different smoothing scales R_s .

As anticipated, we performed a second quantitative test in which we estimate the best fit values for both ε and β obtained at different values of R_s and compared them with the expected values. The results are shown in Figure 6.10. As shown in the right panel, the estimated β parameter is sensitive to the choice of R_s . For values of R_s smaller than the optimal one, nonlinear motions are present and the value of β , which is sensitive to the linear coherent velocities only, is systematically underestimated. For R_s values larger than the optimal one, large scale power is removed from the density field, the Zel'dovich reconstruction is less effective and to compensate the insufficient displacement the β value is overestimated to compensate.

For ε , left panel, the situation is different. This parameter remains more stable than β and stays within a range of two sigma from the true value. In conclusion, this analysis highlights that while β is strongly affected by the choice of the smoothing scale, ε is more robust, though its accuracy still depends on selecting an appropriate R_s .

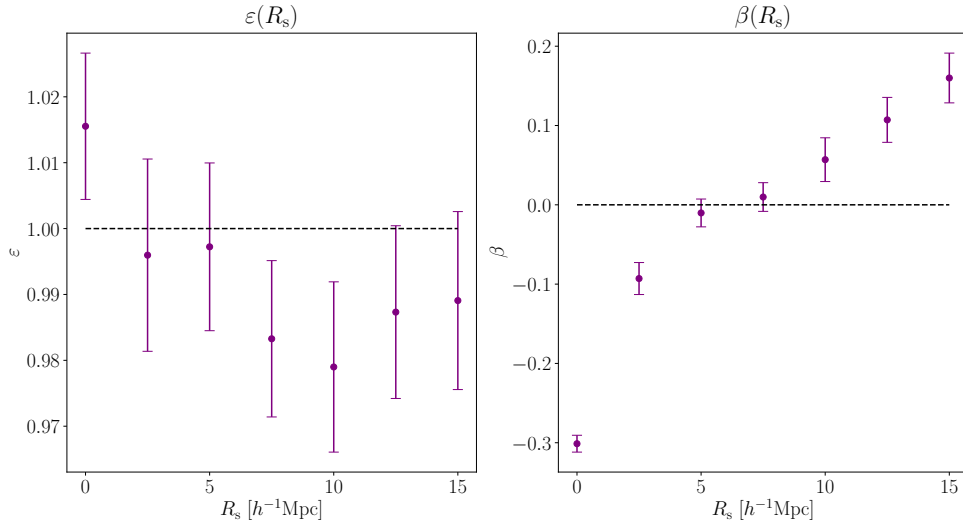


Figure 6.10 Estimated values of the parameters ε (left panel) and β (right panel) for different analyses performed in reconstructed space, each using data reconstructed with a different smoothing scale R_s . The purple dots represent the estimated parameter values for each analysis at a specific R_s , while the black dashed line indicates the expected values, $\varepsilon = 1$ and $\beta = 0$.

Sensitivity to the dynamic distortion parameter β

In this section, we investigate the sensitivity of the reconstruction to an incorrect choice of the β parameter, while assuming the correct cosmological model to convert redshift into distances. In doing this, we are considering β as an independent parameter that is not necessarily obtained from the assumed cosmology.

To establish a sensible range of values where to vary this parameter in this test we proceeded as follows. First, we have set the linear bias value equal to the one estimated from the 2-point autocorrelation of the halos in the mock catalogs, as detailed in Section 5.3.1 and Appendix A. Second, we consider the 5σ uncertainty range for the parameter Ω_m estimated from the Planck analysis of the CMB angular power spectrum (Planck Collaboration et al., 2020) and determine the corresponding range of f values using the Λ CDM relation $f = \Omega_m^{0.55}$. The resulting f range, $[0.728, 0.792]$, encompasses the true simulation value of $f^{\text{true}} = 0.763$, corresponding to a β parameter varying within the range $[0.389, 0.424]$ with a true value of $\beta^{\text{true}} = 0.408$. For each of these cases we ran both the reconstruction and the void-finding algorithm. We calculated the VGCF multipoles using halos and voids identified in reconstructed space. Uncertainties are computed with the jackknife covariance matrices, for each VGCF measurement.

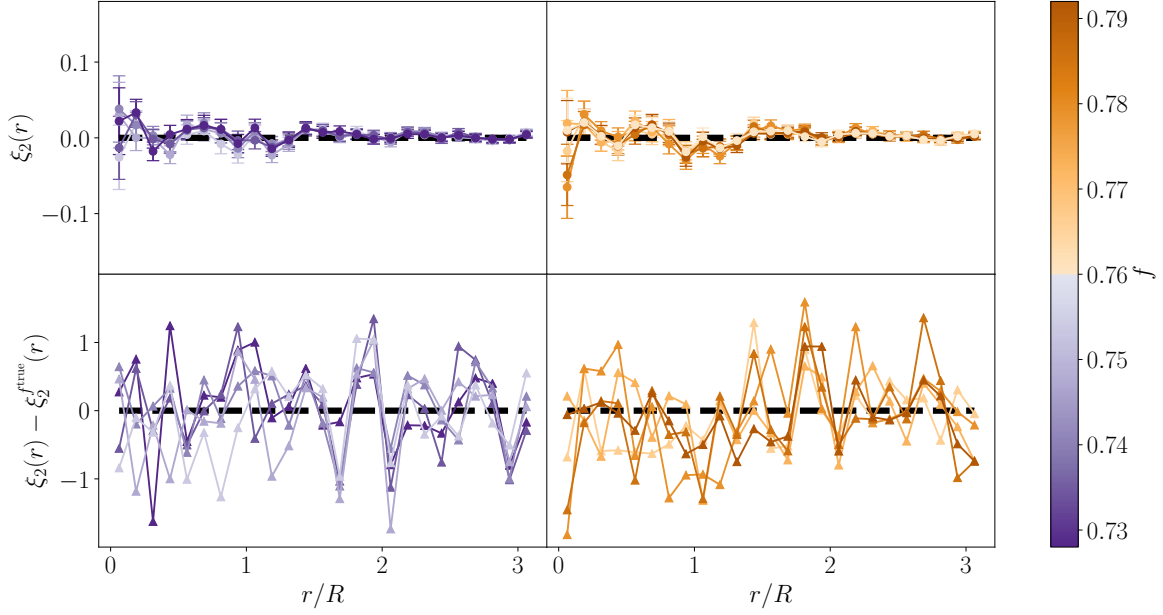


Figure 6.11 *Top panel:* Quadrupole ξ_2 of the stacked void-galaxy cross-correlation function computed with voids and halos in reconstructed space, where reconstruction is computed with different values of f , separating the values of $f < f^{\text{true}}$ (left) and $f > f^{\text{true}}$ (right). *Bottom panel:* Residuals between the quadrupoles of the top panel and the reference quadrupole computed with the fiducial cosmology of the simulation $\xi_2^{f=\text{true}}$, separating the values of $f < f^{\text{true}}$ (left) and $f > f^{\text{true}}$ (right). The color bar indicates the different values of f . Error bars are computed with the diagonals of the covariance matrices.

The top panels of Figure 6.11 show the quadrupole moments computed using different f values in the reconstruction. Different colors, as indicated in the vertical bar, correspond to various choices for f . To avoid overcrowding we separate the reconstructions performed using $f < f^{\text{true}}$ (left) from those performed with $f > f^{\text{true}}$ (right). We again use the quadrupole as a proxy for the quality of the reconstruction, with significant departures from the reference case f^{true} indicating failures in the reconstruction. To facilitate the visual inspection we plot the residuals with respect to the reference case in the bottom panels. Error bars in the top panels are computed from the diagonal element of the individual covariance matrices.

Visual inspection reveals no significant systematic departures from the reference reconstruction and no discernible trend with increasing or decreasing f . The estimated reduced χ^2 values confirm the visual inspection, with most values close to unity and none reaching 2.

We conclude that the results of the VGCF analysis are insensitive to the cosmology assumed in the reconstruction when the f , and consequently β , parameter is varied by approximately 8%, which is consistent with the current uncertainty in relevant cosmological parameters.

Finally, we performed a more quantitative test by comparing the estimated values of the parameters ε and β obtained through the likelihood analysis for each reconstruction using different values of the input parameter f , as shown in Figure 6.12.

When analyzing the behavior of the estimated parameters for different values of f , we find that the results remain quite stable for the various choices of f , which consistently stays centered around its true value ($\beta = 0$). On the other hand, the parameter ε is slightly more sensitive to changes in f , though the estimates still remain within 1σ (or just slightly beyond for the first point on the left). Overall, the results of the analysis in reconstructed space do not appear to be significantly affected by the choice of the input parameter f .

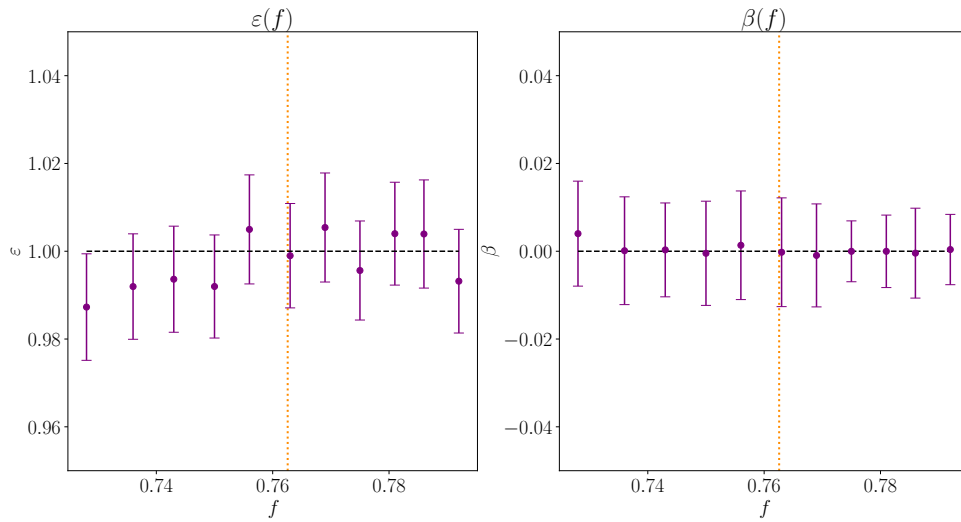


Figure 6.12 Estimated values of the parameters ε (left panel) and β (right panel) for different analyses performed in reconstructed space, each using data reconstructed with a different value of the input parameter f . The purple dots represent the estimated parameter values for each analysis at a specific f , while the black dashed line indicates the expected values, $\varepsilon = 1$ and $\beta = 0$. The orange vertical dotted lines indicate the true value of f .

6.4.2 Sensitivity to the covariance matrices

In the analyses presented in Section 6.3, we opted to utilize the covariance estimated through jackknife resampling. This choice aligns with established practices in the literature and prepares us for future studies where we may lack the necessary mock catalogs to compute the covariance. An alternative method for estimating the covariance matrix involves using the covariance derived from mock simulations; in our case, we have a suite of 100 mocks available. Here, we provide a comparison between these two approaches. The covariance from the mocks was computed in reconstructed space by calculating the multipoles of the

VGCF for all 100 mocks, cross-correlating both voids and halos in reconstructed space, and then determining the covariance of the resulting measurements. We aim to compare the two methods systematically. The first comparison is visual, as shown in Figures 6.13 and 6.14, respectively for the jackknife and numerical estimates, achieved by examining the two normalized covariance matrices defined as:

$$\text{Corr}[\xi]_{ij} = \frac{\text{Cov}[\xi]_{ij}}{\sqrt{\text{Cov}[\xi]_{ii}\text{Cov}[\xi]_{jj}}} . \quad (6.5)$$

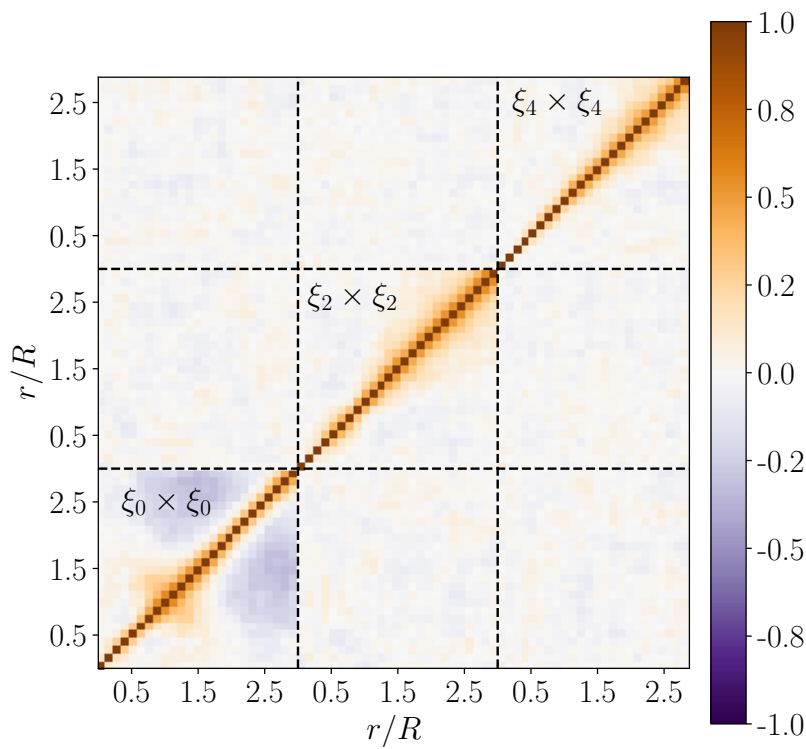


Figure 6.13 Normalized covariance $\text{Corr}[\xi]_{ij}$ obtained from the jackknife resampling.

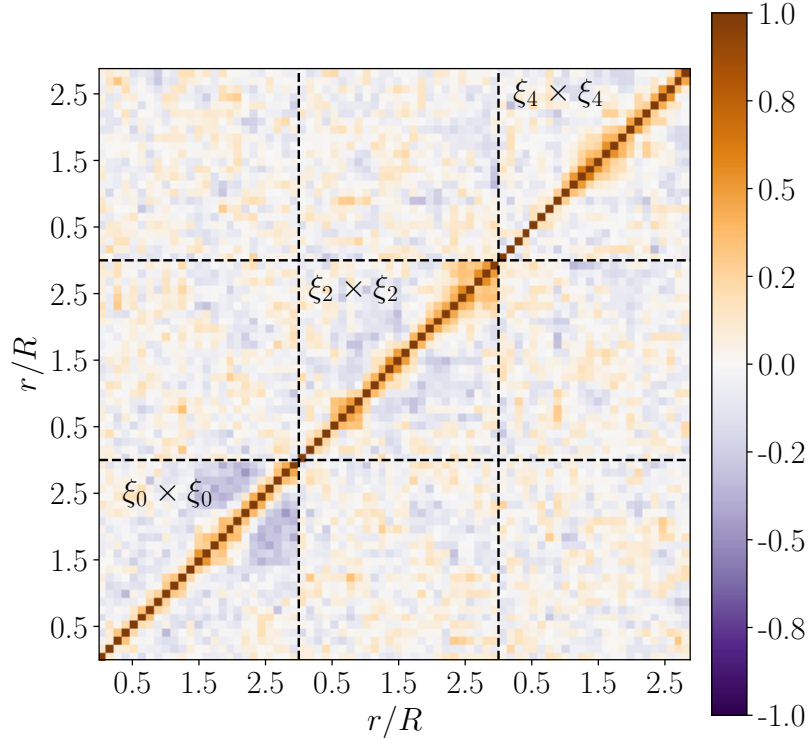


Figure 6.14 Normalized covariance matrix $\text{Corr}[\xi]_{ij}$ obtained from the 100 mocks.

Visually, the two covariance matrices exhibit similarities, particularly in the diagonal elements. However, the covariance derived from the mocks appears noisier in the off-diagonal elements. This discrepancy can be attributed to the relatively small number of mocks (100), which does not allow one to accurately estimate the off-diagonal elements of a 75×75 matrix, being 75 the number of bins utilized in our measurements (25 bins for 3 multipoles), as discussed in Hartlap et al. (2006). Nonetheless, the diagonal elements follow a consistent trend, as shown in Figure 6.15, indicating that both covariance estimations align closely.

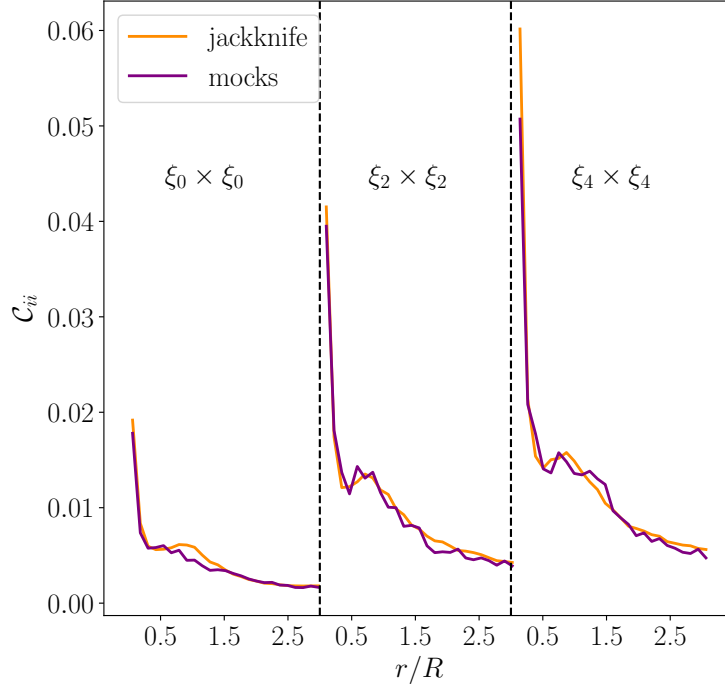


Figure 6.15 Comparison of the elements along the diagonal, C_{ii} of the two covariance matrices, jackknife resampling (orange) and mock covariance (purple). Each panel of the figure represents the diagonal of the i -th multipole as illustrated with the text.

To make this comparison more quantitative we have repeated the same VGCF analysis, in the reconstructed space only, performed in the previous sections using the two matrices. For the numerical covariance, we have applied both the Hartlap (Hartlap et al., 2006) and the Percival (Percival et al., 2010) corrections to rectify the biases induced by the limited number of mocks. The results indicate that the jackknife covariance and mock covariance yield similar posterior probability distributions for all three parameters explored, as depicted in Figure 6.16. Considering all these factors, and acknowledging that jackknife covariance is widely used in the literature, we have chosen to adhere to the latter for our analyses.

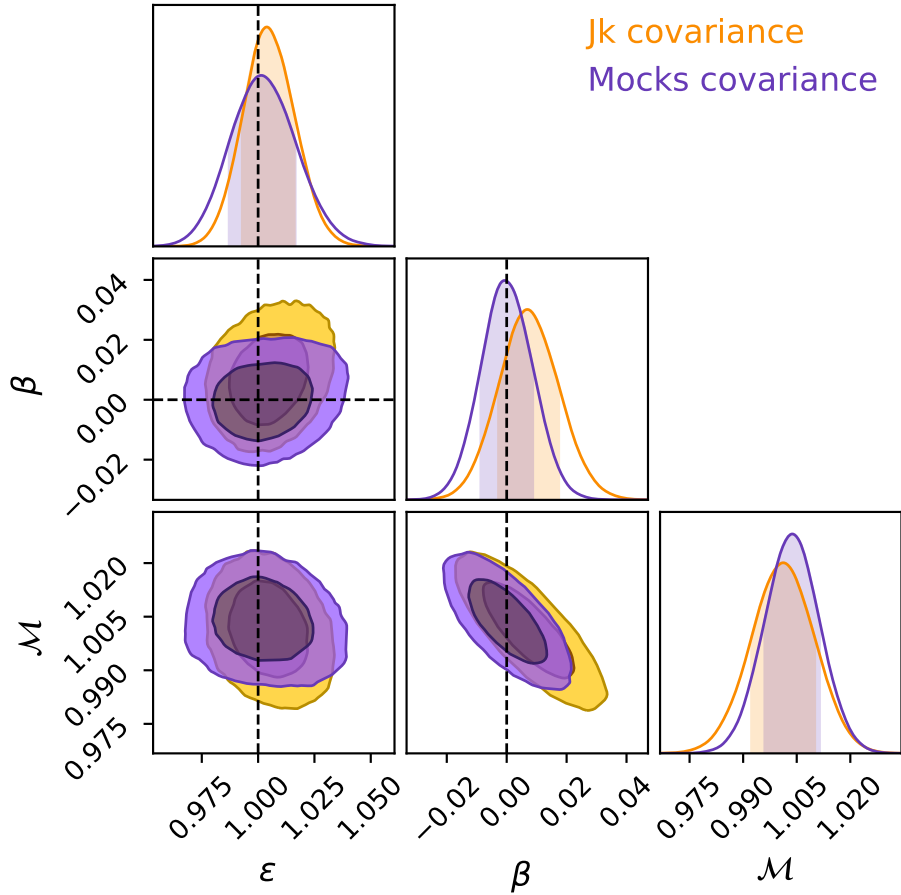


Figure 6.16 Posterior probability distribution of the model parameters computed with the likelihood analysis presented in Section 6.2, from the data of the single mock (mock 0) shown in Fig. 6.4, obtained using two different covariance matrices. Orange: jackknife resampling covariance matrix, and purple: mock covariance matrix corrected with Hartlap and Percival factors. Dark and light-shaded areas represent 68% and 95% confidence regions, and dashed lines indicate fiducial values of the RSD and AP parameters β and ε .

These results also demonstrates that the contribution of the sample variance to the total error budget is negligible. The covariant errors estimated through jackknife technique, that relies on a single realization, significantly underestimate the contribution of the sample variance which, instead, is fully included in the errors estimated from the 100 mocks. This is reassuring since it justifies, a posteriori, the reliability of the analysis presented so far which is based on a single mock catalog, that we now know to be a representative of the cosmic mean.

6.4.3 Consistency test against multiple mocks

To ensure the robustness and consistency of the analysis presented in Section 6.3.2, we extend the study performed on a single mock catalog to a broader set of 100 independent mock realizations. This consistency test allows us to verify that the results obtained from the single simulation are not an outlier and that the methodology is reliable when applied to a larger dataset. By repeating the analysis across multiple simulations, repeating the same steps, we can assess the stability of the estimated parameters and confirm that the findings are statistically sound.

To demonstrate this, we replicate the same type of analysis performed in Section 6.3.2 on the 100 available mocks. We focused on comparing the error estimated from the likelihood analysis for ε in both redshift and reconstructed space. The key takeaway from the analysis is that, with reconstruction, the estimation of ε becomes more precise, leading to smaller error bars compared to redshift space. This is illustrated in Figure 6.17, which shows the distribution of ε errors in reconstructed space versus those in redshift space. As can be seen, the errors from the reconstructed space analysis are consistently smaller than those from redshift space.

The covariance test, as discussed in the previous section, demonstrates that sample variance is negligible for this analysis, making the results from a single mock truly representative. Consequently, this justifies the approach taken here: comparing the errors on ε estimated via the jackknife method (thus disregarding sample variance) for both reconstructed and redshift space, evaluated mock by mock. The results clearly show that the errors estimated in reconstructed space are consistently smaller than those in redshift space, supporting the robustness of this methodology.

In future work, we aim to further investigate this aspect, reproducing the consistency test in more detail to solidify the robustness of the reconstruction process.

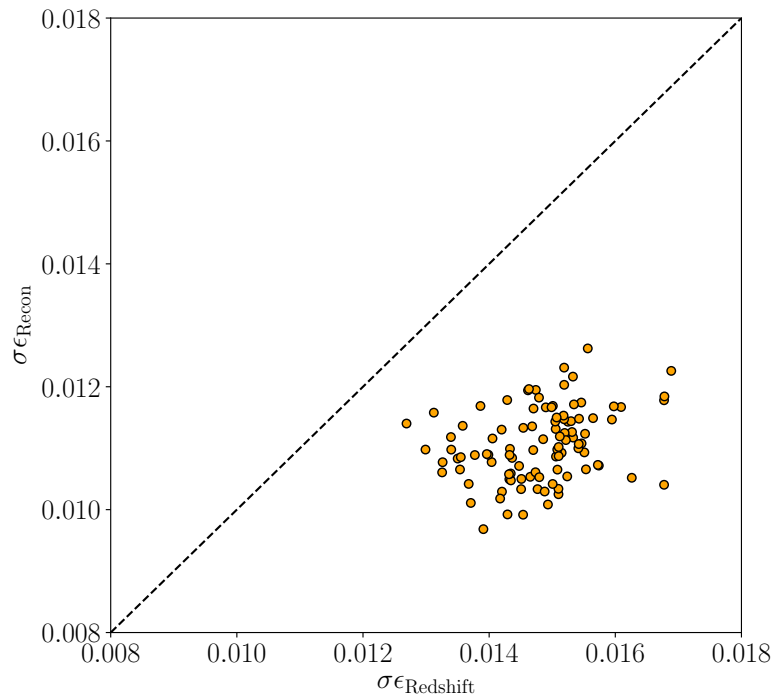


Figure 6.17 Comparison of the error on ϵ estimated from the likelihood analysis for 100 mocks in redshift space (x-axis) and reconstructed space (y-axis). Each point represents the error value from one mock. The figure shows that the errors in reconstructed space are consistently smaller than those in redshift space, highlighting the improvement in precision achieved through the reconstruction process.

7

Cosmology with voids from the Nancy Grace Roman Space Telescope

The content of this chapter is drawn from the paper Verza et al. (2024), submitted to the *American Astronomical Society* journal. This paper presents an analysis aimed at forecasting the expected constraining power of the main void statistics—the void size function and the void-galaxy cross-correlation function—to be measured by the High Latitude Spectroscopic Survey of the Nancy Grace Roman Space Telescope (Wang et al., 2022).

The Roman reference High Latitude Spectroscopic Survey (Roman reference HLSS) from the Nancy Grace Roman Space Telescope, expected to launch no later than May 2027, will cover in its reference design mission 2,000 square degrees with an unprecedented high tracer number density over such a volume¹, therefore providing for the first time a cosmic void sample of exceptional quality down to a few Mpc. Due to the fact that void sizes span a wide range of scales and that a high tracer number density allows a deep sampling of voids, the target population of Roman voids will be complementary to the void populations probed by other past and ongoing spectroscopic galaxy large-scale surveys, effectively opening a new window for cosmic void science.

In this analysis, we investigate the constraining power achievable with void statistics, using light-cone like simulated data that mimic the characteristics of the HLSS survey, within three different cosmological models: Λ CDM, w CDM, and w_0w_a CDM. This work confirms the strong complementarity between different void statistics and demonstrates the constraining power expected from Roman voids, thanks to the combination of high tracer density and large observed volume.

As the second author of this paper, my contribution focused on the analysis of the void-galaxy cross-correlation function analysis.

¹We note that, while the Roman reference HLSS covers 2000 square degrees (Spergel et al., 2015; Wang et al., 2022), the actual survey that the Nancy Grace Roman Space telescope will execute will be decided in an open community process, and may cover an even greater cosmic volume.

7.1 The void-galaxy cross-correlation function

7.1.1 Likelihood analysis

Data vector

In this sub-section we present measurements and the likelihood analysis of the VGCF. In this analysis the measurements are performed using the `VoIager`² publicly available package, which provides a pipeline to perform cosmological analyses using voids identified in large-scale structure survey data. This code measures dynamic and geometric shape distortions in void stacks and propagates the measurement down to constraints on cosmological parameters using Bayesian inference.

The data vector is represented by the VGCF measured in redshift space. As thoroughly discussed in Section 4.3, this function is anisotropic along the LOS, and is therefore two-dimensional, $\xi^s(s_\perp, s_\parallel)$. By re-writing the s_\perp and s_\parallel quantities in term of s and $\mu_s = s_\parallel/s$, it is possible to decompose the VGCF into multipoles as in Equation (4.22), that we rewrite with a slightly different notation:

$$\xi_\ell^s(s) = \frac{2\ell + 1}{2} \int_{-1}^1 \xi^s(s, \mu_s) \mathcal{P}_\ell(\mu_s) d\mu_s. \quad (7.1)$$

We note, however, that in linear theory this quantity is expected to be identically null, Equation (4.38), therefore its interpretation in terms of distortions of the void shape involves higher-order effects.

Even if the multipole decomposition provides a clear physical interpretation, actually for VGCF analyses it is possible to rely on either the 2D cross-correlation function $\xi^s(s_\perp, s_\parallel)$ for model fitting with coordinates along and perpendicular to the LOS (this will, of course, include information on both RSD and AP), or on the decomposition into multipoles of the Legendre polynomials. Here we use the 2D cross-correlation function, since this provides a better balance for the number of bins that sample the inner core of voids with respect to the bins sampling the slope of the void profile (inner bins are more strongly impacted by noise in e.g. the deprojection), but we also provide the multipoles corresponding to $\ell = 0, 2, 4$, for completeness.

For our estimation of the VGCF $\xi^s(s_\perp, s_\parallel)$ we use the Landy-Szalay estimator, Equation 5.4 presented in Section 5.2. The pair counts are binned in s_\perp and s_\parallel . We implemented a fixed binning scheme based on the effective void radius for each individual void, expressing all distances in units of the void radius R_{eff} . Normalizing the void-galaxy distance with

²<https://voIager.readthedocs.io>

respect to the void radius is crucial to coherently overlap regions of similar density, and to enhance the topology of voids, such as the compensation wall, making our observable ideal to extract cosmological information (Hamaus et al., 2022, 2014, 2017, 2020). The catalogs of random voids and galaxies is characterized by the same redshift dependence of the distributions of voids and galaxies, respectively, as measured in the simulated light-cone, except for the normalization, given by the total number of objects (see Section 5.3.2).

Covariance matrix

The covariance matrix:

$$\mathbf{C}_{ij} = \left\langle \left(\xi^s(\mathbf{s}_i) - \langle \xi^s(\mathbf{s}_i) \rangle \right) \left(\xi^s(\mathbf{s}_j) - \langle \xi^s(\mathbf{s}_j) \rangle \right) \right\rangle, \quad (7.2)$$

quantifies the uncertainty of the measured VGCF $\xi^s(s_\perp, s_\parallel)$. In this equation, angled brackets denote the ensemble average of measurements. Since we lack of a large enough number of mock catalogs for a precise estimate of the numerical covariance, we estimate the covariance matrix, \mathbf{C}_{ij} , via the jackknife technique, as in Section 6.2. The jackknife method is implemented by measuring ξ^s through Equation (5.4) several times, by excluding one (non-overlapping) void at a time. In this way we obtain N_v samples, where N_v is the total number of voids, to estimate the corresponding covariance \mathbf{C}_{ij} . This methodology has undergone testing on simulations and validation on mocks in prior analyses (Cai et al., 2016; Correa et al., 2019; Hamaus et al., 2022, 2020; Paz et al., 2013). We note that previous work showed that the Hartlap correction (Hartlap et al., 2006), for systematic biases due to the finite number of independent samples, is expected to be negligible (of a few percent level, see Hamaus et al., 2022), given the number of subsamples, N_v . It has been demonstrated that, in the limit of large sample sizes, the jackknife technique produces consistent covariance estimates compared to those derived from numerous independent mock catalogs (Favole et al., 2021). Any residual discrepancies between the two methods suggest a slight overestimation of covariances by the jackknife approach, thereby rendering our error forecast conservative.

Model

Following Hamaus et al. (2022, 2020), we adopted the empirically motivated model of the VGCF in redshift space illustrated by Equation (4.41) together with the mapping between redshift and real space, represented by Equation (4.42), which introduce the presence of the two nuisance parameters, \mathcal{M} and \mathcal{Q} .

Moreover, since the real-space quantities $\xi(r)$ are not known, we rely on the deprojection technique on the VGCF integrated along the LOS in redshift space, $\xi_p^s(s_\perp)$ presented in Section 4.3.1.

Likelihood From the data vector of Equation (5.4), and the theoretical model from Equations (4.41) and (4.42), we can express the corresponding Gaussian likelihood $L(\hat{\xi}^s|\Theta)$ of the data $\hat{\xi}^s$ considering the model parameter vector $\Theta = (\beta, \varepsilon, \mathcal{M}, \mathcal{Q})$:

$$\ln L(\hat{\xi}^s|\Theta) = -\frac{1}{2} \sum_{i,j} \left(\hat{\xi}^s(\mathbf{s}_i) - \xi^s(\mathbf{s}_i|\Theta) \right) \mathbf{C}_{ij}^{-1} \left(\hat{\xi}^s(\mathbf{s}_j) - \xi^s(\mathbf{s}_j|\Theta) \right).$$

We evaluate the posterior probability distribution by running MCMC analyses with publicly available `emcee` (Foreman-Mackey et al., 2019) Python package. We assess the quality of the maximum-likelihood model (best fit) relying on the evaluation of the reduced χ^2 statistic:

$$\chi^2 = -\frac{2}{N_{\text{dof}}} \ln L(\hat{\xi}^s|\Theta), \quad (7.3)$$

where the number of degrees of freedom is $N_{\text{dof}} = N_{\text{data}} - N_{\text{par}}$, with N_{data} the number of bins and N_{par} the number of free parameters.

In each redshift bin, the data array $\xi^s(s_\perp, s_\parallel)$ is measured in bins of s_\perp and s_\parallel . We consider 18 linearly equi-spaced bins in each of the two dimensions, resulting in $N_{\text{bin}} = 18 \times 18 = 324$ bins. It follows that $N_{\text{dof}} = 320$ in each of the considered redshift bins, as $N_{\text{par}} = 4$. On the one hand this number is much lower than the number of voids per redshift bin considered, therefore guaranteeing enough statistics for a robust estimate of the corresponding covariance matrix, Equation (7.2); on the other hand, N_{bin} is large enough to resolve the features of the 2D VGCF.

7.1.2 Results

The VGCF analysis was conducted using the void sample extracted with `VIDE`, a total of $N_v = 82551$ voids, divided into three redshift bins of equal number of voids each, as explained in Section 5.3.2. Specifically, for the study of the VGCF, the voids underwent post-processing, where a purity cut was applied to avoid the inclusion of spurious Poissonian voids. The cut follows:

$$R_{\text{eff}} > N_s \left(\frac{4\pi}{3} n_g(Z) \right)^{-1/3}, \quad (7.4)$$

where Z represents the redshift of void centers, and the parameter N_s sets the minimum void size in units of the average tracer separation. A void catalog with a low N_s value may be

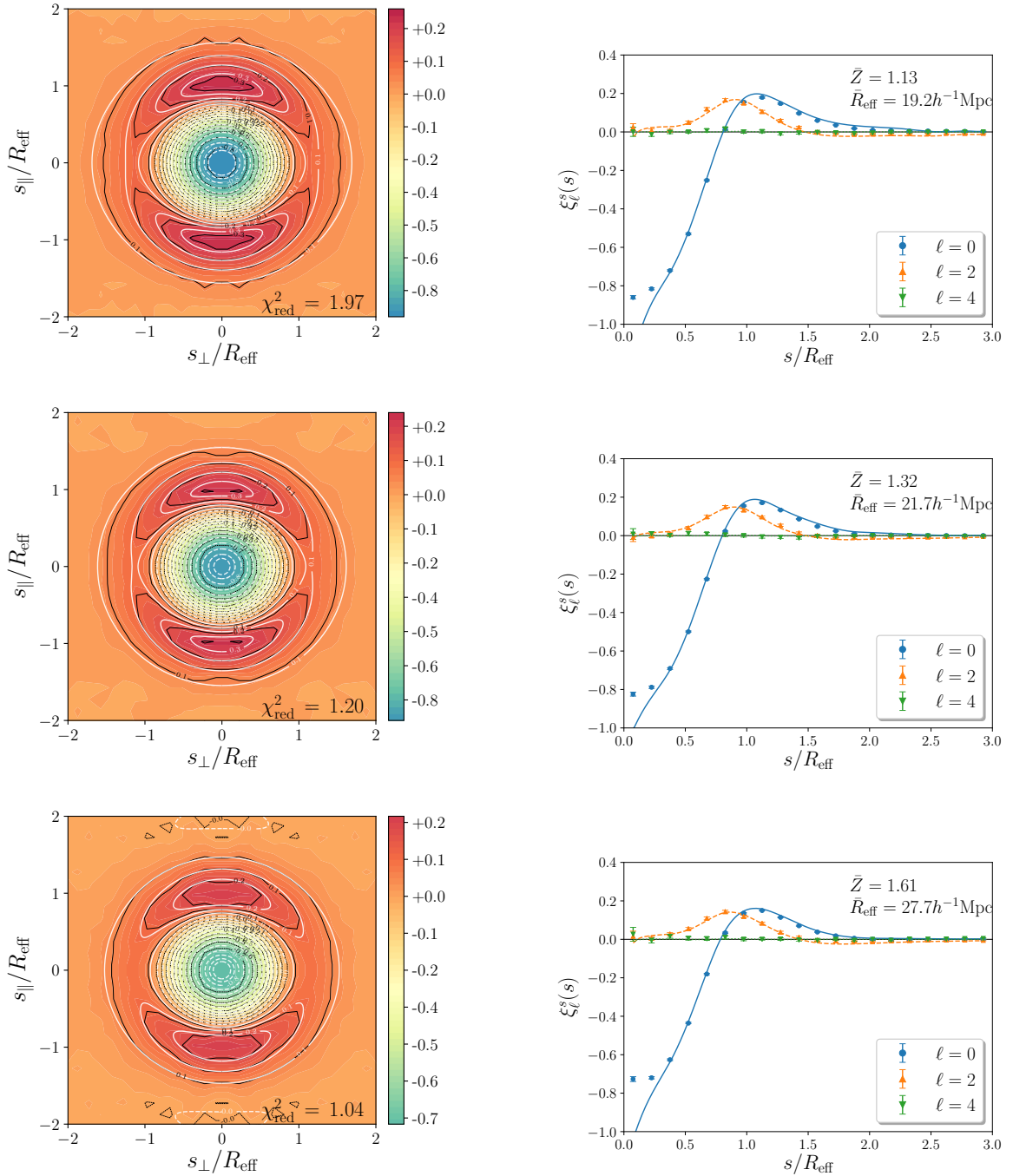


Figure 7.1 Void-galaxy cross-correlation function in redshift space. Left: $\xi^s(s_{\perp}, s_{\parallel})$ in 2D (color scale with black contours) and best-fit model from Equations (4.41) and (4.42) (in white contours). Right: monopole (blue dots), quadrupole (orange triangles) and hexadecapole (green wedges) of $\xi^s(s_{\perp}, s_{\parallel})$ with their best-fit model (solid, dashed, dotted lines). The mean void redshift, \bar{Z} , and effective radius, \bar{R}_{eff} , of each redshift bin are indicated.

prone to stronger spurious void contamination, i.e. voids misidentified due to the sparsity of tracers, Fingers-of-God, or other systematic effects (Correa et al., 2021, 2022; Cousinou et al., 2019; Neyrinck, 2008; Pisani et al., 2015b). On the other hand, a high N_s value can drastically reduce the statistical relevance of the void sample. Choosing the optimal N_s is a trade off between these two effects. In this VGCF analysis, we adopt $N_s = 3$, resulting in a final sample of $N_v = 67158$ voids with a minimum effective radius of $8.0 h^{-1} \text{Mpc}$.

To compute the model for the likelihood analysis via Equations (4.41) and (4.42), it is essential to determine the stacked density profile or VGCF in real-space, $\xi(r)$. This can be achieved using the deprojection technique outlined in Section 4.3.1.

We use `Voiager` to compute the LOS integration of $\hat{\xi}^s(s_\perp, s_\parallel)$ obtaining $\xi_p^s(s_\perp)$. From this quantity we then obtain $\xi(r)$ via the deprojection technique, Equation (4.35). Integration is performed by interpolating both $\xi_p^s(s_\perp)$ and $\xi(r)$ with a cubic spline. Figure 7.2 illustrates the results for $\xi(r)$ (orange triangles interpolated with dotted line) for each of the three redshift bins, together with the projected void-galaxy cross-correlation function $\xi_p^s(s_\perp)$ in redshift space (green wedges, interpolated with dashed line) and the redshift-space monopole $\xi_0^s(s)$ (blue dots) with its best-fit model (blue solid line) based on Equations (4.41) and (4.42), which is shown for comparison. The statistical noise that could be introduced by the deprojection technique is minimal, due to the large number of voids. However, some residual noise is observed in the innermost bins, where separations from the void center are small and tracers are also sparser, which affects the accuracy of the deprojection and the subsequent spline interpolation (Hamaus et al., 2020; Pisani et al., 2014). Consequently, we omit the first radial bin from our model fits. To calculate the model for $\xi(r)$ with the deprojection technique, we rely on the data, which introduces its own covariance, leading to a correlation with $\hat{\xi}^s(s)$. Nevertheless, the model considered, Equation (4.41), considers the amplitude of the VGCF as a free parameter, \mathcal{M} . The results are therefore conservative, since any correlation between data and model would reduce the total covariance in our likelihood estimation. Besides the deprojection technique presented here, other methods can be used to obtain the $\xi(r)$ in real space. Other studies employ a numerical model based on the measurements of the monopole obtained from simulated data in real space, where available (Nadathur et al., 2020b; Radinović et al., 2023). Alternatively, theoretical models could also be used (Verza et al., 2024). By using theoretical models, we could eliminate the potential dependence on the cosmology of the mock data, which would otherwise be introduced when relying on mocks to compute the real-space model. On one hand the use of a full theoretical model can increase the constraining power; on the other hand the model-free methodology explored in this analysis ensures its robustness, as it is less affected by biases related to unknown systematic effects or potential dependencies on the cosmology of the mock data.

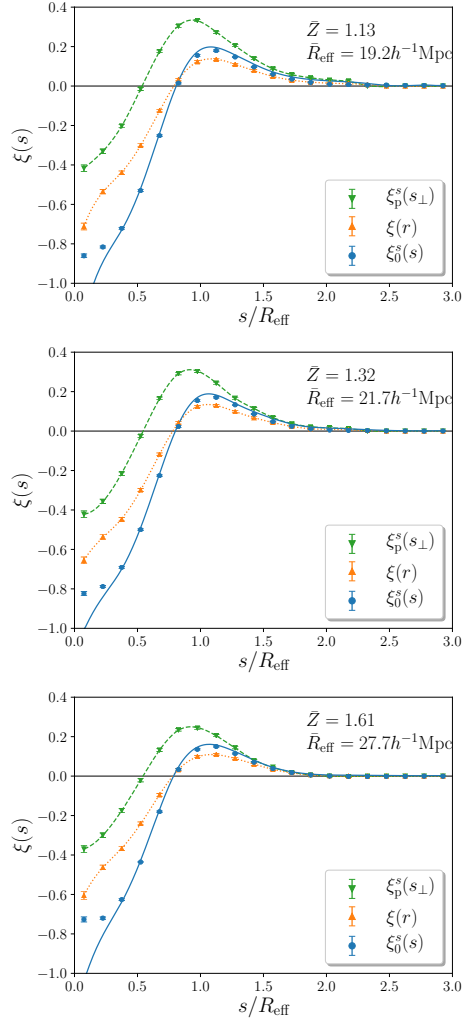


Figure 7.2 Projected void-galaxy cross-correlation function $\xi_p^s(s_\perp)$ in redshift space (green wedges, interpolated with dashed line) and its real-space counterpart $\xi(r)$ in 3D after deprojection (orange triangles interpolated with dotted line). The redshift-space monopole $\xi_0^s(s)$ (blue dots) and its best-fit model based on Equations (4.41) and (4.42) are shown for comparison (solid line). Adjacent bins in redshift increase from top to bottom, with mean void redshift, \bar{Z} , and effective radius, \bar{R}_{eff} , as indicated in each panel.

The data vector in redshift space is constructed using the 2D VGCF, $\xi^s(s_\perp, s_\parallel)$, estimated with the Landy-Szalay estimator. The measurements are performed across three different redshift bins, as presented in Section 5.3.2. The resulting VGCF, along with the corresponding multipoles (dots, triangles, and wedges), are shown in Figure 7.1. We conducted a full MCMC analysis to fit the model described by Equations (4.41) and (4.42) obtaining the marginalized 2D and 1D posterior distributions for the model parameters $\Theta = [f/b, \varepsilon, \mathcal{M}, \mathcal{Q}]$ as illustrated in Figure 7.3. For each MCMC analysis we explore 16 walkers. We then post-process the chains by removing the first 10% of the steps. To ensure that different steps are uncorrelated,

we consider one chain-step every $\tau_{\max}/2$, where τ_{\max} is the maximum value of the multi-dimensional time-covariance of the chain, computed with the Goodman and Weare (2010) estimator. The resulting length of the chains in the three redshift bins is $\sim 4 \times 10^5$. This resulted in a reduced $\chi^2 = 1.97, 1.20, 1.04$ in the three redshift bins, respectively.

We note that the VGCF is sensitive to the growth rate of cosmological perturbations via f/b and to the expansion history of the universe via ε . This observable is also sensitive to other cosmological parameters, such as σ_8 and h . However, the ability to constrain these other quantities depends on the specific VGCF model. In this Chapter we considered a model-independent approach, which exclusively probes a subset of background parameters in a robust and unbiased way, through the AP test.

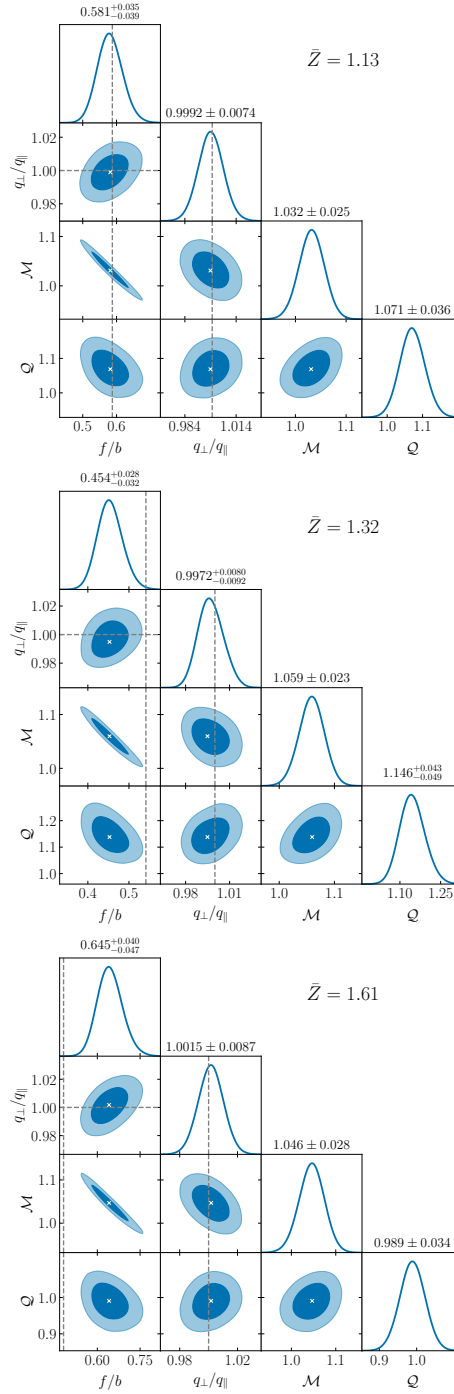


Figure 7.3 VGCF: posterior probability distribution of the model parameters that enter in Equations (4.41) and (4.42), obtained via MCMC from the data shown on the left of Figure 7.1. Dark and light-shaded areas represent the 68% and 95% CL, with a cross marking the best fit, dashed lines indicate fiducial values of the RSD and AP parameters. The top of each column states the mean and standard deviation of the 1D marginal distributions. Adjacent bins in void redshift with mean value \bar{Z} increase from top to bottom, as indicated.

The best-fit $\xi^s(s_\perp, s_\parallel)$ are shown as white contours in the 2D VGCF plots in Figure 7.1. For reference, the corresponding multipole models are also plotted in the panels on the right side. The best-fit models appear to match the data well down to small scales. Our results confirm those correlations found by Hamaus et al. (2020) and Hamaus et al. (2022). Specifically, we observe a degeneracy between ε and β , and a strong correlation between β and \mathcal{M} . The true values, represented by dashed lines in Figure 7.3, are computed as follows. To compute the true value of β , both the values for $f(z)$ and $b(z)$ are required. The growth rate f is computed via

$$f(z) \simeq \left[\frac{\Omega_m(1+z)^3}{H^2/H_0^2} \right]^\gamma, \quad (7.5)$$

with a growth index $\gamma \simeq 0.55$ (Lahav et al., 1991; Linder, 2005), and Ω_m and H_0 are provided by the simulation. For the bias $b(z)$ we assume the relation in Wang et al. (2022). The parameter ε is expected to be equal to 1, as we used the cosmology of the simulation to convert angles and redshifts into distances, introducing no AP effect. The parameters \mathcal{M} and \mathcal{Q} do not have specific values, and their distribution is not relevant to the cosmological interpretation of the posteriors (given their use to account for potential biases due to e.g. spurious voids contamination and noise in the deprojection).

\bar{Z}	b	$\varepsilon \pm \sigma_\varepsilon$	$\beta \pm \sigma_\beta$	$f\sigma_8 \pm \sigma_{f\sigma_8}$	$D_A H/c \pm \sigma_{D_A H/c}$
1.13	1.518	0.999 ± 0.007	0.581 ± 0.037	0.413 ± 0.026	1.607 ± 0.012
1.32	1.687	0.997 ± 0.009	0.454 ± 0.031	0.333 ± 0.022	1.980 ± 0.017
1.61	1.945	1.001 ± 0.009	0.645 ± 0.044	0.489 ± 0.033	2.622 ± 0.023

Table 7.1 VGCF: forecasted constraints on RSD and AP parameters ε , β , $f\sigma_8$, and $D_A H/c$ (mean values with 68% CL). Results are given in three redshift bins with mean \bar{Z} , and large-scale galaxy bias b .

The relative precision of both β and ε measurements, varies across the redshift bins, with values ranging from 6.4% to 6.8% for β and from 0.7% to 0.9% for ε . Notably, ε is measured with high precision and accuracy in all redshift bins, with deviations of only $0.1\sigma_\varepsilon$ to $0.3\sigma_\varepsilon$ from its true value. We note that for f/b some discrepancies may arise—observable here thanks to the high statistical power of the Roman void sample leading to tight error bars—and that could lead to biases in the inferred $f\sigma_8$ due to two reasons. First, the effective bias parameter of the selected mock galaxy sample can be different from its large-scale counterpart (obtained by taking the ratio of galaxy-galaxy 2PCF and $P(k)$ averaged over a suitable range of scales, see Appendix A), especially when small size voids are included in the sample (Pollina et al., 2017; Verza et al., 2022). Second, projection effects in the parameter space, due to the strong degeneracy between f/b and \mathcal{M} , can affect the inferred value of $f\sigma_8$. It is important to note that these deviations in β do not significantly affect the

overall quality of the fit. This is primarily due to the role played by the nuisance parameters \mathcal{M} and \mathcal{Q} , which help to mitigate the impact of the deviations in β without substantially influencing the precision or accuracy of ε .

From the posteriors of $\beta \equiv f/b$ and $\varepsilon \equiv q_{\perp}/q_{\parallel}$, it is possible to derive constraints on $f\sigma_8$ and $D_A H$. For the former, we assume that the amplitude of $\xi(r)$ is proportional to $b\sigma_8$, and thus we multiply f/b by the underlying value of $b\sigma_8$ provided by the mock. Additionally, we assume that the relative precision on f/b and $f\sigma_8$ is the same. Furthermore, we neglect the dependence on h , which enters into the definition of σ_8 and should ideally be marginalized over (Sánchez, 2020). For the latter case, we compute $D_A H$ by multiplying ε by the fiducial $D_A H$, following Equation (4.7).

We summarize all the results in Table 7.1. As expected, the discrepancies observed in the values of β in the second and third redshift bins propagate to the estimated values of $f\sigma_8$.

The measurements of $f\sigma_8$ and $D_A H$ as a function of redshift can be used to constrain cosmological models, for example, focusing on the latter, we can access cosmological parameters by inverting Equations (1.38) and (1.28), that we rewrite for simplicity here (for the case of a flat universe), in a generalized expression:

$$D_A(z) = \int_0^z \frac{c}{H(z')} dz', \quad (7.6)$$

$$H(z) = H_0 \sqrt{\Omega_m(1+z)^3 + \Omega_{\text{de}}(1+z)^{3(1+w_0+w_a)} F(z)}, \quad (7.7)$$

where

$$F(z) = e^{-3w_a z/(1+z)}, \quad (7.8)$$

H_0 is the present-day Hubble constant, Ω_m is the matter density parameter, and Ω_{de} is the dark energy density parameter (with $\Omega_{\text{de}} \equiv \Omega_{\Lambda}$ in the Λ CDM model). The parameters w_0 and w_a describe the dark energy equation of state.

For this analysis we adopt three different cosmological models: Λ CDM, w CDM, and $w_0 w_a$ CDM. These models serve as our fiducial frameworks. In the following results, we focused on the constraints obtained from the product $D_A(z)H(z)$, as these measurements currently provide the most precise and accurate results. For the first model, Λ CDM model, the parameter space is $\Theta = [\Omega_m]$, probed by the AP test. We use flat priors for Ω_m in the range (0.15, 0.65). The second model is the w CDM model, with parameters $\Theta = [\Omega_m, w]$, combining the Λ CDM priors with a flat prior on w in the range $(-3, 2)$. The third model is the $w_0 w_a$ CDM model, with parameters $\Theta = [\Omega_m, w_0, w_a]$, and flat priors identical to those of w CDM, along with w_a in the range $(-8, 5)$.

Model	Ω_m	w_0	w_a
Λ CDM	$0.308^{+0.007}_{-0.009}$	-1	0
w CDM	$0.303^{+0.013}_{-0.015}$	$-1.05^{+0.25}_{-0.27}$	0
w_0w_a CDM	$0.295^{+0.215}_{-0.070}$	$-1.06^{+1.80}_{-0.44}$	$1.04^{+0.70}_{-6.64}$

Table 7.2 VGCF: forecasted constraints on cosmological parameters, Ω_m , w_0 , and, w_a , estimated assuming three different cosmological models: Λ CDM, w CDM, and w_0w_a CDM.

Figure 7.4 shows the 2D marginalized posterior distributions of the cosmological models explored: Λ CDM (blue), w CDM (orange), and w_0w_a CDM (green). The shaded regions represent the 68% confidence level, while the outer contours indicate the 95% confidence level. The true values of the parameters are marked by gray dashed lines. Table 7.2 lists the best-fit values and the 1D 68% confidence intervals for each cosmological parameter in each model. In a Λ CDM model, the one assumed for the simulation, we recover the value of Ω_m with a precision of $\simeq 3\%$ that lays in a 0.1σ interval from the true value. In the second scenario, a w CDM model, Ω_m is estimated with a precision of $\simeq 6.6\%$ and its distance from the true value is 0.3σ . The third and final scenario, the w_0w_a CDM model, is more complex, leading to larger uncertainties and making the best-fit values more challenging to estimate from the posteriors. Typically in future analyses a wider redshift range, more redshift bins, and/or probe combination could potentially break degeneracies. Moreover, in future studies, we should account for projection effects in the posterior distribution (see e.g. Raveri et al. (2024)). To conclude this section, it is worth mentioning that we have relied on the method presented by Hamaus et al. (2020), that significantly improves the constraining power of the VGCF. For a more conservative forecast we have allowed the parameters \mathcal{M} and \mathcal{Q} to vary. While leaving those parameters free to vary is a conservative option, we notice here that the full power of the method can be reached by fixing those parameters, that is when a better understanding of spurious voids and other aforementioned effects is obtained. Further tests to increase our understanding of such parameters, which we aim to conduct in future studies, include the study of the dependence of \mathcal{M} and \mathcal{Q} on the cosmological and structure formation models assumed in the mocks (e.g. on the modelling of galaxy properties). Alternatively, for tighter constraints it is possible to rely on a set of mocks to calibrate the values of \mathcal{M} and \mathcal{Q} that can then be held fixed during the analysis, at the expense of trusting the features of the mocks used for calibration. Given these points, until a better understanding is reached, calibrated results should be considered less robust; therefore, we do not explore the possibility of calibrating them here.

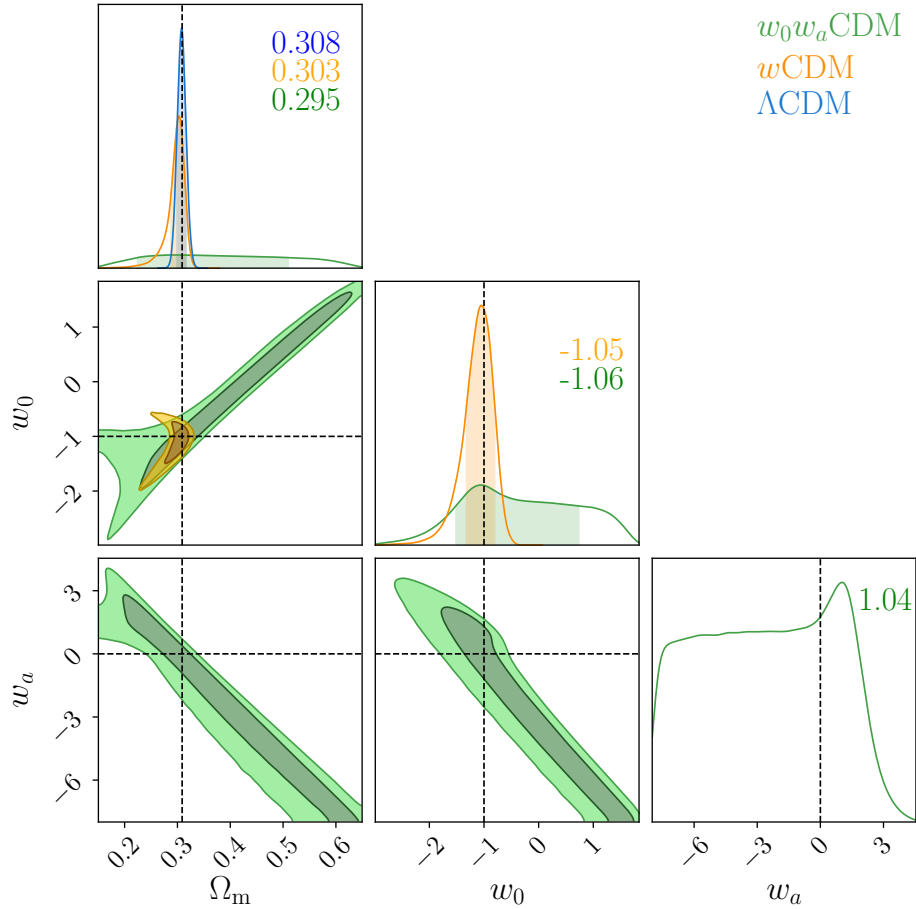


Figure 7.4 VGCF: expected constraints on Ω_m , w_0 , and w_a for the three different cosmologies tested here. In blue we show the Λ CDM model, while orange and green correspond to w CDM and w_0w_a CDM respectively. Dashed lines indicate the true values. Numbers in color correspond to the estimated values for the parameters, for the different cosmological models.

7.2 The void size function

7.2.1 Catalog preparation

The theoretical VSF, presented in Section 4.2, describes the distribution of voids reaching a threshold value in their density contrast field. Therefore, in order to compare data with an analytical VSF model, voids are post-processed to have a fixed value in their mean density contrast in the tracer distribution where they are detected (Beyond-2pt Collaboration et al., 2024; Contarini et al., 2022, 2024, 2019, 2023; Verza et al., 2019).

In this work, we explore a new methodology to post-process the void catalog. The standard methodology for post-processing watershed voids for VSF analyses (Contarini et al.,

2022, 2024, 2019, 2023; Verza et al., 2019) consists of growing a sphere around each void center, finding the maximum radius at which the mean density reaches the void formation threshold in the galaxy distribution³. This methodology represents a simple and robust way to post-process VIDE voids, however it presents some arbitrariness. The first one regards the choice of the void center used to grow the sphere. The standard choice is to adopt the volume-weighted barycenter provided by VIDE. This quantity is the geometrical center of the entire watershed void, and it has been shown to be ideal for measuring the VGCF (Hamaus et al., 2022, 2014, 2016, 2020). However, it is not guaranteed to be as optimal for threshold voids, which consider only the inner part of voids. The other potential issue concerns the fact that the method grows spheres, and this may introduce dependencies on the cosmology adopted to produce the catalog, a topic that recent analyses are investigating (Correa et al., 2021; Radinović et al., 2024, see Section 7.2.4). Moreover, overlaps among the volume of different spherical voids usually occur, leading to the introduction of criteria to select overlapping voids (usually treated as hard spheres, Contarini et al., 2022, 2019; Verza et al., 2019). Finally, a spherical void finder step removes the original void shape information coming from the Voronoi tessellation and watershed algorithm, which has been shown to contain relevant cosmological information (Kreisch et al., 2022).

For this reason, we explored a new methodology that takes advantage of the entire density field estimated through the Voronoi tessellation by VIDE. For each Voronoi cell i we assign a weight equal to their volume, V_i , multiplied by the mean tracer density at the corresponding redshift z , $n_g(z)$: $w_i = V_i(z) n_g(z)$. To avoid numerical noise in the tracer mean density, we fit the measured tracer density with a 4th-order polynomial in z , $n_g(z) = \sum_{i=0}^4 a_i z^i$. The post-processing methodology consists of an iteration of the following steps.

i) We select the Voronoi cell of the watershed void characterized by the highest weight $w_{i_{\max}}$, i.e. the lowest density contrast, and measure the corresponding mean normalized density as $1 + \Delta_{N_v} = 1/w_{i_{\max}}$. We create a set of $N_v = 1$ elements, $I_v = \{i_{\max}\}$, to which, step by step, we add the cells that build up the threshold void.

ii) We then identify the set of Voronoi cells adjacent to the selected one using the Delaunay scheme, i.e. the dual of the Voronoi tessellation (Neyrinck, 2008; Platen et al., 2007), which we call A_{loop} . We grow the threshold void by adding all the Voronoi cells, moving them from A_{loop} to I_v , from the highest to the lowest weight. For each added cell, we update the iteration counter by one, $N_v \rightarrow N_v + 1$, and the corresponding mean normalized density as:

$$1 + \Delta_{N_v} = \frac{\sum_{i \in I_v} n_g^{-1}(z_i)}{\sum_{i \in I_v} V_i} \simeq \frac{N_v n_g^{-1}(z_{i_{\max}})}{\sum_{i \in I_v} V_i}. \quad (7.9)$$

³This methodology is conceptually similar to the spherical overdensity package of the `Subfind` algorithm used to post-process Friend-of-Friends halos (Dolag et al., 2009; Springel et al., 2001)

The last approximate equality follows from the fact that the redshift extension of voids is negligible with respect to the variation scale of $n_g(z)$, $\Delta z \ll 1$.

iii) If Δ_{N_v} exceeds the void formation threshold δ_v , introduced in Section 2.2.1, we interrupt the iteration. Otherwise, we select the Voronoi cell characterized by the highest weight w_i from A_{loop} , and we repeat step ii), avoiding to select cells already belonging to the growing threshold void.

Once all the cells belonging to the threshold void are considered, we compute the standard void quantities provided by `VIDE`, using the Voronoi cells information (Sutter et al., 2015). In particular in this work we consider the volume weighted barycenter, $\mathbf{X}_v = \sum_{i \in I_v} w_i \mathbf{x}_i$, where I_v is the set of Voronoi cells of the void, and the effective radius, i.e. the radius of the sphere with a volume equal to the sum of the Voronoi cells⁴,

$$R_v = \left[\frac{3}{4\pi} \sum_{i \in I_v} V_i \right]^{1/3}. \quad (7.10)$$

These quantities are computed considering the linearly interpolated volume fraction of the last Voronoi cell in such a way that the void formation threshold is exactly matched, i.e. \mathcal{F} s.t. $(N_v - 1 + \mathcal{F}) / (\sum_{j=1}^{N_v-1} w_{I_p[j]} + \mathcal{F} w_{I_p[N_v]}) = 1 + \delta_v^L$, where j are the indexes of the I_v element set.

This algorithm is very similar to the watershed one (Neyrinck, 2008; Platen et al., 2007), but instead of stopping at the watershed, it stops when a precise value of the mean normalized density is reached, making it specifically designed to optimize the VSF analysis. Moreover, it does not assume any symmetry in measuring the mean density contrast, making this algorithm independent of the cosmology adopted to measure distances (for more detail see Section 7.2.4). The algorithm is therefore more informative about the evolution of voids along cosmic history, conserving the void shape information. Additionally, the void center definition keeps the large-scale information about the low density of the environment.

7.2.2 Void size function model

To theoretically describe the VSF, we adopt the model presented in Section 4.2, which relies on the merging of the excursion-set framework and the theory of Lagrangian density peaks, through an effective scale-dependent void formation barrier, detailed in Verza et al. (2024). Since voids do not undergo shell-crossing on the scales reached by voids with Roman, i. e., from $\simeq 2$ to $80 h^{-1} \text{Mpc}$, (see e.g. Biswas et al., 2010; Pisani et al., 2015a), this ensures

⁴We note that we use R_{eff} to indicate the effective radius of `VIDE` voids and R_v to indicate the effective radius of voids when post-processed with the algorithm described in this Section.

z	α	β	γ
1.06–1.22	$0.0967^{+0.0132}_{-0.0168}$	$0.110^{+0.021}_{-0.016}$	$1.81^{+0.25}_{-0.59}$
1.22–1.44	$0.179^{+0.008}_{-0.007}$	$0.0660^{+0.006}_{-0.005}$	$2.62^{+0.70}_{-0.78}$
1.44–1.83	$0.225^{+0.017}_{-0.004}$	$0.0493^{+0.013}_{-0.005}$	$1.98^{+1.05}_{-0.65}$

Table 7.3 Maximum posterior distribution values and 1D 68% CL interval for the moving barrier parameters, see Equation (7.11). The first column lists the redshift bins range, the other columns list the corresponding α , β , and γ parameters, respectively.

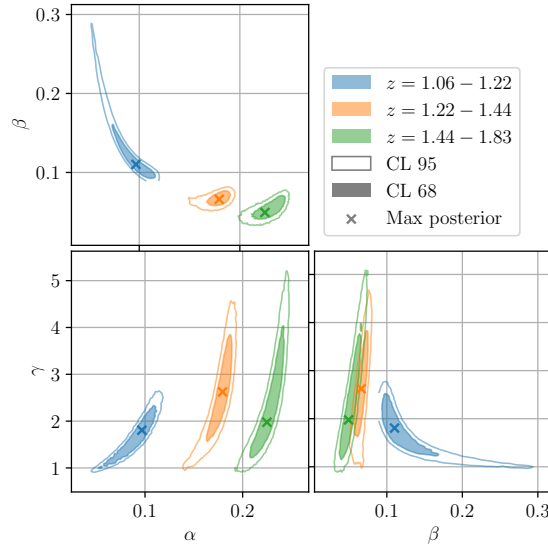


Figure 7.5 2D marginalized posterior distributions for the moving barrier parameters, Equation (7.11), for each redshift bin, as labelled in the legend. The shaded area shows the 68%CL, while the outer contours corresponds to 95%CL. The crosses show the maximum of the posterior distributions.

that in principle evolved voids can always be mapped in Lagrangian space and *vice versa*, considering a simple analytical map for the threshold, radius, and position (Verza et al., 2024). It follows that the Lagrangian void formation threshold can be any negative value that can be chosen according to the given survey’s features (Contarini et al., 2022; Pisani et al., 2015a; Verza et al., 2019, 2024), as long as the theoretical model is coherently computed. In particular, we adopt the multiplicity function, \mathcal{F} , presented in Equation (4.16) for modeling the VSF.

7.2.3 Methodology

The theoretical VSF model describes the number density of voids in the matter distribution, while in survey analyses we have access to the density contrast field of the galaxy distribution

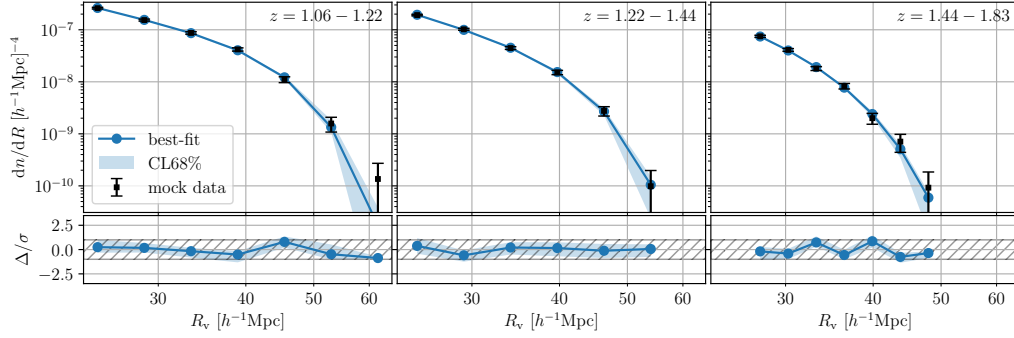


Figure 7.6 From left to right: VSF from the Roman reference HLSS-like mock (Zhai et al., 2021), in each of the three redshift bins considered. Upper panels: black dots with error bars show the measured VSF from the post-processed void catalog as described in Section 7.2.1 with $\delta_{v,g} = -0.7$, the error bars are Poissonian; blue solid lines show the best-fit moving barrier calibrated as described in Section 7.2.3; blue shaded areas show 68% CL. Lower panel: blue solid lines show the relative values of the best VSF theoretical model with respect to measurements in σ units; blue shaded areas show the 68% CL; gray hatched areas show the $\pm 1\sigma$ interval.

in redshift space, that is with biased tracers. Voids are detected in this field, and therefore we have to take into account all the observational effects impacting the VSF. Some of these effects can be accounted for analytically. For example, galaxy bias in voids can be theoretically modeled, recovering the corresponding matter density contrast (Verza et al., 2022). While the apparent enlargement of voids due to RSD can be modeled, this neglects nonlinear effects (Correa et al., 2021). In fact it has been shown that even void detection can be affected (Correa et al., 2022; Massara et al., 2022; Pisani et al., 2015b; Radinović et al., 2024), and the impact on constraints is a topic currently under investigation. Various other observational effects impact the mapping from the measured VSF in the observed galaxy distribution and the corresponding one in the matter distribution. For this reason, in this work we chose to model the effective model barrier for void formation to account for various important observational effects, such as: galaxy bias, linear and nonlinear RSD effects, non-trivial evolution from Lagrangian to Eulerian space⁵, selection effects, etc. We use the following ansatz for the moving barrier $B_S = B(S)$,

$$B(S) = \alpha [1 + (\beta/S)^\gamma] , \quad (7.11)$$

with S defined by Equation (4.17). The free parameters of our VSF model, namely α , β , and γ in the above equation, are functions of redshift, as they depend on the linear growth factor and on the observed tracer population. Figure 7.5 shows the Markov chain Monte

⁵We note that in this approach, the mapping from Lagrangian to Eulerian voids is implicitly accounted for in the moving barrier modeling.

Carlo (MCMC) best-fit of these parameters (crosses), with the 68% and 95% confidence level (CL) represented by the shaded areas and contours, respectively. Each color corresponds to a different redshift bin, as described in the legend. Table 7.3 lists the corresponding best-fit values and 1D 68% CL intervals. A clear redshift dependence of α and β is visible, as expected, while γ can be considered constant at the precision level allowed by simulated data. We note that, according to Equation (7.11), α drives the overall height of the barrier, while β determines the scale at which the exponential cut of the VSF occurs.

It follows that, given the tracer evolution and the various observational effects we considered, the redshift dependence of these parameters is expected. Such expected redshift evolution is confirmed by the posterior distributions of the parameters used in this analysis in each redshift bin, shown in Figure 7.5. While in this Chapter we characterize these parameters independently in each redshift bin considered (which in some way accounts for a redshift dependence), this does not correspond to having a model of the redshift evolution for these parameters. Developing such a model would require for example a unique relationship depending on redshift for each parameter, and would effectively reduce the number of nuisance parameters for VSF analyses. This is, however, beyond the scope of this work, and will be explored in the future. Alongside the redshift evolution, the effective barrier parametrization may be affected by dependencies on cosmology and tracer population. The strongest impact is expected to come from the tracer population via their bias. This would impact the global amplitude of the barrier but not the shape. A similar cosmological dependence is expected from those parameters that modify the amplitude of the linear matter power spectrum, without impacting its shape, as, e.g., σ_8 or a dynamical dark energy component. Finally, a minor dependence on the linear matter power spectrum shape is expected, which can introduce a cosmology dependence for those parameters that impact the power spectrum shape, such as Ω_m . This is due to minor changes in the shape of the correlation between the random walk steps at different scales, from which the multiplicity function is generated. This effect is, however, expected to be sub-dominant (Verza et al., 2024). As mentioned above, exploring the redshift dependence for tracers and cosmology is beyond the scope of this Thesis: we plan to fully characterize these dependencies in future works, by using light-cone mock realizations.

Figure 7.6 shows the VSF in each of the three redshift bins considered. In the upper panels, black dots with error bars show the measured VSF from the post-processed void catalog as described in Section 7.2.1 with $\delta_{v,g} = -0.7$, the error bars are Poissonian. Blue solid lines show the best-fit moving barrier calibrated as described in Section 7.2.3, while blue shaded areas show 68% confidence level (CL). In the lower panel, blue solid lines show

the relative values of the best VSF theoretical model with respect to measurements in σ units, blue shaded areas show the 68% CL, and gray hatched areas show the $\pm 1\sigma$ interval.

7.2.4 Analysis and results

To study the constraining power of the VSF in the Roman reference HLSS, we perform a Bayesian analysis using a MCMC to sample the posterior distribution

$$\mathcal{P}(\Theta|\mathcal{D}) \propto \mathcal{L}(\mathcal{D}|\Theta)p(\Theta), \quad (7.12)$$

where $\mathcal{L}(\mathcal{D}|\Theta)$ is the likelihood, \mathcal{D} is the data vector, i.e. the measured VSF in the three redshift bins, Θ is the array of the cosmological parameters explored plus any extra model parameters, and $p(\Theta)$ is the prior distribution of the parameters. We consider a Gaussian likelihood using the theoretical VSF with the calibration of the effective barrier parameters, presented in Section 7.2.2 and 7.2.3,

$$\begin{aligned} \log[\mathcal{L}(\mathcal{D}|\Theta)] = & -\frac{1}{2} \sum_{ij} (n_i^{\mathcal{D}} - n_i^T) \Sigma_{ij}^{-1} (n_j^{\mathcal{D}} - n_j^T) \\ & - \frac{N_{\mathcal{D}}}{2} \log(2\pi) - \frac{1}{2} \log(\det \Sigma). \end{aligned} \quad (7.13)$$

The indexes $i = i(i_r, i_z)$ and $j = j(j_r, j_z)$ run over all the radius bins, i_r , of the VSF and all the redshift bins considered, i_z , i.e. i and j run from 1 to $N_{\mathcal{D}}$, which is the length of the data vector considered. The $n_i^{\mathcal{D}}$ quantity refers to the measured number density of voids with radius in the radius bin i_r and redshift bin i_z , n_i^T refers to the corresponding theoretical prediction, i.e. the integration of the theoretical VSF over the radius bin. Previous studies on mock catalogs showed that off-diagonal terms of the covariance matrix Σ_{ij} of the measured VSF are negligible (Bayer et al., 2021; Contarini et al., 2023; Kreisch et al., 2022; Pellicciari et al., 2023; Thiele et al., 2024), therefore we consider a diagonal covariance, where the elements correspond to the Poissonian uncertainty provided by the number of voids in a given radius and redshift bin: $\Sigma_{ij} = \sigma_i^2 \delta_{ij}^K$ where δ_{ij}^K is the Kronecker delta, $\sigma_i = \sqrt{N_i}/V_{i_z}$, N_i is the number of voids in the redshift bin i_z with radius in the radius bin i_r , and V_{i_z} is the volume of the redshift bin i_z . We note that we use here a Gaussian likelihood instead of a Poissonian one, since in previous works (Beyond-2pt Collaboration et al., 2024; Contarini et al., 2022) we did not find any relevant difference in the posterior distribution obtained with a Gaussian or a Poissonian prior, respectively.

It is important to note that to obtain the measured VSF we assumed a cosmological model, Λ CDM, with a fixed set of cosmological parameters, which we call ‘‘fiducial cosmology’’.

This is because we converted the observed redshift of galaxies to comoving distances, and we ran the void finder and post-processed voids using these coordinates. At each step of the MCMC, we compute the posterior probability of an assumed “true cosmology”, likely different from the “fiducial” one. It follows that not only the theoretical model, but also the inferred number density $n_i^{\mathcal{D}}$ and the corresponding covariance Σ_{ij} change, due to the introduction of geometrical distortions: the AP and volume effects (Contarini et al., 2022; Verza et al., 2023).

The AP effect impacts the estimated void sizes and introduces an anisotropy between the orthogonal and the parallel directions with respect to the LOS. Let us consider two objects characterized by a mean redshift z , a difference in redshift $\Delta z \ll 1$ and an angular separation $\Delta\theta \ll 1$ rad. Their distance, decomposed in the radial and orthogonal components with respect to the LOS, are illustrated by Equation (4.3), rewritten here for simplicity (Eisenstein et al., 2005; Xu et al., 2013):

$$\begin{aligned} r_{\parallel}^{\text{true}} &= \frac{H^{\text{fid}}(z)}{H^{\text{true}}(z)} r_{\parallel}^{\text{fid}} = q_{\parallel} r_{\parallel}^{\text{fid}}, \\ r_{\perp}^{\text{true}} &= \frac{D_{\text{A}}^{\text{true}}(z)}{D_{\text{A}}^{\text{fid}}(z)} r_{\perp}^{\text{fid}} = q_{\perp} r_{\perp}^{\text{fid}}. \end{aligned} \quad (7.14)$$

The superscripts indicate whether the corresponding quantities are computed considering the fiducial or assumed true cosmology in each MCMC step, respectively. We note that the volume of a Voronoi cell is modified exactly as $V_{\text{cell}}^{\text{true}} = q_{\parallel} q_{\perp}^2 V_{\text{cell}}^{\text{fid}}$. Therefore, by construction, following Equation (7.10), the void radius transforms as $R_{\text{v}}^{\text{true}} = q_{\parallel}^{1/3} q_{\perp}^{2/3} R_{\text{v}}^{\text{fid}}$. This result is already known for voids (Contarini et al., 2022; Correa et al., 2021; Hamaus et al., 2020), for which, however, this relation is an approximation and subject to the cosmology dependence on the void finder or post-processing procedure (Correa et al., 2021; Radinović et al., 2024). In our case, relying on the Voronoi tessellation, the relation is exact in the limit in which Equations (7.14) are satisfied (Verza et al., 2023).

The volume effect changes the mean number density $n_i^{\mathcal{D}}$ and the associated uncertainty σ_i due to the change in the inferred redshift bin volume,

$$V_{i_z} = \frac{\Omega_{[\text{rad}]}}{3} \left[D_{\text{A}}^3(z_{\text{out}}) - D_{\text{A}}^3(z_{\text{in}}) \right] \quad (7.15)$$

where $\Omega_{[\text{rad}]}$ is the sky area in steradian, $D_{\text{A}}(z)$ is the comoving distance corresponding to an object at redshift z , while z_{in} and z_{out} are the inner and outer redshift limits of the redshift

bin i_z . It follows that

$$\sigma_i^{\text{true}} = \sigma_i^{\text{fid}} \frac{D_{\text{A,fid}}^3(z_{\text{out}}) - D_{\text{A,fid}}^3(z_{\text{in}})}{D_{\text{A,true}}^3(z_{\text{out}}) - D_{\text{A,true}}^3(z_{\text{in}})}, \quad (7.16)$$

$$n_i^{\text{true}} = n_i^{\text{fid}} \frac{D_{\text{A,fid}}^3(z_{\text{out}}) - D_{\text{A,fid}}^3(z_{\text{in}})}{D_{\text{A,true}}^3(z_{\text{out}}) - D_{\text{A,true}}^3(z_{\text{in}})}. \quad (7.17)$$

The above relations assume that the number of voids is conserved, i.e. their detection and identification do not depend on the cosmology assumed in running the void finder and in post-processing the void catalog. This condition is only approximately valid for spherical threshold voids (Correa et al., 2021; Radinović et al., 2024), while it is exactly satisfied by both the void finder and the post-process procedure presented in this work (see Section 7.2.1). This is because, under a smooth change of the tracer distance from the observer, the Voronoi tessellation would provide a different cell volume, but the topological structure does not change. In particular, the identification of the Voronoi cells corresponding to the minima in the density field does not change, as well as the identification of the Voronoi cells building up the void. In other words, the redshift and angular coordinates of the minima and void barycenter are not impacted by the assumed cosmology (Verza et al., 2023). Moreover, the threshold value is not affected by geometrical distortions, due to cancellations of the AP terms. We note that $n_g^{\text{true}}(z) = q_{\parallel}^{-1} q_{\perp}^{-2} n_g^{\text{fid}}(z)$, while $V_i^{\text{true}} = q_{\parallel} q_{\perp}^2 V_i^{\text{fid}}$. In the limit in which the AP correction is valid, $\sum_{i \in I_v} V_i^{\text{true}} = q_{\parallel} q_{\perp}^2 \sum_{i \in I_v} V_i^{\text{fid}}$, where q_{\parallel} and q_{\perp}^2 are evaluated at the redshift of the void center. From Equation (7.9) it follows $\delta_v^{\text{fid}} = \delta_v^{\text{true}}$. Therefore, both the relative minima and the cells belonging to threshold voids are conserved, i.e. the void catalog is cosmology independent. We note that even this last relationship is exact for our void catalog, while it is approximate for spherical voids.

For each cosmological model, we perform two analyses, an optimistic one, in which the moving barrier parameters of Section 7.2.3 are considered fixed to the best fit value, and a pessimistic one, in which the effective barrier parameters are considered as nuisance parameters, using as prior for α , β , and γ of Equation (7.11) of each redshift bin the posterior of the calibration described in Section 7.2.3, resulting in a total of 9 nuisance parameters. This choice is due to the fact that we want to explore the constraining power coming from a VSF analysis performed on Roman-like data. The optimistic scenario represents the case in which the theoretical model is fully understood and is able to provide a robust prediction; while the pessimistic case corresponds to the case in which the dependence of the moving barrier on the tracer distribution is unknown. The MCMC analyses are performed using the `emcee`⁶ (Foreman-Mackey et al., 2019) Python package, considering 48 walkers. Each chain

⁶<https://github.com/dfm/emcee>

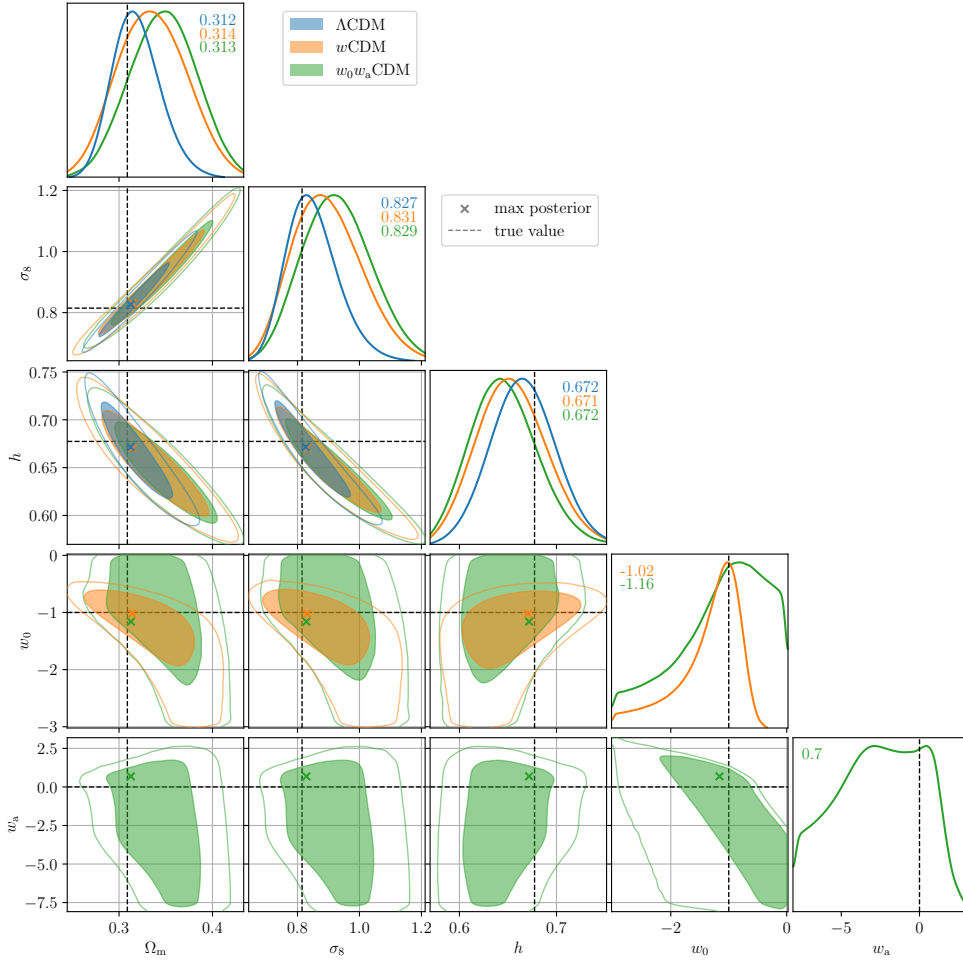


Figure 7.7 VSF: posterior distributions of the cosmological parameters explored in the optimistic scenario, for the three cosmological models explored: Λ CDM (blue), w CDM (orange), w_0w_a CDM (green). The filled internal region shows the 68% CL, the outer line shows the 95% CL. Black dashed lines show the true values, crosses correspond to the maximum of the posterior distribution, the numbers in the panels along the diagonal list the parameter values corresponding to the maximum of the likelihood.

is post-processed by removing the first 2000 steps. Moreover, to ensure that the different steps are not correlated, we consider 1 chain step every 15 computed, resulting in a final chain length of around 2×10^7 , for each of the models considered.

Figures 7.7 and 7.8 show the 2D and 1D marginalized posterior distributions of the explored cosmological models, Λ CDM (blue), w CDM (orange), and w_0w_a CDM (green). Shaded areas show the 68% CL, the outer lines show the 95% CL, crosses correspond to the maximum of the posterior distribution, and dashed gray lines to the true values of the parameters. Table 7.4 lists the best-fit values and 1D 68% CL of each cosmological parameter in both the optimistic and pessimistic cases for each cosmological model considered. It can

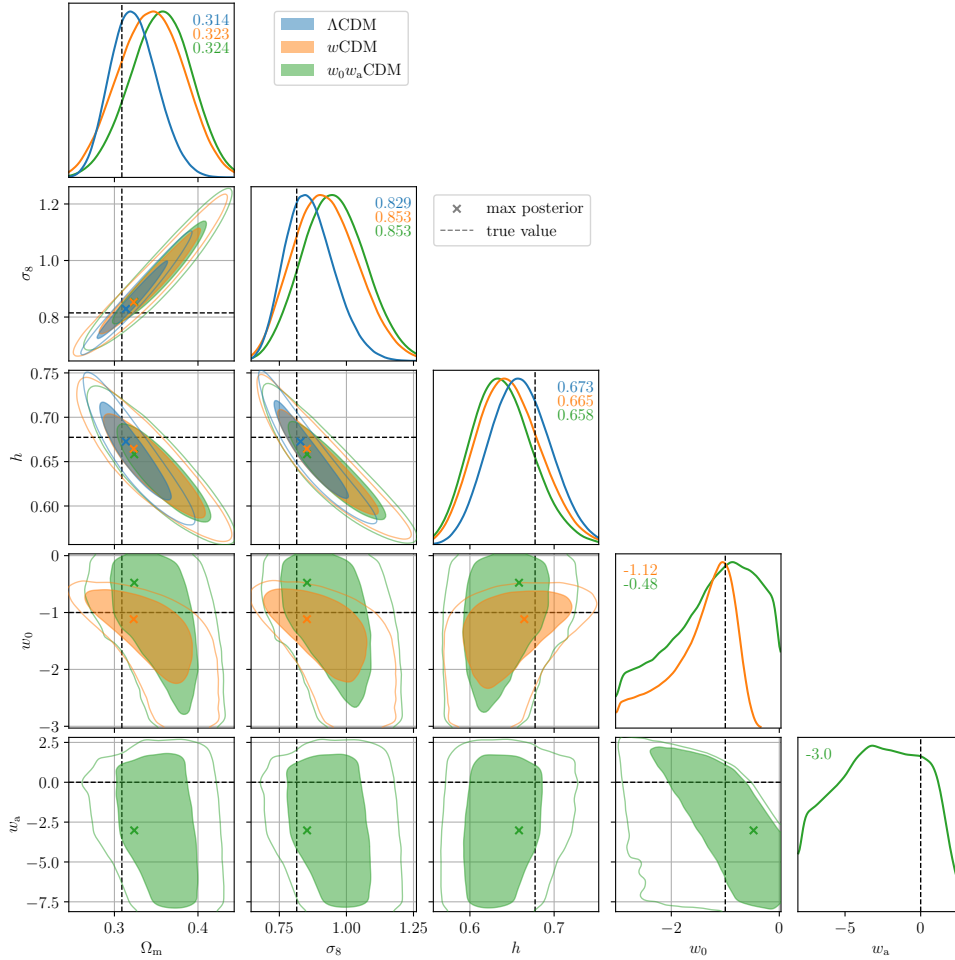


Figure 7.8 VSF: posterior distributions of the cosmological parameters explored in the pessimistic scenario, for the three explored cosmological models. The plot is organized as Figure 7.7.

be noted that in the pessimistic case the 68% CL of each cosmological parameter results slightly enlarged due to the number of nuisance parameters. It is important to recall that in a more realistic case, when the effective barrier parameters will be modeled as a function of redshift, the number of nuisance parameters will decrease with respect to the one explored here.

To conclude this section, we want to stress that this analysis considers the void size function alone. A great advantage of the VSF and other cosmic void statistics comes from their power when combined with other probes (Bayer et al., 2021; Contarini et al., 2022; Kreisch et al., 2022; Pellicciari et al., 2023; Pisani et al., 2015a). Indeed it is possible to greatly tighten the constraints by combining void statistics among themselves (see e.g. Contarini et al., 2022; Kreisch et al., 2022, and discussion in Section 7.3), and with galaxy statistics such as cluster counts and galaxy two-point statistics (Bayer et al., 2021; Contarini et al.,

Model		Ω_m	σ_8	h	w_0	w_a
True		0.3089	0.8147	0.6774	-1	0
Λ CDM	opt.	$0.3125^{+0.0283}_{-0.0216}$	$0.8268^{+0.0880}_{-0.0714}$	$0.6715^{+0.0263}_{-0.0395}$	-1	0
	pess.	$0.3138^{+0.0352}_{-0.0203}$	$0.8288^{+0.1126}_{-0.0675}$	$0.6726^{+0.0214}_{-0.0505}$	-1	0
w CDM	opt.	$0.3142^{+0.0571}_{-0.0175}$	$0.8311^{+0.1610}_{-0.0589}$	$0.6705^{+0.0169}_{-0.0544}$	$-1.022^{+0.318}_{-0.542}$	0
	pess.	$0.3230^{+0.0614}_{-0.0174}$	$0.8527^{+0.1820}_{-0.0587}$	$0.6645^{+0.0164}_{-0.0594}$	$-1.117^{+0.425}_{-0.613}$	0
$w_0 w_a$ CDM	opt.	$0.3126^{+0.0703}_{-0.0008}$	$0.8288^{+0.1998}_{-0.0218}$	$0.6717^{+0.0052}_{-0.0627}$	$-1.160^{+1.160}_{-0.225}$	$0.69^{+0.47}_{-5.28}$
	pess.	$0.3237^{+0.0696}_{-0.0029}$	$0.8533^{+0.2134}_{-0.0210}$	$0.6583^{+0.0121}_{-0.0593}$	$-0.476^{+0.476}_{-1.091}$	$-3.02^{+4.20}_{-1.92}$

Table 7.4 VSF: maximum posterior distribution values and 1D 68% CL interval for the cosmological parameters explored, for each considered cosmological model (we show both the optimistic and pessimistic scenarios).

2022; Pellicciari et al., 2023). The additional power is due to various reasons. Firstly, cosmic voids probe different scales with respect to clusters and galaxies (Contarini et al., 2023; Pellicciari et al., 2023). Secondly, since voids have an extended size, the AP effect on voids acts in a different way compared to how it acts on galaxy statistics. Finally, galaxies and voids probe different environments. Interestingly, the underdense environment of voids is representative of less evolved and pristine regions in the Universe (Bos et al., 2012; Cautun et al., 2014; Lavaux and Wandelt, 2012; Pisani et al., 2015a; Verza et al., 2022). Also, due to their underdense nature, voids are an environment where the dark energy-dark matter density ratio is higher than in the mean universe (Cautun et al., 2014; Pisani et al., 2015a; Verza et al., 2019).

7.3 Voids' probe combination

The full power of the different void statistics can be confirmed by considering voids' probe combination, as the two statistics explored here respond differently to cosmology. The VSF is sensitive to both the cosmological fluctuations, through the linear matter power-spectrum, and the background expansion of the Universe (see Sections 7.2.2–7.2.4). The VGCF is a sensitive probe of the expansion history of the universe, through the AP test. Previous work suggests that the covariance between the VSF and the VGCF is low (Contarini et al., 2024; Kreisch et al., 2022), therefore the constraining power of the joint analysis can be safely estimated by combining the two independent posterior distributions. To showcase the constraining power

Model		Ω_m	σ_8	h	w_0	w_a
True		0.3089	0.8147	0.6774	-1	0
Λ CDM	opt.	$0.3086^{+0.0077}_{-0.0080}$	$0.8145^{+0.0258}_{-0.0272}$	$0.6764^{+0.0164}_{-0.0168}$	-1	0
	pess.	$0.3100^{+0.0066}_{-0.0093}$	$0.8212^{+0.0211}_{-0.0336}$	$0.6726^{+0.0212}_{-0.0147}$	-1	0
w CDM	opt.	$0.3095^{+0.0052}_{-0.0124}$	$0.8167^{+0.0186}_{-0.0392}$	$0.6757^{+0.0215}_{-0.0144}$	$-1.023^{+0.171}_{-0.113}$	0
	pess.	$0.3089^{+0.0063}_{-0.0121}$	$0.8149^{+0.0226}_{-0.0389}$	$0.6801^{+0.0189}_{-0.0208}$	$-1.041^{+0.195}_{-0.101}$	0
w_0w_a CDM	opt.	$0.3238^{+0.0250}_{-0.0262}$	$0.8601^{+0.0721}_{-0.0864}$	$0.6584^{+0.0246}_{-0.0297}$	$-0.934^{+0.216}_{-0.182}$	$-0.47^{+0.93}_{-0.93}$
	pess.	$0.3313^{+0.0247}_{-0.0310}$	$0.8760^{+0.0780}_{-0.0990}$	$0.6563^{+0.0337}_{-0.0370}$	$-0.904^{+0.240}_{-0.208}$	$-0.97^{+1.38}_{-1.23}$

Table 7.5 Combination of the VGCF and VSF: maximum posterior distribution values and 1D 68% CL interval of the cosmological parameters explored for each considered cosmological model (we show both the optimistic and pessimistic scenarios).

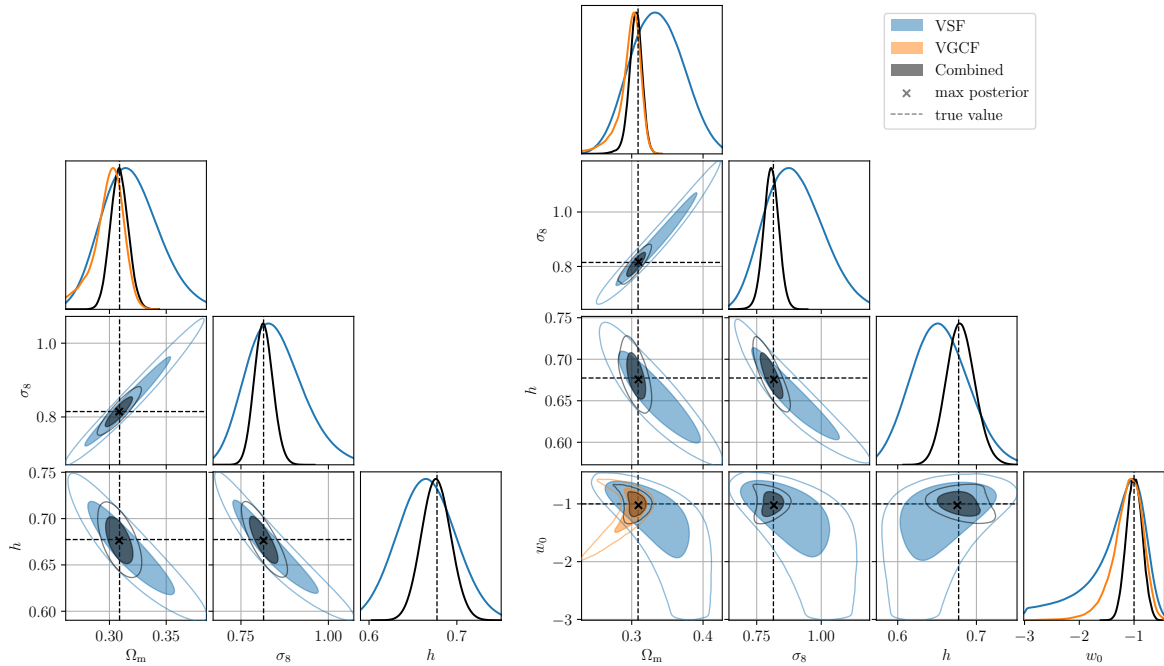


Figure 7.9 Combination of the VGCF and VSF: posterior distributions of the cosmological parameters explored in the Λ CDM (left) and the w CDM model (right), obtained from the VSF (blue), VGCF (orange), and combining the two statistics (dark grey). The filled internal region shows the 68% CL, the outer line shows the 95% CL. Black dashed lines indicate the true values, crosses correspond to the maximum of the posterior distributions.

of a joint void-analysis, Figures 7.9 and 7.10 represent the overlapping forecast contours for the cosmological models and parameters explored in this work, considering the optimistic

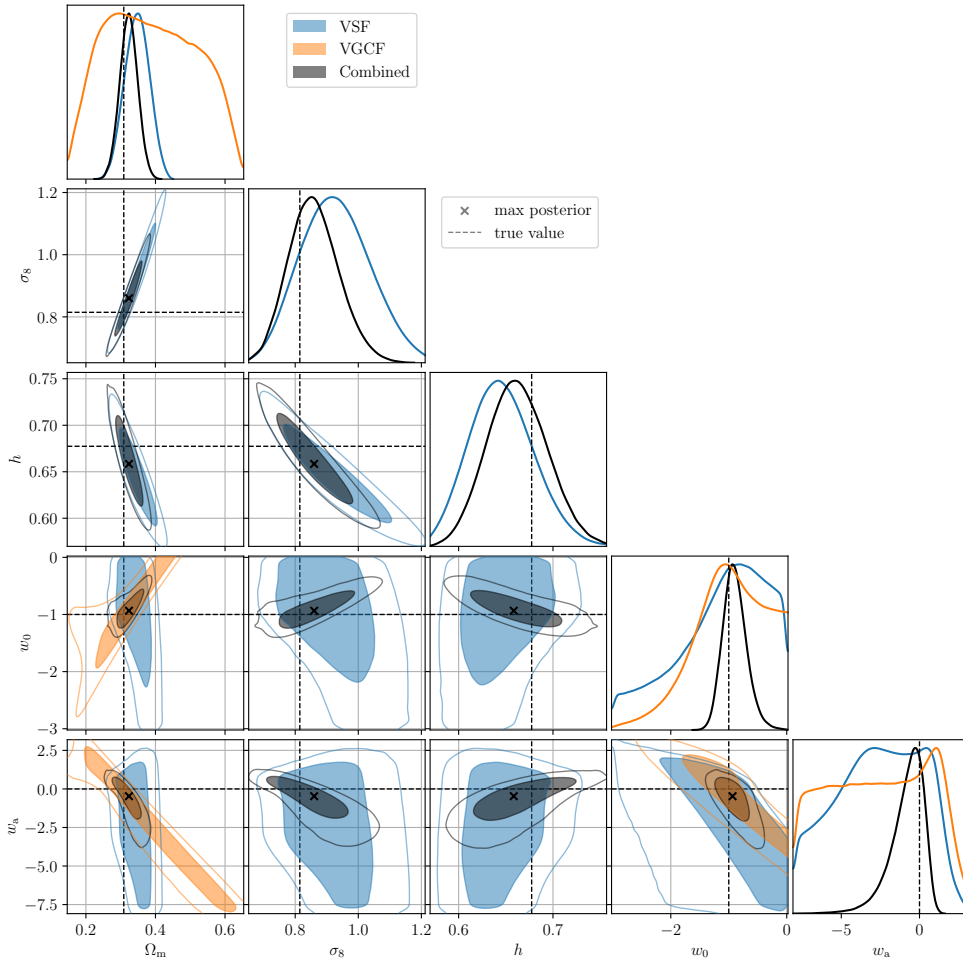


Figure 7.10 Combination of the VGCF and VSF: posterior distributions of the cosmological parameters explored in the w_0w_a CDM model, obtained from the VSF (blue), VGCF (orange), and combining the two statistics (dark grey). The plot is organized as Fig 7.9.

case for the VSF. We list in Table 7.5 the best-fit value and 1D 68% CL for each cosmological parameter from the joint distribution, for both the optimistic and pessimistic scenario. The left panel of Figure 7.9 shows the Λ CDM case, with the marginalized 2D posterior distribution of the VSF in blue, the VGCF in orange, and the combined posterior distribution in dark grey. It should be noted that the narrower posterior distribution for Ω_m in the VGCF case leads to a tightening of constraints even for parameters that are not probed by the VGCF, i.e. σ_8 and h (or H_0). The same observation is valid also for the w CDM case, Figure 7.9 left panel. Moreover, it is important to notice the different orientation, i.e. the complementarity, in the $w - \Omega_m$ plane. For the w_0w_a CDM case, shown in Figure 7.10, the situation is inverted. The VGCF, probing the background expansion of the Universe, shows wider contours, in particular for Ω_m . The corresponding VSF posterior distribution shows a higher constraining

power, probably due to the fact that, together with its impact on the expansion history of the Universe, the dark energy equation of state also affects the growth of structure, i.e. σ_8 , to which the VSF is directly sensitive. The VGCF is, in principle, more sensitive than the VSF to the growth of structures, as it measures their correlation properties. However, this sensitivity is absorbed in the model through the inclusion of nuisance parameters. Additionally, we wish to notice that, while selecting three bins is an effective choice for the analysis of the VGCF when considering the w CDM case, it may be harder to break degeneracies with three bins when considering the w_0w_a CDM case. Nevertheless, the combination of the VSF and the VGCF shows an interesting complementarity for Ω_m and the dark energy parameters, w_0 and w_a , leading to strong constraints for the dynamical dark energy parameters as well.

In future works, when combining the various void statistics, we plan to rely on mock catalogs spanning various cosmological realizations and to consider various galaxy-halo connection models, such as SAM, halo-occupation distribution (HOD), and sub-halos matching techniques (SHAM), and spanning the corresponding parameters. This will allow to properly model the covariance, for both the VSF, the VGCF, and the cross-covariance, modelling the cosmological dependence and marginalizing over galaxy properties, represented by the galaxy-halo connection models. Crucially, we expect the use of mock galaxy catalogs to allow a better understanding of the free parameters of our models, such as the redshift and tracer dependency for the VSF effective barrier in Equation (7.11), and the nuisance parameters \mathcal{M} and \mathcal{Q} for the VGCF model in Equation (4.41). Such understanding, together with the increase in the constraining power for both statistics, will enhance the robustness of our models, alongside with accounting for observational effects (e.g. through the use of realistic survey masks). In the current cosmology landscape, if dynamical dark energy is confirmed (DESI Collaboration et al., 2024), the community will focus on pinning down the dark energy equation of state, and Roman voids are expected to be a powerful, independent probe in this context. The results of these Sections pave the way to using Roman voids to independently constrain cosmological parameters with tight precision.

8

Conclusions

In this Thesis we have used the VGCF to infer cosmological parameters by exploiting the characteristic effects, of both geometrical and dynamical types, that induce systematic distortions in the cosmic voids shapes, causing deviations from the expected average spherical symmetry.

Over the years, void analyses has gained substantial traction in cosmology. The study of cosmic voids is a relatively young and emerging field, and there are many challenges, even for well-established statistics such as the void size function, which measures void abundance, and the void-galaxy cross-correlation function, which characterizes void shape. One of the greatest challenges arises from the presence of distortions in redshift space, which require accurate modeling, especially in the case of RSD, to extract cosmological information that can reveal the underlying model describing the Universe.

In this Thesis, have focused on the VGCF statistics and explored its potential as cosmological probe in two different contexts. The first one is its use in combination with reconstruction techniques to analyze voids in 'reconstructed' datasets from which RSD have been removed. The second its his application, in combination with the VSF statistics, to the future HLSS dataset that will be obtained by the Nancy Grace Roman Space Telescope, specifically analyzing the VGCF in redshift space. This analysis complements the companion study on the VSF and demonstrates the synergistic potential of combining these two void-based statistics.

The main results were presented in Chapters 6 and 7.

In Chapter 7, I presented an analysis aimed at testing a new methodology designed to improve the the power of the AP tests applied to voids by performing a VGCF analysis to a set of reconstructed data. I focused on the single distortion parameter ε which is a proxy to the expansion history of the Universe. This analysis is typically performed using redshift as a distance indicator. The resulting RSD, being partially degenerate with the AP distortions, hampers the precision of the ε estimate, even when an appropriate VGCF model is used to

account for possible biases. The reconstruction, that has been performed using the Zel'dovich approximation, had the scope of removing RSD altogether and therefore has the potential to improve the precision of the measured ε parameter.

In this work, we tested the performance of this new strategy using simulated datasets extracted from the Quijote simulations (see Section 5.3.1). In this test we have compared the analysis in reconstructed space (i.e., cross-correlating both voids and halos in reconstructed space) with the analysis presented in the literature (e.g., (Hamaus et al., 2022, 2020)) conducted in redshift space, which involves cross-correlating both voids and halos in redshift space. The results, presented in Section 6.3, indicate the success of the proposed method. Specifically:

- We demonstrated that the reconstruction algorithm (see Section 3.4.1) is able to effectively eliminate RSD, allowing measurement of the VGCF without RSD, as shown by quadrupole signal consistent with zero at all separations. Additionally, robustness tests were performed to assess the effectiveness of the reconstruction to variations in input parameters. Among these, the most important one, also for future cosmological application, is the sensitivity to the fiducial value of β required to perform the reconstruction. We found that the outcome of the reconstruction, and consequently the estimate of the ε parameter, is remarkably insensitive to the fiducial β value.
- Performing the analysis in reconstructed space results in a more accurate measurement of ε , whose best fit value differs from the true one by 0.3σ , to be compared with a 1.5σ mismatch when the analysis is performed in redshift space. The precision is also increased from a 1.7% relative error in redshift space to a 1.1% error in reconstructed space.
- A key strength of the strategy adopted in my analysis is the possibility to use all voids of the sample extracted by `VIDE` instead of adopting the common practice of discarding the small ones. We have demonstrated that the performance of the analysis do not degrade when including progressively smaller voids down to the smallest ones selected by the void-identification algorithm. Excluding the small voids that induce biases reduces the size of the sample by about 60%, inevitably reducing the precision of the estimated parameters. Hence, we observe a 50% reduction in the statistical error when the analysis is performed in reconstructed rather than redshift space.

The plan is to apply this strategy to first perform the VGCF analysis of the BOSS data (Dawson et al., 2012) and then to the spectroscopic galaxy catalog of the Euclid (Euclid Collaboration et al., 2024) and Roman (Dore et al., 2019; Spergel et al., 2015) satellite missions as soon as they will become available. Applying the method to observational data

will require completing the testing phase, which involves refining the method's performance in the presence of AP distortions and including all survey-specific observational biases and selection effects.

In Chapter 7, I presented a comprehensive cosmological forecast based on void statistics to be measured in the High Latitude Spectroscopic Survey (HLSS) of the Nancy Grace Roman Space Telescope. Void catalogs were constructed from a mock catalogs that simulate those expected from the survey (see Section 5.3.2), and state-of-the-art models were used to extract cosmological constraints from the VSF and VGCF. The results showcase impressive constraining power from both the application of each statistics and, even more so, from their joint analysis.

My contribution focused on performing the VGCF analysis in redshift space, using established models from the literature (Hamaus et al., 2022). Starting from the same set of voids, the VSF was analyzed using the methodology presented in Verza et al. (2024). Both statistics produced promising results, and these were even more compelling when the two probes were combined. This combination confirmed the unique strengths of different void statistics, as the VSF and VGCF respond differently to cosmology, maximizing their joint constraining power.

The main findings are summarized as follows:

- From the VGCF analysis, which I personally conducted, we estimated the parameters ε and β . The primary focus was on ε , enabling us to obtain the combination $D_A(z)H(z)$ that probes the expansion history of the Universe. The parameter β , from which estimates of $f\sigma_8$ can be derived by including the galaxy clustering amplitude parameter, received less focus due to its estimates not being accurate across all redshift bins. The mismatch between the measured and the expected β values likely stems from having assumed a linear bias model, which may not necessarily be accurate for all the redshift bins. An alternative, or additional, possibility is the limited ability of the VGCF model to account for nonlinear dynamical effects. As I have discussed and demonstrated in Chapter 6, repeating the analysis in reconstructed space may solve the problem. We will explore this issue in a dedicated, future analysis. Regarding the estimation of ε , by measuring $D_A(z)H(z)$ across different redshift bins, we have performed a best fit analysis assuming three different cosmological models: Λ CDM (the model used to generate the simulations), w CDM, and w_0w_a CDM. For all cosmologies, we found that the estimated parameters agree with the true ones within the 1σ statistical error. In the w_0w_a CDM scenario, projection effects hinder accurate parameter estimation with the VGCF alone. However, this difficulty can be overcome by removing degeneracies with a combined VGCF and VSF analysis.

- In the VSF analysis we explored two scenarios: an optimistic case, where the theoretical VSF model is fully understood and provides robust predictions, and a pessimistic case, where the dependence of the moving barrier (for the void formation threshold) on the tracer distribution is unknown. The same three cosmological models were explored under both scenarios. The results showed that, as for the VGCF case, all parameter estimates agree with the true values within the 1σ random error, whose amplitude increases, as expected, in the pessimistic scenario due to the large number of nuisance parameters used in the model. It is worth noting that in a more realistic setting, where effective barrier parameters are modeled as functions of redshift, the number of nuisance parameters in the pessimistic scenario should decrease relative to those examined here, leading to a significant reduction of the statistical uncertainties.
- The full potential of combining different void statistics was evident in our analysis, as the VSF and VGCF respond differently to cosmology. The VSF is sensitive to cosmological fluctuations through the linear matter power spectrum and the background expansion of the Universe. Meanwhile, the VGCF probes the expansion history through the AP test. We performed a joint analysis of these two statistics by combining the independent posterior distributions. This combination highlights an interesting complementarity for the mass density parameter Ω_m , and the dark energy parameters, w_0 and w_a , leading to stronger constraints on dynamic dark energy parameters. As shown in Section 7.3, combining these two probes significantly improves the precision of parameter estimates, not only for parameters constrained by both statistics but also for those constrained solely by the VSF.

In conclusion, this analysis underscores the constraining power of void analyses for cosmological parameters, suggesting that with future Roman data, void analysis alone can independently constrain cosmological parameters with high precision, and potentially reveal deviations from the Λ CDM model, as suggested by recent DESI results (DESI Collaboration et al., 2024).

Future work will involve analyses on a larger set of realistic mock catalogs of galaxies and voids. This will enable an improved estimate of the covariance matrix with respect to the jackknife one, for both the VSF and VGCF, as well as their cross-covariance, thereby accounting for cosmological dependence and marginalizing over galaxy properties through galaxy-halo connection models. Additionally, working with more mocks will allow for a more accurate calibration of the nuisance parameters in the VGCF and VSF models.

These analyses underscore the growing importance of cosmic voids as powerful probes in cosmology. The combined use of VGCF and VSF provides promising constraints on

parameters like the cosmic expansion rate and dark energy properties. Moreover, the complementarity between these two statistics strengthens the potential of void studies to address a wide array of cosmological questions. The results presented here highlight that void-based analyses can offer substantial insights and high-precision constraints, positioning cosmic voids as an increasingly valuable tool in the realm of precision cosmology. This Thesis also demonstrates that void analyses, particularly with data from upcoming surveys such as Euclid and the Nancy Grace Roman Space Telescope, will play a pivotal role in extending our understanding of fundamental cosmological models. With the application of advanced techniques like reconstructed space analyses and leveraging the combination of multiple void statistics, cosmic voids constitute a promising cosmological probe that has the potential to stress test the Λ CDM model and to indicate a path to solve the current tensions.

In summary, this Thesis illustrates that the field of cosmic voids is rapidly emerging as a relevant probe for precision cosmology, capable of providing tight constraints on cosmological parameters and offering a unique perspective on the large-scale structure of the Universe. With continued advancements in methodology and observational data, void-based analyses are well-positioned to make valuable contributions to the wider landscape of cosmological research.

A

Halo bias estimate

In this appendix, we describe the methods employed in this work to estimate the large-scale effective linear bias of the tracers used for the analysis presented in Chapter 6. To maximize the precision of the estimates we model the bias with the 100 available mocks in real space, rather than the ones in redshift space. First, we measure the real space 2PCF for the 100 mocks using the publicly available code from the `MeasCorr` package (Farina et al., 2024; Guidi et al., 2023), which implements the Landy-Szalay estimator for the 2PCF (Landy and Szalay, 1993):

$$\xi_{\text{hh}}(r) = \frac{DD(r) - 2DR(r) + \mathcal{R}\mathcal{R}(r)}{\mathcal{R}\mathcal{R}(r)}, \quad (\text{A.1})$$

where the subscript hh indicates that the 2PCF is measured for halos, while DD , DR and $\mathcal{R}\mathcal{R}$ indicate the normalized halo-halo, halo-random and random-random pair counts, respectively. The elements of the covariance matrix of the 2PCF measurements are estimated via:

$$\text{Cov}[\xi_{\text{hh}}]_{i,j} = \frac{1}{N-1} \sum_{n=1}^N \left(\xi_{\text{hh}}^{(n)}(r_i) - \overline{\xi_{\text{hh}}}(r_i) \right) \left(\xi_{\text{hh}}^{(n)}(r_j) - \overline{\xi_{\text{hh}}}(r_j) \right). \quad (\text{A.2})$$

where N is the number of mocks, in this case $N = 100$.

The value of the large-scale bias was calculated by comparing the 2PCF measurements with the reference model, using a fitting procedure implemented in the `BAOFitter` package¹, which is specifically designed for fitting and modeling the BAO imprint in the 2PCF. However, in this case, it can also be used to measure the bias, as we will demonstrate below.

The model is built starting from the linear prediction for the matter power spectrum in real space, $P_{\text{lin}}(k)$, which corresponds to the Fourier transform of the linear 2PCF of dark matter, $\xi_{\text{mm}}(r)$. A term, known as the no-wiggle power spectrum $P_{\text{nw}}(k)$, is added to model the nonlinear effects that cause a damping of the BAO peak in the 2PCF (Eisenstein and Hu,

¹<https://gitlab.com/esarpa1/BAOFit>

1999), or equivalently in Fourier space, the oscillatory wiggles in the power spectrum. The final form of the $P(k)$ model is:

$$P(k) = [P_{\text{lin}}(k) - P_{\text{nw}}(k)] e^{-\Sigma^2 k^2/2} + P_{\text{nw}}(k), \quad (\text{A.3})$$

where Σ is a parameter that models the damping caused by non-linear effects. Once the model for $P(k)$ is obtained, the expected $\xi_{\text{mm}}(r)$ model is derived by applying the inverse Fourier transform. Finally, according to Equation (3.12), this is related to the galaxy 2PCF, giving us the following relation for the large-scale bias parameter:

$$b = \sqrt{\frac{\xi_{\text{mm}}(r)}{\xi_{\text{hh}}(r)}}. \quad (\text{A.4})$$

To fit this model with the data, we use the mean of the 2PCF measurements along with the associated error, which corresponds to the covariance of the mocks, i.e., $\text{Cov}[\xi_{\text{hh}}]/N$. The only free parameters in the `BAOFitter` routine were the bias b , which is the primary parameter of interest, and the damping parameter Σ , which accounts for the suppression of the BAO peak due to nonlinear effects that could also impact the bias measurement.

The minimization was performed using the `iMinuit` routine², with the χ^2 minimization criterion:

$$\chi^2 = \sum_{i,j} [\xi_{\text{data}}(r_i) - \xi_{\text{model}}(r_i)] \text{Cov}_{ij}^{-1} [\xi_{\text{data}}(r_j) - \xi_{\text{model}}(r_j)]. \quad (\text{A.5})$$

This procedure was used to estimate the large-scale halo bias of the mocks described in Section 5.3.1 and used in Chapter 6. The fit was performed in the fitting range $r = [50, 150] h^{-1} \text{Mpc}$, and it lays the following result: $b = 1.87 \pm 0.03$. In Figure A.1 it is possible to see the match between the measured average 2PCF (blue line and dots) and the best fit model (orange solid line), at large scales (i.e., $r > 50 h^{-1} \text{Mpc}$).

²<https://github.com/scikit-hep/iminuit>

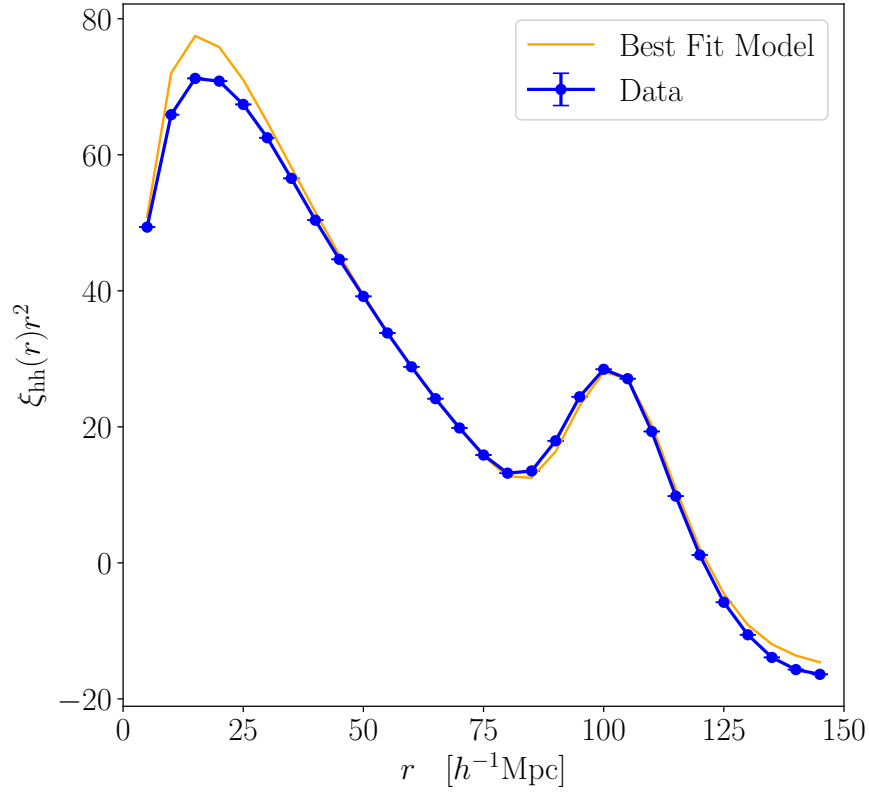


Figure A.1 In blue: measurements of the halo 2PCF $\xi_{\text{hh}}(r)$ of the mocks described in Section 5.3.1, with the associated error bars from the covariance matrix of the mocks $\text{Cov}[\xi_{\text{hh}}]/N$. In orange: the best fit model estimated with the procedure implemented in `BAOFitter`

List of publications

- **On the optimal extraction of the Alcock-Paczynski signal from voids**, Degni et al. in preparation, expected submission to the journal in February 2025.
- Second author in **Cosmology with voids from the Nancy Grace Roman Space Telescope**, Verza et al. (2024). Submitted to AAS journal.

List of contributions

First year

- **“Cosmic voids and their surroundings: a new cosmological probe”** at *Roma Tre Journal Club*, Roma Tre University, Italy, June 2022

Second year

- **“Cosmic voids: modelling distortions”** Contributed talk at *Euclid France Galaxy Clustering Meeting*, Laboratoire d’Astrophysique de Marseille, France, November 2022
- **“Dynamical reconstruction of cosmic voids”**, Contributed talk at *Euclid Consortium Galaxy Clustering Meeting*, Milan University, Italy, February 2023
- **“Cosmic voids: modelling distortions”**, Contributed talk at *Post-Industrial Bispectrum meeting*, Milan University, Italy, June 2023
- **“Cosmic voids: modelling distortions”**, talk at *CPPM’s Journal Club*, CPPM Marseille, France, July 2023
- **“The Void-Galaxy Cross-correlation function”**, talk at *Cosmology meeting*, Princeton University, USA, September 2023
- **“Cosmic voids: modelling distortions”**, Contributed talk at *CosmologyxML internal meeting*, Center for Computational Astrophysics, NYC, October 2023

Third year

- **“Cosmic voids: optimizing extraction of the AP signal with reconstruction”**, talk at *Euclid Galaxy Clustering meeting*, Marseille, France, January 2024

- **“Cosmic voids: optimizing extraction of the AP signal with reconstruction”**, talk at *Euclid Galaxy Clustering meeting*, Rome, Italy, June 2024
- **“On the optimal extraction of the AP signal from voids”**, Contributed talk at *Post-Industrial Trispectrum meeting*, Parma, Italy, June 2024
- **“On the optimal extraction of the AP signal from voids”**, Contributed talk at *The 17th Marcel Grossmann meeting*, Pescara, Italy, July 2024
- **“On the optimal extraction of the AP signal from voids”**, Contributed talk at *Understanding the Galaxy/Matter Connection in the Era of Large Surveys*, Sestri Levante, Italy, September 2024

References

- Sverre J Aarseth and F Hoyle. Dynamical evolution of clusters of galaxies, i. *Monthly Notices of the Royal Astronomical Society*, 126(3):223–255, 1963.
- Elcio Abdalla, Guillermo Franco Abellán, Amin Aboubrahim, Adriano Agnello, Özgür Akarsu, Yashar Akrami, George Alestas, Daniel Aloni, Luca Amendola, Luis A Anchordoqui, et al. Cosmology intertwined: A review of the particle physics, astrophysics, and cosmology associated with the cosmological tensions and anomalies. *Journal of High Energy Astrophysics*, 34:49–211, 2022.
- Tom Abel, Oliver Hahn, and Ralf Kaehler. Tracing the dark matter sheet in phase space. *Mon. Not. R. Astron. Soc.* , 427(1):61–76, November 2012. doi: 10.1111/j.1365-2966.2012.21754.x.
- I. Achitouv. New constraints on the linear growth rate using cosmic voids in the SDSS DR12 datasets. *Phys. Rev. D* , 100(12):123513, December 2019. doi: 10.1103/PhysRevD.100.123513.
- I. Achitouv, C. Blake, P. Carter, J. Koda, and F. Beutler. Consistency of the growth rate in different environments with the 6-degree Field Galaxy Survey: Measurement of the void-galaxy and galaxy-galaxy correlation functions. *Phys. Rev. D* , 95(8):083502, April 2017. doi: 10.1103/PhysRevD.95.083502.
- Ixandra Achitouv. Testing the imprint of nonstandard cosmologies on void profiles using monte carlo random walks. *Physical Review D*, 94(10):103524, 2016.
- Shadab Alam, Metin Ata, Stephen Bailey, Florian Beutler, Dmitry Bizyaev, Jonathan A. Blazek, Adam S. Bolton, Joel R. Brownstein, Angela Burden, Chia-Hsun Chuang, Johan Comparat, Antonio J. Cuesta, Kyle S. Dawson, Daniel J. Eisenstein, Stephanie Escoffier, Héctor Gil-Marín, Jan Niklas Grieb, Nick Hand, Shirley Ho, Karen Kinemuchi, David Kirkby, Francisco Kitaura, Elena Malanushenko, Viktor Malanushenko, Claudia Maraston,

- Cameron K. McBride, Robert C. Nichol, Matthew D. Olmstead, Daniel Oravetz, Nikhil Padmanabhan, Nathalie Palanque-Delabrouille, Kaike Pan, Marcos Pellejero-Ibanez, Will J. Percival, Patrick Petitjean, Francisco Prada, Adrian M. Price-Whelan, Beth A. Reid, Sergio A. Rodríguez-Torres, Natalie A. Roe, Ashley J. Ross, Nicholas P. Ross, Graziano Rossi, Jose Alberto Rubiño-Martín, Shun Saito, Salvador Salazar-Albornoz, Lado Samushia, Ariel G. Sánchez, Siddharth Satpathy, David J. Schlegel, Donald P. Schneider, Claudia G. Scóccola, Hee-Jong Seo, Erin S. Sheldon, Audrey Simmons, Anže Slosar, Michael A. Strauss, Molly E. C. Swanson, Daniel Thomas, Jeremy L. Tinker, Rita Tojeiro, Mariana Vargas Magaña, Jose Alberto Vazquez, Licia Verde, David A. Wake, Yuting Wang, David H. Weinberg, Martin White, W. Michael Wood-Vasey, Christophe Yèche, Idit Zehavi, Zhongxu Zhai, and Gong-Bo Zhao. The clustering of galaxies in the completed SDSS-III Baryon Oscillation Spectroscopic Survey: cosmological analysis of the DR12 galaxy sample. *Mon. Not. R. Astron. Soc.* , 470(3):2617–2652, September 2017. doi: 10.1093/mnras/stx721.
- Shadab Alam, Marie Aubert, Santiago Avila, Christophe Balland, Julian E. Bautista, Matthew A. Bershad, Dmitry Bizyaev, Michael R. Blanton, Adam S. Bolton, Jo Bovy, Jonathan Brinkmann, Joel R. Brownstein, Etienne Burtin, Solène Chabanier, Michael J. Chapman, Peter Doohyun Choi, Chia-Hsun Chuang, Johan Comparat, Marie-Claude Cousinou, Andrei Cuceu, Kyle S. Dawson, Sylvain de la Torre, Arnaud de Mattia, Victoria de Sainte Agathe, Héliion du Mas des Bourboux, Stephanie Escoffier, Thomas Etourneau, James Farr, Andreu Font-Ribera, Peter M. Frinchaboy, Sebastien Fromenteau, Héctor Gil-Marín, Jean-Marc Le Goff, Alma X. Gonzalez-Morales, Violeta Gonzalez-Perez, Kathleen Grabowski, Julien Guy, Adam J. Hawken, Jiamin Hou, Hui Kong, James Parker, Mark Klaene, Jean-Paul Kneib, Sicheng Lin, Daniel Long, Brad W. Lyke, Axel de la Macorra, Paul Martini, Karen Masters, Faizan G. Mohammad, Jeongin Moon, Eva-Maria Mueller, Andrea Muñoz-Gutiérrez, Adam D. Myers, Seshadri Nadathur, Richard Neveux, Jeffrey A. Newman, Pasquier Noterdaeme, Audrey Oravetz, Daniel Oravetz, Nathalie Palanque-Delabrouille, Kaike Pan, Romain Paviot, Will J. Percival, Ignasi Pérez-Ràfols, Patrick Petitjean, Matthew M. Pieri, Abhishek Prakash, Anand Raichoor, Corentin Ravoux, Mehdi Rezaie, James Rich, Ashley J. Ross, Graziano Rossi, Rossana Ruggeri, Vanina Ruhlmann-Kleider, Ariel G. Sánchez, F. Javier Sánchez, José R. Sánchez-Gallego, Conor Sayres, Donald P. Schneider, Hee-Jong Seo, Arman Shafieloo, Anže Slosar, Alex Smith, Julianna Stermer, Amelie Tamone, Jeremy L. Tinker, Rita Tojeiro, Mariana Vargas-Magaña, Andrei Variu, Yuting Wang, Benjamin A. Weaver, Anne-Marie Weijmans, Christophe Yèche, Pauline Zarrouk, Cheng Zhao, Gong-Bo Zhao, and Zheng Zheng. Completed SDSS-IV extended Baryon Oscillation Spectroscopic Survey: Cosmological implications from two

- decades of spectroscopic surveys at the Apache Point Observatory. *Phys. Rev. D* , 103(8): 083533, April 2021. doi: 10.1103/PhysRevD.103.083533.
- C. Alcock and B. Paczynski. An evolution free test for non-zero cosmological constant. *Nature*, 281:358, October 1979. doi: 10.1038/281358a0.
- R. A. Alpher, H. Bethe, and G. Gamow. The origin of chemical elements. *Phys. Rev.*, 73: 803–804, Apr 1948. doi: 10.1103/PhysRev.73.803. URL <https://link.aps.org/doi/10.1103/PhysRev.73.803>.
- Marie Aubert, Marie-Claude Cousinou, Stéphanie Escoffier, Adam J. Hawken, Seshadri Nadathur, Shadab Alam, Julian Bautista, Etienne Burtin, Chia-Hsun Chuang, Axel de la Macorra, Arnaud de Mattia, Héctor Gil-Marín, Jiamin Hou, Eric Jullo, Jean-Paul Kneib, Richard Neveux, Graziano Rossi, Donald Schneider, Alex Smith, Amélie Tamone, Mariana Vargas Magaña, and Cheng Zhao. The completed SDSS-IV extended Baryon Oscillation Spectroscopic Survey: growth rate of structure measurement from cosmic voids. *Mon. Not. R. Astron. Soc.* , 513(1):186–203, June 2022. doi: 10.1093/mnras/stac828.
- Marco Baldi and Francisco Villaescusa-Navarro. Cosmic degeneracies ii: Structure formation in joint simulations of warm dark matter and $f(r)$ gravity, 2016. URL <https://arxiv.org/abs/1608.08057>.
- W. E. Ballinger, J. A. Peacock, and A. F. Heavens. Measuring the cosmological constant with redshift surveys. *Mon. Not. R. Astron. Soc.* , 282:877, October 1996. doi: 10.1093/mnras/282.3.877.
- Arka Banerjee and Neal Dalal. Simulating nonlinear cosmological structure formation with massive neutrinos. *Journal of Cosmology and Astroparticle Physics*, 2016(11):015–015, November 2016. ISSN 1475-7516. doi: 10.1088/1475-7516/2016/11/015. URL <http://dx.doi.org/10.1088/1475-7516/2016/11/015>.
- J. M. Bardeen, J. R. Bond, N. Kaiser, and A. S. Szalay. The Statistics of Peaks of Gaussian Random Fields. *Astrophys. J.* , 304:15, May 1986. doi: 10.1086/164143.
- Adrian E. Bayer, Francisco Villaescusa-Navarro, Elena Massara, Jia Liu, David N. Spergel, Licia Verde, Benjamin D. Wandelt, Matteo Viel, and Shirley Ho. Detecting Neutrino Mass by Combining Matter Clustering, Halos, and Voids. *Astrophys. J.* , 919(1):24, September 2021. doi: 10.3847/1538-4357/ac0e91.
- C. L. Bennett, D. Larson, J. L. Weiland, N. Jarosik, G. Hinshaw, N. Odegard, K. M. Smith, R. S. Hill, B. Gold, M. Halpern, E. Komatsu, M. R. Nolta, L. Page, D. N. Spergel,

- E. Wollack, J. Dunkley, A. Kogut, M. Limon, S. S. Meyer, G. S. Tucker, and E. L. Wright. Nine-year Wilkinson Microwave Anisotropy Probe (WMAP) Observations: Final Maps and Results. *Astrophys. J. Suppl.* , 208(2):20, October 2013. doi: 10.1088/0067-0049/208/2/20.
- Andrew J. Benson. G ALACTICUS: A semi-analytic model of galaxy formation. *New Astronomy*, 17(2):175–197, February 2012. doi: 10.1016/j.newast.2011.07.004.
- Gianfranco Bertone and Dan Hooper. History of dark matter. *Reviews of Modern Physics*, 90(4):045002, 2018.
- Beyond-2pt Collaboration, :, Elisabeth Krause, Yosuke Kobayashi, Andrés N. Salcedo, Mikhail M. Ivanov, Tom Abel, Kazuyuki Akitsu, Raul E. Angulo, Giovanni Cabass, Sofia Contarini, Carolina Cuesta-Lazaro, ChangHoon Hahn, Nico Hamaus, Donghui Jeong, Chirag Modi, Nhat-Minh Nguyen, Takahiro Nishimichi, Enrique Paillas, Marcos Pellejero Ibañez, Oliver H. E. Philcox, Alice Pisani, Fabian Schmidt, Satoshi Tanaka, Giovanni Verza, Sihan Yuan, and Matteo Zennaro. A Parameter-Masked Mock Data Challenge for Beyond-Two-Point Galaxy Clustering Statistics. *arXiv e-prints*, art. arXiv:2405.02252, May 2024. doi: 10.48550/arXiv.2405.02252.
- Rahul Biswas, Esfandiar Alizadeh, and Benjamin D Wandelt. Voids as a precision probe of dark energy. *Physical Review D—Particles, Fields, Gravitation, and Cosmology*, 82(2):023002, 2010.
- Michael R Blanton, David W Hogg, Neta A Bahcall, J Brinkmann, Malcolm Britton, Andrew J Connolly, István Csabai, Masataka Fukugita, Jon Loveday, Avery Meiksin, et al. The galaxy luminosity function and luminosity density at redshift $z=0.1$. *The Astrophysical Journal*, 592(2):819, 2003.
- J. R. Bond, S. Cole, G. Efstathiou, and N. Kaiser. Excursion Set Mass Functions for Hierarchical Gaussian Fluctuations. *Astrophys. J.* , 379:440, October 1991. doi: 10.1086/170520.
- M. Bonici, C. Carbone, S. Davini, P. Vielzeuf, L. Paganin, V. Cardone, N. Hamaus, A. Pisani, A. J. Hawken, A. Kovacs, S. Nadathur, S. Contarini, G. Verza, I. Tutusaus, F. Marulli, L. Moscardini, M. Aubert, C. Giocoli, A. Pourtsidou, S. Camera, S. Escoffier, A. Caminata, S. Di Domizio, M. Martinelli, M. Pallavicini, V. Pettorino, Z. Sakr, D. Sapone, G. Testera, S. Tosi, V. Yankelevich, A. Amara, N. Auricchio, M. Baldi, D. Bonino, E. Branchini, M. Brescia, J. Brinchmann, V. Capobianco, J. Carretero, M. Castellano, S. Cavuoti,

- R. Cledassou, G. Congedo, L. Conversi, Y. Copin, L. Corcione, F. Courbin, M. Cropper, A. Da Silva, H. Degaudenzi, M. Douspis, F. Dubath, C. A. J. Duncan, X. Dupac, S. Dusini, A. Ealet, S. Farrens, S. Ferriol, P. Fosalba, M. Frailis, E. Franceschi, M. Fumana, P. Gómez-Alvarez, B. Garilli, B. Gillis, A. Grazian, F. Grupp, L. Guzzo, S. V. H. Haugan, W. Holmes, F. Hormuth, A. Hornstrup, K. Jahnke, M. Kümmel, S. Kermiche, A. Kiessling, M. Kilbinger, M. Kunz, H. Kurki-Suonio, R. Laureijs, S. Ligi, P. B. Lilje, I. Lloro, E. Maiorano, O. Mansutti, O. Marggraf, K. Markovic, R. Massey, E. Medinaceli, M. Melchior, M. Meneghetti, G. Meylan, M. Moresco, E. Munari, S. M. Niemi, C. Padilla, S. Paltani, F. Pasian, K. Pedersen, W. J. Percival, S. Pires, G. Polenta, M. Poncet, L. Popa, F. Raison, R. Rebolo, A. Renzi, J. Rhodes, E. Rossetti, R. Saglia, B. Sartoris, M. Scodreggio, A. Secroun, G. Seidel, C. Sirignano, G. Sirri, L. Stanco, J. L. Starck, C. Surace, P. Tallada-Crespí, D. Tavagnacco, A. N. Taylor, I. Tereno, R. Toledo-Moreo, F. Torradeflot, E. A. Valentijn, L. Valenziano, Y. Wang, J. Weller, G. Zamorani, J. Zoubian, and S. Andreon. Euclid: Forecasts from the void-lensing cross-correlation. *Astron. Astrophys.*, 670:A47, February 2023. doi: 10.1051/0004-6361/202244445.
- E. G. Patrick Bos, Rien van de Weygaert, Klaus Dolag, and Valeria Pettorino. The darkness that shaped the void: dark energy and cosmic voids. *Mon. Not. R. Astron. Soc.*, 426(1): 440–461, October 2012. doi: 10.1111/j.1365-2966.2012.21478.x.
- R. Bracewell. *The Fourier Transform and Its Applications, 3rd ed.* McGraw-Hill, 1999.
- T. J. Broadhurst, R. S. Ellis, D. C. Koo, and A. S. Szalay. Large-scale distribution of galaxies at the Galactic poles. *Nature*, 343(6260):726–728, February 1990. doi: 10.1038/343726a0.
- Yan-Chuan Cai, Nelson Padilla, and Baojiu Li. Testing gravity using cosmic voids. *Monthly Notices of the Royal Astronomical Society*, 451(1):1036–1055, 2015.
- Yan-Chuan Cai, Andy Taylor, John A. Peacock, and Nelson Padilla. Redshift-space distortions around voids. *Mon. Not. R. Astron. Soc.*, 462(3):2465–2477, November 2016. doi: 10.1093/mnras/stw1809.
- Marius Cautun, Rien van de Weygaert, Bernard J. T. Jones, and Carlos S. Frenk. Evolution of the cosmic web. *Mon. Not. R. Astron. Soc.*, 441(4):2923–2973, July 2014. doi: 10.1093/mnras/stu768.
- Marius Cautun, Yan-Chuan Cai, and Carlos S Frenk. The view from the boundary: a new void stacking method. *Monthly Notices of the Royal Astronomical Society*, 457(3):2540–2553, 2016.

- Marius Cautun, Enrique Paillas, Yan-Chuan Cai, Sownak Bose, Joaquin Armijo, Baojiu Li, and Nelson Padilla. The santiago–harvard–edinburgh–durham void comparison–i. shedding light on chameleon gravity tests. *Monthly Notices of the Royal Astronomical Society*, 476(3):3195–3217, 2018.
- Laura Ceccarelli, D Paz, Marcelo Lares, Nelson Padilla, and D García Lambas. Clues on void evolution–i. large-scale galaxy distributions around voids. *Monthly Notices of the Royal Astronomical Society*, 434(2):1435–1442, 2013.
- Laura Ceccarelli, Andrés N Ruiz, Marcelo Lares, Dante J Paz, Victoria E Maldonado, Heliana E Luparello, and Diego Garcia Lambas. The sparkling universe: a scenario for cosmic void motions. *Monthly Notices of the Royal Astronomical Society*, 461(4):4013–4021, 2016.
- Kwan Chuen Chan, Nico Hamaus, and Vincent Desjacques. Large-scale clustering of cosmic voids. *Physical Review D*, 90(10):103521, 2014.
- Kwan Chuen Chan, Nico Hamaus, and Matteo Biagetti. Constraint of void bias on primordial non-gaussianity. *Physical Review D*, 99(12):121304, 2019.
- Michel Chevallier and David Polarski. Accelerating Universes with Scaling Dark Matter. *International Journal of Modern Physics D*, 10(2):213–223, January 2001. doi: 10.1142/S0218271801000822.
- Chia-Hsun Chuang, Francisco-Shu Kitaura, Yu Liang, Andreu Font-Ribera, Cheng Zhao, Patrick McDonald, and Charling Tao. Linear redshift space distortions for cosmic voids based on galaxies in redshift space. *Physical Review D*, 95(6):063528, 2017.
- Chia-Hsun Chuang, Gustavo Yepes, Francisco-Shu Kitaura, Marcos Pellejero-Ibanez, Sergio Rodríguez-Torres, Yu Feng, Robert Benton Metcalf, Risa H. Wechsler, Cheng Zhao, Chun-Hao To, Shadab Alam, Arka Banerjee, Joseph DeRose, Carlo Giocoli, Alexander Knebe, and Guillermo Reyes. UNIT project: Universe N-body simulations for the Investigation of Theoretical models from galaxy surveys. *Mon. Not. R. Astron. Soc.* , 487(1):48–59, July 2019. doi: 10.1093/mnras/stz1233.
- Joseph Clampitt, Yan-Chuan Cai, and Baojiu Li. Voids in modified gravity: excursion set predictions. *Monthly Notices of the Royal Astronomical Society*, 431(1):749–766, 2013.
- Jörg M Colberg, Frazer Pearce, Caroline Foster, Erwin Platen, Riccardo Brunino, Mark Neyrinck, Spyros Basilakos, Anthony Fairall, Hume Feldman, Stefan Gottlöber, et al.

- The aspen–amsterdam void finder comparison project. *Monthly Notices of the Royal Astronomical Society*, 387(2):933–944, 2008.
- Peter Coles, Adrian L. Melott, and Sergei F. Shandarin. Testing approximations for non-linear gravitational clustering. *Mon. Not. R. Astron. Soc.*, 260(4):765–776, February 1993. doi: 10.1093/mnras/260.4.765.
- S. Contarini, G. Verza, A. Pisani, N. Hamaus, M. Sahlén, C. Carbone, S. Dusini, F. Marulli, L. Moscardini, A. Renzi, C. Sirignano, L. Stanco, M. Aubert, M. Bonici, G. Castignani, H. M. Courtois, S. Escoffier, D. Guinet, A. Kovacs, G. Lavaux, E. Massara, S. Nadathur, G. Pollina, T. Ronconi, F. Ruppin, Z. Sakr, A. Veropalumbo, B. D. Wandelt, A. Amara, N. Auricchio, M. Baldi, D. Bonino, E. Branchini, M. Brescia, J. Brinchmann, S. Camera, V. Capobianco, J. Carretero, M. Castellano, S. Cavuoti, R. Cledassou, G. Congedo, C. J. Conselice, L. Conversi, Y. Copin, L. Corcione, F. Courbin, M. Cropper, A. Da Silva, H. Degaudenzi, F. Dubath, C. A. J. Duncan, X. Dupac, A. Ealet, S. Farrens, S. Ferriol, P. Fosalba, M. Frailis, E. Franceschi, B. Garilli, W. Gillard, B. Gillis, C. Giocoli, A. Grazian, F. Grupp, L. Guzzo, S. Haugan, W. Holmes, F. Hormuth, K. Jahnke, M. Kümmel, S. Kermiche, A. Kiessling, M. Kilbinger, M. Kunz, H. Kurki-Suonio, R. Laureijs, S. Ligi, P. B. Lilje, I. Lloro, E. Maiorano, O. Mansutti, O. Marggraf, K. Markovic, R. Massey, M. Melchior, M. Meneghetti, G. Meylan, M. Moresco, E. Munari, S. M. Niemi, C. Padilla, S. Paltani, F. Pasian, K. Pedersen, W. J. Percival, V. Pettorino, S. Pires, G. Polenta, M. Poncet, L. Popa, L. Pozzetti, F. Raison, J. Rhodes, E. Rossetti, R. Saglia, B. Sartoris, P. Schneider, A. Secroun, G. Seidel, G. Sirri, C. Surace, P. Tallada-Crespí, A. N. Taylor, I. Tereno, R. Toledo-Moreo, F. Torradeflot, E. A. Valentijn, L. Valenziano, Y. Wang, J. Weller, G. Zamorani, J. Zoubian, S. Andreon, D. Maino, and S. Mei. Euclid: Cosmological forecasts from the void size function. *Astron. Astrophys.*, 667:A162, November 2022. doi: 10.1051/0004-6361/202244095.
- S. Contarini, A. Pisani, N. Hamaus, F. Marulli, L. Moscardini, and M. Baldi. The perspective of voids on rising cosmology tensions. *Astron. Astrophys.*, 682:A20, February 2024. doi: 10.1051/0004-6361/202347572.
- Sofia Contarini, Tommaso Ronconi, Federico Marulli, Lauro Moscardini, Alfonso Veropalumbo, and Marco Baldi. Cosmological exploitation of the size function of cosmic voids identified in the distribution of biased tracers. *Mon. Not. R. Astron. Soc.*, 488(3): 3526–3540, September 2019. doi: 10.1093/mnras/stz1989.

- Sofia Contarini, Alice Pisani, Nico Hamaus, Federico Marulli, Lauro Moscardini, and Marco Baldi. Cosmological Constraints from the BOSS DR12 Void Size Function. *Astrophys. J.* , 953(1):46, August 2023. doi: 10.3847/1538-4357/acde54.
- Asantha Cooray and Ravi Sheth. Halo models of large scale structure. *Physics reports*, 372(1):1–129, 2002.
- Carlos M. Correa, Dante J. Paz, Nelson D. Padilla, Andrés N. Ruiz, Raúl E. Angulo, and Ariel G. Sánchez. Non-fiducial cosmological test from geometrical and dynamical distortions around voids. *Mon. Not. R. Astron. Soc.* , 485(4):5761–5772, Jun 2019. doi: 10.1093/mnras/stz821.
- Carlos M. Correa, Dante J. Paz, Ariel G. Sánchez, Andrés N. Ruiz, Nelson D. Padilla, and Raúl E. Angulo. Redshift-space effects in voids and their impact on cosmological tests. Part I: the void size function. *Mon. Not. R. Astron. Soc.* , 500(1):911–925, January 2021. doi: 10.1093/mnras/staa3252.
- Carlos M. Correa, Dante J. Paz, Nelson D. Padilla, Ariel G. Sánchez, Andrés N. Ruiz, and Raúl E. Angulo. Redshift-space effects in voids and their impact on cosmological tests - II. The void-galaxy cross-correlation function. *Mon. Not. R. Astron. Soc.* , 509(2):1871–1884, January 2022. doi: 10.1093/mnras/stab3070.
- HM Courtois, A Dupuy, D Guinet, G Baulieu, F Ruppin, and P Brenas. Gravity in the local universe: density and velocity fields using cosmicflows-4. *Astronomy & Astrophysics*, 670:L15, 2023.
- M. C. Cousinou, A. Pisani, A. Tilquin, N. Hamaus, A. J. Hawken, and S. Escoffier. Multi-variate analysis of cosmic void characteristics. *Astronomy and Computing*, 27:53, April 2019. doi: 10.1016/j.ascom.2019.03.001.
- Christopher T Davies, Enrique Paillas, Marius Cautun, and Baojiu Li. Optimal void finders in weak lensing maps. *Monthly Notices of the Royal Astronomical Society*, 500(2):2417–2439, 2021.
- M. Davis and P. J. E. Peebles. A survey of galaxy redshifts. V. The two-point position and velocity correlations. *Astrophys. J.* , 267:465–482, April 1983. doi: 10.1086/160884.
- Marc Davis, George Efstathiou, Carlos S Frenk, and Simon DM White. The evolution of large-scale structure in a universe dominated by cold dark matter. *Astrophysical Journal, Part 1 (ISSN 0004-637X)*, vol. 292, May 15, 1985, p. 371-394. Research supported by the Science and Engineering Research Council of England and NASA., 292:371–394, 1985.

Kyle S. Dawson, David J. Schlegel, Christopher P. Ahn, Scott F. Anderson, Éric Aubourg, Stephen Bailey, Robert H. Barkhouser, Julian E. Bautista, Alessandra Beifiori, Andreas A. Berlind, Vaishali Bhardwaj, Dmitry Bizyaev, Cullen H. Blake, Michael R. Blanton, Michael Blomqvist, Adam S. Bolton, Arnaud Borde, Jo Bovy, W. N. Brandt, Howard Brewington, Jon Brinkmann, Peter J. Brown, Joel R. Brownstein, Kevin Bundy, N. G. Busca, William Carithers, Aurelio R. Carnero, Michael A. Carr, Yanmei Chen, Johan Comparat, Natalia Connolly, Frances Cope, Rupert A. C. Croft, Antonio J. Cuesta, Luiz N. da Costa, James R. A. Davenport, Timothée Delubac, Roland de Putter, Saurav Dhital, Anne Ealet, Garrett L. Ebelke, Daniel J. Eisenstein, S. Escoffier, Xiaohui Fan, N. Filiz Ak, Hayley Finley, Andreu Font-Ribera, R. Génova-Santos, James E. Gunn, Hong Guo, Daryl Haggard, Patrick B. Hall, Jean-Christophe Hamilton, Ben Harris, David W. Harris, Shirley Ho, David W. Hogg, Diana Holder, Klaus Honscheid, Joe Huehnerhoff, Beatrice Jordan, Wendell P. Jordan, Guinevere Kauffmann, Eyal A. Kazin, David Kirkby, Mark A. Klaene, Jean-Paul Kneib, Jean-Marc Le Goff, Khee-Gan Lee, Daniel C. Long, Craig P. Loomis, Britt Lundgren, Robert H. Lupton, Marcio A. G. Maia, Martin Makler, Elena Malanushenko, Viktor Malanushenko, Rachel Mandelbaum, Marc Manera, Claudia Maraston, Daniel Margala, Karen L. Masters, Cameron K. McBride, Patrick McDonald, Ian D. McGreer, Richard G. McMahon, Olga Mena, Jordi Miralda-Escudé, Antonio D. Montero-Dorta, Francesco Montesano, Demitri Muna, Adam D. Myers, Tracy Naugle, Robert C. Nichol, Pasquier Noterdaeme, Sebastián E. Nuza, Matthew D. Olmstead, Audrey Oravetz, Daniel J. Oravetz, Russell Owen, Nikhil Padmanabhan, Nathalie Palanque-Delabrouille, Kaike Pan, John K. Parejko, Isabelle Pâris, Will J. Percival, Ismael Pérez-Fournon, Ignasi Pérez-Ràfols, Patrick Petitjean, Robert Pfaffenberger, Janine Pforr, Matthew M. Pieri, Francisco Prada, Adrian M. Price-Whelan, M. Jordan Raddick, Rafael Rebolo, James Rich, Gordon T. Richards, Constance M. Rockosi, Natalie A. Roe, Ashley J. Ross, Nicholas P. Ross, Graziano Rossi, J. A. Rubiño-Martin, Lado Samushia, Ariel G. Sánchez, Conor Sayres, Sarah J. Schmidt, Donald P. Schneider, C. G. Scóccola, Hee-Jong Seo, Alaina Shelden, Erin Sheldon, Yue Shen, Yiping Shu, Anže Slosar, Stephen A. Smee, Stephanie A. Snedden, Fritz Stauffer, Oliver Steele, Michael A. Strauss, Alina Streblyanska, Nao Suzuki, Molly E. C. Swanson, Tomer Tal, Masayuki Tanaka, Daniel Thomas, Jeremy L. Tinker, Rita Tojeiro, Christy A. Tremonti, M. Vargas Magaña, Licia Verde, Matteo Viel, David A. Wake, Mike Watson, Benjamin A. Weaver, David H. Weinberg, Benjamin J. Weiner, Andrew A. West, Martin White, W. M. Wood-Vasey, Christophe Yèche, Idit Zehavi, Gong-Bo Zhao, and Zheng Zheng. The baryon oscillation spectroscopic survey of sdss-iii. *The Astronomical Journal*, 145(1):10, December 2012. ISSN 1538-3881. doi: 10.1088/0004-6256/145/1/10. URL <http://dx.doi.org/10.1088/0004-6256/145/1/10>.

- P. de Bernardis, P.A.R. Ade, R. Artusa, J.J. Bock, A. Boscaleri, B.P. Crill, G. De Troia, P.C. Farese, M. Giacometti, V.V. Hristov, A. Iacoangeli, A.E. Lange, A.T. Lee, S. Masi, L. Martinis, P.V. Mason, P.D. Mauskopf, F. Melchiorri, L. Miglio, T. Montroy, C.B. Netterfield, E. Pascale, F. Piacentini, P.L. Richards, J.E. Ruhl, and F. Scaramuzzi. Mapping the cmb sky: The boomerang experiment. *New Astronomy Reviews*, 43(2–4):289–296, July 1999. ISSN 1387-6473. doi: 10.1016/s1387-6473(99)00022-6. URL [http://dx.doi.org/10.1016/S1387-6473\(99\)00022-6](http://dx.doi.org/10.1016/S1387-6473(99)00022-6).
- P. de Bernardis, P. A. R. Ade, J. J. Bock, J. R. Bond, J. Borrill, A. Boscaleri, K. Coble, B. P. Crill, G. De Gasperis, P. C. Farese, P. G. Ferreira, K. Ganga, M. Giacometti, E. Hivon, V. V. Hristov, A. Iacoangeli, A. H. Jaffe, A. E. Lange, L. Martinis, S. Masi, P. V. Mason, P. D. Mauskopf, A. Melchiorri, L. Miglio, T. Montroy, C. B. Netterfield, E. Pascale, F. Piacentini, D. Pogosyan, S. Prunet, S. Rao, G. Romeo, J. E. Ruhl, F. Scaramuzzi, D. Sforna, and N. Vittorio. A flat universe from high-resolution maps of the cosmic microwave background radiation. *Nature*, 404(6781):955–959, April 2000. ISSN 1476-4687. doi: 10.1038/35010035. URL <http://dx.doi.org/10.1038/35010035>.
- Valérie De Lapparent, Margaret J Geller, and John P Huchra. A slice of the universe. *Astrophysical Journal, Part 2-Letters to the Editor (ISSN 0004-637X)*, vol. 302, March 1, 1986, p. L1-L5. Research supported by the Smithsonian Institution., 302:L1–L5, 1986.
- DESI Collaboration, B. Abareschi, J. Aguilar, S. Ahlen, Shadab Alam, David M. Alexander, R. Alfarsy, L. Allen, C. Allende Prieto, O. Alves, J. Ameel, E. Armengaud, J. Asorey, Alejandro Aviles, S. Bailey, A. Balaguera-Antolínez, O. Ballester, C. Baltay, A. Bault, S. F. Beltran, B. Benavides, S. BenZvi, A. Berti, R. Besuner, Florian Beutler, D. Bianchi, C. Blake, P. Blanc, R. Blum, A. Bolton, S. Bose, D. Bramall, S. Brieden, A. Brodzeller, D. Brooks, C. Brownell, E. Buckley-Geer, R. N. Cahn, Z. Cai, R. Canning, R. Capasso, A. Carnero Rosell, P. Carton, R. Casas, F. J. Castander, J. L. Cervantes-Cota, S. Chabanier, E. Chaussidon, C. Chuang, C. Circosta, S. Cole, A. P. Cooper, L. da Costa, M. C. Cousinou, A. Cuceu, T. M. Davis, K. Dawson, R. de la Cruz-Noriega, A. de la Macorra, A. de Mattia, J. Della Costa, P. Demmer, M. Derwent, A. Dey, B. Dey, G. Dhungana, Z. Ding, C. Dobson, P. Doel, J. Donald-McCann, J. Donaldson, K. Douglass, Y. Duan, P. Dunlop, J. Edelman, S. Eftekharzadeh, D. J. Eisenstein, M. Enriquez-Vargas, S. Escoffier, M. Evatt, P. Fagrellius, X. Fan, K. Fanning, V. A. Fawcett, S. Ferraro, J. Ereza, B. Flaugher, A. Font-Ribera, J. E. Forero-Romero, C. S. Frenk, S. Fromenteau, B. T. Gänsicke, C. Garcia-Quintero, L. Garrison, E. Gaztañaga, F. Gerardi, H. Gil-Marín, S. Gontcho A Gontcho, Alma X. Gonzalez-Morales, G. Gonzalez-de-Rivera, V. Gonzalez-Perez, C. Gordon, O. Graur, D. Green, C. Grove, D. Gruen, G. Gutierrez, J. Guy, C. Hahn, S. Harris, D. Herrera,

- Hiram K. Herrera-Alcantar, K. Honscheid, C. Howlett, D. Huterer, V. Iršič, M. Ishak, P. Jelinsky, L. Jiang, J. Jimenez, Y. P. Jing, R. Joyce, E. Jullo, S. Juneau, N. G. Karaçaylı, M. Karamanis, A. Karcher, T. Karim, R. Kehoe, S. Kent, D. Kirkby, T. Kisner, F. Kitaura, S. E. Kopolov, A. Kovács, A. Kremin, Alex Krolewski, B. L’Huillier, O. Lahav, A. Lambert, C. Lamman, Ting-Wen Lan, M. Landriau, S. Lane, D. Lang, J. U. Lange, J. Lasker, L. Le Guillou, A. Leauthaud, A. Le Van Suu, Michael E. Levi, T. S. Li, C. Magneville, M. Manera, Christopher J. Manser, B. Marshall, Paul Martini, W. McCollam, P. McDonald, Aaron M. Meisner, J. Mena-Fernández, J. Meneses-Rizo, M. Mezcua, T. Miller, R. Miquel, P. Montero-Camacho, J. Moon, J. Moustakas, E. Mueller, Andrea Muñoz-Gutiérrez, Adam D. Myers, S. Nadathur, J. Najita, L. Napolitano, E. Neilsen, Jeffrey A. Newman, J. D. Nie, Y. Ning, G. Niz, P. Norberg, Hernán E. Noriega, T. O’Brien, A. Obuljen, N. Palanque-Delabrouille, A. Palmese, P. Zhiwei, D. Pappalardo, X. PENG, W. J. Percival, S. Perruchot, R. Pogge, C. Poppett, A. Porredon, F. Prada, J. Prochaska, R. Pucha, A. Pérez-Fernández, I. Pérez-Ràfols, D. Rabinowitz, A. Raichoor, S. Ramirez-Solano, César Ramírez-Pérez, C. Ravoux, K. Reil, M. Rezaie, A. Rocher, C. Rockosi, N. A. Roe, A. Roodman, A. J. Ross, G. Rossi, R. Ruggeri, V. Ruhlmann-Kleider, C. G. Sabiu, S. Gaines, K. Said, A. Saintonge, Javier Salas Catonga, L. Samushia, E. Sanchez, C. Saulder, E. Schaan, E. Schlafly, D. Schlegel, J. Schmoll, D. Scholte, M. Schubnell, A. Secroun, H. Seo, S. Serrano, Ray M. Sharples, Michael J. Sholl, Joseph Harry Silber, D. R. Silva, M. Sirk, M. Siudek, A. Smith, D. Sprayberry, R. Staten, B. Stupak, T. Tan, Gregory Tarlé, Suk Sien Tie, R. Tojeiro, L. A. Ureña-López, F. Valdes, O. Valenzuela, M. Valluri, M. Vargas-Magaña, L. Verde, M. Walther, B. Wang, M. S. Wang, B. A. Weaver, C. Weaverdyck, R. Wechsler, Michael J. Wilson, J. Yang, Y. Yu, S. Yuan, Christophe Yèche, H. Zhang, K. Zhang, Cheng Zhao, Rongpu Zhou, Zhimin Zhou, H. Zou, J. Zou, S. Zou, and Y. Zu. Overview of the Instrumentation for the Dark Energy Spectroscopic Instrument. *Astron. J.* , 164(5):207, November 2022. doi: 10.3847/1538-3881/ac882b.
- DESI Collaboration, A. G. Adame, J. Aguilar, S. Ahlen, S. Alam, D. M. Alexander, M. Alvarez, O. Alves, A. Anand, U. Andrade, E. Armengaud, S. Avila, A. Aviles, H. Awan, B. Bahr-Kalus, S. Bailey, C. Baltay, A. Bault, J. Behera, S. BenZvi, A. Bera, F. Beutler, D. Bianchi, C. Blake, R. Blum, S. Brieden, A. Brodzeller, D. Brooks, E. Buckley-Geer, E. Burtin, R. Calderon, R. Canning, A. Carnero Rosell, R. Cereskaite, J. L. Cervantes-Cota, S. Chabanier, E. Chaussidon, J. Chaves-Montero, S. Chen, X. Chen, T. Claybaugh, S. Cole, A. Cuceu, T. M. Davis, K. Dawson, A. de la Macorra, A. de Mattia, N. Deiosso, A. Dey, B. Dey, Z. Ding, P. Doel, J. Edelstein, S. Eftekharzadeh, D. J. Eisenstein, A. Elliott, P. Fagrelus, K. Fanning, S. Ferraro, J. Ereza, N. Findlay, B. Flaugher, A. Font-Ribera, D. Forero-Sánchez, J. E. Forero-Romero, C. S. Frenk, C. Garcia-Quintero, E. Gaztañaga,

- H. Gil-Marín, S. Gontcho A Gontcho, A. X. Gonzalez-Morales, V. Gonzalez-Perez, C. Gordon, D. Green, D. Gruen, R. Gsponer, G. Gutierrez, J. Guy, B. Hadzhiyska, C. Hahn, M. M. S Hanif, H. K. Herrera-Alcantar, K. Honscheid, C. Howlett, D. Huterer, V. Iršič, M. Ishak, S. Juneau, N. G. Karaçaylı, R. Kehoe, S. Kent, D. Kirkby, A. Kremin, A. Krolewski, Y. Lai, T. W. Lan, M. Landriau, D. Lang, J. Lasker, J. M. Le Goff, L. Le Guillou, A. Leauthaud, M. E. Levi, T. S. Li, E. Linder, K. Lodha, C. Magneville, M. Manera, D. Margala, P. Martini, M. Maus, P. McDonald, L. Medina-Varela, A. Meisner, J. Mena-Fernández, R. Miquel, J. Moon, S. Moore, J. Moustakas, N. Mudur, E. Mueller, A. Muñoz-Gutiérrez, A. D. Myers, S. Nadathur, L. Napolitano, R. Neveux, J. A. Newman, N. M. Nguyen, J. Nie, G. Niz, H. E. Noriega, N. Padmanabhan, E. Paillas, N. Palanque-Delabrouille, J. Pan, S. Penmetsa, W. J. Percival, M. M. Pieri, M. Pinon, C. Poppett, A. Porredon, F. Prada, A. Pérez-Fernández, I. Pérez-Ràfols, D. Rabinowitz, A. Raichoor, C. Ramírez-Pérez, S. Ramirez-Solano, C. Ravoux, M. Rashkovetskyi, M. Rezaie, J. Rich, A. Rocher, C. Rockosi, N. A. Roe, A. Rosado-Marin, A. J. Ross, G. Rossi, R. Ruggeri, V. Ruhlmann-Kleider, L. Samushia, E. Sanchez, C. Saulder, E. F. Schlafly, D. Schlegel, M. Schubnell, H. Seo, A. Shafieloo, R. Sharples, J. Silber, A. Slosar, A. Smith, D. Sprayberry, T. Tan, G. Tarlé, P. Taylor, S. Trusov, L. A. Ureña-López, R. Vaisakh, D. Valcin, F. Valdes, M. Vargas-Magaña, L. Verde, M. Walther, B. Wang, M. S. Wang, B. A. Weaver, N. Weaverdyck, R. H. Wechsler, D. H. Weinberg, M. White, J. Yu, Y. Yu, S. Yuan, C. Yèche, E. A. Zaborowski, P. Zarrouk, H. Zhang, C. Zhao, R. Zhao, R. Zhou, T. Zhuang, and H. Zou. DESI 2024 VI: Cosmological Constraints from the Measurements of Baryon Acoustic Oscillations. *arXiv e-prints*, art. arXiv:2404.03002, April 2024. doi: 10.48550/arXiv.2404.03002.
- Vincent Desjacques, Donghui Jeong, and Fabian Schmidt. Large-scale galaxy bias. *Physics reports*, 733:1–193, 2018.
- R. H. Dicke, P. J. E. Peebles, P. G. Roll, and D. T. Wilkinson. Cosmic Black-Body Radiation. *Astrophys. J.* , 142:414–419, July 1965. doi: 10.1086/148306.
- Robert Henry Dicke. Gravitation and the universe. *Gravitation and the universe*, 1972.
- Scott Dodelson and Fabian Schmidt. *Modern cosmology*. Academic press, 2020.
- K. Dolag, S. Borgani, G. Murante, and V. Springel. Substructures in hydrodynamical cluster simulations. *Mon. Not. R. Astron. Soc.* , 399(2):497–514, October 2009. doi: 10.1111/j.1365-2966.2009.15034.x.

- Olivier Dore, C Hirata, Y Wang, D Weinberg, Tim Eifler, RJ Foley, C He Heinrich, E Krause, S Perlmutter, A Pisani, et al. Wfirst: the essential cosmology space observatory for the coming decade. *arXiv preprint arXiv:1904.01174*, 2019.
- Daniel J. Eisenstein and Wayne Hu. Power Spectra for Cold Dark Matter and Its Variants. *Astrophys. J.* , 511(1):5–15, January 1999. doi: 10.1086/306640.
- Daniel J. Eisenstein, Idit Zehavi, David W. Hogg, Roman Scoccimarro, Michael R. Blanton, Robert C. Nichol, Ryan Scranton, Hee-Jong Seo, Max Tegmark, Zheng Zheng, Scott F. Anderson, Jim Annis, Neta Bahcall, Jon Brinkmann, Scott Burles, Francisco J. Castander, Andrew Connolly, Istvan Csabai, Mamoru Doi, Masataka Fukugita, Joshua A. Frieman, Karl Glazebrook, James E. Gunn, John S. Hendry, Gregory Hennessy, Zeljko Ivezić, Stephen Kent, Gillian R. Knapp, Huan Lin, Yeong-Shang Loh, Robert H. Lupton, Bruce Margon, Timothy A. McKay, Avery Meiksin, Jeffery A. Munn, Adrian Pope, Michael W. Richmond, David Schlegel, Donald P. Schneider, Kazuhiro Shimasaku, Christopher Stoughton, Michael A. Strauss, Mark SubbaRao, Alexander S. Szalay, István Szapudi, Douglas L. Tucker, Brian Yanny, and Donald G. York. Detection of the Baryon Acoustic Peak in the Large-Scale Correlation Function of SDSS Luminous Red Galaxies. *Astrophys. J.* , 633(2):560–574, November 2005. doi: 10.1086/466512.
- AA Elyiv, ID Karachentsev, VE Karachentseva, OV Melnyk, and DI Makarov. Low-density structures in the local universe. ii. nearby cosmic voids. *Astrophysical Bulletin*, 68:1–13, 2013.
- Andrii Elyiv, Federico Marulli, Giorgia Pollina, Marco Baldi, Enzo Branchini, Andrea Cimatti, and Lauro Moscardini. Cosmic voids detection without density measurements. *Monthly Notices of the Royal Astronomical Society*, 448(1):642–653, 2015.
- K. A. Eriksen, A. R. Marble, C. D. Impey, L. Bai, and C. E. Petry. The Alcock-Paczynski Test for the Ly α Forest: First Results from Magellan and the MMT. In S. C. Wolff and T. R. Lauer, editors, *Observing Dark Energy*, volume 339 of *Astronomical Society of the Pacific Conference Series*, page 172, August 2005.
- Euclid Collaboration, Y. Mellier, Abdurro’uf, J. A. Acevedo Barroso, A. Achúcarro, J. Adamek, R. Adam, G. E. Addison, N. Aghanim, M. Aguena, V. Ajani, Y. Akrami, A. Al-Bahlawan, A. Alavi, I. S. Albuquerque, G. Alestas, G. Alguero, A. Allaoui, S. W. Allen, V. Allevalo, A. V. Alonso-Tetilla, B. Altieri, A. Alvarez-Candal, S. Alvi, A. Amara, L. Amendola, J. Amiaux, I. T. Andika, S. Andreon, A. Andrews, G. Angora, R. E. Angulo, F. Annibali, A. Anselmi, S. Anselmi, S. Arcari, M. Archidiacono, G. Aricò, M. Arnaud,

S. Arnouts, M. Asgari, J. Asorey, L. Atayde, H. Atek, F. Atrio-Barandela, M. Aubert, E. Aubourg, T. Auphan, N. Auricchio, B. Aussel, H. Aussel, P. P. Avelino, A. Avgoustidis, S. Avila, S. Awan, R. Azzollini, C. Baccigalupi, E. Bachelet, D. Bacon, M. Baes, M. B. Bagley, B. Bahr-Kalus, A. Balaguera-Antolinez, E. Balbinot, M. Balcells, M. Baldi, I. Baldry, A. Balestra, M. Ballardini, O. Ballester, M. Balogh, E. Bañados, R. Barbier, S. Bardelli, M. Baron, T. Barreiro, R. Barrena, J. C. Barriere, B. J. Barros, A. Barthelemy, N. Bartolo, A. Basset, P. Battaglia, A. J. Battisti, C. M. Baugh, L. Baumont, L. Bazzanini, J. P. Beaulieu, V. Beckmann, A. N. Belikov, J. Bel, F. Bellagamba, M. Bella, E. Bellini, K. Benabed, R. Bender, G. Benevento, C. L. Bennett, K. Benson, P. Bergamini, J. R. Bermejo-Climent, F. Bernardeau, D. Bertacca, M. Berthe, J. Berthier, M. Bethermin, F. Beutler, C. Bevillon, S. Bhargava, R. Bhatawdekar, D. Bianchi, L. Bisigello, A. Biviano, R. P. Blake, A. Blanchard, J. Blazek, L. Blot, A. Bosco, C. Bodendorf, T. Boenke, H. Böhringer, P. Boldrini, M. Bolzonella, A. Bonchi, M. Bonici, D. Bonino, L. Bonino, C. Bonvin, W. Bon, J. T. Booth, S. Borgani, A. S. Borlaff, E. Borsato, A. Bosco, B. Bose, M. T. Botticella, A. Boucaud, F. Bouche, J. S. Boucher, D. Boutigny, T. Bouvard, R. Bouwens, H. Bouy, R. A. A. Bowler, V. Bozza, E. Bozzo, E. Branchini, G. Brando, S. Brau-Nogue, P. Brekke, M. N. Bremer, M. Brescia, M. A. Breton, J. Brinchmann, T. Brinckmann, C. Brockley-Blatt, M. Brodwin, L. Brouard, M. L. Brown, S. Bruton, J. Bucko, H. Buddelmeijer, G. Buenadicha, F. Buitrago, P. Burger, C. Burigana, V. Busillo, D. Busonero, R. Cabanac, L. Cabayol-Garcia, M. S. Cagliari, A. Caillat, L. Caillat, M. Calabrese, A. Calabro, G. Calderone, F. Calura, B. Camacho Quevedo, S. Camera, L. Campos, G. Canas-Herrera, G. P. Candini, M. Cantiello, V. Capobianco, E. Cappellaro, N. Cappelluti, A. Cappi, K. I. Caputi, C. Cara, C. Carbone, V. F. Cardone, E. Carella, R. G. Carlberg, M. Carle, L. Carminati, F. Caro, J. M. Carrasco, J. Carretero, P. Carrilho, J. Carron Duque, B. Carry, A. Carvalho, C. S. Carvalho, R. Casas, S. Casas, P. Casenove, C. M. Casey, P. Cassata, F. J. Castander, D. Castelao, M. Castellano, L. Castiblanco, G. Castignani, T. Castro, C. Cavet, S. Cavuoti, P. Y. Chabaud, K. C. Chambers, Y. Charles, S. Charlot, N. Chartab, R. Chary, F. Chaumeil, H. Cho, G. Chon, E. Ciancetta, P. Ciliegi, A. Cimatti, M. Cimino, M. R. L. Cioni, R. Claydon, C. Cleland, B. Clément, D. L. Clements, N. Clerc, S. Clesse, S. Codis, F. Cogato, J. Colbert, R. E. Cole, P. Coles, T. E. Collett, R. S. Collins, C. Colodro-Conde, C. Colombo, F. Combes, V. Conforti, G. Congedo, S. Conseil, C. J. Conselice, S. Contarini, T. Contini, L. Conversi, A. R. Cooray, Y. Copin, P. S. Corasaniti, P. Corcho-Caballero, L. Corcione, O. Cordes, O. Corpacci, M. Correnti, M. Costanzi, A. Costille, F. Courbin, L. Courcoult Mifsud, H. M. Courtois, M. C. Cousinou, G. Covone, T. Cowell, C. Cragg, G. Cresci, S. Cristiani, M. Crocce, M. Cropper, P. E. Crouzet, B. Csizi, J. G. Cuby, E. Cucchetti, O. Cucciati, J. C. Cuillandre,

P. A. C. Cunha, V. Cuozzo, E. Daddi, M. D'Addona, C. Dafonte, N. Dagoneau, E. Dalessandro, G. B. Dalton, G. D'Amico, H. Dannerbauer, P. Danto, I. Das, A. Da Silva, R. da Silva, W. d'Assignies Doumerg, G. Daste, J. E. Davies, S. Davini, P. Dayal, T. de Boer, R. Decarli, B. De Caro, H. Degaudenzi, G. Degni, J. T. A. de Jong, L. F. de la Bella, S. de la Torre, F. Delhaise, D. Delley, G. Delucchi, G. De Lucia, J. Denniston, F. De Paolis, M. De Petris, A. Derosa, S. Desai, V. Desjacques, G. Despali, G. Desprez, J. De Vicente-Albendea, Y. Deville, J. D. F. Dias, A. Díaz-Sánchez, J. J. Diaz, S. Di Domizio, J. M. Diego, D. Di Ferdinando, A. M. Di Giorgio, P. Dimauro, J. Dinis, K. Dolag, C. Dolding, H. Dole, H. Domínguez Sánchez, O. Doré, F. Dournac, M. Douspis, H. Dreihahn, B. Droge, B. Dryer, F. Dubath, P. A. Duc, F. Ducret, C. Duffy, F. Dufresne, C. A. J. Duncan, X. Dupac, V. Duret, R. Durrer, F. Durret, S. Dusini, A. Ealet, A. Eggemeier, P. R. M. Eisenhardt, D. Elbaz, M. Y. Elkhatab, A. Ellien, J. Endicott, A. Enia, T. Erben, J. A. Escartin Vigo, S. Escoffier, I. Escudero Sanz, J. Essert, S. Etori, M. Ezziati, G. Fabbian, M. Fabricius, Y. Fang, A. Farina, M. Farina, R. Farinelli, S. Farrens, F. Faustini, A. Feltre, A. M. N. Ferguson, P. Ferrando, A. G. Ferrari, A. Ferré-Mateu, P. G. Ferreira, I. Ferreras, I. Ferrero, S. Ferriol, P. Ferruit, D. Filleul, F. Finelli, S. L. Finkelstein, A. Finoguenov, B. Fiorini, F. Flentge, P. Focardi, J. Fonseca, A. Fontana, F. Fontanot, F. Fornari, P. Fosalba, M. Fossati, S. Fotopoulou, D. Fouchez, N. Fourmanoit, M. Frailis, D. Fraix-Burnet, E. Franceschi, A. Franco, P. Franzetti, J. Friehoefer, C. . S. Frenk, G. Frittoli, P. A. Frugier, N. Frusciante, A. Fumagalli, M. Fumagalli, M. Fumana, Y. Fu, L. Gabarra, S. Galeotta, L. Galluccio, K. Ganga, H. Gao, J. García-Bellido, K. Garcia, J. P. Gardner, B. Garilli, L. M. Gaspar-Venancio, T. Gasparetto, V. Gautard, R. Gavazzi, E. Gaztanaga, L. Genolet, R. Genova Santos, F. Gentile, K. George, M. Gerbino, Z. Ghaffari, F. Giacomini, F. Gianotti, G. P. S. Gibb, W. Gillard, B. Gillis, M. Ginolfi, C. Giocoli, M. Girardi, S. K. Giri, L. W. K. Goh, P. Gómez-Alvarez, V. Gonzalez-Perez, A. H. Gonzalez, E. J. Gonzalez, J. C. Gonzalez, S. Gouyou Beauchamps, G. Gozaliasl, J. Gracia-Carpio, S. Grandis, B. R. Granett, M. Granvik, A. Grazian, A. Gregorio, C. Grenet, C. Grillo, F. Grupp, C. Gruppioni, A. Gruppuso, C. Guerbuez, S. Guerrini, M. Guidi, P. Guillard, C. M. Gutierrez, P. Guttridge, L. Guzzo, S. Gwyn, J. Haapala, J. Haase, C. R. Haddow, M. Hailey, A. Hall, D. Hall, N. Hamaus, B. S. Haridasu, J. Harnois-Déraps, C. Harper, W. G. Hartley, G. Hasinger, F. Hassani, N. A. Hatch, S. V. H. Haugan, B. Häußler, A. Heavens, L. Heisenberg, A. Helmi, G. Helou, S. Hemmati, K. Henares, O. Herent, C. Hernández-Monteagudo, T. Heuberger, P. C. Hewett, S. Heydenreich, H. Hildebrandt, M. Hirschmann, J. Hjorth, J. Hoar, H. Hoekstra, A. D. Holland, M. S. Holliman, W. Holmes, I. Hook, B. Horeau, F. Hormuth, A. Hornstrup, S. Hosseini, D. Hu, P. Hudelot, M. J. Hudson, M. Huertas-Company, E. M. Huff, A. C. N. Hughes, A. Humphrey, L. K. Hunt, D. D. Huynh, R. Ibata,

- K. Ichikawa, S. Iglesias-Groth, O. Ilbert, S. Ilić, L. Ingoglia, E. Iodice, H. Israel, U. E. Israelsson, L. Izzo, P. Jablonka, N. Jackson, J. Jacobson, M. Jafariyazani, K. Jahnke, B. Jain, H. Jansen, M. J. Jarvis, J. Jasche, M. Jauzac, N. Jeffrey, M. Jhabvala, Y. Jimenez-Teja, A. Jimenez Muñoz, B. Joachimi, P. H. Johansson, S. Joudaki, E. Jullo, J. J. E. Kajava, Y. Kang, A. Kannawadi, V. Kansal, D. Karagiannis, M. Kärcher, A. Kashlinsky, M. V. Kazandjian, F. Keck, E. Keihänen, E. Kerins, S. Kermiche, A. Khalil, A. Kiessling, K. Kiiveri, M. Kilbinger, J. Kim, R. King, C. C. Kirkpatrick, T. Kitching, M. Kluge, M. Knabenhans, J. H. Knapen, A. Knebe, J. P. Kneib, R. Kohley, L. V. E. Koopmans, H. Koskinen, E. Koulouridis, R. Kou, A. Kovács, I. Kovačić, A. Kowalczyk, K. Koyama, K. Kraljic, O. Krause, S. Kruk, B. Kubik, U. Kuchner, K. Kuijken, M. Kümmel, M. Kunz, H. Kurki-Suonio, F. Lacasa, C. G. Lacey, F. La Franca, N. Lagarde, O. Lahav, C. Laigle, A. La Marca, O. La Marle, B. Lamine, M. C. Lam, A. Lançon, H. Landt, M. Langer, A. Lapi, C. Larcheveque, S. S. Larsen, M. Lattanzi, F. Laudisio, D. Laugier, R. Laureijs, V. Laurent, G. Lavaux, A. Lawrenson, A. Lazanu, T. Lazeyras, Q. Le Boulc'h, A. M. C. Le Brun, V. Le Brun, F. Leclercq, S. Lee, J. Le Graet, L. Legrand, K. N. Leirvik, M. Le Jeune, M. Lembo, D. Le Mignant, M. D. Lepinzan, F. Lepori, A. Le Reun, G. Leroy, G. F. Lesci, J. Lesgourgues, L. Leuzzi, M. E. Levi, T. I. Liaudat, G. Libet, P. Liebing, S. Ligori, P. B. Lilje, C. C. Lin, D. Linde, E. Linder, V. Lindholm, L. Linke, S. S. Li, S. J. Liu, I. Lloro, F. S. N. Lobo, N. Lodieu, M. Lombardi, L. Lombriser, P. Lonare, G. Longo, M. López-Caniego, X. Lopez Lopez, J. Lorenzo Alvarez, A. Loureiro, J. Loveday, E. Lusso, J. Macias-Perez, T. Maciaszek, G. Maggio, M. Magliocchetti, F. Magnard, E. A. Magnier, A. Magro, G. Mahler, G. Mainetti, D. Maino, E. Maiorano, E. Maiorano, N. Malavasi, G. A. Mamon, C. Mancini, R. Mandelbaum, M. Manera, A. Manjón-García, F. Mannucci, O. Mansutti, M. Manteiga Outeiro, R. Maoli, C. Maraston, S. Marcin, P. Marcos-Arenal, B. Margalef-Bentabol, O. Marggraf, D. Marinucci, M. Marinucci, K. Markovic, F. R. Marleau, J. Marpaud, J. Martignac, J. Martín-Fleitas, P. Martin-Moruno, E. L. Martin, M. Martinelli, N. Martinet, H. Martin, C. J. A. P. Martins, F. Marulli, D. Massari, R. Massey, D. C. Masters, S. Matarrese, Y. Matsuoka, S. Matthew, B. J. Maughan, N. Mauri, L. Maurin, S. Maurogordato, K. McCarthy, A. W. McConnachie, H. J. McCracken, I. McDonald, J. D. McEwen, C. J. R. McPartland, E. Medinaceli, V. Mehta, S. Mei, M. Melchior, J. B. Melin, B. Ménard, J. Mendes, J. Mendez-Abreu, M. Meneghetti, A. Mercurio, E. Merlin, R. B. Metcalf, G. Meylan, M. Migliaccio, M. Mignoli, L. Miller, M. Miluzio, B. Milvang-Jensen, J. P. Mimoso, R. Miquel, H. Miyatake, B. Mobasher, J. J. Mohr, P. Monaco, M. Monguió, A. Montoro, A. Mora, A. Moradinezhad Dizgah, M. Moresco, C. Moretti, G. Morgante, N. Morisset, T. J. Moriya, P. W. Morris, D. J. Mortlock, L. Moscardini, D. F. Mota, S. Mottet, L. A. Moustakas, T. Moutard, T. Müller,

E. Munari, G. Murphree, C. Murray, N. Murray, P. Musi, S. Nadathur, B. C. Nagam, T. Nagao, K. Naidoo, R. Nakajima, C. Nally, P. Natoli, A. Navarro-Alsina, D. Navarro Girones, C. Neissner, A. Nersesian, S. Nesseris, H. N. Nguyen-Kim, L. Nicastro, R. C. Nichol, M. Nielbock, S. M. Niemi, S. Nieto, K. Nilsson, J. Noller, P. Norberg, A. Nourizono, P. Ntelis, A. A. Nucita, P. Nugent, N. J. Nunes, T. Nutma, I. Ocampo, J. Odier, P. A. Oesch, M. Oguri, D. Magalhaes Oliveira, M. Onoue, T. Oosterbroek, F. Oppizzi, C. Ordenovic, K. Osato, F. Pacaud, F. Pace, C. Padilla, K. Paech, L. Pagano, M. J. Page, E. Palazzi, S. Paltani, S. Pamuk, S. Pandolfi, D. Paoletti, M. Paolillo, P. Papaderos, K. Pardede, G. Parimbelli, A. Parmar, C. Partmann, F. Pasian, F. Passalacqua, K. Paterson, L. Patrizii, C. Pattison, A. Paulino-Afonso, R. Paviot, J. A. Peacock, F. R. Pearce, K. Pedersen, A. Peel, R. F. Peletier, M. Pellejero Ibanez, R. Pello, M. T. Penny, W. J. Percival, A. Perez-Garrido, L. Perotto, V. Pettorino, A. Pezzotta, S. Pezzuto, A. Philippon, M. Pierre, O. Piersanti, M. Pietroni, L. Piga, L. Pilo, S. Pires, A. Pisani, A. Pizzella, L. Pizzuti, C. Plana, G. Polenta, J. E. Pollack, M. Poncet, M. Pöntinen, P. Pool, L. A. Popa, V. Popa, J. Popp, C. Porciani, L. Porth, D. Potter, M. Poulain, A. Poursidou, L. Pozzetti, I. Prandoni, G. W. Pratt, S. Prezelus, E. Prieto, A. Pugno, S. Quai, L. Quilley, G. D. Racca, A. Raccanelli, G. Rácz, S. Radinović, M. Radovich, A. Ragagnin, U. Ragnit, F. Raison, N. Ramos-Chernenko, C. Ranc, Y. Rasera, N. Raylet, R. Rebolo, A. Refregier, P. Reimberg, T. H. Reiprich, F. Renk, A. Renzi, J. Retre, Y. Revaz, C. Reylé, L. Reynolds, J. Rhodes, F. Ricci, M. Ricci, G. Riccio, S. O. Ricken, S. Rissanen, I. Risso, H. W. Rix, A. C. Robin, B. Rocca-Volmerange, P. F. Rocci, M. Rodenhuis, G. Rodighiero, M. Rodriguez Monroy, R. P. Rollins, M. Romanello, J. Roman, E. Romelli, M. Romero-Gomez, M. Roncarelli, P. Rosati, C. Rosset, E. Rossetti, W. Roster, H. J. A. Rottgering, A. Rozas-Fernández, K. Ruane, J. A. Rubino-Martin, A. Rudolph, F. Ruppin, B. Rusholme, S. Sacquegna, I. Sáez-Casares, S. Saga, R. Saglia, M. Sahlén, T. Saifollahi, Z. Sakr, J. Salvalaggio, R. Salvaterra, L. Salvati, M. Salvato, J. C. Salvignol, A. G. Sánchez, E. Sanchez, D. B. Sanders, D. Sapone, M. Saponara, E. Sarpa, F. Sarron, S. Sartori, B. Sartoris, B. Sassolas, L. Sauniere, M. Sauvage, M. Sawicki, R. Scaramella, C. Scarlata, L. Scharré, J. Schaye, J. A. Schewtschenko, J. T. Schindler, E. Schinnerer, M. Schirmer, F. Schmidt, F. Schmidt, M. Schmidt, A. Schneider, M. Schneider, P. Schneider, N. Schöneberg, T. Schrabback, M. Schultheis, S. Schulz, N. Schuster, J. Schwartz, D. Sciotti, M. Scodeggio, D. Scognamiglio, D. Scott, V. Scottez, A. Secroun, E. Sefusatti, G. Seidel, M. Seiffert, E. Sellentin, M. Selwood, E. Semboloni, M. Sereno, S. Serjeant, S. Serrano, G. Setnikar, F. Shankar, R. M. Sharples, A. Short, A. Shulevski, M. Shuntov, M. Sias, G. Sikkema, A. Silvestri, P. Simon, C. Sirignano, G. Sirri, J. Skottfelt, E. Slezak, D. Sluse, G. P. Smith, L. C. Smith, R. E. Smith, S. J. A. Smit, F. Soldano, B. G. B. Solheim, J. G. Sorce, F. Sorrenti, E. Soubrie,

- L. Spinoglio, A. Spurio Mancini, J. Stadel, L. Stagnaro, L. Stanco, S. A. Stanford, J. L. Starck, P. Stassi, J. Steinwagner, D. Stern, C. Stone, P. Strada, F. Strafella, D. Stramaccioni, C. Surace, F. Sureau, S. H. Suyu, I. Swindells, M. Szafraniec, I. Szapudi, S. Taamoli, M. Talia, P. Tallada-Crespí, K. Tanidis, C. Tao, P. Tarrío, D. Tavagnacco, A. N. Taylor, J. E. Taylor, P. L. Taylor, E. M. Teixeira, M. Tenti, P. Teodoro Idiago, H. I. Teplitz, I. Tereno, N. Tessore, V. Testa, G. Testera, M. Tewes, R. Teyssier, N. Theret, C. Thizy, P. D. Thomas, Y. Toba, S. Toft, R. Toledo-Moreo, E. Tolstoy, E. Tommasi, O. Torbaniuk, F. Torradeflot, C. Tortora, S. Tosi, S. Tosti, M. Trifoglio, A. Troja, T. Trombetti, A. Tronconi, M. Tsedrik, A. Tsyganov, M. Tucci, I. Tutusaus, C. Uhlemann, L. Ulivi, M. Urbano, L. Vacher, L. Vailion, P. Valageas, I. Valdes, E. A. Valentijn, L. Valenziano, C. Valieri, J. Valiviita, M. Van den Broeck, T. Vassallo, R. Vavrek, J. Vega-Ferrero, B. Venemans, A. Venhola, S. Ventura, G. Verdoes Kleijn, D. Vergani, A. Verma, F. Vernizzi, A. Veropalumbo, G. Verza, C. Vescovi, D. Vibert, M. Viel, P. Vielzeuf, C. Viglione, A. Viitanen, F. Villaescusa-Navarro, S. Vinciguerra, F. Visticot, K. Voggel, M. von Wietersheim-Kramsta, W. J. Vriend, S. Wachter, M. Walmsley, G. Walth, D. M. Walton, N. A. Walton, M. Wander, L. Wang, Y. Wang, J. R. Weaver, J. Weller, M. Wetzstein, D. J. Whalen, I. H. Whittam, A. Widmer, M. Wiesmann, J. Wilde, O. R. Williams, H. A. Winther, A. Wittje, J. H. W. Wong, A. H. Wright, V. Yankelevich, H. W. Yeung, M. Yoon, S. Youles, L. Y. A. Yung, A. Zacchei, L. Zalesky, G. Zamorani, A. Zamorano Vitorelli, M. Zannoni Marc, M. Zennaro, F. M. Zerbi, I. A. Zinchenko, J. Zoubian, E. Zucca, and M. Zumalacarregui. Euclid. I. Overview of the Euclid mission. *arXiv e-prints*, art. arXiv:2405.13491, May 2024. doi: 10.48550/arXiv.2405.13491.
- Bridget Falck, Kazuya Koyama, Gong-Bo Zhao, and Marius Cautun. Using voids to unscreen modified gravity. *Monthly Notices of the Royal Astronomical Society*, 475(3):3262–3272, 2018.
- Yen Fang, Nico Hamaus, B. Jain, S. Pandey, G. Pollina, C. Sánchez, A. Kovács, C. Chang, J. Carretero, F. J. Castander, et al. Dark energy survey year 1 results: the relationship between mass and light around cosmic voids. *Monthly Notices of the Royal Astronomical Society*, 490(3):3573–3587, 2019.
- Antonio Farina, Alfonso Veropalumbo, Enzo Branchini, and Massimo Guidi. Modeling and measuring the anisotropic halo 3-point correlation function: a coordinated study, 2024. URL <https://arxiv.org/abs/2408.03036>.
- Ginevra Favole, Benjamin R. Granett, Javier Silva Lafaunie, and Domenico Sapone. Does jackknife scale really matter for accurate large-scale structure covariances? *Mon. Not. R.*

- Astron. Soc.* , 505(4):5833–5845, August 2021. doi: 10.1093/mnras/stab1720.
- G. J. Ferland, R. L. Porter, P. A. M. van Hoof, R. J. R. Williams, N. P. Abel, M. L. Lykins, G. Shaw, W. J. Henney, and P. C. Stancil. The 2013 Release of Cloudy. , 49:137–163, April 2013. doi: 10.48550/arXiv.1302.4485.
- Alexei V. Filippenko and Adam G. Riess. Results from the high- z supernova search team. *Physics Reports*, 307(1–4):31–44, December 1998. ISSN 0370-1573. doi: 10.1016/S0370-1573(98)00052-0. URL [http://dx.doi.org/10.1016/S0370-1573\(98\)00052-0](http://dx.doi.org/10.1016/S0370-1573(98)00052-0).
- Daniel Foreman-Mackey, Will Farr, Manodeep Sinha, Anne Archibald, David Hogg, Jeremy Sanders, Joe Zuntz, Peter Williams, Andrew Nelson, Miguel de Val-Borro, Tobias Erhardt, Ilya Pashchenko, and Oriol Pla. emcee v3: A Python ensemble sampling toolkit for affine-invariant MCMC. *The Journal of Open Source Software*, 4(43):1864, November 2019. doi: 10.21105/joss.01864.
- JE Forero-Romero, Y Hoffman, S Gottlöber, A Klypin, and G Yepes. A dynamical classification of the cosmic web. *Monthly Notices of the Royal Astronomical Society*, 396(3): 1815–1824, 2009.
- Tristan S. Fraser, Enrique Paillas, Will J. Percival, Seshadri Nadathur, Slađana Radinović, and Hans A. Winther. Modelling the BOSS void-galaxy cross-correlation function using a neural-network emulator. *arXiv e-prints*, art. arXiv:2407.03221, July 2024. doi: 10.48550/arXiv.2407.03221.
- Joshua A Frieman, Michael S Turner, and Dragan Huterer. Dark energy and the accelerating universe. *Annu. Rev. Astron. Astrophys.*, 46(1):385–432, 2008.
- JN Fry. Cosmological density fluctuations and large-scale structure from n -point correlation functions to the probability distribution. *Astrophysical Journal, Part 1 (ISSN 0004-637X)*, vol. 289, Feb. 1, 1985, p. 10-17. *NASA-supported research.*, 289:10–17, 1985.
- G. Gamow. The Origin of Elements and the Separation of Galaxies. *Physical Review*, 74(4): 505–506, August 1948. doi: 10.1103/PhysRev.74.505.2.
- Jonathan Goodman and Jonathan Weare. Ensemble samplers with affine invariance. *Communications in Applied Mathematics and Computational Science*, 5(1):65–80, January 2010. doi: 10.2140/camcos.2010.5.65.
- Stephen A Gregory and Laird A Thompson. The coma/a1367 supercluster and its environs. 1978.

- M. Guidi, Alfonso Veropalumbo, Enzo Branchini, Alexander Eggemeier, and Carmelita Carbone. Modelling the next-to-leading order matter three-point correlation function using fftlog. *Journal of Cosmology and Astroparticle Physics*, 2023:066, 08 2023. doi: 10.1088/1475-7516/2023/08/066.
- James E Gunn and J Richard Gott III. On the infall of matter into clusters of galaxies and some effects on their evolution. *Astrophysical Journal*, vol. 176, p. 1, 176:1, 1972.
- Alan H Guth and So-Young Pi. Fluctuations in the new inflationary universe. *Physical Review Letters*, 49(15):1110, 1982.
- Oliver Hahn, Raul E Angulo, and Tom Abel. The properties of cosmic velocity fields. *Monthly Notices of the Royal Astronomical Society*, 454(4):3920–3937, 2015.
- N. Hamaus, M. Aubert, A. Pisani, S. Contarini, G. Verza, M. C. Cousinou, S. Escoffier, A. Hawken, G. Lavaux, G. Pollina, B. D. Wandelt, J. Weller, M. Bonici, C. Carbone, L. Guzzo, A. Kovacs, F. Marulli, E. Massara, L. Moscardini, P. Ntelis, W. J. Percival, S. Radinović, M. Sahlén, Z. Sakr, A. G. Sánchez, H. A. Winther, N. Auricchio, S. Awan, R. Bender, C. Bodendorf, D. Bonino, E. Branchini, M. Brescia, J. Brinchmann, V. Capobianco, J. Carretero, F. J. Castander, M. Castellano, S. Cavauoti, A. Cimatti, R. Cledassou, G. Congedo, L. Conversi, Y. Copin, L. Corcione, M. Cropper, A. Da Silva, H. Degaudenzi, M. Douspis, F. Dubath, C. A. J. Duncan, X. Dupac, S. Dusini, A. Ealet, S. Ferriol, P. Fosalba, M. Frailis, E. Franceschi, P. Franzetti, M. Fumana, B. Garilli, B. Gillis, C. Giocoli, A. Grazian, F. Grupp, S. V. H. Haugan, W. Holmes, F. Hormuth, K. Jahnke, S. Kermiche, A. Kiessling, M. Kilbinger, T. Kitching, M. Kümmel, M. Kunz, H. Kurki-Suonio, S. Ligori, P. B. Lilje, I. Lloro, E. Maiorano, O. Marggraf, K. Markovic, R. Massey, S. Maurogordato, M. Melchior, M. Meneghetti, G. Meylan, M. Moresco, E. Munari, S. M. Niemi, C. Padilla, S. Paltani, F. Pasian, K. Pedersen, V. Pettorino, S. Pires, M. Poncet, L. Popa, L. Pozzetti, R. Rebolo, J. Rhodes, H. Rix, M. Roncarelli, E. Rossetti, R. Saglia, P. Schneider, A. Secroun, G. Seidel, S. Serrano, C. Sirignano, G. Sirri, J. L. Starck, P. Tallada-Crespí, D. Tavagnacco, A. N. Taylor, I. Tereno, R. Toledo-Moreo, F. Torradeflot, E. A. Valentijn, L. Valenziano, Y. Wang, N. Welikala, G. Zamorani, J. Zoubian, S. Andreon, M. Baldi, S. Camera, S. Mei, C. Neissner, and E. Romelli. Euclid: Forecasts from redshift-space distortions and the Alcock-Paczynski test with cosmic voids. *Astron. Astrophys.* , 658: A20, February 2022. doi: 10.1051/0004-6361/202142073.
- Nico Hamaus, P. M. Sutter, and Benjamin D. Wandelt. Universal Density Profile for Cosmic Voids. *Phys. Rev. Lett.* , 112(25):251302, June 2014. doi: 10.1103/PhysRevLett.112.251302.

- Nico Hamaus, PM Sutter, Guilhem Lavaux, and Benjamin D Wandelt. Testing cosmic geometry without dynamic distortions using voids. *Journal of Cosmology and Astroparticle Physics*, 2014(12):013, 2014a.
- Nico Hamaus, Benjamin D Wandelt, PM Sutter, Guilhem Lavaux, and Michael S Warren. Cosmology with void-galaxy correlations. *Physical Review Letters*, 112(4):041304, 2014b.
- Nico Hamaus, Alice Pisani, P. M. Sutter, Guilhem Lavaux, Stéphanie Escoffier, Benjamin D. Wandelt, and Jochen Weller. Constraints on Cosmology and Gravity from the Dynamics of Voids. *Phys. Rev. Lett.* , 117(9):091302, August 2016. doi: 10.1103/PhysRevLett.117.091302.
- Nico Hamaus, Marie-Claude Cousinou, Alice Pisani, Marie Aubert, Stéphanie Escoffier, and Jochen Weller. Multipole analysis of redshift-space distortions around cosmic voids. *Journal of Cosmology and Astro-Particle Physics*, 2017(7):014, July 2017. doi: 10.1088/1475-7516/2017/07/014.
- Nico Hamaus, Alice Pisani, Jin-Ah Choi, Guilhem Lavaux, Benjamin D. Wandelt, and Jochen Weller. Precision cosmology with voids in the final BOSS data. *Journal of Cosmology and Astro-Particle Physics*, 2020(12):023, December 2020. doi: 10.1088/1475-7516/2020/12/023.
- AJS Hamilton. Galaxy clustering and the method of voids. *Astrophysical Journal, Part 2-Letters to the Editor (ISSN 0004-637X)*, vol. 292, May 15, 1985, p. L35-L39., 292: L35–L39, 1985.
- AJS Hamilton. Linear redshift distortions: A review. *The Evolving Universe: Selected Topics on Large-Scale Structure and on the Properties of Galaxies*, pages 185–275, 1998.
- J. Hartlap, P. Simon, and P. Schneider. Why your model parameter confidences might be too optimistic. unbiased estimation of the inverse covariance matrix. *Astronomy and Astrophysics*, 464(1):399–404, December 2006. ISSN 1432-0746. doi: 10.1051/0004-6361:20066170. URL <http://dx.doi.org/10.1051/0004-6361:20066170>.
- A. J. Hawken, B. R. Granett, A. Iovino, L. Guzzo, J. A. Peacock, S. de la Torre, B. Garilli, M. Bolzonella, M. Scodeggio, U. Abbas, C. Adami, D. Bottini, A. Cappi, O. Cucciati, I. Davidzon, A. Fritz, P. Franzetti, J. Krywult, V. Le Brun, O. Le Fèvre, D. Maccagni, K. Małek, F. Marulli, M. Polletta, A. Pollo, L. A. M. Tasca, R. Tojeiro, D. Vergani, A. Zanichelli, S. Arnouts, J. Bel, E. Branchini, G. De Lucia, O. Ilbert, L. Moscardini, and W. J. Percival. The VIMOS Public Extragalactic Redshift Survey. Measuring the growth

- rate of structure around cosmic voids. *Astron. Astrophys.* , 607:A54, November 2017. doi: 10.1051/0004-6361/201629678.
- Adam J. Hawken, Marie Aubert, Alice Pisani, Marie-Claude Cousinou, Stephanie Escoffier, Seshadri Nadathur, Graziano Rossi, and Donald P. Schneider. Constraints on the growth of structure around cosmic voids in eBOSS DR14. *Journal of Cosmology and Astro-Particle Physics*, 2020(6):012, June 2020. doi: 10.1088/1475-7516/2020/06/012.
- Alan Heavens, Yabebal Fantaye, Elena Sellentin, Hans Eggers, Zafirah Hosenie, Steve Kroon, and Arrykrishna Mootoovaloo. No evidence for extensions to the standard cosmological model. *Physical review letters*, 119(10):101301, 2017.
- G. Hinshaw, D. Larson, E. Komatsu, D. N. Spergel, C. L. Bennett, J. Dunkley, M. R. Nolte, M. Halpern, R. S. Hill, N. Odegard, L. Page, K. M. Smith, J. L. Weiland, B. Gold, N. Jarosik, A. Kogut, M. Limon, S. S. Meyer, G. S. Tucker, E. Wollack, and E. L. Wright. Nine-year Wilkinson Microwave Anisotropy Probe (WMAP) Observations: Cosmological Parameter Results. *Astrophys. J. Suppl.* , 208(2):19, October 2013. doi: 10.1088/0067-0049/208/2/19.
- Wayne Hu and Naoshi Sugiyama. Small-scale cosmological perturbations: An analytic approach. *The Astrophysical Journal*, 471(2):542–570, November 1996. ISSN 1538-4357. doi: 10.1086/177989. URL <http://dx.doi.org/10.1086/177989>.
- Wayne Hu and Martin White. CMB anisotropies: Total angular momentum method. *Phys. Rev. D* , 56(2):596–615, July 1997. doi: 10.1103/PhysRevD.56.596.
- Lam Hui, Albert Stebbins, and Scott Burles. A geometrical test of the cosmological energy contents using the ly forest. *The Astrophysical Journal*, 511(1):L5, dec 1998. doi: 10.1086/311826. URL <https://dx.doi.org/10.1086/311826>.
- Vincent Icke. Voids and filaments. *Monthly Notices of the Royal Astronomical Society*, 206 (1):1P–3P, 1984.
- Željko Ivezić, Steven M. Kahn, J. Anthony Tyson, Bob Abel, Emily Acosta, Robyn Allsman, David Alonso, Yusra AlSayyad, Scott F. Anderson, John Andrew, James Roger P. Angel, George Z. Angeli, Reza Ansari, Pierre Antilogus, Constanza Araujo, Robert Armstrong, Kirk T. Arndt, Pierre Astier, Éric Aubourg, Nicole Auza, Tim S. Axelrod, Deborah J. Bard, Jeff D. Barr, Aurelian Barrau, James G. Bartlett, Amanda E. Bauer, Brian J. Bauman, Sylvain Baumont, Ellen Bechtol, Keith Bechtol, Andrew C. Becker, Jacek Becla, Cristina Beldica, Steve Bellavia, Federica B. Bianco, Rahul Biswas, Guillaume Blanc, Jonathan

Blazek, Roger D. Blandford, Josh S. Bloom, Joanne Bogart, Tim W. Bond, Michael T. Booth, Anders W. Borgland, Kirk Borne, James F. Bosch, Dominique Boutigny, Craig A. Brackett, Andrew Bradshaw, William Nielsen Brandt, Michael E. Brown, James S. Bullock, Patricia Burchat, David L. Burke, Gianpietro Cagnoli, Daniel Calabrese, Shawn Callahan, Alice L. Callen, Jeffrey L. Carlin, Erin L. Carlson, Srinivasan Chandrasekharan, Glenaver Charles-Emerson, Steve Chesley, Elliott C. Cheu, Hsin-Fang Chiang, James Chiang, Carol Chirino, Derek Chow, David R. Ciardi, Charles F. Claver, Johann Cohen-Tanugi, Joseph J. Cockrum, Rebecca Coles, Andrew J. Connolly, Kem H. Cook, Asantha Cooray, Kevin R. Covey, Chris Cribbs, Wei Cui, Roc Cutri, Philip N. Daly, Scott F. Daniel, Felipe Daruich, Guillaume Daubard, Greg Daues, William Dawson, Francisco Delgado, Alfred Dellapenna, Robert de Peyster, Miguel de Val-Borro, Seth W. Digel, Peter Doherty, Richard Dubois, Gregory P. Dubois-Felsmann, Josef Durech, Frossie Economou, Tim Eifler, Michael Eracleous, Benjamin L. Emmons, Angelo Fausti Neto, Henry Ferguson, Enrique Figueroa, Merlin Fisher-Levine, Warren Focke, Michael D. Foss, James Frank, Michael D. Freemon, Emmanuel Gangler, Eric Gawiser, John C. Geary, Perry Gee, Marla Geha, Charles J. B. Gessner, Robert R. Gibson, D. Kirk Gilmore, Thomas Glanzman, William Glick, Tatiana Goldina, Daniel A. Goldstein, Iain Goodenow, Melissa L. Graham, William J. Gressler, Philippe Gris, Leanne P. Guy, Augustin Guyonnet, Gunther Haller, Ron Harris, Patrick A. Hascall, Justine Haupt, Fabio Hernandez, Sven Herrmann, Edward Hileman, Joshua Hoblitt, John A. Hodgson, Craig Hogan, James D. Howard, Dajun Huang, Michael E. Huffer, Patrick Ingraham, Walter R. Innes, Suzanne H. Jacoby, Bhuvnesh Jain, Fabrice Jammes, M. James Jee, Tim Jenness, Garrett Jernigan, Darko Jevremović, Kenneth Johns, Anthony S. Johnson, Margaret W. G. Johnson, R. Lynne Jones, Claire Juramy-Gilles, Mario Jurić, Jason S. Kalirai, Nitya J. Kallivayalil, Bryce Kalmbach, Jeffrey P. Kantor, Pierre Karst, Mansi M. Kasliwal, Heather Kelly, Richard Kessler, Veronica Kinnison, David Kirkby, Lloyd Knox, Ivan V. Kotov, Victor L. Krabbendam, K. Simon Krughoff, Petr Kubánek, John Kuczewski, Shri Kulkarni, John Ku, Nadine R. Kurita, Craig S. Lage, Ron Lambert, Travis Lange, J. Brian Langton, Laurent Le Guillou, Deborah Levine, Ming Liang, Kian-Tat Lim, Chris J. Lintott, Kevin E. Long, Margaux Lopez, Paul J. Lotz, Robert H. Lupton, Nate B. Lust, Lauren A. MacArthur, Ashish Mahabal, Rachel Mandelbaum, Thomas W. Markiewicz, Darren S. Marsh, Philip J. Marshall, Stuart Marshall, Morgan May, Robert McKercher, Michelle McQueen, Joshua Meyers, Myriam Migliore, Michelle Miller, David J. Mills, Connor Miraval, Joachim Moeyens, Fred E. Moolekamp, David G. Monet, Marc Moniez, Serge Monkewitz, Christopher Montgomery, Christopher B. Morrison, Fritz Mueller, Gary P. Muller, Freddy Muñoz Arancibia, Douglas R. Neill, Scott P. Newbry, Jean-Yves Nief, Andrei Nomerotski, Martin Nordby, Paul

- O'Connor, John Oliver, Scot S. Olivier, Knut Olsen, William O'Mullane, Sandra Ortiz, Shawn Osier, Russell E. Owen, Reynald Pain, Paul E. Palecek, John K. Parejko, James B. Parsons, Nathan M. Pease, J. Matt Peterson, John R. Peterson, Donald L. Petravick, M. E. Libby Petrick, Cathy E. Petry, Francesco Pierfederici, Stephen Pietrowicz, Rob Pike, Philip A. Pinto, Raymond Plante, Stephen Plate, Joel P. Plutchak, Paul A. Price, Michael Prouza, Veljko Radeka, Jayadev Rajagopal, Andrew P. Rasmussen, Nicolas Regnault, Kevin A. Reil, David J. Reiss, Michael A. Reuter, Stephen T. Ridgway, Vincent J. Riot, Steve Ritz, Sean Robinson, William Roby, Aaron Roodman, Wayne Rosing, Cecille Roucelle, Matthew R. Rumore, Stefano Russo, Abhijit Saha, Benoit Sassolas, Terry L. Schalk, Pim Schellart, Rafe H. Schindler, Samuel Schmidt, Donald P. Schneider, Michael D. Schneider, William Schoening, German Schumacher, Megan E. Schwamb, Jacques Sebag, Brian Selvy, Glenn H. Sembroski, Lynn G. Seppala, Andrew Serio, Eduardo Serrano, Richard A. Shaw, Ian Shipsey, Jonathan Sick, Nicole Silvestri, Colin T. Slater, J. Allyn Smith, R. Chris Smith, Shahram Sobhani, Christine Soldahl, Lisa Storrie-Lombardi, Edward Stover, Michael A. Strauss, Rachel A. Street, Christopher W. Stubbs, Ian S. Sullivan, Donald Sweeney, John D. Swinbank, Alexander Szalay, Peter Takacs, Stephen A. Tether, Jon J. Thaler, John Gregg Thayer, Sandrine Thomas, Adam J. Thornton, Vaikunth Thukral, Jeffrey Tice, David E. Trilling, Max Turri, Richard Van Berg, Daniel Vanden Berk, Kurt Vetter, Francoise Virieux, Tomislav Vucina, William Wahl, Lucianne Walkowicz, Brian Walsh, Christopher W. Walter, Daniel L. Wang, Shin-Yawn Wang, Michael Warner, Oliver Wiecha, Beth Willman, Scott E. Winters, David Wittman, Sidney C. Wolff, W. Michael Wood-Vasey, Xiuqin Wu, Bo Xin, Peter Yoachim, and Hu Zhan. LSST: From Science Drivers to Reference Design and Anticipated Data Products. *Astrophys. J.* , 873(2):111, March 2019. doi: 10.3847/1538-4357/ab042c.
- J. C. Jackson. A critique of Rees's theory of primordial gravitational radiation. *Mon. Not. R. Astron. Soc.* , 156:1P, January 1972. doi: 10.1093/mnras/156.1.1P.
- A. Jenkins, C. S. Frenk, S. D. M. White, J. M. Colberg, S. Cole, A. E. Evrard, H. M. P. Couchman, and N. Yoshida. The mass function of dark matter haloes. *Mon. Not. R. Astron. Soc.* , 321(2):372–384, February 2001. doi: 10.1046/j.1365-8711.2001.04029.x.
- Elise Jennings, Yin Li, and Wayne Hu. The abundance of voids and the excursion set formalism. *Mon. Not. R. Astron. Soc.* , 434(3):2167–2181, September 2013. doi: 10.1093/mnras/stt1169.
- N. Kaiser. On the spatial correlations of Abell clusters. *Astrophys. J. Lett.* , 284:L9–L12, September 1984. doi: 10.1086/184341.

- Nick Kaiser. Clustering in real space and in redshift space. *Mon. Not. R. Astron. Soc.* , 227: 1–21, July 1987. doi: 10.1093/mnras/227.1.1.
- Robert P Kirshner, Augustus Oemler Jr, Paul L Schechter, and Stephen A Sackett. A million cubic megaparsec void in bootes. *Astrophysical Journal, Part 2-Letters to the Editor*, vol. 248, Sept. 1, 1981, p. L57-L60., 248:L57–L60, 1981.
- Tetsu Kitayama and Yasushi Suto. Semianalytic Predictions for Statistical Properties of X-Ray Clusters of Galaxies in Cold Dark Matter Universes. *Astrophys. J.* , 469:480, October 1996. doi: 10.1086/177797.
- E. Komatsu, K. M. Smith, J. Dunkley, C. L. Bennett, B. Gold, G. Hinshaw, N. Jarosik, D. Larson, M. R. Nolta, L. Page, D. N. Spergel, M. Halpern, R. S. Hill, A. Kogut, M. Limon, S. S. Meyer, N. Odegard, G. S. Tucker, J. L. Weiland, E. Wollack, and E. L. Wright. Seven-year Wilkinson Microwave Anisotropy Probe (WMAP) Observations: Cosmological Interpretation. *Astrophys. J. Suppl.* , 192(2):18, February 2011. doi: 10.1088/0067-0049/192/2/18.
- Christina D. Kreisch, Alice Pisani, Carmelita Carbone, Jia Liu, Adam J. Hawken, Elena Massara, David N. Spergel, and Benjamin D. Wandelt. Massive neutrinos leave fingerprints on cosmic voids. *Mon. Not. R. Astron. Soc.* , 488(3):4413–4426, September 2019. doi: 10.1093/mnras/stz1944.
- Christina D. Kreisch, Alice Pisani, Francisco Villaescusa-Navarro, David N. Spergel, Benjamin D. Wandelt, Nico Hamaus, and Adrian E. Bayer. The GIGANTES Data Set: Precision Cosmology from Voids in the Machine-learning Era. *Astrophys. J.* , 935(2):100, August 2022. doi: 10.3847/1538-4357/ac7d4b.
- Ofer Lahav, Per B. Lilje, Joel R. Primack, and Martin J. Rees. Dynamical effects of the cosmological constant. *Mon. Not. R. Astron. Soc.* , 251:128–136, July 1991. doi: 10.1093/mnras/251.1.128.
- Diego García Lambas, Marcelo Lares, Laura Ceccarelli, Andrés N Ruiz, Dante J Paz, Victoria E Maldonado, and Heliana E Luparello. The sparkling universe: the coherent motions of cosmic voids. *Monthly Notices of the Royal Astronomical Society: Letters*, 455 (1):L99–L103, 2015.
- Stephen D. Landy and Alexander S. Szalay. Bias and Variance of Angular Correlation Functions. *Astrophys. J.* , 412:64, July 1993. doi: 10.1086/172900.

- Marcelo Lares, Heliana E Luparello, Victoria Maldonado, Andrés N Ruiz, Dante J Paz, Laura Ceccarelli, and Diego Garcia Lambas. Voids and superstructures: correlations and induced large-scale velocity flows. *Monthly Notices of the Royal Astronomical Society*, 470(1): 85–94, 2017.
- Guilhem Lavaux and Benjamin D. Wandelt. Precision cosmology with voids: definition, methods, dynamics. *Monthly Notices of the Royal Astronomical Society*, 403(3): 1392–1408, April 2010. ISSN 1365-2966. doi: 10.1111/j.1365-2966.2010.16197.x. URL <http://dx.doi.org/10.1111/j.1365-2966.2010.16197.x>.
- Guilhem Lavaux and Benjamin D. Wandelt. Precision Cosmography with Stacked Voids. *Astrophys. J.*, 754(2):109, August 2012. doi: 10.1088/0004-637X/754/2/109.
- Jounghun Lee and Daeseong Park. Constraining the dark energy equation of state with cosmic voids. *The Astrophysical Journal*, 696(1):L10, 2009.
- Seokcheon Lee. Spherical collapse model with and without curvature. *Physics Letters B*, 685(2-3):110–114, March 2010. doi: 10.1016/j.physletb.2010.01.058.
- Baojiu Li and George Efstathiou. An extended excursion set approach to structure formation in chameleon models. *Monthly Notices of the Royal Astronomical Society*, 421(2):1431–1442, 2012.
- Yu Liang, Cheng Zhao, Chia-Hsun Chuang, Francisco-Shu Kitaura, and Charling Tao. Measuring baryon acoustic oscillations from the clustering of voids. *Monthly Notices of the Royal Astronomical Society*, 459(4):4020–4028, 2016.
- E. V. Linder. Cosmic growth history and expansion history. *Phys. Rev. D*, 72(4):043529, August 2005. doi: 10.1103/PhysRevD.72.043529.
- Eric V. Linder. Exploring the Expansion History of the Universe. *Phys. Rev. Lett.*, 90(9): 091301, March 2003. doi: 10.1103/PhysRevLett.90.091301.
- Donald Lynden-Bell. Statistical mechanics of violent relaxation in stellar systems. *Monthly Notices of the Royal Astronomical Society*, Vol. 136, p. 101, 136:101, 1967.
- Roger Lynds and Vahe Petrosian. Luminous arcs in clusters of galaxies. *Astrophysical Journal, Part 1 (ISSN 0004-637X)*, vol. 336, Jan. 1, 1989, p. 1-8., 336:1–8, 1989.
- Qingqing Mao, Andreas A. Berlind, Robert J. Scherrer, Mark C. Neyrinck, Román Scoccamarro, Jeremy L. Tinker, Cameron K. McBride, and Donald P. Schneider. Cosmic Voids

- in the SDSS DR12 BOSS Galaxy Sample: The Alcock-Paczynski Test. *Astrophys. J.* , 835 (2):160, February 2017. doi: 10.3847/1538-4357/835/2/160.
- Federico Marulli, Davide Bianchi, Enzo Branchini, Luigi Guzzo, Lauro Moscardini, and Raul E. Angulo. Cosmology with clustering anisotropies: disentangling dynamic and geometric distortions in galaxy redshift surveys: Disentangling dynamics and geometry. *Monthly Notices of the Royal Astronomical Society*, 426(3):2566–2580, October 2012. ISSN 0035-8711. doi: 10.1111/j.1365-2966.2012.21875.x. URL <http://dx.doi.org/10.1111/j.1365-2966.2012.21875.x>.
- Elena Massara and Ravi K. Sheth. Density and velocity profiles around cosmic voids. *arXiv e-prints*, art. arXiv:1811.03132, November 2018. doi: 10.48550/arXiv.1811.03132.
- Elena Massara, Francisco Villaescusa-Navarro, Matteo Viel, and P. M. Sutter. Voids in massive neutrino cosmologies. *Journal of Cosmology and Astro-Particle Physics*, 2015 (11):018–018, November 2015. doi: 10.1088/1475-7516/2015/11/018.
- Elena Massara, Will J. Percival, Neal Dalal, Seshadri Nadathur, Slađana Radinović, Hans A. Winther, and Alex Woodfinden. Velocity profiles of matter and biased tracers around voids. *Mon. Not. R. Astron. Soc.* , 517(3):4458–4471, December 2022. doi: 10.1093/mnras/stac2892.
- J. C. Mather, E. S. Cheng, D. A. Cottingham, Jr. Eplee, R. E., D. J. Fixsen, T. Hewagama, R. B. Isaacman, K. A. Jensen, S. S. Meyer, P. D. Noerdlinger, S. M. Read, L. P. Rosen, R. A. Shafer, E. L. Wright, C. L. Bennett, N. W. Boggess, M. G. Hauser, T. Kelsall, Jr. Moseley, S. H., R. F. Silverberg, G. F. Smoot, R. Weiss, and D. T. Wilkinson. Measurement of the Cosmic Microwave Background Spectrum by the COBE FIRAS Instrument. *Astrophys. J.* , 420:439, January 1994. doi: 10.1086/173574.
- Alexander Merson, Yun Wang, Andrew Benson, Andreas Faisst, Daniel Masters, Alina Kiessling, and Jason Rhodes. Predicting H α emission-line galaxy counts for future galaxy redshift surveys. *Mon. Not. R. Astron. Soc.* , 474(1):177–196, February 2018. doi: 10.1093/mnras/stx2649.
- D Micheletti, A Iovino, AJ Hawken, BR Granett, M Bolzonella, A Cappi, L Guzzo, U Abbas, C Adami, S Arnouts, et al. The vimos public extragalactic redshift survey-searching for cosmic voids. *Astronomy & Astrophysics*, 570:A106, 2014.
- H. J. Mo and S. D. M. White. An analytic model for the spatial clustering of dark matter haloes. *Mon. Not. R. Astron. Soc.* , 282(2):347–361, September 1996. doi: 10.1093/mnras/282.2.347.

- V. Motta, Miguel A. García-Aspeitia, A. Hernández-Almada, J. Magaña, and Tomás Verdugo. Taxonomy of dark energy models, 2021. URL <https://arxiv.org/abs/2104.04642>.
- N. H. Abel. *Oeuvres Completes*. 1842.
- Seshadri Nadathur and Will J Percival. An accurate linear model for redshift space distortions in the void–galaxy correlation function. *Monthly Notices of the Royal Astronomical Society*, 483(3):3472–3487, December 2018. ISSN 1365-2966. doi: 10.1093/mnras/sty3372. URL <http://dx.doi.org/10.1093/mnras/sty3372>.
- Seshadri Nadathur, Paul Carter, and Will J Percival. A zeldovich reconstruction method for measuring redshift space distortions using cosmic voids. *Monthly Notices of the Royal Astronomical Society*, 482(2):2459–2470, 2019.
- Seshadri Nadathur, Will J. Percival, Florian Beutler, and Hans A. Winther. Testing Low-Redshift Cosmic Acceleration with Large-Scale Structure. *Phys. Rev. Lett.* , 124(22): 221301, June 2020a. doi: 10.1103/PhysRevLett.124.221301.
- Seshadri Nadathur, Alex Woodfinden, Will J. Percival, Marie Aubert, Julian Bautista, Kyle Dawson, Stéphanie Escoffier, Sebastien Fromenteau, Héctor Gil-Marín, James Rich, Ashley J. Ross, Graziano Rossi, Mariana Vargas Magaña, Joel R. Brownstein, and Donald P. Schneider. The completed SDSS-IV extended baryon oscillation spectroscopic survey: geometry and growth from the anisotropic void-galaxy correlation function in the luminous red galaxy sample. *Mon. Not. R. Astron. Soc.* , 499(3):4140–4157, December 2020b. doi: 10.1093/mnras/staa3074.
- M. C. Neyrinck. ZOBOV: a parameter-free void-finding algorithm. *Mon. Not. R. Astron. Soc.* , 386:2101–2109, June 2008. doi: 10.1111/j.1365-2966.2008.13180.x.
- Adi Nusser. Evidence for high ω from large scale structure. In *Cosmological Aspects of X-Ray Clusters of Galaxies*, pages 461–480. Springer, 1994.
- Adi Nusser. The alcock-paczynski test in redshifted 21-cm maps. *Monthly Notices of the Royal Astronomical Society*, 364(2):743–750, December 2005. ISSN 1365-2966. doi: 10.1111/j.1365-2966.2005.09603.x. URL <http://dx.doi.org/10.1111/j.1365-2966.2005.09603.x>.
- Adi Nusser and Enzo Branchini. On the least action principle in cosmology. *Monthly Notices of the Royal Astronomical Society*, 313(3):587–595, 2000.

- Yasuhiro Ohta, Issha Kayo, and Atsushi Taruya. Evolution of the Cosmological Density Distribution Function from the Local Collapse Model. *Astrophys. J.* , 589(1):1–16, May 2003. doi: 10.1086/374375.
- Yasuhiro Ohta, Issha Kayo, and Atsushi Taruya. Cosmological Density Distribution Function from the Ellipsoidal Collapse Model in Real Space. *Astrophys. J.* , 608(2):647–662, June 2004. doi: 10.1086/420762.
- J. H. Oort. Some Problems Concerning the Structure and Dynamics of the Galactic System and the Elliptical Nebulae NGC 3115 and 4494. *Astrophys. J.* , 91:273, April 1940. doi: 10.1086/144167.
- J. P. Ostriker and Paul J. Steinhardt. The observational case for a low-density Universe with a non-zero cosmological constant. *Nature*, 377(6550):600–602, October 1995. doi: 10.1038/377600a0.
- F. Pace, J. C. Waizmann, and M. Bartelmann. Spherical collapse model in dark-energy cosmologies. *Mon. Not. R. Astron. Soc.* , 406(3):1865–1874, August 2010. doi: 10.1111/j.1365-2966.2010.16841.x.
- Nikhil Padmanabhan, Martin White, and J. D. Cohn. Reconstructing baryon oscillations: A lagrangian theory perspective. *Physical Review D*, 79(6), March 2009. ISSN 1550-2368. doi: 10.1103/physrevd.79.063523. URL <http://dx.doi.org/10.1103/PhysRevD.79.063523>.
- Nikhil Padmanabhan, Xiaoying Xu, Daniel J Eisenstein, Richard Scalzo, Antonio J Cuesta, Kushal T Mehta, and Eyal Kazin. A 2 per cent distance to $z=0.35$ by reconstructing baryon acoustic oscillations—i. methods and application to the sloan digital sky survey. *Monthly Notices of the Royal Astronomical Society*, 427(3):2132–2145, 2012.
- Enrique Paillas, Marius Cautun, Baojiu Li, Yan-Chuan Cai, Nelson Padilla, Joaquín Armijo, and Sownak Bose. The santiago–harvard–edinburgh–durham void comparison ii: unveiling the vainshtein screening using weak lensing. *Monthly Notices of the Royal Astronomical Society*, 484(1):1149–1165, 2019.
- D. Paz, M. Lares, L. Ceccarelli, N. Padilla, and D. G. Lambas. Clues on void evolution-II. Measuring density and velocity profiles on SDSS galaxy redshift space distortions. *Mon. Not. R. Astron. Soc.* , 436:3480–3491, December 2013. doi: 10.1093/mnras/stt1836.
- Dante J Paz, Carlos M Correa, Sebastián R Gualpa, Andres N Ruiz, Carlos S Bederián, R Dario Graña, and Nelson D Padilla. Guess the cheese flavour by the size of its holes: a

- cosmological test using the abundance of popcorn voids. *Monthly Notices of the Royal Astronomical Society*, 522(2):2553–2569, 2023.
- J. A. Peacock and A. F. Heavens. Alternatives to the Press-Schechter cosmological mass function. *Mon. Not. R. Astron. Soc.* , 243:133–143, March 1990. doi: 10.1093/mnras/243.1.133.
- P. J. E. Peebles. *The large-scale structure of the universe*. 1980.
- P. J. E. Peebles. The void phenomenon. *The Astrophysical Journal*, 557(2):495–504, August 2001. ISSN 1538-4357. doi: 10.1086/322254. URL <http://dx.doi.org/10.1086/322254>.
- PJE Peebles. Structure of the coma cluster of galaxies. *Astronomical Journal*, Vol. 75, p. 13 (1970), 75:13, 1970.
- D. Pellicciari, S. Contarini, F. Marulli, L. Moscardini, C. Giocoli, G. F. Lesci, and K. Dolag. Exploring the cosmological synergy between galaxy cluster and cosmic void number counts. *Mon. Not. R. Astron. Soc.* , 522(1):152–164, June 2023. doi: 10.1093/mnras/stad956.
- A. A. Penzias and R. W. Wilson. A Measurement of Excess Antenna Temperature at 4080 Mc/s. *Astrophys. J.* , 142:419–421, July 1965. doi: 10.1086/148307.
- Will J Percival. Baryon acoustic oscillations: A cosmological ruler. *Physics Today*, 70(12): 32–38, 2017.
- Will J. Percival, Beth A. Reid, Daniel J. Eisenstein, Neta A. Bahcall, Tamas Budavari, Joshua A. Frieman, Masataka Fukugita, James E. Gunn, Željko Ivezić, Gillian R. Knapp, Richard G. Kron, Jon Loveday, Robert H. Lupton, Timothy A. McKay, Avery Meiksin, Robert C. Nichol, Adrian C. Pope, David J. Schlegel, Donald P. Schneider, David N. Spergel, Chris Stoughton, Michael A. Strauss, Alexander S. Szalay, Max Tegmark, Michael S. Vogeley, David H. Weinberg, Donald G. York, and Idit Zehavi. Baryon acoustic oscillations in the Sloan Digital Sky Survey Data Release 7 galaxy sample. *Mon. Not. R. Astron. Soc.* , 401(4):2148–2168, February 2010. doi: 10.1111/j.1365-2966.2009.15812.x.
- Eder LD Perico, Rodrigo Voivodic, Marcos Lima, and David F Mota. Cosmic voids in modified gravity scenarios. *Astronomy & Astrophysics*, 632:A52, 2019.
- S. Perlmutter, G. Aldering, G. Goldhaber, R. A. Knop, P. Nugent, P. G. Castro, S. Deustua, S. Fabbro, A. Goobar, D. E. Groom, I. M. Hook, A. G. Kim, M. Y. Kim, J. C. Lee, N. J. Nunes, R. Pain, C. R. Pennypacker, R. Quimby, C. Lidman, R. S. Ellis, M. Irwin, R. G.

- McMahon, P. Ruiz-Lapuente, N. Walton, B. Schaefer, B. J. Boyle, A. V. Filippenko, T. Matheson, A. S. Fruchter, N. Panagia, H. J. M. Newberg, W. J. Couch, and The Supernova Cosmology Project. Measurements of Ω and Λ from 42 High-Redshift Supernovae. *Astrophys. J.* , 517(2):565–586, June 1999. doi: 10.1086/307221.
- Saul Perlmutter. Supernovae, dark energy, and the accelerating universe. *Physics today*, 56(4):53–60, 2003.
- A. Pisani, G. Lavaux, P. M. Sutter, and B. D. Wandelt. Real-space density profile reconstruction of stacked voids. *Mon. Not. R. Astron. Soc.* , 443(4):3238–3250, October 2014. doi: 10.1093/mnras/stu1399.
- Alice Pisani, P. M. Sutter, Nico Hamaus, Esfandiar Alizadeh, Rahul Biswas, Benjamin D. Wandelt, and Christopher M. Hirata. Counting voids to probe dark energy. *Phys. Rev. D* , 92(8):083531, October 2015a. doi: 10.1103/PhysRevD.92.083531.
- Alice Pisani, P. M. Sutter, and B. D. Wandelt. Mastering the effects of peculiar velocities in cosmic voids. *arXiv e-prints*, art. arXiv:1506.07982, June 2015b. doi: 10.48550/arXiv.1506.07982.
- Alice Pisani, Elena Massara, David N Spergel, David Alonso, Tessa Baker, Yan-Chuan Cai, Marius Cautun, Christopher Davies, Vasilii Demchenko, Olivier Doré, et al. Cosmic voids: a novel probe to shed light on our universe. *arXiv preprint arXiv:1903.05161*, 2019.
- Planck Collaboration, P. A. R. Ade, N. Aghanim, M. Arnaud, M. Ashdown, J. Aumont, C. Baccigalupi, A. J. Banday, R. B. Barreiro, J. G. Bartlett, N. Bartolo, E. Battaner, R. Battye, K. Benabed, A. Benoît, A. Benoit-Lévy, J. P. Bernard, M. Bersanelli, P. Bielewicz, J. J. Bock, A. Bonaldi, L. Bonavera, J. R. Bond, J. Borrill, F. R. Bouchet, F. Boulanger, M. Bucher, C. Burigana, R. C. Butler, E. Calabrese, J. F. Cardoso, A. Catalano, A. Challinor, A. Chamballu, R. R. Chary, H. C. Chiang, J. Chluba, P. R. Christensen, S. Church, D. L. Clements, S. Colombi, L. P. L. Colombo, C. Combet, A. Coulais, B. P. Crill, A. Curto, F. Cuttaia, L. Danese, R. D. Davies, R. J. Davis, P. de Bernardis, A. de Rosa, G. de Zotti, J. Delabrouille, F. X. Désert, E. Di Valentino, C. Dickinson, J. M. Diego, K. Dolag, H. Dole, S. Donzelli, O. Doré, M. Douspis, A. Ducout, J. Dunkley, X. Dupac, G. Efstathiou, F. Elsner, T. A. Enßlin, H. K. Eriksen, M. Farhang, J. Fergusson, F. Finelli, O. Forni, M. Frailis, A. A. Fraisse, E. Franceschi, A. Frejsel, S. Galeotta, S. Galli, K. Ganga, C. Gauthier, M. Gerbino, T. Ghosh, M. Giard, Y. Giraud-Héraud, E. Giusarma, E. Gjerløw, J. González-Nuevo, K. M. Górski, S. Gratton, A. Gregorio, A. Gruppuso, J. E. Gudmundsson, J. Hamann, F. K. Hansen, D. Hanson, D. L. Harrison, G. Helou, S. Henrot-Versillé,

- C. Hernández-Monteagudo, D. Herranz, S. R. Hildebrandt, E. Hivon, M. Hobson, W. A. Holmes, A. Hornstrup, W. Hovest, Z. Huang, K. M. Huffenberger, G. Hurier, A. H. Jaffe, T. R. Jaffe, W. C. Jones, M. Juvela, E. Keihänen, R. Keskitalo, T. S. Kisner, R. Kneissl, J. Knoche, L. Knox, M. Kunz, H. Kurki-Suonio, G. Lagache, A. Lähteenmäki, J. M. Lamarre, A. Lasenby, M. Lattanzi, C. R. Lawrence, J. P. Leahy, R. Leonardi, J. Lesgourgues, F. Levrier, A. Lewis, M. Liguori, P. B. Lilje, M. Linden-Vørnle, M. López-Caniiego, P. M. Lubin, J. F. Macías-Pérez, G. Maggio, D. Maino, N. Mandolesi, A. Mangilli, A. Marchini, M. Maris, P. G. Martin, M. Martinelli, E. Martínez-González, S. Masi, S. Matarrese, P. McGehee, P. R. Meinhold, A. Melchiorri, J. B. Melin, L. Mendes, A. Mennella, M. Migliaccio, M. Millea, S. Mitra, M. A. Miville-Deschênes, A. Moneti, L. Montier, G. Morgante, D. Mortlock, A. Moss, D. Munshi, J. A. Murphy, P. Naselsky, F. Nati, P. Natoli, C. B. Netterfield, H. U. Nørgaard-Nielsen, F. Noviello, D. Novikov, I. Novikov, C. A. Oxborrow, F. Paci, L. Pagano, F. Pajot, R. Paladini, D. Paoletti, B. Partridge, F. Pasian, G. Patanchon, T. J. Pearson, O. Perdereau, L. Perotto, F. Perrotta, V. Pettorino, F. Piacentini, M. Piat, E. Pierpaoli, D. Pietrobon, S. Plaszczynski, E. Pointecouteau, G. Polenta, L. Popa, G. W. Pratt, G. Prézeau, S. Prunet, J. L. Puget, J. P. Rachen, W. T. Reach, R. Rebolo, M. Reinecke, M. Remazeilles, C. Renault, A. Renzi, I. Ristorcelli, G. Rocha, C. Rosset, M. Rossetti, G. Roudier, B. Rouillé d'Orfeuil, M. Rowan-Robinson, J. A. Rubiño-Martín, B. Rusholme, N. Said, V. Salvatelli, L. Salvati, M. Sandri, D. Santos, M. Savelainen, G. Savini, D. Scott, M. D. Seiffert, P. Serra, E. P. S. Shellard, L. D. Spencer, M. Spinelli, V. Stolyarov, R. Stompor, R. Sudiwala, R. Sunyaev, D. Sutton, A. S. Suur-Uski, J. F. Sygnet, J. A. Tauber, L. Terenzi, L. Toffolatti, M. Tomasi, M. Tristram, T. Trombetti, M. Tucci, J. Tuovinen, M. Türler, G. Umama, L. Valenziano, J. Valiviita, F. Van Tent, P. Vielva, F. Villa, L. A. Wade, B. D. Wandelt, I. K. Wehus, M. White, S. D. M. White, A. Wilkinson, D. Yvon, A. Zacchei, and A. Zonca. Planck 2015 results. XIII. Cosmological parameters. *Astron. Astrophys.*, 594:A13, September 2016. doi: 10.1051/0004-6361/201525830.
- Planck Collaboration, N. Aghanim, Y. Akrami, M. Ashdown, J. Aumont, C. Baccigalupi, M. Ballardini, A. J. Banday, R. B. Barreiro, N. Bartolo, S. Basak, R. Battye, K. Benabed, J. P. Bernard, M. Bersanelli, P. Bielewicz, J. J. Bock, J. R. Bond, J. Borrill, F. R. Bouchet, F. Boulanger, M. Bucher, C. Burigana, R. C. Butler, E. Calabrese, J. F. Cardoso, J. Carron, A. Challinor, H. C. Chiang, J. Chluba, L. P. L. Colombo, C. Combet, D. Contreras, B. P. Crill, F. Cuttaia, P. de Bernardis, G. de Zotti, J. Delabrouille, J. M. Delouis, E. Di Valentino, J. M. Diego, O. Doré, M. Douspis, A. Ducout, X. Dupac, S. Dusini, G. Efstathiou, F. Elsner, T. A. Enßlin, H. K. Eriksen, Y. Fantaye, M. Farhang, J. Fergusson, R. Fernandez-Cobos, F. Finelli, F. Forastieri, M. Frailis, A. A. Fraisse, E. Franceschi, A. Frolov, S. Galeotta, S. Galli, K. Ganga, R. T. Génova-Santos, M. Gerbino, T. Ghosh, J. González-Nuevo,

- K. M. Górski, S. Gratton, A. Gruppuso, J. E. Gudmundsson, J. Hamann, W. Handley, F. K. Hansen, D. Herranz, S. R. Hildebrandt, E. Hivon, Z. Huang, A. H. Jaffe, W. C. Jones, A. Karakci, E. Keihänen, R. Keskitalo, K. Kiiveri, J. Kim, T. S. Kisner, L. Knox, N. Krachmalnicoff, M. Kunz, H. Kurki-Suonio, G. Lagache, J. M. Lamarre, A. Lasenby, M. Lattanzi, C. R. Lawrence, M. Le Jeune, P. Lemos, J. Lesgourgues, F. Levrier, A. Lewis, M. Liguori, P. B. Lilje, M. Lilley, V. Lindholm, M. López-Cañiego, P. M. Lubin, Y. Z. Ma, J. F. Macías-Pérez, G. Maggio, D. Maino, N. Mandolesi, A. Mangilli, A. Marcos-Caballero, M. Maris, P. G. Martin, M. Martinelli, E. Martínez-González, S. Matarrese, N. Mauri, J. D. McEwen, P. R. Meinhold, A. Melchiorri, A. Mennella, M. Migliaccio, M. Millea, S. Mitra, M. A. Miville-Deschênes, D. Molinari, L. Montier, G. Morgante, A. Moss, P. Natoli, H. U. Nørgaard-Nielsen, L. Pagano, D. Paoletti, B. Partridge, G. Patanchon, H. V. Peiris, F. Perrotta, V. Pettorino, F. Piacentini, L. Polastri, G. Polenta, J. L. Puget, J. P. Rachen, M. Reinecke, M. Remazeilles, A. Renzi, G. Rocha, C. Rosset, G. Roudier, J. A. Rubiño-Martín, B. Ruiz-Granados, L. Salvati, M. Sandri, M. Savelainen, D. Scott, E. P. S. Shellard, C. Sirignano, G. Sirri, L. D. Spencer, R. Sunyaev, A. S. Suur-Uski, J. A. Tauber, D. Tavagnacco, M. Tenti, L. Toffolatti, M. Tomasi, T. Trombetti, L. Valenziano, J. Valiviita, B. Van Tent, L. Vibert, P. Vielva, F. Villa, N. Vittorio, B. D. Wandelt, I. K. Wehus, M. White, S. D. M. White, A. Zacchei, and A. Zonca. Planck 2018 results. VI. Cosmological parameters. *Astron. Astrophys.* , 641:A6, September 2020. doi: 10.1051/0004-6361/201833910.
- Erwin Platen, Rien van de Weygaert, and Bernard J. T. Jones. A cosmic watershed: the WVF void detection technique. *Mon. Not. R. Astron. Soc.* , 380(2):551–570, Sep 2007. doi: 10.1111/j.1365-2966.2007.12125.x.
- G Pollina, N Hamaus, K Paech, K Dolag, J Weller, C Sánchez, E S Rykoff, B Jain, T M C Abbott, S Allam, S Avila, R A Bernstein, E Bertin, D Brooks, D L Burke, A Carnero Rosell, M Carrasco Kind, J Carretero, C E Cunha, C B D’Andrea, L N da Costa, J De Vicente, D L DePoy, S Desai, H T Diehl, P Doel, A E Evrard, B Flaugher, P Fosalba, J Frieman, J García-Bellido, D W Gerdes, T Giannantonio, D Gruen, J Gschwend, G Gutierrez, W G Hartley, D L Hollowood, K Honscheid, B Hoyle, D J James, T Jeltema, K Kuehn, N Kuropatkin, M Lima, M March, J L Marshall, P Melchior, F Menanteau, R Miquel, A A Plazas, A K Romer, E Sanchez, V Scarpine, R Schindler, M Schubnell, I Sevilla-Noarbe, M Smith, M Soares-Santos, F Sobreira, E Suchyta, G Tarle, A R Walker, and W Wester. On the relative bias of void tracers in the dark energy survey. *Monthly Notices of the Royal Astronomical Society*, 487(2):2836–2852, May 2019. ISSN 1365-2966. doi: 10.1093/mnras/stz1470. URL <http://dx.doi.org/10.1093/mnras/stz1470>.

- Giorgia Pollina, Marco Baldi, Federico Marulli, and Lauro Moscardini. Cosmic voids in coupled dark energy cosmologies: the impact of halo bias. *Monthly Notices of the Royal Astronomical Society*, 455(3):3075–3085, 2016.
- Giorgia Pollina, Nico Hamaus, Klaus Dolag, Jochen Weller, Marco Baldi, and Lauro Moscardini. On the linearity of tracer bias around voids. *Mon. Not. R. Astron. Soc.*, 469(1): 787–799, July 2017. doi: 10.1093/mnras/stx785.
- William H Press and Paul Schechter. Formation of galaxies and clusters of galaxies by self-similar gravitational condensation. *Astrophysical Journal*, Vol. 187, pp. 425-438 (1974), 187:425–438, 1974.
- S. Radinović, S. Nadathur, H. A. Winther, W. J. Percival, A. Woodfinden, E. Massara, E. Paillas, S. Contarini, N. Hamaus, A. Kovacs, A. Pisani, G. Verza, M. Aubert, A. Amara, N. Auricchio, M. Baldi, D. Bonino, E. Branchini, M. Brescia, S. Camera, V. Capobianco, C. Carbone, V. F. Cardone, J. Carretero, M. Castellano, S. Cavuoti, A. Cimatti, R. Cledassou, G. Congedo, L. Conversi, Y. Copin, L. Corcione, F. Courbin, A. Da Silva, M. Douspis, F. Dubath, X. Dupac, S. Farrens, S. Ferriol, P. Fosalba, M. Frailis, E. Franceschi, M. Fumana, S. Galeotta, B. Garilli, W. Gillard, B. Gillis, C. Giocoli, A. Grazian, F. Grupp, S. V. H. Haugan, W. Holmes, A. Hornstrup, K. Jahnke, M. Kümmel, A. Kiessling, M. Kilbinger, T. Kitching, H. Kurki-Suonio, S. Ligori, P. B. Lilje, I. Lloro, E. Maiorano, O. Mansutti, O. Marggraf, K. Markovic, F. Marulli, R. Massey, S. Mei, M. Melchior, Y. Mellier, M. Meneghetti, E. Merlin, G. Meylan, M. Moresco, L. Moscardini, S. M. Niemi, J. W. Nightingale, T. Nutma, C. Padilla, S. Paltani, F. Pasian, K. Pedersen, V. Pettorino, S. Pires, G. Polenta, M. Poncet, L. A. Popa, L. Pozzetti, F. Raison, A. Renzi, J. Rhodes, G. Riccio, E. Romelli, M. Roncarelli, C. Rosset, R. Saglia, D. Sapone, B. Sartoris, P. Schneider, A. Secroun, G. Seidel, S. Serrano, C. Sirignano, G. Sirri, L. Stanco, J. L. Starck, C. Surace, P. Tallada-Crespí, I. Tereno, R. Toledo-Moreo, F. Torradeflot, I. Tutusaus, E. A. Valentijn, L. Valenziano, T. Vassallo, Y. Wang, J. Weller, G. Zamorani, J. Zoubian, and V. Scottez. Euclid: Cosmology forecasts from the void-galaxy cross-correlation function with reconstruction. *Astron. Astrophys.*, 677:A78, September 2023. doi: 10.1051/0004-6361/202346121.
- Sladana Radinović, Hans A. Winther, Seshadri Nadathur, Will J. Percival, Enrique Paillas, Tristan Sohrab Fraser, Elena Massara, and Alex Woodfinden. Alcock-Paczyński effect on void-finding: Implications for void-galaxy cross-correlation modelling. *arXiv e-prints*, art. arXiv:2407.02699, July 2024.

- Marco Raveri, Cyrille Doux, and Shivam Pandey. Understanding posterior projection effects with normalizing flows. 2024. URL <https://arxiv.org/abs/2409.09101>.
- Darren S Reed, Aurel Schneider, Robert E Smith, Doug Potter, Joachim Stadel, and Ben Moore. The same with less: the cosmic web of warm versus cold dark matter dwarf galaxies. *Monthly Notices of the Royal Astronomical Society*, 451(4):4413–4423, 2015.
- Beth Reid, Shirley Ho, Nikhil Padmanabhan, Will J Percival, Jeremy Tinker, Rita Tojeiro, Martin White, Daniel J Eisenstein, Claudia Maraston, Ashley J Ross, et al. Sdss-iii baryon oscillation spectroscopic survey data release 12: galaxy target selection and large-scale structure catalogues. *Monthly Notices of the Royal Astronomical Society*, 455(2):1553–1573, 2016.
- Adam G. Riess, Alexei V. Filippenko, Peter Challis, Alejandro Clocchiatti, Alan Diercks, Peter M. Garnavich, Ron L. Gilliland, Craig J. Hogan, Saurabh Jha, Robert P. Kirshner, B. Leibundgut, M. M. Phillips, David Reiss, Brian P. Schmidt, Robert A. Schommer, R. Chris Smith, J. Spyromilio, Christopher Stubbs, Nicholas B. Suntzeff, and John Tonry. Observational Evidence from Supernovae for an Accelerating Universe and a Cosmological Constant. *Astron. J.*, 116(3):1009–1038, September 1998. doi: 10.1086/300499.
- Adam G. Riess, Wenlong Yuan, Lucas M. Macri, Dan Scolnic, Dillon Brout, Stefano Casertano, David O. Jones, Yukei Murakami, Gagandeep S. Anand, Louise Breuval, Thomas G. Brink, Alexei V. Filippenko, Samantha Hoffmann, Saurabh W. Jha, W. D’arcy Kenworthy, John Mackenty, Benjamin E. Stahl, and WeiKang Zheng. A comprehensive measurement of the local value of the hubble constant with 1 km s⁻¹ mpc⁻¹ uncertainty from the hubble space telescope and the sh0es team. *The Astrophysical Journal Letters*, 934(1):L7, July 2022. ISSN 2041-8213. doi: 10.3847/2041-8213/ac5c5b. URL <http://dx.doi.org/10.3847/2041-8213/ac5c5b>.
- Tommaso Ronconi, Sofia Contarini, Federico Marulli, Marco Baldi, and Lauro Moscardini. Cosmic voids uncovered—first-order statistics of depressions in the biased density field. *Monthly Notices of the Royal Astronomical Society*, 488(4):5075–5084, 2019.
- Tommaso Ronconi, Andrea Lapi, Matteo Viel, and Alberto Sartori. scampy—a sub-halo clustering and abundance matching based python interface for painting galaxies on the dark matter halo/sub-halo hierarchy. *Monthly Notices of the Royal Astronomical Society*, 498(2):2095–2113, 2020.
- Ashley J. Ross, Florian Beutler, Chia-Hsun Chuang, Marcos Pellejero-Ibanez, Hee-Jong Seo, Mariana Vargas-Magaña, Antonio J. Cuesta, Will J. Percival, Angela Burden, Ariel G.

- Sánchez, Jan Niklas Grieb, Beth Reid, Joel R. Brownstein, Kyle S. Dawson, Daniel J. Eisenstein, Shirley Ho, Francisco-Shu Kitaura, Robert C. Nichol, Matthew D. Olmstead, Francisco Prada, Sergio A. Rodríguez-Torres, Shun Saito, Salvador Salazar-Albornoz, Donald P. Schneider, Daniel Thomas, Jeremy Tinker, Rita Tojeiro, Yuting Wang, Martin White, and Gong-bo Zhao. The clustering of galaxies in the completed SDSS-III Baryon Oscillation Spectroscopic Survey: observational systematics and baryon acoustic oscillations in the correlation function. *Mon. Not. R. Astron. Soc.* , 464(1):1168–1191, January 2017. doi: 10.1093/mnras/stw2372.
- Andrés N Ruiz, Dante J Paz, Marcelo Lares, Heliana E Luparello, Laura Ceccarelli, and Diego García Lambas. Clues on void evolution—iii. structure and dynamics in void shells. *Monthly Notices of the Royal Astronomical Society*, 448(2):1471–1482, 2015.
- Barbara S. Ryden. Measuring Q_0 from the Distortion of Voids in Redshift Space. *Astrophys. J.* , 452:25, October 1995. doi: 10.1086/176277.
- Martin Sahlén. Cluster-void degeneracy breaking: Neutrino properties and dark energy. *Phys. Rev. D* , 99(6):063525, March 2019. doi: 10.1103/PhysRevD.99.063525.
- Martin Sahlén and Joseph Silk. Cluster-void degeneracy breaking: Modified gravity in the balance. *Physical Review D*, 97(10):103504, 2018.
- Martin Sahlén, Íñigo Zubeldía, and Joseph Silk. Cluster-void degeneracy breaking: Dark energy, planck and the largest cluster & void. *arXiv preprint arXiv:1511.04075*, 2015.
- Martin Sahlén, Íñigo Zubeldía, and Joseph Silk. Cluster-Void Degeneracy Breaking: Dark Energy, Planck, and the Largest Cluster and Void. *Astrophys. J. Lett.* , 820(1):L7, March 2016. doi: 10.3847/2041-8205/820/1/L7.
- Ariel G. Sánchez. Arguments against using h^{-1} Mpc units in observational cosmology. *Phys. Rev. D* , 102(12):123511, December 2020. doi: 10.1103/PhysRevD.102.123511.
- Carles Sánchez, Joseph Clampitt, András Kovacs, B Jain, J García-Bellido, S Nadathur, D Gruen, N Hamaus, D Huterer, P Vielzeuf, et al. Cosmic voids and void lensing in the dark energy survey science verification data. *Monthly Notices of the Royal Astronomical Society*, page stw2745, 2016.
- E Sarpa, A Veropalumbo, C Schimd, E Branchini, and S Matarrese. Extended fast action minimization method: application to sdss-dr12 combined sample. *Monthly Notices of the Royal Astronomical Society*, 503(1):540–556, February 2021. ISSN 1365-2966. doi: 10.1093/mnras/stab378. URL <http://dx.doi.org/10.1093/mnras/stab378>.

- E Sarpa, A Longobardi, K Kraljic, A Veropalumbo, and C Schimd. Tracing the environmental history of observed galaxies via extended fast action minimization method. *Monthly Notices of the Royal Astronomical Society*, 516(1):231–244, July 2022. ISSN 1365-2966. doi: 10.1093/mnras/stac2125. URL <http://dx.doi.org/10.1093/mnras/stac2125>.
- W. E. Schaap and R. van de Weygaert. Continuous fields and discrete samples: reconstruction through Delaunay tessellations. *Astron. Astrophys.* , 363:L29–L32, Nov 2000.
- Nico Schuster, Nico Hamaus, Alice Pisani, Carmelita Carbone, Christina D. Kreisch, Giorgia Pollina, and Jochen Weller. The bias of cosmic voids in the presence of massive neutrinos. *Journal of Cosmology and Astroparticle Physics*, 2019(12):055–055, December 2019. ISSN 1475-7516. doi: 10.1088/1475-7516/2019/12/055. URL <http://dx.doi.org/10.1088/1475-7516/2019/12/055>.
- Nico Schuster, Nico Hamaus, Klaus Dolag, and Jochen Weller. Why cosmic voids matter: nonlinear structure & linear dynamics. *Journal of Cosmology and Astro-Particle Physics*, 2023(5):031, May 2023. doi: 10.1088/1475-7516/2023/05/031.
- Arman Shafieloo and Chris Clarkson. Model independent tests of the standard cosmological model. *Physical Review D—Particles, Fields, Gravitation, and Cosmology*, 81(8):083537, 2010.
- Sergei F. Shandarin. The multi-stream flows and the dynamics of the cosmic web. *Journal of Cosmology and Astro-Particle Physics*, 2011(5):015, May 2011. doi: 10.1088/1475-7516/2011/05/015.
- Sergei F Shandarin and Ya B Zeldovich. The large-scale structure of the universe: Turbulence, intermittency, structures in a self-gravitating medium. *Reviews of Modern Physics*, 61(2):185, 1989.
- Ravi K Sheth and Giuseppe Tormen. Large-scale bias and the peak background split. *Monthly Notices of the Royal Astronomical Society*, 308(1):119–126, 1999.
- Ravi K. Sheth and Rien van de Weygaert. A hierarchy of voids: much ado about nothing. *Mon. Not. R. Astron. Soc.* , 350(2):517–538, May 2004. doi: 10.1111/j.1365-2966.2004.07661.x.
- Ravi K. Sheth and Rien van de Weygaert. A hierarchy of voids: much ado about nothing. *Monthly Notices of the Royal Astronomical Society*, 350(2):517–538, May 2004. ISSN 1365-2966. doi: 10.1111/j.1365-2966.2004.07661.x. URL <http://dx.doi.org/10.1111/j.1365-2966.2004.07661.x>.

- Ravi K. Sheth, H. J. Mo, and Giuseppe Tormen. Ellipsoidal collapse and an improved model for the number and spatial distribution of dark matter haloes. *Mon. Not. R. Astron. Soc.* , 323(1):1–12, May 2001. doi: 10.1046/j.1365-8711.2001.04006.x.
- G. F. Smoot, C. L. Bennett, A. Kogut, E. L. Wright, J. Aymon, N. W. Boggess, E. S. Cheng, G. de Amici, S. Gulkis, M. G. Hauser, G. Hinshaw, P. D. Jackson, M. Janssen, E. Kaita, T. Kelsall, P. Keegstra, C. Lineweaver, K. Loewenstein, P. Lubin, J. Mather, S. S. Meyer, S. H. Moseley, T. Murdock, L. Rokke, R. F. Silverberg, L. Tenorio, R. Weiss, and D. T. Wilkinson. Structure in the COBE Differential Microwave Radiometer First-Year Maps. *Astrophys. J. Lett.* , 396:L1, September 1992. doi: 10.1086/186504.
- D. Spergel, N. Gehrels, C. Baltay, D. Bennett, J. Breckinridge, M. Donahue, A. Dressler, B. S. Gaudi, T. Greene, O. Guyon, C. Hirata, J. Kalirai, N. J. Kasdin, B. Macintosh, W. Moos, S. Perlmutter, M. Postman, B. Rauscher, J. Rhodes, Y. Wang, D. Weinberg, D. Benford, M. Hudson, W. S. Jeong, Y. Mellier, W. Traub, T. Yamada, P. Capak, J. Colbert, D. Masters, M. Penny, D. Savransky, D. Stern, N. Zimmerman, R. Barry, L. Bartusek, K. Carpenter, E. Cheng, D. Content, F. Dekens, R. Demers, K. Grady, C. Jackson, G. Kuan, J. Kruk, M. Melton, B. Nemati, B. Parvin, I. Poberezhskiy, C. Peddie, J. Ruffa, J. K. Wallace, A. Whipple, E. Wollack, and F. Zhao. Wide-field infrared survey telescope-astronomy focused telescope assets wfirst-afta 2015 report, 2015. URL <https://arxiv.org/abs/1503.03757>.
- Douglas Spolyar, Martin Sahlén, and Joe Silk. Topology and dark energy: testing gravity in voids. *Physical Review Letters*, 111(24):241103, 2013.
- Volker Springel, Naoki Yoshida, and Simon D. M. White. GADGET: a code for collisionless and gasdynamical cosmological simulations. *New Astronomy*, 6(2):79–117, April 2001. doi: 10.1016/S1384-1076(01)00042-2.
- Yasushi Suto, Katsuhiko Sato, and Humitaka Sato. Expansion of voids in a matter-dominated universe. *Progress of theoretical physics*, 71(5):938–945, 1984.
- P. M. Sutter, Guilhem Lavaux, Nico Hamaus, Benjamin D. Wandelt, David H. Weinberg, and Michael S. Warren. Sparse sampling, galaxy bias, and voids. *Mon. Not. R. Astron. Soc.* , 442(1):462–471, July 2014a. doi: 10.1093/mnras/stu893.
- P. M. Sutter, Guilhem Lavaux, Nico Hamaus, Benjamin D. Wandelt, David H. Weinberg, and Michael S. Warren. Sparse sampling, galaxy bias, and voids. *Mon. Not. R. Astron. Soc.* , 442(1):462–471, July 2014b. doi: 10.1093/mnras/stu893.

- P. M. Sutter, G. Lavaux, N. Hamaus, A. Pisani, B. D. Wandelt, M. Warren, F. Villaescusa-Navarro, P. Zivick, Q. Mao, and B. B. Thompson. VIDE: The Void IDentification and Examination toolkit. *Astronomy and Computing*, 9:1–9, March 2015. doi: 10.1016/j.ascom.2014.10.002.
- PM Sutter, Pascal Elahi, Bridget Falck, Julian Onions, Nico Hamaus, Alexander Knebe, Chaichalit Srisawat, and Aurel Schneider. The life and death of cosmic voids. *Monthly Notices of the Royal Astronomical Society*, 445(2):1235–1244, 2014.
- István Szapudi, András Kovács, Benjamin R Granett, Zsolt Frei, Joseph Silk, Will Burgett, Shaun Cole, Peter W Draper, Daniel J Farrow, Nicholas Kaiser, et al. Detection of a supervoid aligned with the cold spot of the cosmic microwave background. *Monthly Notices of the Royal Astronomical Society*, 450(1):288–294, 2015.
- Leander Thiele, Elena Massara, Alice Pisani, ChangHoon Hahn, David N. Spergel, Shirley Ho, and Benjamin Wandelt. Neutrino Mass Constraint from an Implicit Likelihood Analysis of BOSS Voids. *Astrophys. J.*, 969(2):89, July 2024. doi: 10.3847/1538-4357/ad434e.
- Anton V Tikhonov and Igor D Karachentsev. Minivooids in the local volume. *The Astrophysical Journal*, 653(2):969, 2006.
- R. van de Weygaert and E. van Kampen. Voids in Gravitational Instability Scenarios - Part One - Global Density and Velocity Fields in an Einstein - De-Sitter Universe. *Mon. Not. R. Astron. Soc.*, 263:481, July 1993. doi: 10.1093/mnras/263.2.481.
- Rien van de Weygaert and Willem Schaap. The cosmic web: Geometric analysis. *Data analysis in cosmology*, pages 291–413, 2009.
- Rien van de Weygaert and Eelco van Kampen. Voids in gravitational instability scenarios—i. global density and velocity fields in an einstein–de sitter universe. *Monthly Notices of the Royal Astronomical Society*, 263(2):481–526, 1993.
- Rien van de Weygaert, S Shandarin, E Saar, and J Einasto. The zeldovich universe: genesis and growth of the cosmic web. *The Zeldovich Universe: Genesis and Growth of the Cosmic Web*, 308, 2016.
- Punyakoti Ganeshiah Veena, Robert Lilow, and Adi Nusser. Large-scale density and velocity field reconstructions with neural networks. 12 2022. doi: 10.1093/mnras/stad1222.

- Giovanni Verza. *COSMIC VOID STATISTICS AS A PROBE FOR COSMOLOGY*. PhD thesis, Università degli studi di Padova, 2022.
- Giovanni Verza, Alice Pisani, Carmelita Carbone, Nico Hamaus, and Luigi Guzzo. The void size function in dynamical dark energy cosmologies. *Journal of Cosmology and Astro-Particle Physics*, 2019(12):040, December 2019. doi: 10.1088/1475-7516/2019/12/040.
- Giovanni Verza, Carmelita Carbone, and Alessandro Renzi. The Halo Bias inside Cosmic Voids. *Astrophys. J. Lett.*, 940(1):L16, November 2022. doi: 10.3847/2041-8213/ac9d98.
- Giovanni Verza, Carmelita Carbone, Alice Pisani, and Alessandro Renzi. DEMNUni: disentangling dark energy from massive neutrinos with the void size function. *Journal of Cosmology and Astro-Particle Physics*, 2023(12):044, December 2023. doi: 10.1088/1475-7516/2023/12/044.
- Giovanni Verza, Carmelita Carbone, Alice Pisani, Cristiano Porciani, and Sabino Matarrese. The universal multiplicity function: counting halos and voids. *arXiv e-prints*, art. arXiv:2401.14451, January 2024. doi: 10.48550/arXiv.2401.14451.
- Giovanni Verza, Giulia Degni, Alice Pisani, Nico Hamaus, Elena Massara, Andrew Benson, Stéphanie Escoffier, Yun Wang, Zhongxu Zhai, and Olivier Doré. Cosmology with voids from the nancy grace roman space telescope, 2024. URL <https://arxiv.org/abs/2410.19713>.
- Francisco Villaescusa-Navarro, ChangHoon Hahn, Elena Massara, Arka Banerjee, Ana Maria Delgado, Doogesh Kodi Ramanah, Tom Charnock, Elena Giusarma, Yin Li, Erwan Allys, Antoine Brochard, Cora Uhlemann, Chi-Ting Chiang, Siyu He, Alice Pisani, Andrej Obuljen, Yu Feng, Emanuele Castorina, Gabriella Contardo, Christina D. Kreisch, Andrina Nicola, Justin Alsing, Roman Scoccimarro, Licia Verde, Matteo Viel, Shirley Ho, Stephane Mallat, Benjamin Wandelt, and David N. Spergel. The quijote simulations. *The Astrophysical Journal Supplement Series*, 250(1):2, August 2020. ISSN 1538-4365. doi: 10.3847/1538-4365/ab9d82. URL <http://dx.doi.org/10.3847/1538-4365/ab9d82>.
- Rodrigo Voivodic, Henrique Rubira, and Marcos Lima. The halo void (dust) model of large scale structure. *Journal of Cosmology and Astroparticle Physics*, 2020(10):033, 2020.
- Yun Wang, Zhongxu Zhai, Anahita Alavi, Elena Massara, Alice Pisani, Andrew Benson, Christopher M. Hirata, Lado Samushia, David H. Weinberg, James Colbert, Olivier Doré, Tim Eifler, Chen Heinrich, Shirley Ho, Elisabeth Krause, Nikhil Padmanabhan, David Spergel, and Harry I. Teplitz. The high latitude spectroscopic survey on the nancy grace

- roman space telescope. *The Astrophysical Journal*, 928(1):1, March 2022. ISSN 1538-4357. doi: 10.3847/1538-4357/ac4973. URL <http://dx.doi.org/10.3847/1538-4357/ac4973>.
- Martin White. Reconstruction code. 2021. URL https://github.com/martinjameswhite/recon_code/blob/master/notes.pdf.
- Simon DM White. The hierarchy of correlation functions and its relation to other measures of galaxy clustering. *Monthly Notices of the Royal Astronomical Society*, 186(2):145–154, 1979.
- Radosław Wojtak, Devon Powell, and Tom Abel. Voids in cosmological simulations over cosmic time. *Monthly Notices of the Royal Astronomical Society*, 458(4):4431–4442, 2016.
- Alex Woodfinden, Seshadri Nadathur, Will J. Percival, Sladana Radinovic, Elena Massara, and Hans A. Winther. Measurements of cosmic expansion and growth rate of structure from voids in the Sloan Digital Sky Survey between redshift 0.07 and 1.0. *Mon. Not. R. Astron. Soc.*, 516(3):4307–4323, November 2022. doi: 10.1093/mnras/stac2475.
- Alex Woodfinden, Will J. Percival, Seshadri Nadathur, Hans A. Winther, T. S. Fraser, Elena Massara, Enriquer Paillas, and Slađana Radinović. Cosmological measurements from void-galaxy and galaxy-galaxy clustering in the Sloan Digital Sky Survey. *Mon. Not. R. Astron. Soc.*, 523(4):6360–6370, August 2023. doi: 10.1093/mnras/stad1725.
- Xiaoying Xu, Antonio J. Cuesta, Nikhil Padmanabhan, Daniel J. Eisenstein, and Cameron K. McBride. Measuring D_A and H at $z=0.35$ from the SDSS DR7 LRGs using baryon acoustic oscillations. *Mon. Not. R. Astron. Soc.*, 431(3):2834–2860, May 2013. doi: 10.1093/mnras/stt379.
- Lin F Yang, Mark C Neyrinck, Miguel A Aragón-Calvo, Bridget Falck, and Joseph Silk. Warmth elevating the depths: shallower voids with warm dark matter. *Monthly Notices of the Royal Astronomical Society*, 451(4):3606–3614, 2015.
- Ya. B. Zel’dovich. Gravitational instability: An approximate theory for large density perturbations. *Astron. Astrophys.*, 5:84–89, March 1970.
- Ya B Zeldovich. A hypothesis, unifying the structure and the entropy of the universe. *Monthly Notices of the Royal Astronomical Society*, 160(1):1P–3P, 1972.
- Ya B Zeldovich, J Einasto, and SF Shandarin. Giant voids in the universe. *Nature*, 300(5891):407–413, 1982.

- Zhongxu Zhai, Chia-Hsun Chuang, Yun Wang, Andrew Benson, and Gustavo Yepes. Clustering in the simulated H α galaxy redshift survey from Nancy Grace Roman Space Telescope. *Mon. Not. R. Astron. Soc.* , 501(3):3490–3501, March 2021. doi: 10.1093/mnras/staa3911.
- Paul Zivick, PM Sutter, Benjamin D Wandelt, Baojiu Li, and Tsz Yan Lam. Using cosmic voids to distinguish f (r) gravity in future galaxy surveys. *Monthly Notices of the Royal Astronomical Society*, 451(4):4215–4222, 2015.
- F. Zwicky. On the Masses of Nebulae and of Clusters of Nebulae. *Astrophys. J.* , 86:217, October 1937. doi: 10.1086/143864.